MONASH University

Physical Layer Waveform Design for High Mobility Wireless Channels

Tharaj Thaj

Doctor of Philosophy

A Thesis Submitted for the Degree of Doctor of Philosophy at
Monash University in 2022
Electrical and Computer Systems Engineering Department

Copyright notice

©Tharaj Thaj (2022).

I certify that I have made all reasonable efforts to secure copyright permissions for third-party content included in this thesis and have not knowingly added copyright content to my work without the owner's permission.

Abstract

With the advent of high-speed trains, unmanned aerial vehicles, and drones, reliable communications in high mobility wireless channels have become necessary for next-generation wireless networks. Orthogonal frequency division multiplexing (OFDM) has been the standard physical-layer modulation scheme deployed in 4G and 5G mobile systems, where the wireless channel typically exhibits time-varying multipath fading due to mobility. OFDM is known to achieve a near-capacity performance over such channels when the Doppler effect is limited but suffers from severe performance degradation in high-mobility environments. Hence, new robust modulation techniques in both slow and fast time-varying channels are needed, which is among the key areas under investigation to solve the 'reliable communications' problem for 6G wireless networks in doubly-selective wireless channels. In this thesis, we investigate new physical layer techniques for high mobility wireless channels focusing on receiver algorithms for a recently proposed waveform known as orthogonal time frequency space (OTFS) modulation.

Orthogonal time frequency and space (OTFS) is a new two dimensional (2D) modulation technique that transforms information symbols in the delay-Doppler domain to the familiar time-frequency domain by spreading all the information symbols (e.g., QAM) over both time and frequency to achieve maximum *effective* diversity. As a result, a time-frequency selective channel, due to multipath fading and mobility, is converted into a *separable* and *quasi-orthogonal* interaction, where all received information symbols experience roughly the same localized impairment. Hence, the received components in all the delay-Doppler diversity branches can be separated and coherently combined for each information symbol.

This thesis includes theoretical and experimental works focusing on the design of receiver algorithms for OTFS and related waveforms. Several theoretical works have been published since the seminal paper on OTFS was presented in 2017, with practical works being far and few, especially in academic research. So, to reduce the gap between the theoretical and practical works and to verify the advantages of OTFS over traditional modulation schemes in real-time channels, the first work we did was the implementation of OTFS on software-defined radio (SDR) platform. This was the first academic test-bed implementation of OTFS, leading to profound insights regarding the practical issues related to OTFS, including hardware impairments. One of those issues, that we focused on next, was the high complexity of detection.

Traditional linear equalization techniques incur a polynomial complexity per information symbol and do not take advantage of the sparsity of the channel matrix available in the delay-Doppler domain. To this effect, we proposed a significant improvement with a new iterative Rake detection receiver based on maximal ratio combining (MRC) by taking

advantage of the special structure of the OTFS channel matrix. The Rake detector can be implemented with a complexity that scales only linearly with the number of delay paths in the channel and is independent of the QAM size and the channel Doppler spread, making it convenient for high mobility wireless channels. Further, the low complexity detection algorithms for single-input single-output (SISO) OTFS were extended to the multiple-input multiple-output (MIMO) OTFS case, considering the practical degrading effects of spatial correlation at the transmitter and receiver and methods to compensate for the same.

Finally, intending to design novel waveforms that can outperform OTFS in either detection complexity or error performance, we proposed a new waveform, orthogonal time sequency multiplexing (OTSM), based on the Walsh-Hadamard transform (WHT). Like OTFS, OTSM also spreads information symbols in all the sub-carriers and time-slots using 2-D orthogonal basis functions. We then generalized such modulation schemes as a family of unitary-precoded single-carrier waveforms by replacing the DFT (or WHT in the case of OTSM) with any unitary transform. Finally, the low complexity receiver design and real-time implementation using an SDR platform is done to validate the performance of USC waveforms in practical environments.

Thesis including published works declaration

I hereby declare that this thesis contains no material which has been accepted for the award of any other degree or diploma at any university or equivalent institution and that, to the best of my knowledge and belief, this thesis contains no material previously published or written by another person, except where due reference is made in the text of the thesis.

This thesis includes 5 original papers published in peer reviewed journals. The core theme of the thesis is Thesis by Publication. The ideas, development and writing up of all the papers in the thesis were the principal responsibility of myself, the student, working within the Electrical and Computer Systems department under the supervision of Prof. Emanuele Viterbo.

In the case of 2, 3, 4, 5 and 6 my contribution to the work involved the following:

(The inclusion of co-authors reflects the fact that the work came from active collaboration between researchers and acknowledges input into team-based research.)

Thesis Chapter	Publication Title	Status (published in press, accepted or returned for revision, submitted)	Nature and % of student contribution	Co-author name(s), Nature and % of Co-author's contribution*	Co-author(s), Monash student Y/N*
2	OTFS Modem SDR Implementation and Experimental Study of Receiver Impairment Effects	Published	70%. Concept, theoretical calculations, practical implementation, writing the paper.	1) E. Viterbo, 30% concept and revision	No
3	Low Complexity Iterative Rake Decision Feedback Equalizer for Zero-Padded OTFS Systems	Published	70%. Concept, theoretical calculations, writing the paper.	1) E. Viterbo, 30% concept and revision	No
4	Low-Complexity Linear Diversity-Combining Detector for MIMO-OTFS	Published	70%. Concept, theoretical calculations, writing the paper.	1) E. Viterbo, 30 % concept and revision	No
5	Orthogonal Time Sequency Multiplexing Modulation: Analysis and Low-Complexity Receiver Design	Published	50%. Concept, theoretical calculations, writing the paper.	1) E. Viterbo, 30% concept and revision 2) Y. Hong, 20% writing and revision	No
6	Unitary-Precoded Single-Carrier Waveforms for High Mobility: Detection and Channel Estimation	Accepted	70%. Concept, theoretical calculations, writing the paper.	1) E. Viterbo, 30% concept and revision	No

I have renumbered sections of submitted or published papers in order to generate a consistent presentation within the thesis.

Student name: Tharaj Thaj

Student signature: **Date:** 29-04-2022

I hereby certify that the above declaration correctly reflects the nature and extent of the student's and co-authors' contributions to this work. In instances where I am not the responsible author I have consulted with the responsible author to agree on the respective contributions of the authors.

Main Supervisor name: Prof. Emanuele Viterbo

Main Supervisor signature: **Date:** 29-04-2022

Publications during enrolment

Conference(s)

1) T. Thaj and E. Viterbo, "OTFS Modem SDR Implementation and Experimental Study of Receiver Impairment Effects," *IEEE International Conference on Communications Workshops (ICC Workshops)*, Shanghai, China, May 2019.

2) T. Thaj and E. Viterbo, "Low Complexity Iterative Rake Detector for Orthogonal Time Frequency Space Modulation," in *Proc. IEEE Wireless Communications and Networking Conference (WCNC)*, Seoul, Korea (South), May 2020.

3) T. Thaj and E. Viterbo,"Orthogonal Time Sequency Multiplexing Modulation," *Proc. IEEE Wireless Communications and Networking Conference (WCNC)*, 2021, pp. 1-7, doi: 10.1109/WCNC49053.2021.9417451.

4) T. Thaj, and E. Viterbo. "Unitary-Precoded Single-Carrier Waveforms for High Mobility: Detection and Channel Estimation" Accepted in *Proc. IEEE Wireless Communications and Networking Conference (WCNC) 2022*, doi: arXiv:2201.10218

Journal(s)

5) T. Thaj and E. Viterbo, "Low Complexity Iterative Rake Decision Feedback Equalizer for Zero-Padded OTFS Systems," in *IEEE Transactions on Vehicular Technology*, vol. 69, no. 12, pp. 15606-15622, Dec. 2020, doi: 10.1109/TVT.2020.3044276.

6) T. Thaj, E. Viterbo and Y. Hong,"Orthogonal Time Sequency Multiplexing Modulation: Analysis and Low-Complexity Receiver Design" in *IEEE Transactions on Wireless Communications*, vol. 20, no. 12, pp. 7842-7855, Dec. 2021, doi: 10.1109/TWC.2021.3088479.

7) T. Thaj and E. Viterbo, "Low-Complexity Linear Diversity-Combining Detector for MIMO-OTFS," in *IEEE Wireless Communications Letters*, vol. 11, no. 2, pp. 288-292, Feb. 2022, doi: 10.1109/LWC.2021.3125986.

Book(s)

8) Y. Hong, T. Thaj, E. Viterbo, "Delay-Doppler Communications: Principles and Applications", Academic Press, 2022, ISBN:9780323850285

Acknowledgements

First and foremost, I would like to express my sincere gratitude to my main supervisor, Prof. Emanuele Viterbo, for accepting me as a Ph.D. student. He was always available for discussions, technical and otherwise, leading to the conception of many ideas organically that was eventually published and are presented in this work. His vast experience in communications played a crucial role in helping select the research problem and methods to tackle it. I am incredibly grateful for his help and advice and for being a constant source of motivation throughout the course.

I would like to sincerely thank Dr. Yi Hong, who played a significant role in providing insightful comments and suggestions and helping in preparing publications. I am thankful and honored for allowing me to write a scientific book alongside her as a co-author. I sincerely thank Emanuele and Yi for their valuable contribution to my research and publication work.

I am particularly grateful for the financial assistance provided by Monash University and the Faculty of Engineering, ECSE Department, to pursue my Ph.D. through the Monash Graduate Scholarship (MGS) and Faculty of Engineering International Postgraduate Research Scholarship (FEIPRS). This work in this thesis was supported by the Australian Research Council (ARC) through the Discovery Project under Grant DP200100096.

I would also like to express my heartfelt appreciation to Dr. Harish and my co-supervisor Dr. Raviteja, who helped make my transition to life in Melbourne smooth also by helping with and providing much-needed guidance for all matters, including technical writing, seminar, and presentations. I would also like to thank my lab mates and friends, Dr. Vidhuranga, Dr. Rowshan, and Dr. Fariba, for the endless support and discussions.

Last but not least, I would like to thank my parents, Mrs. Mariamma and Mr. Thajudeen, for always being my pillar of support and encouragement especially in these testing times.

Contents

Copyright notice i

Abstract ii

Thesis including published works declaration iv

Publications during enrolment vii

Acknowledgements viii

List of Figures xi

Abbreviations xii

1 Research Aims, Background and Structure 1
- 1.1 Motivation . . . 1
- 1.2 Literature Survey . . . 2
  - 1.2.1 Wireless Channel Representation . . . 3
    - 1.2.1.1 Continuous-time baseband channel model . . . 3
    - 1.2.1.2 Discrete-time baseband channel model . . . 6
  - 1.2.2 OFDM modulation . . . 7
    - 1.2.2.1 OFDM drawbacks . . . 9
  - 1.2.3 OTFS modulation . . . 11
    - 1.2.3.1 System Model . . . 11
    - 1.2.3.2 Input-Output Relation . . . 12
    - 1.2.3.3 OTFS vs OFDM . . . 14
- 1.3 Thesis Format . . . 15
  - 1.3.1 Theme Selection . . . 15
  - 1.3.2 Structure . . . 15
- 1.4 Research Questions . . . 20

2 OTFS Modem SDR Implementation and Experimental Study of Receiver Impairment Effects 30

3 Low Complexity Iterative Rake Decision Feedback Equalizer for Zero-Padded OTFS Systems 37

4 Low-Complexity Linear Diversity-Combining Detector for MIMO-OTFS 55

5 Orthogonal Time Sequency Multiplexing Modulation: Analysis and Low-Complexity Receiver Design **61**

6 Unitary-Precoded Single-Carrier Waveforms for High Mobility: Detection and Channel Estimation **77**

7 Conclusion and Future Directions **84**

7.1 Contributions 84

7.1.1 Brief answers to research questions 86

7.2 Future Directions 89

List of Figures

1.1 Different representations of a time-variant multipath channel 4
1.2 Channel in Time–frequency $H(t, f)$ and delay–Doppler $h(\tau, \nu)$ 5
1.3 CP-OFDM system model 8
1.4 OTFS system model for rectangular pulse shaping waveforms 12
1.5 OTFS signals 14

Abbreviations

4G	**F**ourth Generation
5G	**F**ifth Generation
AD	**A**nalog to **D**igital
BER	**B**it **e**rror **r**ate
AWGN	**A**dditive **W**hite **G**uassian **N**oise
BER	**B**it **E**rror **R**ate
CFO	**C**arrier **F**requency **O**ffset
CP	**C**yclic **P**refix
DA	**D**igital to **A**nalog
DFT	**D**iscrete **F**ourier **T**ransform
DC	**D**irect **C**urrent
DZT	**D**iscrete **Z**ak **T**ransform
FBMC	**F**ilter **B**ank **M**ulti-**C**arrier
GFDM	**G**eneralized **F**requency **D**ivision **M**ultiplexing
UFMC	**U**niversal **F**iltered **M**ulti-**C**arrier
FFT	**F**ast **F**ourier **T**ransform
ICI	**I**nter **C**arrier **I**nterference
ISI	**I**nter **S**ymbol **I**nterference
IFFT	**I**nverse **F**ast **F**ourier **T**ransform
ISFFT	**I**nverse **S**ymplectic **F**ast **F**ourier **T**ransform
IQI	**I**nphase **Q**uadrature **I**mbalance
LTE	**L**ong **T**erm **E**volution
LTI	**L**inear **T**ime-**I**nvariant
LTV	**L**inear **T**ime-**V**ariant
MMSE	**M**inimum **M**ean **S**quare **E**rror

MP	**M**essage **P**assing
MRC	**M**aximal **R**atio **C**ombining
MTC	**M**achine **T**ype **C**ommunications
MIMO	**M**ultiple-**I**nput **M**ultiple-**O**utput
OFDM	**O**rthogonal **F**requency **D**ivision **M**ultiplexing
OTFS	**O**rthogonal **T**ime **F**requency **S**pace
PA	**P**ower **A**mplifier
PAPR	**P**eak-to-**Average** Power Ratio
QAM	**Q**uadrature **A**mplitude **M**odulation
SFFT	**S**ymplectic **F**ast **F**ourier **T**ransform
SISO	**S**ingle **I**nput **S**ingle **O**utput
SC	**S**ingle **C**arrier
SNR	**S**ignal-to-**N**oise **R**atio
SIC	**S**uccessive **I**nterference **Cancellation**
USC	**U**nitary-Precoded **S**ingle **C**arrier
WHT	**W**alsh **Hadamard T**ransform
ZP	**Z**ero **P**adding
ZF	**Z**ero **F**orcing

Chapter 1

Research Aims, Background and Structure

1.1 Motivation

Next-generation communication networks are expected to deal with many fold increase in traffic requirements with some of the broad range of use cases, including enhanced mobile broadband, massive machine-type communications (MTC), and critical MTC covering frequency ranges up to hundreds of GHz [1, 2, 4]. The development of physical layer techniques such as waveform design, spectrum shift towards very high frequencies, and massive multiple-input multiple-output (MIMO) based multiuser systems are some of the fundamental research directions that are being investigated to satisfy some of the future network requirements discussed above. With the advent of high-speed rails, autonomous vehicles, and drones, other set of challenges that have gained considerable attraction include reliable communications, accurate position tracking and localization in high mobility wireless channels, making it an integral part of the 6G communications, [5]. Most of the current communications systems are designed for users with low or medium mobility, and high mobility significantly limits the coverage area and transmission rate, [6]. This thesis focuses on physical layer techniques to improve the performance of communications systems in high mobility wireless channels.

Waveform design refers to the strategies for packing information symbols in a given bandwidth and time resource and forms the basic building block of communications systems.

Waveform design should satisfy a comprehensive set of metrics that can include orthogonality of the basis functions in a multipath channel, ease of channel estimation with low pilot overhead, the complexity of equalization, out of band (OOB) emission, low peak-to-average power ratio (PAPR), robustness to synchronization errors and performance and complexity of detection and channel estimation in multiuser and point to point MIMO systems. Cyclic prefix (CP) based orthogonal frequency division multiplexing (OFDM) has been the standard waveform used for deployment in 4G LTE owing to its low complexity of equalization and control over the time-frequency resources. However, high mobility may cause wide Doppler spreads resulting in significant inter-carrier interference leading to performance degradation in current communications systems based on the traditional OFDM waveform. Therefore it is imperative to develop new theories and technologies explicitly designed for high mobility environments, [6]. Further, they should be able to cope with the challenges and take advantage of the opportunities of high mobility communications.

In this thesis, we focus on the physical layer design of waveforms to combat the effects of multipath fading in a time-variant wireless channel. A new modulation scheme called orthogonal time frequency space (OTFS) was proposed recently in [7] that shows significant performance gains over OFDM and its' variants in time-variant wireless channels. In the next section, we present some background on wireless channels, provide an overview of OFDM and present some basic concepts of OTFS modulation. Finally, we elaborate on our detailed chapter-wise contributions in this thesis, followed by some research questions answered through this thesis.

1.2 Literature Survey

This section starts with some background on the different representations of the wireless channel, followed by an overview of the CP-OFDM waveform. Finally, we introduce the basic concepts of OTFS modulation with more details covered in the subsequent chapters.

Notations: The following notations are used: a, $\mathbf{a}$, $\mathbf{A}$ represent a scalar, vector, and matrix, respectively; $\mathbf{a}(n)$ and $\mathbf{A}(m,n)$ represent the n-th and (m,n)-th element of $\mathbf{a}$ and $\mathbf{A}$, respectively; $\mathbf{A}^{\dagger}$, $\mathbf{A}^{*}$ and $\mathbf{A}^{n}$ represent the Hermitian transpose, complex

conjugate and n-th power of $\mathbf{A}$. The set of $M \times N$ dimensional matrices with complex entries are denoted by $\mathbb{C}^{N \times M}$. Let $\circledast$ represent circular convolution, $\otimes$, the Kronecker product, $\circ$, the Hadamard product (i.e., the element wise multiplication) and, $\oslash$, the Hadamard division (i.e., the element wise division). Let $[.]_M$ denote the modulo-M operation, $|\mathcal{S}|$ the cardinality of the set $\mathcal{S}$, $\mathrm{tr}(A)$, the trace of the square matrix $\mathbf{A}$, $\mathrm{vec}(\mathbf{A})$, the column-wise vectorization of the matrix $\mathbf{A}$ and $\mathrm{vec}^{-1}_{N,M}(\mathbf{a})$ is the matrix formed by folding a vector $\mathbf{a}$ into a $N \times M$ matrix by filling it column wise. Let $\mathbf{F}_N$ and $\mathbf{W}_N$ be the normalized N point discrete Fourier transform (DFT) matrix and the normalized N-point WHT matrix, respectively.

1.2.1 Wireless Channel Representation

Any signal transmitted into the air undergoes variations due to the physical characteristics of the propagation medium as well as the relative position of the transmitter, receiver and scatterers, commonly termed as fading. Fading is broadly classified into *large scale* and *small scale* fading. Large scale fading deals with variations in signal level due to transmission over a large area (such as path-loss and shadowing) whereas small scale fading is variation in the signal level due to the presence of obstacles in the vicinity of the receiver. Waveform design in a communications system is primarily aimed at compensating the effect of small scale fading at the receiver. Therefore, in the following, we focus on the channel representation of small scale fading which arises as a result of the multipath propagation of the transmitted signal.

1.2.1.1 Continuous-time baseband channel model

Consider a transmitted signal $s(t)$ of duration T_{f} transmitted into the wireless channel at a carrier frequency f_c occupying the band $[f_c - B/2, f_c + B/2]$. After the transmitted signal passes through a *linear time-invariant* (LTI) wireless multipath channel, the received signal will be an aggregation of the delayed reflections of the transmitted signal due to the scatterers in the vicinity of the receiver. The delay depends on the distance of each propagation path relative to the shortest path, which more often is the line-of-sight (LOS) path. The received signal $r(t)$ can then be written as

$$r(t) = \int_{\tau} g(\tau) s(t - \tau) d\tau \tag{1.1}$$

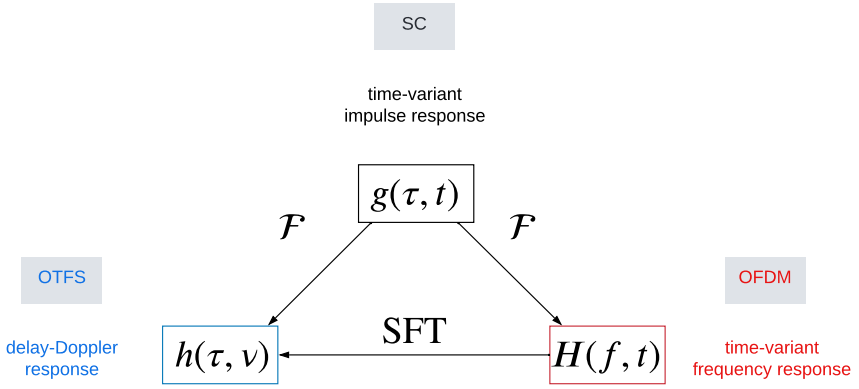

FIGURE 1.1: Different representations of a time-variant multipath channel

where $g(\tau)$ is channel impulse response. For an LTI channel, the received signal is simply the convolution of the transmitted signal with the impulse response.

However, LTI system model is not sufficient to represent a mobile wireless channel where the terminals and scatterers are in relative motion. In such channels, the received echoes of the transmit signal are not only delayed, but also Doppler shifted resulting in a *linear time-variant* (LTV) channel. Such multipath fading channels can be modeled as a time-varying impulse response or a time-varying frequency response given as,

$$r(t) = \int_{\tau} g(\tau, t)s(t-\tau)d\tau \tag{1.2}$$

$$= \int_{f} H(f, t)S(f)e^{j2\pi ft}df \tag{1.3}$$

where $g(\tau, t)$ is the time-varying impulse or the delay-time channel response and $H(f, t)$ is the time-varying frequency response of the wireless channel.

This is the appropriate representation for wireless OFDM based systems like long-term evolution (LTE). In LTE, the frequency response is estimated for every OFDM symbol to equalize the channel. Higher mobility results in a faster variation of the multipath components. Since constructive and destructive addition of these multipath components causes signal fading, faster variation of these components leads to more rapid fluctuations in the channel. The frequency response rate of variation is also proportional to the signal carrier frequency. Thus, the faster the reflectors, transmitters, and/or receivers move, the higher the frequency band, the more rapidly the channel frequency response changes occur. As the channel coherence time in the time-frequency domain is the inverse of

its Doppler, the impulse response for this channel varies rapidly over a fraction of a millisecond. Hence, in an LTE/OFDM system, there is insufficient time to estimate the channel, let alone provide feedback of the channel state to the transmitter. Compared to the time-varying impulse response, or time-varying frequency response, the delay Doppler representation of the channel varies much slower over a longer observation time. The received signal can also be written in terms of the delay-Doppler channel response as

$$r(t) = \int_{\tau} \int_{\nu} h(\tau, \nu) s(t - \tau) e^{j2\pi\nu t} d\tau d\nu \tag{1.4}$$

The delay-time, frequency-time and delay-Doppler channel responses are all related using Fourier transforms as shown in Fig. 1.1. The modulation schemes that operate in each of these domains are also labelled alongside, i.e., single-carrier (SC) operates in the delay-time domain, OFDM in the time-frequency domain and OTFS in the delay-Doppler domain. The frequency-time response is obtained by applying a Fourier transform along the delay dimension of the delay-time response. On the other hand, the delay-Doppler response is obtained by applying a Fourier transform along the time dimension of the delay-time response. Finally time-frequency and delay-Doppler channels are related by the two-dimensional symplectic Fourier transform as

$$h(\tau, \nu) = \int \int H(t, f) e^{-j2\pi(\nu t - f\tau)} dt df \tag{1.5}$$

$$H(t, f) = \int \int h(\tau, \nu) e^{j2\pi(\nu t - f\tau)} d\tau d\nu \tag{1.6}$$

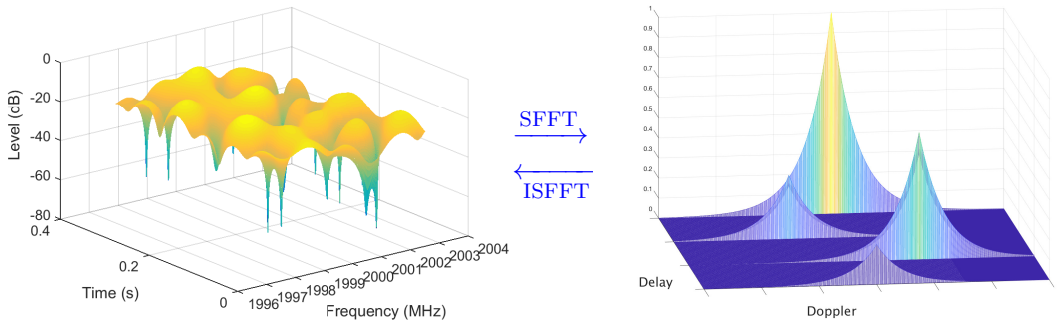

FIGURE 1.2: Channel in Time–frequency $H(t, f)$ and delay–Doppler $h(\tau, \nu)$

Fig. 1.2 shows a typical time-frequency (left) and delay-Doppler (right) channel response for a doubly-selective channel related by the symplectic fast Fourier transform (SFFT).

It can be observed that the channel representation is sparse in the delay-Doppler domain and can be represented using fewer coefficients as compared to the rapidly fluctuating time-frequency channel.

1.2.1.2 Discrete-time baseband channel model

In the previous section, we looked at a continuous representation of the channel. Any practical receiver can observe only a limited number of samples and therefore it is useful to look at the discrete-time baseband model of the channel. Let $\mathbf{s}$ and $\mathbf{r}$ be the transmitted and received discrete-time signal obtained by sampling $s(t)$ and $r(t)$, respectively, at $B = M\Delta f$ [Hz] such that $\mathbf{s}[q] = s(t = \frac{q}{B})$ and $\mathbf{r}[q] = r(t = \frac{q}{B})$. Let $T_{\mathrm{f}} = NT$ be the duration of the frame such that $T = \frac{1}{\Delta f}$, i.e., the signal is critically sampled for any pulse shaping waveform. Consider a wireless channel with P propagation paths with g_i, τ_i and ν_i be the channel gain, delay and Doppler-shift corresponding to the i-th propagation path. The delay-Doppler response provides a sparse representation of the channel given as

$$h(\tau, \nu) = \sum_{i=1}^{P} g_i \delta(\tau - \tau_i)\delta(\nu - \nu_i) \tag{1.7}$$

Let l_i and k_i be the *normalized* delay and *normalized* Doppler-shift such that

$$\tau_i = \frac{l_i}{B}, \quad \nu_i = \frac{k_i}{T_{\mathrm{f}}} \tag{1.8}$$

For ease of discussion, we assume that the normalized delay and Doppler shifts l_i and k_i are integers. The case with the more practical non-integer cases are investigated in Chapter 3. The received signal $\mathbf{r}$ after passing $\mathbf{s}$ through a LTV channel with P paths can be written as

$$\mathbf{r}[q] = \sum_{i=1}^{P} g_i e^{j\frac{2\pi}{NM}k_i(q-l_i)}\mathbf{s}[q - l_i] + \mathbf{w}[q], \quad q \in \mathbb{Z} \tag{1.9}$$

where $\mathbf{w}[q]$ is the AWGN noise with variance σ_w^2. The discrete delay-time channel response $\bar{g}[l, q] = g(\tau, t)$ at delay shift $\tau = l/B$ and sampling instant $t = q/B$ is given as

$$\bar{g}[l, q] = \sum_{i=1}^{P} g_i e^{j\frac{2\pi}{NM}k_i(q-l_i)}\delta[l - l_i] \tag{1.10}$$

The delay-time and delay-Doppler channel responses in the case of fractional delay and Doppler-shifts is investigated in Chapter 3. The general theory to model wireless channels can be found in [8–10]. High mobility time-varying channels and their delay-Doppler representation are specifically discussed in [11].

1.2.2 OFDM modulation

The basic idea of OFDM is to multiplex information symbols on closely spaced sub-carriers that are orthogonal to each other. This is achieved by choosing the sub-carrier frequency to be integer multiples of $\frac{1}{T}$, where T is the duration of an OFDM symbol. As a result, the orthogonality of these sub-carriers remains intact in a *frequency-selective* multipath channel, and the wireless channel is converted into M parallel sub-channels corresponding to the M orthogonal sub-carriers. The key advantage due to this orthogonality is the low complexity of equalization facilitated by the fact that there is no inter-carrier interference (ICI) and inter-symbol interference (ISI) (due to CP/ZP).

Consider an OFDM symbol with bandwidth $B = M\Delta f$ and duration T, where M is the number of sub-carriers and $\Delta f = \frac{1}{T}$ is the sub-carrier spacing. Let $\mathbf{x}$ be the vector containing the M information symbols (for example: QAM). The $M \times 1$ time domain samples $\mathbf{s}$ are generated as

$$\mathbf{s} = \mathbf{F}_M^{\dagger} \cdot \mathbf{x} \tag{1.11}$$

where $\mathbf{F}_M$ is the *normalized* M-point DFT matrix. A CP is added to the start by copying the last $l_{\max}$ samples of the OFDM symbol where $l_{\max}$ is the maximum discrete delay spread. The time domain samples are digital to analog (DA) converted and transmitted into the physical medium.

At the receiver, let $\mathbf{r}$ be the discrete-time signal obtained after analog to digital (AD) conversion and sampling at $M\Delta f$ [Hz]. The transmitter operations are then reversed to get back the received frequency domain symbols. An M-point FFT is applied on the discrete-time samples $\mathbf{r}$ to get the received frequency domain symbols $\mathbf{y}$ as

$$\mathbf{y} = \mathbf{F}_M \cdot \mathbf{r} \tag{1.12}$$

Figure 1.3 shows the block diagram for the CP-OFDM system. The DA and AD converter blocks are omitted for brevity.

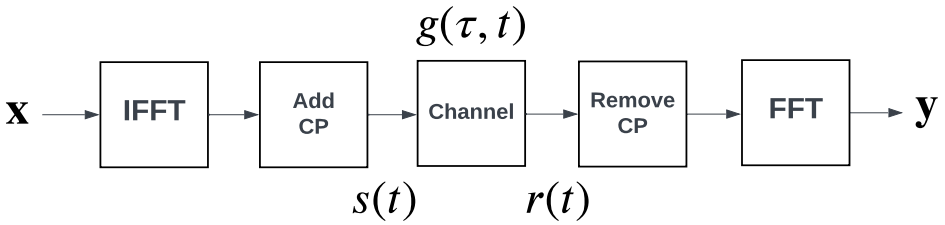

FIGURE 1.3: CP-OFDM system model

Now, let us take a look at how a typical wireless channel affects the frequency domain information symbols. First, consider a frequency-selective *only* multipath channel with P paths, i.e., $k_i = 0 \; \forall \; i =\in \{0, \ldots, P\}$. From (1.9), the received signal $\mathbf{r}$ after passing $\mathbf{s}$ through the channel can be written as

$$\mathbf{r}[q] = \sum_{i=1}^{P} g_i \mathbf{s}[q - l_i]_M + \mathbf{w}[q], \quad q = 0, \ldots, M-1 \tag{1.13}$$

where $\mathbf{w}[q]$ is the AWGN noise with variance σ_w^2. The modulo-M operation in (1.13) is due to the CP. The time domain input-output relation can be written in the vector form as

$$\mathbf{r} = \mathbf{g} \circledast \mathbf{s} + \mathbf{w} \tag{1.14}$$

where $\mathbf{g}[l] = \sum_{i=1}^{P} g_i \delta[l - l_i]$. It can be noted from (1.14) that due to the CP, the received signal is the output of a time domain circular convolution between the transmitted OFDM symbol and the wireless channel. This property is critical as it enables the design of low complexity equalizers for OFDM, which will be discussed shortly. Substituting (1.14) in (1.12) (and omitting noise for brevity), we get

$$\begin{aligned} \mathbf{y} &= \mathbf{F}_M \cdot \mathbf{r} \\ &= \mathbf{F}_M \cdot (\mathbf{g} \circledast \mathbf{s}) && (1.15) \\ &= (\mathbf{F}_M \cdot \mathbf{g}) \circ (\mathbf{F}_M \cdot \mathbf{s}) && (1.16) \\ &= \mathbf{h} \circ \mathbf{x} && (1.17) \end{aligned}$$

where $\circ$ denotes element-wise multiplication and $\mathbf{h} \in \mathbb{C}_{M \times 1}$ is the frequency domain channel. The steps in (1.15) and (1.16) are as a result of the multiplication and convolution property of DFT, which states that the circular convolution between two equal length vectors $\mathbf{a}$ and $\mathbf{b}$ is converted to element-wise multiplication in the Fourier domain, i.e., FFT$\{\mathbf{a} \circledast \mathbf{b}\}$=FFT$\{\mathbf{a}\}\circ$ FFT$\{\mathbf{b}\}$. As a result a convolutional channel in the time

domain is converted to element-wise multiplication in the frequency domain as

$$\mathbf{y}[m] = \mathbf{h}[m]\mathbf{x}[m] + \mathbf{w}[m] \tag{1.18}$$

The information symbols can then be easily estimated using a zero-forcing equalizer as

$$\hat{\mathbf{x}}[m] = \frac{\mathbf{y}[m]}{\mathbf{h}[m]} \tag{1.19}$$

A ZF equalizer may lead to noise enhancement when the channel gain $\mathbf{h}[m]$ is small. We can use the MMSE equalizer instead as

$$\hat{\mathbf{x}}[m] = \frac{\mathbf{h}^*[m]\mathbf{y}[m]}{\mathbf{h}^*[m]\mathbf{h}[m] + \sigma_w^2} \tag{1.20}$$

It is clear from (1.19) and (1.20) that equalization for OFDM in a static channel with just delay spread is simple and of low complexity. Theory and practice of OFDM techniques for wireless communications were presented in [12]. Readers can refer to [13–17] for a background on pulse shaping designs for OFDM, based on various optimization criteria. For analysis of multicarrier modulation schemes proposed as improvements over OFDM such as FBMC, UFMC, and GFDM see [18–25]. We now discuss some major drawbacks of OFDM in the following.

1.2.2.1 OFDM drawbacks

- **Unequal sub-carrier gains in a multipath channel:** CP-OFDM converts a multipath channel with no Doppler spread into a multiplicative channel in the time-frequency domain, with each sub-carrier acting as a parallel channel. The advantage is the ease of equalization, as shown in the previous section. However, the channel delay spread may lead to unequal sub-carrier gains, and the worst sub-carrier may dominate the overall system performance. As done in GFDM and FBMC, one solution to this is spreading the information symbols on multiple independent sub-carriers (through some form of filtering) so that even if one of the sub-carriers has a low channel gain, there is still a chance of recovering the information symbols from the other sub-carriers. However, this solution comes at the cost of loss of orthogonality, leading to increased detection complexity.

- **ICI due to high mobility channels:** Consider a mobile channel where each propagation path is characterized by its channel gain g_i, *normalized* delay l_i and *normalized* Doppler shifts k_i (normalized as given in 1.8). The time domain input-output relation in (1.13) can be modified to include the effects of Doppler spread as

$$\mathbf{r}[q] = \sum_{i=1}^{P} g_i e^{j\frac{2\pi}{NM}k_i(q-l_i)}\mathbf{s}[q-l_i]_M + \mathbf{w}[q], \quad q = 0, \ldots, M-1 \tag{1.21}$$

  It can be noted that Doppler shifts result in a time-varying phase $e^{j\frac{2\pi}{NM}k_i(q-l_i)}$ due to which the time-domain input-output relation is no more a circular convolution as given in (1.14). This additional phase shift results in inter-carrier interference (ICI) in the time-frequency domain:

$$\mathbf{y}[m] = \mathbf{h}[m]\mathbf{x}[m] + \text{ICI} + \mathbf{w}[m] \tag{1.22}$$

  The ICI leads to performance degradation if the simple equalization methods given in (1.19) and (1.20) are used.

- **Sensitivity to synchronization errors:** One of the main drawbacks of OFDM is its requirement for proper synchronization. Error in the estimation of the CFO in OFDM leads to a loss of orthogonality across sub-carriers. This leads to severe performance degradation due to ICI. Though this drawback is easily rectified using synchronization, the complexity and time spent on these procedures cost us in terms of overheads and latencies.

- **High overhead due to channel estimation:**

  In the case of a static or frequency-selective only channel, different sub-carriers may experience different gains, but it does not change over time. As a result, the channel experienced by an OFDM symbol will roughly be the same and hence can be re-used for the next time slot. However, in a double-selective channel, the pilots need to be interleaved along the sub-carriers and time-slots to capture and reconstruct the rapidly fluctuating time-frequency channel. The number of pilots required increases with increasing UE speed leading to very high overhead in high mobility channels. The solution for OFDM channel estimation in time variant channels are often a trade off between pilot overhead, spectral efficiency and computational complexity, some of which are discussed in [26–32].

1.2.3 OTFS modulation

OTFS is a recently proposed modulation scheme where the information symbols are multiplexed in the delay-Doppler domain, [7]. As a result, all the information symbols are spread in the entire available time-frequency resource using 2-D orthogonal basis functions. This is unlike the traditional OFDM scheme, where each information symbol occupies only a fraction of the available time frequency resource.

1.2.3.1 System Model

Consider an OTFS frame of bandwidth $B = M\Delta f$ and duration NT, where M and N are the number of sub-carriers and time slots, respectively, and $\Delta f = \frac{1}{T}$ is the sub-carrier spacing. Let $\mathbf{X}$ be the $M \times N$ containing the MN information symbols (for example: QAM). The time frequency samples are generated from the delay-Doppler domain information symbols using the ISFFT operation as

$$\mathbf{X}_{\text{tf}} = \mathbf{F}_M \cdot \mathbf{X} \cdot \mathbf{F}_N^{\dagger} \tag{1.23}$$

Finally, the time domain samples to be DA converted and transmitted into the physical medium are generated from the time-frequency domain using the Heisenberg transform as

$$\mathbf{s} = \text{vec}\left(\mathbf{G}_{\text{tx}} \cdot \mathbf{F}_M^{\dagger} \cdot \mathbf{X}_{\text{tf}}\right) \tag{1.24}$$

where $\mathbf{G}_{\text{tx}} \in \mathbb{C}^{M\times M}$ is the pulse shaping waveform at the transmitter and has the samples of the transmit pulse $p_{\text{tx}}(t)$ as its entries: $\mathbf{G}_{\text{tx}} = \text{diag}[p_{\text{tx}}(0), p_{\text{tx}}(T/M), \ldots, p_{\text{tx}}((M-1)T/M)] \in \mathbb{C}^{M\times M}$. Depending on the OTFS variant, a single CP/ZP or multiple CP/ZPs of length $l_{\max}$ are added to the time-domain samples before being DA converted and transmitted into the physical medium. The different variants are discussed in detail in [77].

In this section we consider an OTFS frame with a single CP per frame or reduced CP (RCP). At the receiver, let $\mathbf{r} \in \mathbb{C}^{NM\times 1}$ be the discrete-time signal obtained after AD conversion, sampling at $M\Delta f$ [Hz] and the CP/ZP removal. The transmitter operations are then reversed to get back the received frequency domain symbols. An M-point FFT is applied on the discrete samples $\mathbf{r}$ to get the received time-frequency domain symbols

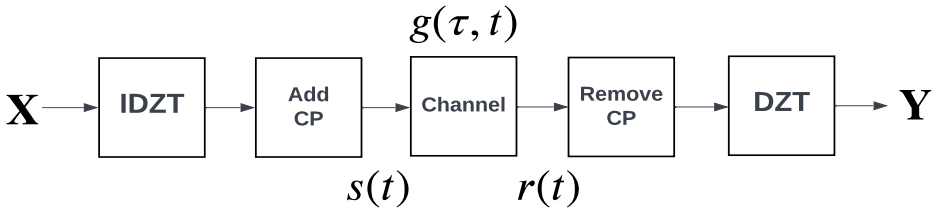

FIGURE 1.4: OTFS system model for rectangular pulse shaping waveforms

y as

$$\mathbf{Y}_{\text{tf}} = \mathbf{F}_M \cdot \text{vec}^{-1}_{M\times N}\left(\mathbf{G}_{\text{rx}} \cdot \mathbf{r}\right) \tag{1.25}$$

where $\mathbf{G}_{\text{rx}}$ denotes the receiver pulse shaping waveform and has the samples of the receiver pulse $p_{\text{rx}}(t)$ as its entries: $\mathbf{G}_{\text{rx}} = \text{diag}[p_{\text{rx}}(0), p_{\text{rx}}(T/M), \ldots, p_{\text{rx}}((M-1)T/M)] \in \mathbb{C}^{M\times M}$. The delay-Doppler received symbols are then obtained by an SFFT operation on the time-frequency samples as

$$\mathbf{Y} = \mathbf{F}^{\dagger}_M \cdot \mathbf{Y}_{\text{tf}} \cdot \mathbf{F}_N \tag{1.26}$$

For rectangular pulse shaping waveforms, i.e., $\mathbf{G}_{\text{tx}} = \mathbf{G}_{\text{rx}} = \mathbf{I}_M$, the two-step modulation in (1.23,1.24) is simplified to the well known inverse discrete Zak transform:

$$\mathbf{s} = \text{vec}\left(\mathbf{X} \cdot \mathbf{F}^{\dagger}_N\right) \tag{1.27}$$

and the two step demodulation in (1.25,1.26) is simplified to the discrete Zak transform:

$$\mathbf{Y} = \text{vec}^{-1}_{M\times N}(\mathbf{r}) \cdot \mathbf{F}_N \tag{1.28}$$

The simplified modulation and demodulation steps for OTFS using the DZT are shown in Fig. 1.4, omitting the AD and DA conversion steps for brevity.

1.2.3.2 Input-Output Relation

Consider a multipath wireless channel with P paths as described in Section 1.2.1.2. Fig. 1.5 shows what happens to the input signals in the delay-Doppler domain. The input symbols are placed with sufficient spacing in the delay-Doppler domain so that the readers can observe what happens to each information symbol. Note that, in reality,

the symbols are closely spaced. Fig. 1.5(a) is the input signal (for example: QAM) and Fig. 1.5(b) denotes a multipath channel with $P = 4$ propagation paths. Both delay and Doppler shifts are assumed to be integers in this case.

After passing through the channel, the received signal in the delay-Doppler domain is a 2-D twisted convolution between the input signal and the channel. The twisted convolution is because of the time-varying phase rotations $\phi_{m,n}(l_i, k_i)$ as given (omitting the noise terms for brevity) in (1.29).

$$\mathbf{Y}[m,n] = \sum_{i=1}^{P} g_i \phi_{m,n}(l_i,k_i)\mathbf{X}[[m-l_i]_M,[n-k_i]_N] \tag{1.29}$$

$$\approx \mathbf{H}[m,n] \circledast \mathbf{X}[m,n] \quad \text{(2D Circular Convolution if we ignore } \phi_{m,n}(l_i,k_i)) \tag{1.30}$$

where $\phi_{m,n}(l_i,k_i) = e^{\frac{j2\pi k_i(m-l_i)}{NM}} e^{j\frac{2\pi}{N}(n-k_i)\left\lfloor \frac{m-l_i}{M} \right\rfloor}$; denotes the RCP-OTFS phase variations in the delay-Doppler channel coefficients due to the Doppler shifts $k_i \neq 0$, [46, 77].

If the phase rotations are ignored (which can be done for very small values of l_i and k_i with minor loss of accuracy), the input-output relation becomes a 2-D circular convolution as given in (1.30). There are several efficient methods in the literature to recover $\mathbf{X}$ from a 2-D circular convolution problem. However, making such assumptions (ignoring $\phi_{m,n}(l_i,k_i)$) may cause degradation in detector performance for high mobility wireless channels.

The input-output relation for different OTFS variants and detection methods to solve for this twisted convolution problem is covered in detail in Chapters 2 and 3. The OTFS input-output relations were explicitly derived for RZP/RCP-OTFS in [33–35]. Then the OTFS input-output relations in matrix form for RZP/RCP-OTFS were presented in [36–38], and the relation for ZP/CP-OTFS in [39–45, 57, 61]. OTFS modulation was derived using Zak transform principles in [46, 47]. OTFS was generalized in the form of 2D orthogonal precoding in the time-frequency domain in [53]. An error performance analysis was conducted for OTFS in delay-Doppler domain in [48, 49]. It can also be noted that the OTFS modulation is similar to asymmetric OFDM proposed for static wireless channels [50]. The connections of OTFS modulation to other modulation techniques were explored in [43, 51, 52].

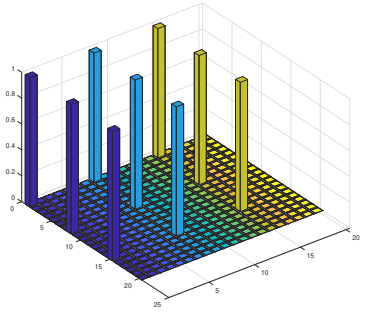

(a) Input signal **X**

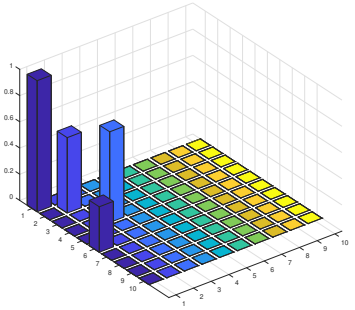

(b) Channel **H**

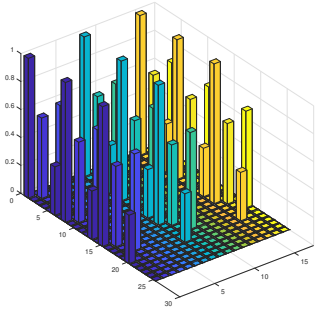

(c) Output signal **Y**

FIGURE 1.5: OTFS signals

1.2.3.3 OTFS vs OFDM

- OTFS exhibits better performance than OFDM in high Doppler as OTFS can exploit the delay-Doppler diversity offered by doubly-selective channels.
- Sparse channel representation in the delay-Doppler domain and ease of channel estimation with low pilot overhead as compared to OFDM. Channel estimation in OTFS can be done in the delay-Doppler domain using a single pilot and some guard symbols, where as OFDM requires multiple pilots interleaved along the time slots and sub-carriers to capture the time-frequency channel.
- Less sensitive to frequency synchronization errors. In the case of OTFS, timing offset and CFO are captured as a path with delay equal to the timing offset and Doppler shift equal to the CFO and can be estimated as part of the channel when performing channel estimation. In OFDM, CFO causes ICI leading to pilot symbols leaking into the nearby sub-carriers carrying data symbols. This leads to channel estimation error in channels with wide Doppler spreads.

- Compatibility with OFDM architecture as OTFS can be overlaid on top of the current OFDM systems as a 2-D precoding (ISFFT).

1.3 Thesis Format

1.3.1 Theme Selection

A significant portion of this research work, including a background in wireless communications and current physical layer techniques, in-depth study of OTFS, and fundamentals of delay-Doppler communications, have been written and published as a scientific book (240 pages) published by Elsevier at the time of writing this thesis (publication number 8 on page vii), [77]. Therefore, this thesis is chosen to be written with the theme of "thesis by publication" to showcase the outcomes of this research. The author would like to invite the readers to refer to this book for more details.

1.3.2 Structure

This thesis studies several aspects of waveform design for high mobility channels, such as detection, channel estimation algorithms, and the practical design, implementation, and validation of the proposed algorithms on real-time platforms, focusing primarily on OTFS systems. This section provides an overview of the thesis structure and flow across chapters and outlines the chapter-wise contributions in the following.

Chapter 2: OTFS Modem SDR Implementation and Experimental Study of Receiver Impairment Effects

Since presenting the seminal work on OTFS by Hadani *et al.* in WCNC 2017, there has been a lot of theoretical research that shows the superior performance of OTFS over OFDM in doubly selective channels. The topic is still in its infancy as practical implementation work is far and few. Most of the literature's work assumes ideal conditions for OTFS; hence, the utility of such works is not verified in experimental conditions. In Chapter 2, we first implemented OTFS on software-defined radio (SDR) platform, which was the first academic testbed implementation of OTFS, leading to profound insights

regarding the practical issue related to OTFS. The frame detection and timing synchronization was performed by prepending a preamble following the IEEE 802.15.4 standard and using a low complexity correlation and peak search based method as given in [65]. Channel estimation for OTFS is performed following the embedded pilot based method given in [59]. The power of the delay-Doppler domain single impulse based pilot is chosen and fixed so that the corresponding transmitted pilot components in the time domain are not clipped and distorted due to power amplifier limitations and non-linearity. We study the effect of receiver impairments such as carrier frequency offset (CFO) and direct current (DC) offset on OTFS implemented using a universal software radio peripheral (USRP) device, [66]. Further, the performance of OTFS is compared with the standard OFDM waveform using the same hardware setup in a real-time indoor frequency selective channel and partially emulated double selective channel. The detection algorithm used in the SDR implementation was the state-of-the-art message passing (MP) detection, [33]. Even though the MP detector offers excellent performance, its complexity increases linearly with the number of information symbols and QAM size, and exponentially with the number of propagation paths P. Similarly, other detection methods based on MMSE and SIC methods do not take into account the special structure of the OTFS channel matrix leading to polynomial complexity of detection. Despite superior error performance, efficient detection methods are necessary if OTFS is to replace the current communication systems based on OFDM, which leads to the contribution in Chapter 3.

Resulting publications:

- T. Thaj and E. Viterbo, "OTFS Modem SDR Implementation and Experimental Study of Receiver Impairment Effects," *IEEE International Conference on Communications Workshops (ICC Workshops)*, Shanghai, China, May 2019.

Chapter 3: Low Complexity Iterative Rake Decision Feedback Equalizer for Zero-Padded OTFS Systems

To solve the issue of the high complexity of OTFS detection, in Chapter 3, we propose a low complexity maximal ratio combining (MRC) based detection method by taking advantage of the special block circulant structure of the OTFS channel matrix. Diversity

combining techniques are well studied in the literature, starting from Brennan's paper on linear diversity combining [68]. Rake receivers for time domain combining using a variety of combining schemes like MRC and SC are proposed in literature [69, 70]. To facilitate the use of MRC, we first propose a new variant of OTFS known as ZP-OTFS, where null symbols are placed in the delay-Doppler domain, which after OTFS modulation, acts as guard intervals in the time domain between the different time domain blocks (similar to a ZP or CP between the time domain blocks in an OFDM system). This allows the time domain blocks to be processed independently at the receiver allowing parallel processing and reducing the latency due to detection. Then, the OTFS input-output relation for ZP-OTFS is analyzed in the delay-Doppler, delay-time, and the time domain. The ZPs convert the delay-Doppler channel matrix to a lower block triangular matrix with circulant blocks. This structure is utilized to propose an MRC-based algorithm in the delay-Doppler domain, and then the complexity is reduced by performing most of the detector computations in the delay-time domain, where the sparsity of the channel matrix is less than that of the delay-Doppler domain in a high mobility channel. This is due to the fact that Doppler shifts cannot be resolved in the time domain, and hence the delay-time and time domain channel matrices contain only L non-zero elements in each row of the channel matrix as opposed to P non-zero elements in the delay-Doppler channel matrix, where L is the number of unique delay taps. The proof of convergence of the proposed algorithm and methods to speed up convergence is provided. Finally, the uncoded and coded BER performance is compared with the standard OFDM waveform using standard 3GPP channel models, [67].

Resulting publications:

- T. Thaj and E. Viterbo, "Low Complexity Iterative Rake Detector for Orthogonal Time Frequency Space Modulation," in *Proc. IEEE Wireless Communications and Networking Conference (WCNC)*, Seoul, Korea (South), May 2020.
- T. Thaj and E. Viterbo, "Low Complexity Iterative Rake Decision Feedback Equalizer for Zero-Padded OTFS Systems," in *IEEE Transactions on Vehicular Technology*, vol. 69, no. 12, pp. 15606-15622, Dec. 2020, doi: 10.1109/TVT.2020.3044276.

Chapter 4: Low-Complexity Linear Diversity-Combining Detector for MIMO-OTFS

MIMO systems can scale channel capacity by utilizing multiple antennas to transmit and receive and is a crucial technology for increasing spectral usage in next-generation communication systems. OTFS-based MIMO systems are shown to provide high-performance gains over MIMO-OFDM systems in high Doppler scenarios, [40, 55, 72–75]. However, the main concern is the high receiver complexity due to inter-antenna interference, which is even more difficult to compensate for when the signal received in different antennas is correlated. The relative positions of the transmitter and receiver antennas result in a spatial correlation between the channels observed by the different (Tx-Rx) antenna pairs. This spatial correlation causes performance degradation due to loss of diversity. Chapter 4 proposes a channel estimation and linear-complexity detection method for the OTFS MIMO case for point-to-point communication. First, we propose a sample-based approach to estimate the channel coefficients and the spatial correlation between them which are modelled according to the exponential correlation matrix given in [76]. Secondly, we modify the combining weights of the MRC detector by taking into account the effect of spatial correlation so that the interference in the different diversity branches is decorrelated before combining. Finally, the MIMO-OTFS complexity and performance of the proposed detection method are compared with other state-of-the-art detectors based on MP and LMMSE methods, and LMMSE based MIMO-OFDM systems for different levels of spatial correlation.

Resulting publications:

- T. Thaj and E. Viterbo, "Low-Complexity Linear Diversity-Combining Detector for MIMO-OTFS," in *IEEE Wireless Communications Letters*, vol. 11, no. 2, pp. 288-292, Feb. 2022, doi: 10.1109/LWC.2021.3125986.

Chapter 5: Orthogonal Time Sequency Multiplexing Modulation: Analysis and Low-Complexity Receiver Design

As discussed earlier, the main reason for the superior performance of OTFS over OFDM is the spreading of information symbols in the entire time-frequency domain using 2-D orthogonal basis functions (SFFT in the case of OTFS). In [53, 54], it was shown

that any 2D unitary transformation in the time-frequency domain could offer the same error performance as the ISFFT for OTFS. This opens up many opportunities to choose time-frequency precoding without sacrificing performance. In Chapter 5, intending to design novel waveforms that can outperform OTFS in either detection complexity or error performance, we propose a new waveform, orthogonal time sequency multiplexing (OTSM). Like OTFS, OTSM places information symbols in a 2-D domain, which in this case is the delay-sequency domain, and in the case of OTFS is the delay-Doppler domain. Sequency here is defined as the number of zero-crossings in unit time. The key difference between the two schemes mentioned above is that OTFS is based on the discrete Fourier transform (DFT), whereas OTSM is based on the Walsh-Hadamard transform (WHT). Due to the low complexity associated with WHT, OTSM offers the same performance as OTFS but with significantly lower transceiver complexity. The success of a candidate waveform for high mobility wireless communications is tied to the transceiver complexity as well as the availability of efficient detection methods to solve a $\mathbf{y} = \mathbf{H} \cdot \mathbf{x} + \mathbf{noise}$; detection problem at the receiver. Some properties of the channel matrix $\mathbf{H}$, such as sparsity and eigenvalue distribution, determine the complexity of the detection process. This leads us to the motivation behind proposing OTSM: (i) low complexity transceiver design due to using only WHT, (ii) low complexity detection comparable to a traditional baseline OFDM scheme, and (iii) good performance in high mobility channels similar to the most advanced modulations schemes in the literature such as orthogonal time-frequency space modulation (OTFS), [7]. In this chapter, we show how OTSM achieves the above demands and outperforms OTFS (in terms of complexity) by comparing the OTSM uncoded BER performance with OTFS using similar low complexity detectors among the ones proposed for OTFS in the literature [33, 34, 39, 53, 55, 60, 61].

Resulting Publications:

- T. Thaj and E. Viterbo,"Orthogonal Time Sequency Multiplexing Modulation," *Proc. IEEE Wireless Communications and Networking Conference (WCNC)*, 2021, pp. 1-7, doi: 10.1109/WCNC49053.2021.9417451.

- T. Thaj, E. Viterbo and Y. Hong,"Orthogonal Time Sequency Multiplexing Modulation: Analysis and Low-Complexity Receiver Design" in *IEEE Transactions on Wireless Communications*, vol. 20, no. 12, pp. 7842-7855, Dec. 2021, doi: 10.1109/TWC.2021.3088479.

Chapter 6: Unitary-Precoded Single-Carrier Waveforms for High Mobility: Detection and Channel Estimation

In Chapter 6, we generalize the modulation schemes OTFS and OTSM under a family of unitary-precoded single-carrier waveforms by replacing the DFT (or WHT in the case of OTSM) with any unitary transform. First, the input-output relation in the matrix form is derived, and then channel estimation and detection methods are proposed, which can be used for all USC waveforms. Any choice of the unitary matrix was shown to offer the same performance as the recently proposed OTFS modulation but differs in cost of implementation depending on the unitary transform complexity. Finally, the low complexity receiver design and real-time implementation using an SDR platform are done to validate the proposed solutions in practical environments.

Resulting Publications:

- T. Thaj, and E. Viterbo. "Unitary-Precoded Single-Carrier Waveforms for High Mobility: Detection and Channel Estimation" Accepted in *Proc. IEEE Wireless Communications and Networking Conference (WCNC) 2022*, doi: arXiv:2201.10218

Finally, the MATLAB codes for all the waveforms and algorithms developed in this thesis is provided free online for use of researchers worldwide in [77].

1.4 Research Questions

In this section, based on the motivation presented in Section 1.1, we present some core research questions that is addressed in Chapters 2-6 of this thesis.

- What are the drawbacks of current systems based on OFDM and what is the potential candidate waveform to replace OFDM? Why is the new waveform expected to offer better performance than OFDM?
- Has the performance of OTFS been verified in practical scenarios and what are the issues faced by OTFS when implemented in real hardware? How to compensate for hardware impairments?

- What are available OTFS detection methods in the literature? Can we design an OTFS detector with complexity comparable to OFDM? Can OFDM get close to OTFS in terms of error performance with the help of a powerful error-correcting code?

- How can detection, and channel estimation in SISO OTFS be extended to MIMO OTFS? What are the practical issues and challenges faced in a MIMO setting and how to compensate for them? How does the performance and complexity compare against MIMO OFDM?

- Are there other waveforms that can offer better performance than OTFS in high mobility channels? What is the common requirement for such waveforms and in what scenarios do they outperform OTFS?

Bibliography

[1] CEWiT, "Discussion on new waveforms", 3GPP Standard Contribution (R1-163311), Busan, Korea, Apr. 11-15 2016

[2] Qualcomm Inc.,"Waveform Requirements" 3GPP Standard Contribution (R1-162198), Busan, Korea, Apr. 11-15 2016

[3] Qualcomm Inc.,"Waveform Candidates" 3GPP Standard Contribution (R1-162199), Busan, Korea, Apr. 11-15 2016

[4] Motorola Mobility.,"Waveform for New Radio" 3GPP Standard Contribution (R1-163327), Busan, Korea, Apr. 11-15 2016

[5] NGMN Alliance, "6G use cases and analysis", Feb, 2022, https://www.ngmn.org/wp-content/uploads/220222-NGMN-6G-Use-Cases-and-Analysis-1.pdf

[6] J. Wu and P. Fan,"A Survey on High Mobility Wireless Communications: Challenges, Opportunities and Solutions" in *IEEE Access*, vol. 4, pp. 450-476, 2016, doi: 10.1109/ACCESS.2016.2518085

[7] R. Hadani, S. Rakib, M. Tsatsanis, A. Monk, A. J. Goldsmith, A. F. Molisch, and R. Calderbank, "Orthogonal time frequency space modulation," in *Proc. IEEE Wireless Commun. Netw. Conf. (WCNC)*, San Francisco, CA, USA, Mar. 2017.

[8] A. Goldsmith, Wireless Communications, Cambridge University Press, 2005.

[9] D. Tse, P. Viswanath, Fundamentals of Wireless Communication, 3rd edi- tion, Cambridge University Press, 2005.

[10] F. Molisch, Wireless Communications, Second Edition, John Wiley & Sons, 2011

[11] F. Hlawatsch, G. Matz, Wireless Communications Over Rapidly Time-Varying Channels, 1st Edition, Academic Press, Inc., USA, 2011.

[12] Y. G. Li, G. L. Stuber, Orthogonal Frequency Division Multiplexing for Wireless Communications, Springer, 2006.

[13] W. Kozek and A. F. Molisch,"Nonorthogonal pulseshapes for multicarrier communications in doubly dispersive channels," in *IEEE Journal on Selected Areas in Communications*, vol. 16, no. 8, pp. 1579-1589, Oct. 1998, doi: 10.1109/49.730463.

[14] S. Das and P. Schniter,"Max-SINR ISI/ICI-Shaping Multicarrier Communication Over the Doubly Dispersive Channel" in *IEEE Transactions on Signal Processing*, vol. 55, no. 12, pp. 5782-5795, Dec. 2007, doi: 10.1109/TSP.2007.901660.

[15] D. Schafhuber, G. Matz and F. Hlawatsch, "Pulse-shaping OFDM/BFDM systems for time-varying channels: ISI/ICI analysis, optimal pulse design, and efficient implementation" *The 13th IEEE International Symposium on Personal, Indoor and Mobile Radio Communications*, 2002, pp. 1012-1016 vol.3, doi: 10.1109/PIMRC.2002.1045180.

[16] T. Strohmer and S. Beaver,"Optimal OFDM design for time-frequency dispersive channels" in *IEEE Transactions on Communications*, vol. 51, no. 7, pp. 1111-1122, July 2003, doi: 10.1109/TCOMM.2003.814200.

[17] H. Bölcskei, "Orthogonal frequency division multiplexing based on offset QAM", in *Advances in Gabor analysis*, Springer, 2003, pp. 321–352.

[18] M. G. Bellanger,"Specification and design of a prototype filter for filter bank based multicarrier transmission" *2001 IEEE International Conference on Acoustics, Speech, and Signal Processing. Proceedings*, 2001, pp. 2417-2420 vol.4, doi: 10.1109/ICASSP.2001.940488.

[19] P. Siohan, C. Siclet and N. Lacaille, "Analysis and design of OFDM/OQAM systems based on filterbank theory," in *IEEE Transactions on Signal Processing*, vol. 50, no. 5, pp. 1170-1183, May 2002, doi: 10.1109/78.995073.

[20] B. Farhang-Boroujeny, "OFDM Versus Filter Bank Multicarrier," in *IEEE Signal Processing Magazine*, vol. 28, no. 3, pp. 92-112, May 2011, doi: 10.1109/MSP.2011.940267.

[21] V. Vakilian, T. Wild, F. Schaich, S. ten Brink and J. Frigon, "Universal-filtered multi-carrier technique for wireless systems beyond LTE," *2013 IEEE Globecom Workshops (GC Wkshps)*, 2013, pp. 223-228, doi: 10.1109/GLOCOMW.2013.6824990.

[22] G. Fettweis, M. Krondorf and S. Bittner, "GFDM - Generalized Frequency Division Multiplexing," *VTC Spring 2009 - IEEE 69th Vehicular Technology Conference*, 2009, pp. 1-4, doi: 10.1109/VETECS.2009.5073571.

[23] N. Michailow et al., "Generalized Frequency Division Multiplexing for 5th Generation Cellular Networks," in *IEEE Transactions on Communications*, vol. 62, no. 9, pp. 3045-3061, Sept. 2014, doi: 10.1109/TCOMM.2014.2345566.

[24] F. Schaich and T. Wild,"Waveform contenders for 5G — OFDM vs. FBMC vs. UFMC," *2014 6th International Symposium on Communications, Control and Signal Processing (ISCCSP)*, 2014, pp. 457-460, doi: 10.1109/ISCCSP.2014.6877912.

[25] M. Matthe, Waveform Design for Generalized Frequency Division Multiplexing: A survey on pulse shaping filters, AV Akademikerverlag, 2014.

[26] A. Bourdoux, H. Cappelle and A. Dejonghe, "Channel Tracking for Fast Time-Varying Channels in IEEE802.11p Systems," *2011 IEEE Global Telecommunications Conference*, 2011, pp. 1-6, doi: 10.1109/GLOCOM.2011.6134024.

[27] S. Sibecas, C. A. Corral, S. Emami, G. Stratis and G. Rasor, "Pseudo-pilot OFDM scheme for 802.11a and R/A in DSRC applications," *2003 IEEE 58th Vehicular Technology Conference*, 2003, pp. 1234-1237 Vol.2, doi: 10.1109/VETECF.2003.1285219.

[28] D. Schafhuber, G. Matz and F. Hlawatsch, "Adaptive Wiener filters for time-varying channel estimation in wireless OFDM systems," *2003 IEEE International Conference on Acoustics, Speech, and Signal Processing*, 2003, pp. IV-688, doi: 10.1109/ICASSP.2003.1202736.

[29] O. Edfors, M. Sandell, J. . -J. van de Beek, S. K. Wilson and P. O. Borjesson, "OFDM channel estimation by singular value decomposition," in *IEEE Transactions on Communications,* vol. 46, no. 7, pp. 931-939, July 1998, doi: 10.1109/26.701321.

[30] Seung Young Park, Yeun Gu Kim and Chung Gu Kang, "Iterative receiver for joint detection and channel estimation in OFDM systems under mobile radio channels," in

IEEE Transactions on Vehicular Technology, vol. 53, no. 2, pp. 450-460, March 2004, doi: 10.1109/TVT.2004.823536.

[31] F. A. Dietrich and W. Utschick, "Pilot-assisted channel estimation based on second-order statistics," in *IEEE Transactions on Signal Processing,* vol. 53, no. 3, pp. 1178-1193, March 2005, doi: 10.1109/TSP.2004.842176.

[32] P. Salvo Rossi and R. R. Muller, "Slepian-Based Two-Dimensional Estimation of Time-Frequency Variant MIMO-OFDM Channels," in *IEEE Signal Processing Letters*, vol. 15, pp. 21-24, 2008, doi: 10.1109/LSP.2007.910289.

[33] P. Raviteja, K. T. Phan, Y. Hong and E. Viterbo, "Interference Cancellation and Iterative Detection for Orthogonal Time Frequency Space Modulation," in *IEEE Transactions on Wireless Communications*, vol. 17, no. 10, pp. 6501-6515, Oct. 2018, doi: 10.1109/TWC.2018.2860011.

[34] K. R. Murali and A. Chockalingam, "On OTFS Modulation for High-Doppler Fading Channels," *2018 Information Theory and Applications Workshop (ITA)*, 2018, pp. 1-10, doi: 10.1109/ITA.2018.8503182.

[35] L. Gaudio, M. Kobayashi, G. Caire and G. Colavolpe, "On the Effectiveness of OTFS for Joint Radar Parameter Estimation and Communication" in *IEEE Transactions on Wireless Communications,* vol. 19, no. 9, pp. 5951-5965, Sept. 2020, doi: 10.1109/TWC.2020.2998583.

[36] P. Raviteja, Y. Hong, E. Viterbo and E. Biglieri, "Practical Pulse-Shaping Waveforms for Reduced-Cyclic-Prefix OTFS," in *IEEE Transactions on Vehicular Technology*, vol. 68, no. 1, pp. 957-961, Jan. 2019, doi: 10.1109/TVT.2018.2878891.

[37] P. Raviteja, Y. Hong, E. Viterbo and E. Biglieri, "Effective Diversity of OTFS Modulation," in *IEEE Wireless Communications Letters*, vol. 9, no. 2, pp. 249-253, Feb. 2020, doi: 10.1109/LWC.2019.2951758.

[38] S. Tiwari, S. S. Das, "Circularly pulse-shaped orthogonal time frequency space modulation", *Electronics Letters* 56 (2) (2020) 249–253.doi:10.1109/LWC.2019.2951758

[39] A. Farhang, A. RezazadehReyhani, L. E. Doyle and B. Farhang-Boroujeny, "Low Complexity Modem Structure for OFDM-Based Orthogonal Time Frequency Space

Modulation," in *IEEE Wireless Communications Letters*, vol. 7, no. 3, pp. 344-347, June 2018, doi: 10.1109/LWC.2017.2776942.

[40] A. RezazadehReyhani, A. Farhang, M. Ji, R. R. Chen and B. Farhang-Boroujeny, "Analysis of Discrete-Time MIMO OFDM-Based Orthogonal Time Frequency Space Modulation," *2018 IEEE International Conference on Communications (ICC)*, 2018, pp. 1-6, doi: 10.1109/ICC.2018.8422467.

[41] W. Shen, L. Dai, S. Han, I. Chih-Lin and R. W. Heath, "Channel Estimation for Orthogonal Time Frequency Space (OTFS) Massive MIMO," *2019 IEEE International Conference on Communications (ICC)*, 2019, pp. 1-6, doi: 10.1109/ICC.2019.8761362.

[42] M. K. Ramachandran, G. D. Surabhi and A. Chockalingam, "OTFS: A New Modulation Scheme for High-Mobility Use Cases", *J. Indian Inst. Sci.* 100, 315–336 (2020). https://doi.org/10.1007/s41745-020-00167-4

[43] V. Rangamgari, S. Tiwari, S. S. Das, S. C. Mondal, "OTFS: Interleaved OFDM with block CP", in *2020 IEEE National Conference on Communications (NCC)*, 2020, pp. 1–6. doi:10.1109/NCC48643.2020.9056003

[44] S. S. Das, V. Rangamgari, S. Tiwari and S. C. Mondal, "Time Domain Channel Estimation and Equalization of CP-OTFS Under Multiple Fractional Dopplers and Residual Synchronization Errors," in *IEEE Access*, vol. 9, pp. 10561-10576, 2021, doi: 10.1109/ACCESS.2020.3046487.

[45] D. Shi et al., "Deterministic Pilot Design and Channel Estimation for Downlink Massive MIMO-OTFS Systems in Presence of the Fractional Doppler," in *IEEE Transactions on Wireless Communications*, vol. 20, no. 11, pp. 7151-7165, Nov. 2021, doi: 10.1109/TWC.2021.3081164.

[46] S. K. Mohammed, "Derivation of OTFS Modulation From First Principles," in *IEEE Transactions on Vehicular Technology*, vol. 70, no. 8, pp. 7619-7636, Aug. 2021, doi: 10.1109/TVT.2021.3069913.

[47] S. K. Mohammed, "Time-Domain to Delay-Doppler Domain Conversion of OTFS Signals in Very High Mobility Scenarios," in *IEEE Transactions on Vehicular Technology*, vol. 70, no. 6, pp. 6178-6183, June 2021, doi: 10.1109/TVT.2021.3071942.

[48] E. Biglieri, P. Raviteja and Y. Hong, "Error Performance of Orthogonal Time Frequency Space (OTFS) Modulation," *2019 IEEE International Conference on Communications Workshops (ICC Workshops)*, 2019, pp. 1-6, doi: 10.1109/ICCW.2019.8756831.

[49] Z. Wei, W. Yuan, S. Li, J. Yuan and D. W. K. Ng, "Transmitter and Receiver Window Designs for Orthogonal Time-Frequency Space Modulation," in *IEEE Transactions on Communications*, vol. 69, no. 4, pp. 2207-2223, April 2021, doi: 10.1109/TCOMM.2021.3051386.

[50] J. Zhang, A. D. S. Jayalath and Y. Chen, "Asymmetric OFDM Systems Based on Layered FFT Structure," in *IEEE Signal Processing Letters*, vol. 14, no. 11, pp. 812-815, Nov. 2007, doi: 10.1109/LSP.2007.903230.

[51] A. Nimr, M. Chafii, M. Matthe and G. Fettweis, "Extended GFDM Framework: OTFS and GFDM Comparison," *2018 IEEE Global Communications Conference (GLOBECOM)*, 2018, pp. 1-6, doi: 10.1109/GLOCOM.2018.8647704.

[52] G. D. Surabhi, R. M. Augustine and A. Chockalingam, "Peak-to-Average Power Ratio of OTFS Modulation," in *IEEE Communications Letters*, vol. 23, no. 6, pp. 999-1002, June 2019, doi: 10.1109/LCOMM.2019.2914042.

[53] T. Zemen, M. Hofer, D. Löschenbrand and C. Pacher, "Iterative Detection for Orthogonal Precoding in Doubly Selective Channels," in *Proc. 2018 IEEE 29th Annu. Int. Symp. Personal Indoor and Mobile Radio Commun. (PIMRC)*, Bologna, 2018.

[54] T. Zemen, D. Löschenbrand, M. Hofer, C. Pacher and B. Rainer, "Orthogonally Precoded Massive MIMO for High Mobility Scenarios," in IEEE Access, vol. 7, pp. 132979-132990, 2019, doi: 10.1109/ACCESS.2019.2941316.

[55] M. K. Ramachandran, and A. Chockalingam, "MIMO-OTFS in High-Doppler Fading Channels: Signal Detection and Channel Estimation," in *Proc. of 2018 IEEE Global Communications Conference (GLOBECOM)*, pp. 1-6, Abu Dhabi,UAE, Dec. 2018.

[56] T. Thaj and E. Viterbo, "Orthogonal Time Sequency Multiplexing Modulation" in *Proc. IEEE Wireless Commun. Netw. Conf.*, pp. 1-7, 2021

[57] T. Thaj, E. Viterbo and Y. Hong, "Orthogonal Time Sequency Multiplexing Modulation: Analysis and Low-Complexity Receiver Design" in *IEEE Trans. on Wireless Commun.*, 2021, doi: 10.1109/TWC.2021.3088479.

[58] D. S. Stoffer, "Walsh-Fourier Analysis and Its Statistical Applications," *J. American Statistical Association,* vol. 86, no. 414, pp. 461–479.

[59] P. Raviteja, K. T. Phan, and Y. Hong, "Embedded Pilot-Aided Channel Estimation for OTFS in Delay–Doppler Channels," *IEEE Trans. Veh. Technol.,* vol. 68, no. 5, pp. 4906-4917, May 2019.

[60] T. Thaj and E. Viterbo, "Low Complexity Iterative Rake Detector for Orthogonal Time Frequency Space Modulation," in *Proc. IEEE Wireless Commun. Netw. Conf. (WCNC)*, Seoul, Korea (South), May 2020.

[61] T. Thaj and E. Viterbo, "Low Complexity Iterative Rake Decision Feedback Equalizer for Zero Padded OTFS Systems," *IEEE Trans. on Veh. Tech.*, Dec 2020. doi: 10.1109/TVT.2020.3044276

[62] S. K. Mohammed,"Derivation of OTFS Modulation From First Principles." in *IEEE Trans. on Veh. Tech.*, vol. 70, no. 8, pp. 7619-7636, Aug. 2021, doi: 10.1109/TVT.2021.3069913.

[63] A. Björck, *Numerical Methods for Least Squares Problems,* SIAM, 1996. doi: 10.1137/1.9781611971484

[64] T. Thaj and E. Viterbo, "OTFS Modem SDR Implementation and Experimental Study of Receiver Impairment Effects," in *2019 IEEE Int. Conf. on Commun. Workshops,* pp. 1-6, 2019, doi: 10.1109/ICCW.2019.8757167.

[65] Kai-Hsin Chen and Hsi-Pin Ma,"A low power ZigBee baseband processor,", in *2008 International SoC Design Conference*, 2008, pp. I-40-I-43, doi: 10.1109/SOCDC.2008.481556

[66] USRP-2954 Specifications - National Instruments, Available online: https://www.ni.com/pdf/manuals/375725c.pdf

[67] "LTE Evolved Universal Terrestrial Radio Access (E-UTRA); Base Station (BS) radio transmission and reception," 3GPP TS 36.104 version 8.6.0 Release 8, Jul. 2009, ETSI TS. doi: 10.1109/MCOM.2009.4752682

[68] D. Brennan, “Linear diversity combining techniques,“ *Proc. IRE*, vol. 47, pp. 1075-1102, June 1959

[69] S. Kondo and B. Milstein, ”Performance of multicarrier DS CDMA systems,” in IEEE Transactions on Communications, vol. 44, no. 2, pp. 238-246, Feb. 1996.

[70] S. Imada and T. Ohtsuki, ”Pre-RAKE diversity combining for UWB systems in IEEE 802.15 UWB multipath channel,” 2004 International Workshop on Ultra Wideband Systems Joint with Conference on Ultra Wideband Systems and Technologies. Joint UWBST and IWUWBS 2004 (IEEE Cat. No.04EX812), Kyoto, Japan, 2004, pp. 236-240.

[71] S. Tiwari, S.S. Das and V. Rangamgari, “Low-complexity LMMSE receiver for OTFS,” *IEEE Commun. Lett.*, Oct. 2019.

[72] R. M. Augustine, G. Surabhi, and A. Chockalingam, “Space-time Coded OTFS Modulation in High-Doppler channels,” in *Proc. IEEE 89th Veh. Tech. Conf. (VTC)*, May 2019.

[73] G. D. Surabhi and A. Chockalingam, “Low-complexity Linear Equalization for 2×2 MIMO-OTFS Signals,” in *IEEE 21st Int. Workshop on Signal Process. Advances in Wireless Commun. (SPAWC),* 2020.

[74] B. C. Pandey, S. K. Mohammed, P. Raviteja, Y. Hong and E. Viterbo, “Low Complexity Precoding and Detection in Multi-User Massive MIMO OTFS Downlink,” in *IEEE Trans. on Veh. Tech.,* vol. 70, no. 5, pp. 4389-4405, May 2021.

[75] P. Singh, H. B. Mishra, and R. Budhiraja, “Low-Complexity Linear MIMO-OTFS Receivers,” *2021 IEEE Int. Conf. on Commun. Workshops (ICC Workshops),* June 2021.

[76] S. L. Loyka, “Channel capacity of MIMO architecture using the exponential correlation matrix,” *IEEE Commun. Lett.*, vol. 5, no. 9, pp. 369–371, Sep. 2001

[77] Y. Hong, T. Thaj, E. Viterbo, “Delay-Doppler Communications: Principles and Applications”, Academic Press, 2022, ISBN:9780323850285

Chapter 2

OTFS Modem SDR Implementation and Experimental Study of Receiver Impairment Effects

Citing info:

T. Thaj and E. Viterbo, "OTFS Modem SDR Implementation and Experimental Study of Receiver Impairment Effects," in *IEEE International Conference on Communications Workshops (ICC Workshops)*, 2019, pp. 1-6, doi: 10.1109/ICCW.2019.8757167.

Copyright Statement:

©[2019] IEEE. Reprinted, with permission, from [Tharaj Thaj, Emanuele Viterbo, OTFS Modem SDR Implementation and Experimental Study of Receiver Impairment Effects, IEEE International Conference on Communications Workshops (ICC Workshops), 2019]

OTFS Modem SDR Implementation and Experimental Study of Receiver Impairment Effects

Tharaj Thaj and Emanuele Viterbo
ECSE Department, Monash University, Clayton, VIC 3800, Australia
Email: {tharaj.thaj, emanuele.viterbo}@monash.edu

***Abstract*—This paper presents a software defined radio (SDR) design and implementation of an orthogonal time frequency space (OTFS) modem. OTFS is a novel modulation scheme based on multiplexing information symbols over localized pulses in the delay–Doppler signal representation. Traditional OFDM modulation operates in the frequency-time domain. In contrast, OTFS modulation operates in the delay-Doppler domain, which are related to frequency and time by the symplectic Fourier transform (similar to a two-dimensional discrete Fourier transform). OTFS is shown to perform very well under the 5G usage scenarios such as high speed vehicle to vehicle communication with wide Doppler spreads, where the traditional OFDM system performance degrades. Like any other communications system, the OTFS modem is not free from receiver impairments such as DC offset and carrier frequency offset, which affects the channel estimation and hence the decoding process. We study the effects of these receiver impairments on the receiver performance from real time experiments conducted on the implemented OTFS modem in a real indoor wireless channel. We also compare the performance of OTFS modulation and OFDM modulation using the same hardware setup and environment for the real indoor frequency selective and partially emulated doubly selective channel.**

***Index Terms*—Delay–Doppler channel, OTFS, modem, Software Defined Radio**

I. Introduction

Wireless multipath fading channel can be modelled as time varying impulse response or as a time varying frequency response. This is the appropriate representation for wireless OFDM-based systems like LTE. In LTE the frequency response is estimated every OFDM symbol in order to equalize the channel. Higher mobility results in faster variation of the multipath components. Since constructive and destructive addition of these multipath components causes signal fading, faster variation of these components leads to more rapid fluctuations in the channel. The frequency response rate of variation is also proportional to the signal carrier frequency. Thus, the faster the reflectors, transmitters, and/or receivers move, the higher the frequency band, the more rapidly changes in the channel frequency response occur.

As the channel coherence time in the time-frequency domain is the inverse of its Doppler, the impulse response for this channel varies rapidly over a fraction of a millisecond. Hence, in an LTE/OFDM system there is not sufficient time to estimate the channel, let alone provide feedback of the channel state to the transmitter. As compared to the time varying impulse response, or time varying frequency response, the delay Doppler representation of the channel varies much slower over a longer observation time.

Orthogonal Time Frequency and Space (OTFS) is a new 2D modulation technique that transforms information symbols in the delay–Doppler coordinate system to the familiar time-frequency domain [1], [2]. By spreading all the information carrying symbols (e.g., QAM) over both time and frequency to achieve maximum diversity. As a result, the time-frequency selective channel is converted into an invariant, separable and orthogonal interaction, where all received QAM symbols experience the same localized impairment and all the delay-Doppler diversity branches are coherently combined.

Software defined radio (SDR) is a radio communication system where all or most of the physical layer functions have been implemented in software. Traditional hardware based radio devices limits cross functionality and needs to be physically modified each time a different waveform standard is proposed, which leads to high production costs and low flexibility. On the other hand, a SDR handles a lot of the signal processing functions in a general purpose processor, which allows for transmitting and receiving a wide variety of waveforms and protocols.

For our implementation, we use the National Instruments Universal Software Radio Peripheral (USRP) device. Like any typical radio, SDR is also affected by DC offset and carrier frequency offset (CFO), that can degrade the receiver performance. OTFS is expected to be robust towards CFO. This is due to the fact that it will be sensed in channel estimation phase as an additional Doppler shift and will be very simply corrected.

On the other hand, a DC offset can severely corrupt the channel estimation. In this paper we study the effects of CFO and DC offset on channel estimation and hence on receiver performance using real time experiments conducted on the implemented OTFS modem inside a real indoor wireless channel. Further we will discuss how we can correct in the delay-Doppler domain, using the pilot symbols, CFO and DC Offset in the case when both remains constant for the duration of one OTFS frame.

The paper is organized as follows. In Section II, we discuss the implementation aspects of the OTFS modem. In Section III, we discuss the pilot information extraction, channel estimation and effects of receiver impairments on estimating the channel and hence the receiver performance . The experimental setup and the results are provided in Section IV. Section V contains our concluding remarks.

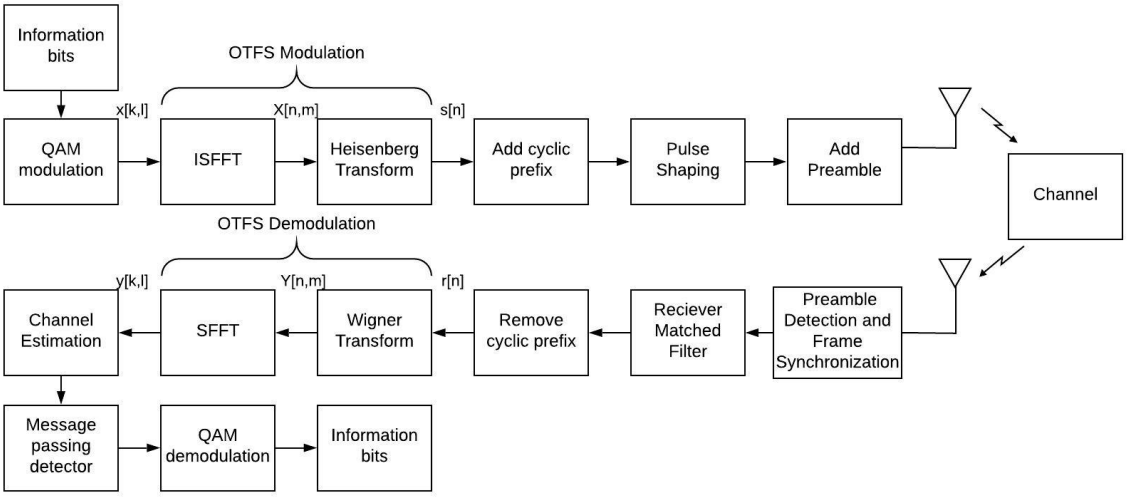

Fig. 1. OTFS-Transmitter and Receiver process

II. OTFS SDR Implementation Aspects

In this section, we describe the system model for SDR Implementation of OTFS transmitter and receiver following [1]–[3].

A. Basic OTFS concepts/notations

The *time–frequency signal plane* is discretized to a N by M *grid* (for some integers $N, M > 0$) by sampling the time and frequency axes at intervals of T (seconds) and $\Delta f = 1/T$ (Hz), respectively, i.e.,

$$\Lambda = \big\{(nT, m\Delta f),\ n = 0, \ldots, N-1, m = 0, \ldots, M-1\big\}$$

The modulated *time–frequency* samples $X[n, m], n = 0, \ldots, N-1, m = 0, \ldots, M-1$ are transmitted over an OTFS frame with duration $T_f = NT$ and occupy a bandwidth $B = M\Delta f$.

The *delay–Doppler plane* in the region $(0, T] \times (-\Delta f/2, \Delta f/2]$ is discretized to an N by M *grid*

$$\Gamma = \left\{\left(\frac{k}{NT}, \frac{l}{M\Delta f}\right),\ k = 0, \ldots, N-1, l = 0, \ldots, M-1\right\},$$

where $1/M\Delta f$ and $1/NT$ represents the quantization steps or the resolution of the delay and Doppler frequency axes, respectively and $x[k, l]$ represents the *delay–Doppler* symbols. For our experiments, we will use an OTFS frame with N=32 and M=32. That means we have N and M quantization steps for delay and Doppler shifts with respectively with delay resolution = $1/M\Delta f$ and Doppler resolution = $1/NT$.$x[k, l]$ and $y[k, l]$ are the transmitted and received symbols in the *delay–Doppler plane* and $X[n, m]$ and $Y[n, m]$ are the transmitted and received symbols in *time-frequency plane* respectively, after sampling, matched filtering and removing the cyclic prefix .

B. Hardware and Software

The hardware platform is based on National Instruments Universal Radio Software Peripheral (USRP) Software Defined Radio Reconfigurable Device (NI-USRP-2943R) designed by Ettus Research [10]. The NI USRP RIO software defined radio platform combines 2 full-duplex transmit and receive channels with 120 MHz/channel of real-time bandwidth with frequency options that span from 1.2 GHz to 6 GHz. The maximum I/Q sample rate is 200 MSPS. PCIe Express x4 connects the host PC and the USRP and allows up to 800MB/s of streaming data transfer. A terminal is implemented with an USRP-2943R connected to a host PC running the National Instruments LabView. The software is based on LabView 2018. We set the carrier frequency at 4 GHz and the sampling rate at 100 mega samples per second(MSPS) at the transmitter and receiver terminals.

C. Transmitter

The signal generation process is shown in the upper chain of Fig.1. The information bits are Q-ary QAM modulated.The modulated symbols are placed in the discretized delay-Doppler grid $x[k, l]$ as shown in Fig.2. Along with the data symbols some pilot symbols are also placed in the 2D grid Γ for channel estimation. The placement of pilot signals is discussed in [7] and [8].We will discuss it more later. The delay-Doppler and time-frequency signal plane is related through a transformation known as the *symplectic fast fourier transform* (SFFT). We do an *inverse symplectic fast fourier transform* (ISFFT),shown in (1), on the initial delay-Doppler 2D matrix of QAM symbols $x[k, l]$ to map it to samples $X[n, m]$ which is now in the time-frequency plane and from there we apply the *Heisenberg transform* [1] with rectangular transmit pulse

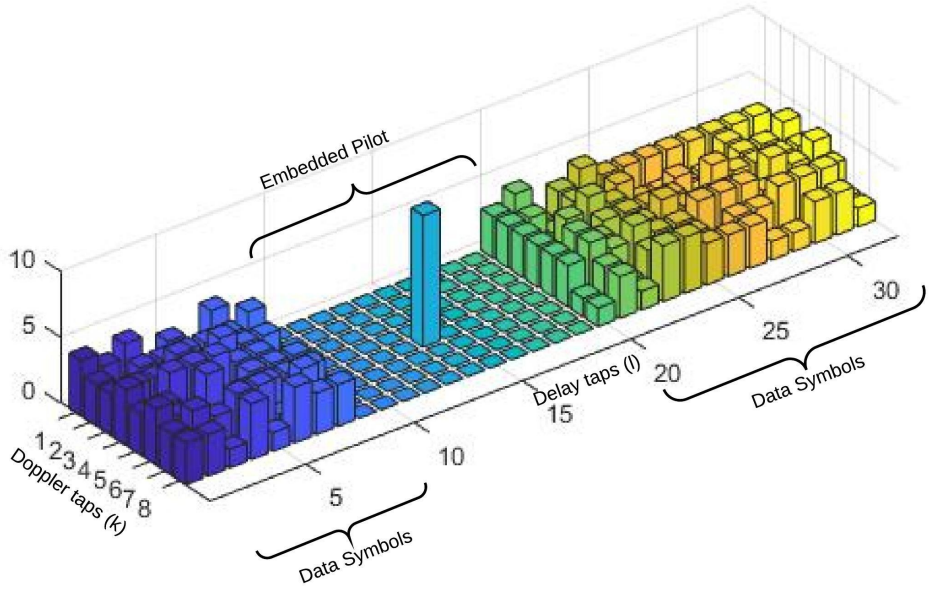

Fig. 2. OTFS-magnitude of transmitted 16-QAM symbols in the delay-Doppler plane $x[k,l]$

on the time-frequency symbols to convert it to a time domain signal which is to be transmitted over the wireless channel.

$$X[n,m] = \frac{1}{NM}\sum_{k=0}^{N-1}\sum_{l=0}^{M-1} x[k,l]e^{j2\pi\left(\frac{nk}{N}-\frac{ml}{N}\right)} \quad (1)$$

The two steps *ISFFT* and *Heisenberg transform* together constitute the OTFS Modulation. For implementation we can combine these two steps to a single step as shown in [3] by taking an N point IFFT across the columns (Doppler axis) of the 2D matrix in the delay-Doppler plane for each delay tap and then converting it to a time domain signal, which is 1-D vector by taking elements of the matrix row-wise (along the delay axes). Unlike OFDM where a cyclic prefix (CP) is added for each of N symbols in the frame, in OTFS a CP is added for each frame in the time domain. This considerably reduces the CP overhead. Pulse shaping is done followed by addition of a preamble for frame detection and synchronization.

D. Receiver

The processing steps at the receiver is as shown in the lower chain of Fig.1. Once the preamble is detected,we find the start of the frame. The next step is converting the time domain signal back to symbols in the delay-Doppler domain . The time domain signal is first converted to the time frequency samples $Y[n][m]$ by taking the *Wigner transform* [1] and then do the SFFT on $Y[n][m]$ to get the received symbols $y[k][l]$ in the delay-Doppler plane (2).

$$y[k,l] = \frac{1}{NM}\sum_{k=0}^{N-1}\sum_{l=0}^{M-1} Y[n,m]e^{-j2\pi\left(\frac{nk}{N}-\frac{ml}{N}\right)} \quad (2)$$

Just like at the transmitter, for implementation, these two steps can be simplified by doing the reverse of what was done at the transmitter as explained in [3]. The time domain signal is first folded in to a 2D matrix with the elements being placed row wise. An N point FFT is taken across the columns(Time axis) of the matrix . The resulting matrix is in the delay-Doppler domain with Doppler across the columns and delay across the rows. Once the OTFS demodulation is done, the pilot symbols are extracted and channel estimation is done. The channel information along with the received symbols in the delay-Doppler domain is passed to the message passing detector described in [5], [6] which in turn does a iterative probabilistic symbol decoding to estimate the transmitted symbols. The estimated Q-ary QAM symbols are then converted to information bits.

III. OTFS Receiver Impairment effects on Channel Estimation

A. Channel Estimation

Channel Estimation is an important part of the decoding process. We try to achieve this by transmitting some pilot symbols along with the data symbols in the OTFS frame. Once the received OTFS time domain samples are converted to the symbols in the delay-Doppler plane, we extract the channel information (channel coefficients and the respective delay and Doppler paths) from the received pilot symbols and pass it to the message passing detector. So it is important that the pilot symbols are free from any interference from the data symbols for accurate channel estimation. Guard symbols are placed around the pilot symbols to prevent this corruption. The

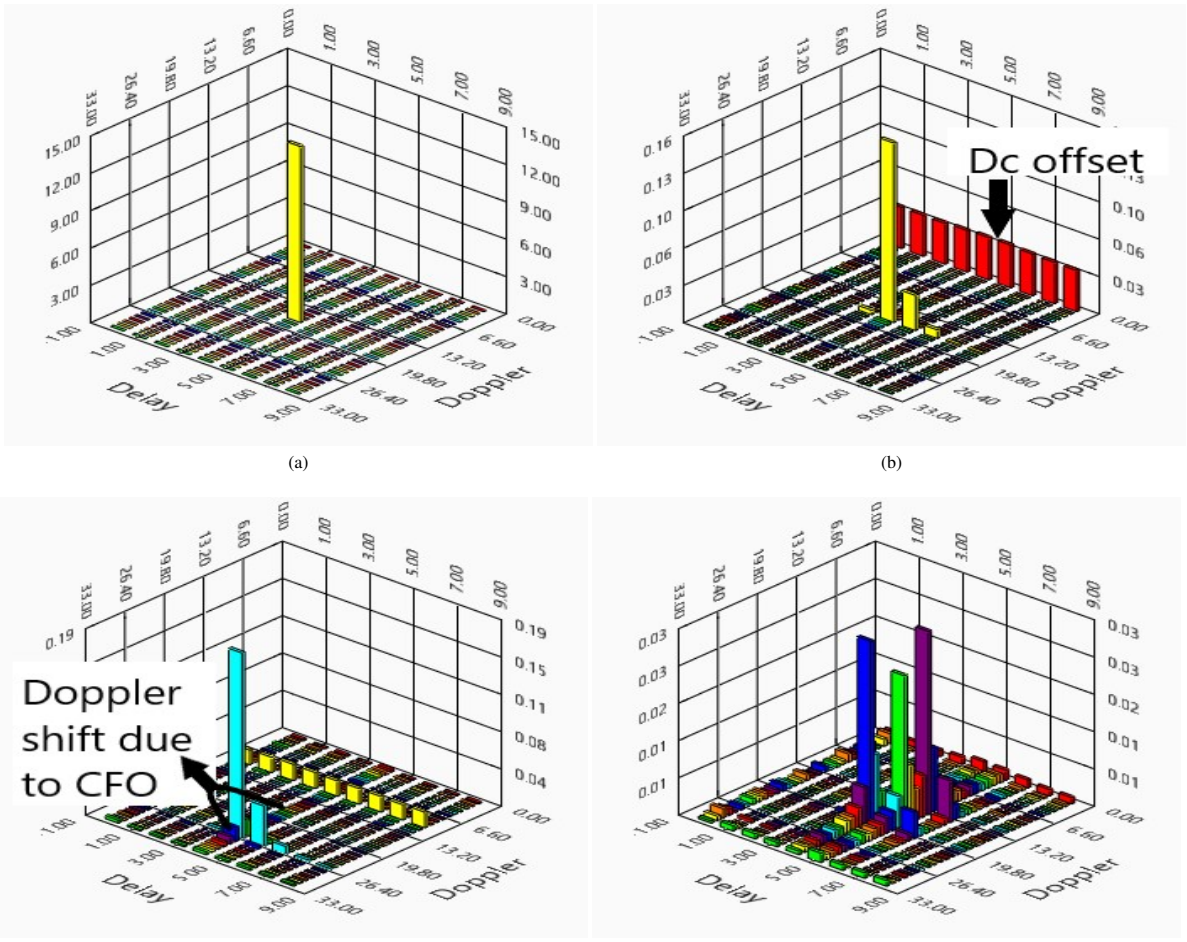

Fig. 3. OTFS-Receiver Impairment effects on the pilot (magnitude) in the indoor wireless channel (received SNR = 25dB) (a).Transmitted embedded pilot (b).Received Pilot with DC-Offset of -10 dB relative to signal power (c).Received Pilot with CFO of 150 KHz (5 Doppler taps shift) (d).Received pilot with channel emulator at the transmitter with 10 paths (paths shown with the same colour undergoes the same Doppler shift)

pilot and guard symbol placements are discussed in detail in [7] and [8]. A pilot symbol is placed in the delay-Doppler grid as shown in the Fig.2. This is for a delay-Doppler grid with N=8 and M=32. The pilot symbol placement used in our experiments (N=M=32) is shown in Fig.3a . The pilot symbol is surrounded by guard symbols to avoid interference due to delay and Doppler spread of other data symbols on the channel estimation. The pilot symbol will undergo similar Doppler and delay shifts as experienced by the data symbols and thanks to OTFS modulation, all the symbols undergo roughly the same channel effect. The number of guard cells across the delay and Doppler axis depends on the delay and Doppler spread of the channel respectively. For our present implementation in an indoor wireless radio environment where the maximum delay spread is less than 100 nano secs as we observed from our channel measurements, we need only 4 delay taps to accommodate the delay spread as our delay resolution is 40 nano secs (see Table.I). Since there is no movement inside the room, the only Doppler shift is due to the carrier frequency offset. Once the channel information is extracted, the received OTFS demodulated frame along with the channel information is passed to the message passing detector, which in turn estimates the QAM symbols. For our experiments we choose a certain delay or Doppler tap as a channel if the corresponding signal power in that tap is greater than 3 times noise variance.

B. Effect of DC Offset on Channel Estimation

Direct conversion receiver (DCR), also known as zero-IF or homodyne receivers have become very popular especially in the realm of Software Designed Radios. There are many benefits to using DCRs compared to the classical superheterodyne receivers, such as reduction in bulky off-chip front

end components,which leads to higher level of integration and lower costs. But DCRs also come with some serious drawbacks ,the largest being DC Offset and IQ imbalances, as explained in [9]. DC offset manifests itself as a large spike in the center of the spectrum. This happens in DCRs due to a few different factors. One is ADC being off by a single LSB will yield a DC offset.Another is the output of the low pass filters where any DC bias will propagate through. The last is at the mixer where the local oscillator being at the center of the desired frequency band will leak back to the receiver front end and mix with itself (known as self mixing). Since DC-Offsets can have a negative impact on the performance of our receiver, it is important to estimate the DC offset. In our received OTFS frame, in the delay-Doppler grid, DC offset manifests itself as a constant signal in the Doppler axes corresponding to zero Doppler shift. As you can see from the experiments Fig.3b the DC offset remains fairly constant throughout the frame. This gives us an opportunity to correct the DC offset by estimating the DC offset and subtracting it from the zero Doppler shift row (1st row) of the OTFS demodulated frame. DC offset can be estimated by taking the average of the zero Doppler shift row (1st row) of the embedded pilot. To avoid the effect of DC offset on channel information, we reserve the first row of the embedded pilot for DC offset estimation.

C. Effect of Carrier Frequency Offset on Channel Estimation

The mismatch between local oscillators at the transmitter and receiver introduces a carrier frequency offset (CFO). While in simulations CFO can be set to zero, this is not the case in reality. IEEE specifies that the transmit center frequency error shall be a maximum of 20 ppm in both directions for the high speed 5 GHz band . For our NI USRP SDR that we are using, a frequency accuracy of 2.5 ppm is being specified [10]. So for a 4 GHz carrier frequency we can expect a CFO range of 10 KHz in either directions.An OFDM signal can be adversely affected by even a small CFO as it causes the subcarriers to lose its orthogonality property but in OTFS, a CFO can be considered as a constant Doppler shift, experienced by a mobile receiver moving at a constant velocity in the same direction relative to the transmitter. Here in this Fig.3c we show the effects of carrier shift on the pilot symbols. As you can see from the above figure, the pilot symbols just undergo a shift along the Doppler axis which manifests itself as a new path with a Doppler shift equal to the CFO and can be estimated and corrected using the message passing decoder.

IV. Experimental Setup and Study

Fig.6 shows the experimental setup for SDR Implementation of an OTFS TestBed. The transmitter and receiver terminals consists of two USRP-2943R SDRs, each connected to a host PC. The transmitter and receiver modem design and implementation is realized in LABView, running on the host PC. A LabView design or a program is called a virtual instrument (VI). The modem is implemented as two VIs, one for transmitter and one for receiver. The ADC, DAC and the Digital Up/Down conversion is realized by the FPGA, while

TABLE I
Experiment Parameters

Symbol	Parameter	Value
f_c	Carrier frequency	4 GHz
M	Number of subcarriers	32
N	Number of symbols	32
Q	Modulation alphabet size	4,16
T	Symbol Time	1.28 micro secs
Δf	Subcarrier spacing	781.25 KHz
$1/M\Delta f$	delay resolution	40 nano secs
$1/NT$	Doppler resolution	24.4 KHz
Fd_{max}	Maximum Doppler spread	400KHz
d	Tx-Rx Distance	1.5 meters

the rest of the digital signal processing including preamble detection and frame synchronization is done in LabView, using a combination of Labview Graphical Interface Blocks and C Code. LabView can call functions written in C Code only as dynamic linked libraries (DLL). The message passing decoder algorithm proposed in [5], [6] was written as a function in a DLL file written in C. The carrier frequency, sampling rate, number of subcarriers, symbols and modulation order can be set at run time of the VI. Transmitter and receiver gain can also be set at run time. The gain range of the USRP device is 0 dB to 31.5 dB.

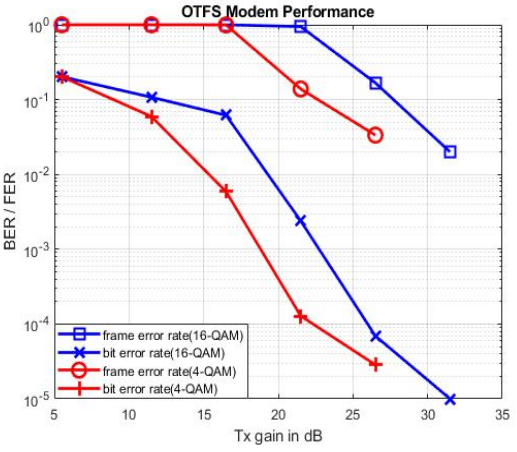

Fig. 4. Bit and Frame Error rates vs Transmitter gain for 4-QAM and 16-QAM

For our experiments we have chosen the modem parameters as given in Table I. We send OTFS frames continuously for each transmit gain configuration from 6.5 to 31.5 dB in steps of 5 dB while keeping the receiver gain constant at 0. The maximum transmit power (at a gain of 31.5 dB) at 4 GHz is in the range 5 mW to 32 mW. Fig.4 shows the bit error rate and frame error rate vs transmit gain for 4-QAM and 16-QAM information symbols. The total transmit power of each OTFS

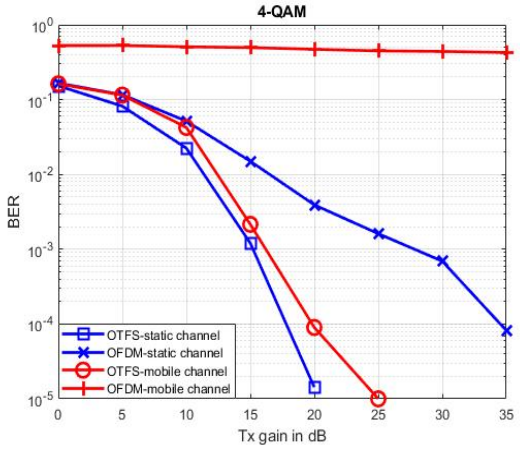

Fig. 5. Bit Error rates vs Transmitter gain for 4-QAM OTFS and OFDM modulation

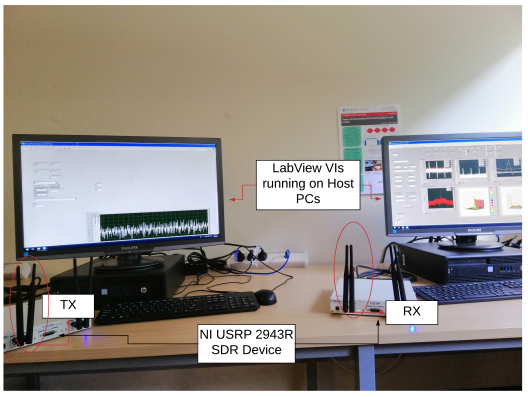

Fig. 6. OTFS setup

frame is kept constant to normalize power for 4-QAM and 16-QAM. The measurements were averaged over 10,000 frames for each transmit gain configuration. We observe that the 4-QAM achieves better error performance compared to 16-QAM for the same transmit power.

To emulate a mobile environment, we designed and placed a channel emulator block at the transmitter. It generates Doppler paths randomly from a uniform distribution with the specified maximum number of Doppler paths and maximum Doppler spread. We set 3 as the maximum number of Doppler taps and 400 KHz as the maximum Doppler spread (Fd_{max}) (which equates to a maximum relative velocity of 30 km/s). The transmitter can then be imagined as a mobile transmitter travelling with a velocity which is related to the emulator parameters. The generated signal is then transmitted through a real time wireless indoor channel which is frequency selective, hence simulating a doubly dispersive channel at the receiver as seen in Fig.3d. The performance of the OTFS modem is compared with OFDM with a single tap equalizer using the same hardware setup for both time and frequency selective channels. For a fair comparison, an OTFS frame and an OFDM frame with the same number of pilot and data symbols is send back to back so that both the frames undergo the same channel dispersion and hardware impairments. Both the frames are processed and decoded at the same receiver. As you can see in Fig. 5 the BER plot indicates a superior performance for OTFS modulation scheme in both the channel scenarios.

V. Conclusion

In this paper, we have successfully implemented an OTFS Modem TestBed with a SDR platform and discussed the block by block steps involved. We also discussed the effects of CFO and DC-Offset on the receiver performance and how it can be easily corrected in the delay-Doppler domain in the case when it remains fairly constant within an OTFS frame. The experiments were conducted in a real indoor wireless environment. To simulate mobility conditions the generated OTFS frame is passed through a channel emulator to introduce time selectivity before transmitting it into a frequency selective real indoor wireless channel. The OTFS modulation bit error rate performance is compared with OFDM using the same hardware setup to highlight the superior performance of OTFS in a doubly dispersive channel with similar receiver impairments. This testbed will be useful to study and develop a variety of OTFS receiver algorithms.

References

[1] R. Hadani, S. Rakib, M. Tsatsanis, A. Monk, A. J. Goldsmith, A. F. Molisch, and R. Calderbank, "Orthogonal time frequency space modulation," in *Proc. IEEE Wireless Communications and Networking Conference (WCNC)*, San Francisco, CA, USA, March 2017.

[2] R. Hadani, S. Rakib, S. Kons, M. Tsatsanis, A. Monk, C. Ibars, J. Delfeld, Y. Hebron, A. J. Goldsmith, A.F. Molisch, and R. Calderbank, "Orthogonal time frequency space modulation," Available online: https://arxiv.org/pdf/1808.00519.pdf.

[3] A. Farhang, A. RezazadehReyhani, L. E. Doyle, and B. Farhang-Boroujeny, "Low complexity modem structure for OFDM-based orthogonal time frequency space modulation," in *IEEE Wireless Communications Letters,* vol. 7, no. 3, pp. 344-347, June 2018.

[4] P. Raviteja, Y. Hong, E. Viterbo, and E. Biglieri, "Practical pulse-shaping waveforms for reduced-cyclic-prefix OTFS," *IEEE Trans. on Vehicular Technology*, Oct. 2018, doi: 10.1109/TVT.2018.2878891.

[5] P. Raviteja, et al., "Interference cancellation and iterative detection for orthogonal time frequency space modulation," *IEEE Trans. Wireless Commun.*, vol. 17, no. 10, pp. 6501-6515, Oct. 2018.

[6] P. Raviteja, et al., "Low-complexity iterative detection for orthogonal time frequency space modulation," in *Proc. IEEE Wireless Communications and Networking Conference (WCNC),* Barcelona, April 2018.

[7] P. Raviteja, K. T. Phan, Y. Hong, and E. Viterbo, "Embedded delay-Doppler channel estimation for orthogonal time frequency space modulation," in *Proc. IEEE VTC2018-fall,* Chicago, USA, August 2018.

[8] P. Raviteja, K. T. Phan, and Y. Hong, "Embedded pilot-aided channel estimation for OTFS in delay-Doppler channels," submitted in *IEEE Transactions on Vehicular Technology*.

[9] R. Svitek, S. Raman, "DC offsets in direct-conversion receivers: Characterization and implications," *IEEE Microwave Magazine*., pp. 76-86, Sep. 2005.

[10] USRP-2943 (Software Defined Radio Reconfigurable Device), Accessed: Jan. 2017, Available online: http://www.ni.com/enus/support/model.usrp-2943.html

Chapter 3

Low Complexity Iterative Rake Decision Feedback Equalizer for Zero-Padded OTFS Systems

Citing info:

T. Thaj and E. Viterbo, "Low Complexity Iterative Rake Decision Feedback Equalizer for Zero-Padded OTFS Systems" in *IEEE Transactions on Vehicular Technology*, vol. 69, no. 12, pp. 15606-15622, Dec. 2020, doi: 10.1109/TVT.2020.3044276.

Publishing Journal Info:

Impact factor: 5.978 , CiteScore: 10.9 , JCI ranked 10/105 (category TELECOMMUNICATIONS)

Copyright Statement:

©[2019] IEEE. Reprinted, with permission, from [Tharaj Thaj, Emanuele Viterbo, Low Complexity Iterative Rake Decision Feedback Equalizer for Zero-Padded OTFS Systems, IEEE Transactions on Vehicular Technology, 2020]

15606 IEEE TRANSACTIONS ON VEHICULAR TECHNOLOGY, VOL. 69, NO. 12, DECEMBER 2020

Low Complexity Iterative Rake Decision Feedback Equalizer for Zero-Padded OTFS Systems

Tharaj Thaj and Emanuele Viterbo, *Fellow, IEEE*

***Abstract*—This paper presents a linear complexity iterative rake detector for the recently proposed orthogonal time frequency space (OTFS) modulation scheme. The basic idea is to extract and coherently combine the received multipath components of the transmitted symbols in the delay-Doppler grid using maximal ratio combining (MRC) to improve the SNR of the combined signal. We reformulate the OTFS input-output relation in simple vector form by placing guard null symbols or zero padding (ZP) in the delay-Doppler grid and exploiting the resulting circulant property of the blocks of the channel matrix. Using this vector input-output relation we propose a low complexity iterative decision feedback equalizer (DFE) based on MRC. The performance and complexity of the proposed detector favorably compares with the state of the art message passing detector. An alternative time domain MRC based detector is also proposed for even faster detection. We further propose a Gauss-Seidel based over-relaxation parameter in the rake detector to improve the performance and the convergence speed of the iterative detection. We also show how the MRC detector can be combined with outer error-correcting codes to operate as a turbo DFE scheme to further improve the error performance. All results are compared with a baseline orthogonal frequency division multiplexing (OFDM) scheme employing a single tap minimum mean square error (MMSE) equalizer.**

***Index Terms*—DFE, decoder, delay–doppler channel, detector, gauss seidel, maximal ratio combining, OTFS, rake, successive over-relaxation, turbo.**

I. Introduction

ORTHOGONAL time frequency and space (OTFS) is a new two dimensional (2D) modulation technique that transforms information symbols in the delay-Doppler domain to the familiar time-frequency domain by spreading all the information symbols (e.g., QAM) over both time and frequency to achieve maximum *effective*[1] diversity [1], [2]. As a result, a time-frequency selective channel due to multipath fading and mobility, is converted into a *separable* and *quasi-orthogonal* interaction, where all received information symbols experience roughly the same localized impairment [1]. Hence, for each information symbol, the received components in all the delay-Doppler diversity branches can be separated and coherently combined.

OTFS can also be interpreted as a two-dimensional code division multiple access (CDMA) scheme, where information symbols are spread in both time and frequency, differently from conventional CDMA systems [1]. In direct sequence CDMA operating in a multipath fading channel, a rake receiver works by combining the delayed components (or echoes) of the transmitted symbols extracted by using matched filters tuned to the respective delay shifts. Similarly, in the case of OTFS, the received delay shifted and Doppler shifted components of the transmitted information symbols can be extracted and coherently combined using linear diversity combining techniques to improve the SNR of the accumulated signal.

Diversity combining techniques are well studied in the literature starting from Brennan's paper on linear diversity combining [4]. Rake receivers for time domain combining using a variety of linear combining schemes like maximal ratio combining (MRC), equal gain combining (EGC) and selection combining (SC) are discussed in [5], [6]. MRC is shown to be optimal in the case of correlated and uncorrelated branches, even for unequal noise and interference power in the branches [7]. Moreover, iterative rake combining schemes and its variants are shown to combat inter-symbol interference better and are well investigated in the literature for CDMA systems [8].

In this paper, we propose an iterative rake receiver for the OTFS system using the maximal ratio combining scheme. Following [3], we group the delay-Doppler grid symbols into vectors according to their delay index and reformulate the input-output relation between the transmitted and received frames in terms of these transmitted and received vectors. By placing some null symbols (zero-padding (ZP)) in the delay-Doppler domain we arrive at a reduced input-output relation, which allows the use of the maximal ratio combining to design a low complexity detector for OTFS. The overhead of the null guard symbols, needed for the proposed detection scheme, also allows to insert pilot symbols at no additional cost [10]. These null symbols in the delay-Doppler domain act as interleaved ZP guard bands in the time-domain. Taking advantage of this interleaved time-domain ZP, we further present an alternate low complexity time-domain MRC based detection for OTFS.

Manuscript received April 24, 2020; revised August 12, 2020, September 27, 2020, November 15, 2020, and November 25, 2020; accepted December 6, 2020. Date of publication December 14, 2020; date of current version January 22, 2021. This work was supported by the Australian Research Council through the Discovery Project under Grant DP200100096. Simulations were undertaken with the assistance of resources, and services from the National Computational Infrastructure (NCI), which is supported by the Australian Government. A preliminary version of this work was presented in part at the IEEE Wireless Communications, and Networking Conference (WCNC), May 2020, [3]. The review of this article was coordinated by Prof. Shu-Hung Leung. *(Corresponding author: Emanuele Viterbo.)*

The authors are with the Department of Electrical, and Computer Systems Engineering, Monash University, Clayton, VIC 3800, Australia (e-mail: tharaj.thaj@monash.edu; emanuele.viterbo@monash.edu).

Digital Object Identifier 10.1109/TVT.2020.3044276

[1]Effective diversity introduced for OTFS in [2] is a more meaningful measure of the actual diversity at practical SNR values, when the number of transmitted symbols is large.

0018-9545 © 2020 IEEE. Personal use is permitted, but republication/redistribution requires IEEE permission.
See https://www.ieee.org/publications/rights/index.html for more information.

Authorized licensed use limited to: Monash University. Downloaded on March 22,2022 at 09:25:19 UTC from IEEE Xplore. Restrictions apply.

OTFS with the ZP guard band as mentioned above is similar to the Doppler-resilient orthogonal signal division multiplexing (D-OSDM) scheme recently proposed in [11] for under water acoustic channels [12] which is modelled as relatively faster time-varying as compared to the vehicular channel model assumption [13]. Even though the information symbols in both schemes are transmitted in the delay-Doppler domain, the main advantage of the general OTFS transceiver structure is the provision to insert arbitrary frequency domain windowing, which is not a part of the D-OSDM scheme. Windowing allows OTFS to select a subset of sub-carriers for transmission and reception, which is particularly useful in multi-user communication schemes.

The rest of the paper is organized as follows. In Section II, we discuss the system model and derive the input-output relation in the vector form. To understand the operation of the proposed detector, we look at the input-output relation in delay-time and time domains in Section III. In Section IV, the proposed MRC based iterative rake detector, its low complexity implementation and the conditions for convergence are described. In Section V, we propose further improvements to the rake detector providing faster convergence and better error performance. The simulation results are given in Section VI followed by a discussion on the complexity of the proposed algorithm in Section VII. Section VIII contains our concluding remarks and future research directions.

II. OTFS System Model

A. Notations

The following notations will be followed in this paper: a, $\mathbf{a}$, $\mathbf{A}$ represent a scalar, vector, and matrix, respectively; $\mathbf{a}(n)$ and $\mathbf{A}(m,n)$ represent the n-th and (m,n)-th element of $\mathbf{a}$ and $\mathbf{A}$, respectively; $\mathbf{A}^{\dagger}$, $\mathbf{A}^{*}$ and $\mathbf{A}^{n}$ represent the Hermitian transpose, complex conjugate and n-th power of $\mathbf{A}$. The set of $M \times N$ dimensional matrices with complex entries are denoted by $\mathbb{C}^{N\times M}$. Let $\circledast$ represent circular convolution, $\otimes$, the Kronecker product, $\circ$, the Hadamard product (i.e., the element wise multiplication) and, $\oslash$, the Hadamard division (i.e., the element wise division). Let $|\mathcal{S}|$ denote the cardinality of the set $\mathcal{S}$, $\mathrm{tr}(A)$, the trace of the square matrix $\mathbf{A}$, $\mathrm{vec}(\mathbf{A})$, the column-wise vectorization of the matrix $\mathbf{A}$ and $\mathrm{vec}^{-1}_{N,M}(\mathbf{a})$ is the matrix formed by folding a vector $\mathbf{a}$ into a $N \times M$ matrix by filling it column wise. Let $\mathbf{F}_N$ be the normalized N point discrete Fourier transform (DFT) matrix with elements $\mathbf{F}_N(i,k) = N^{-1/2}\mathrm{e}^{-j2\pi ik/N}$ and $\mathbf{F}_N^{\dagger}$ the inverse discrete Fourier transform (IDFT) matrix, $\mathbf{I}_M$, the $M \times M$ identity matrix. The vectors $\mathbf{0}_N$ and $\mathbf{1}_N$ denote a N length column vector of zeros and ones, respectively. The scalar $z = \mathrm{e}^{\frac{j2\pi}{MN}}$.

B. Transmitter and Receiver Operation

The transmitter and receiver operations for the general OTFS system are described in [9], [15]. We will be using the following matrix/vector representation throughout the paper. Let $\mathbf{X}$, $\mathbf{Y} \in \mathbb{C}^{M\times N}$ be the transmitted and received two-dimensional delay-Doppler grid, forming a *frame* of $M \times N$ $\mathcal{Q}$-QAM symbols, with unit average energy. Let $\mathbf{x}_m, \mathbf{y}_m \in \mathbb{C}^{N\times 1}$ be column vectors containing the symbols in the m-th row of $\mathbf{X}$ and $\mathbf{Y}$, respectively: $\mathbf{x}_m = [\mathbf{X}(m,0), \mathbf{X}(m,1), \ldots, \mathbf{X}(m,N-1)]^{\mathrm{T}}$ and $\mathbf{y}_m = [\mathbf{Y}(m,0), \mathbf{Y}(m,1), \ldots, \mathbf{Y}(m,N-1)]^{\mathrm{T}}$, where m and n denote the delay (row) and Doppler (column) indices, respectively, in the two-dimensional grid. The total frame duration and bandwidth of the transmitted OTFS signal frame are $T_f = NT$ and $B = M\Delta f$, respectively. We consider the case where $T\Delta f = 1$, i.e., the OTFS signal is critically sampled for any pulse shaping waveform.

1) Basic OTFS Transmitter and Receiver: The delay-Doppler domain symbols in $\mathbf{X}$ is converted to the time-frequency domain ($\mathbf{X}_{\mathrm{tf}}$) using the inverse symplectic fast Fourier transform (ISFFT) operation.

$$\mathbf{X}_{\mathrm{tf}} = \mathbf{F}_M \cdot \mathbf{X} \cdot \mathbf{F}_N^{\dagger} \tag{1}$$

The "Heisenberg transform modulator" generates the time domain signal from the time-frequency samples using an M-point IFFT along with the pulse-shaping waveform $g_{\mathrm{tx}}(t)$. The transmitted signal can be written as

$$\mathbf{S} = \mathbf{G}_{\mathrm{tx}} \cdot (\mathbf{F}_M^{\dagger} \cdot \mathbf{X}_{\mathrm{tf}}) = \mathbf{G}_{\mathrm{tx}} \cdot (\mathbf{X} \cdot \mathbf{F}_N^{\dagger}) \tag{2}$$

where the diagonal matrix $\mathbf{G}_{\mathrm{tx}}$ has the samples of $g_{\mathrm{tx}}(t)$ as its entries: $\mathbf{G}_{\mathrm{tx}} = \mathrm{diag}[g_{\mathrm{tx}}(0), g_{\mathrm{tx}}(T/M), \ldots, g_{\mathrm{tx}}((M-1)T/M)] \in \mathcal{C}^{M\times M}$. Let $\tilde{\mathbf{X}}$ be the matrix containing the delay-time samples before applying pulse shaping waveform and is related to the delay-Doppler domain symbols as

$$\tilde{\mathbf{X}}^{\mathrm{T}} = [\tilde{\mathbf{x}}_0, \ldots, \tilde{\mathbf{x}}_{M-1}] = \mathbf{F}_N^{\dagger}[\mathbf{x}_0, \ldots, \mathbf{x}_{M-1}] = \mathbf{F}_N^{\dagger} \cdot \mathbf{X}^{\mathrm{T}}. \tag{3}$$

The time domain vector $\mathbf{s} \in \mathcal{C}^{NM\times 1}$, to be transmitted into the physical channel can be written as

$$\mathbf{s} = \mathrm{vec}(\mathbf{G}_{\mathrm{tx}} \cdot \tilde{\mathbf{X}}). \tag{4}$$

These samples are pulse shaped and transmitted as a continuous time signal $s(t)$. At the receiver, the delay-time samples are obtained from the sampled received time domain waveform $\mathbf{r} \in \mathbb{C}^{NM\times 1}$ as

$$\tilde{\mathbf{Y}} = \mathrm{vec}^{-1}_{N,M}((\mathbf{I}_M \otimes \mathbf{G}_{\mathrm{rx}}) \cdot \mathbf{r}), \tag{5}$$

where the diagonal matrix $\mathbf{G}_{\mathrm{rx}}$ has the samples of $g_{\mathrm{rx}}(t)$ as its entries: $\mathbf{G}_{\mathrm{rx}} = \mathrm{diag}[g_{\mathrm{rx}}(0), g_{\mathrm{rx}}(T/M), \ldots, g_{\mathrm{rx}}((M-1)T/M)] \in \mathcal{C}^{M\times M}$ is the pulse shaping filter at the receiver. The received delay-Doppler and delay-time domain symbols are related as

$$\mathbf{Y}^{\mathrm{T}} = [\mathbf{y}_0, \ldots, \mathbf{y}_{M-1}] = \mathbf{F}_N[\tilde{\mathbf{y}}_0, \ldots, \tilde{\mathbf{y}}_{M-1}] = \mathbf{F}_N \cdot \tilde{\mathbf{Y}}^{\mathrm{T}}. \tag{6}$$

2) Rectangular Pulse Shaping Waveforms: In this paper, we consider rectangular transmit and received pulse shaping waveforms which is equivalent to time-domain windowing, i.e., $\mathbf{G}_{\mathrm{tx}} = \mathbf{G}_{\mathrm{rx}} = \mathbf{I}_M$.[2] The transmitted and received time domain

[2]In general, the pulse shaping waveforms ($\mathbf{G}_{\mathrm{tx}}$) could be circulant matrices (equivalent to time-domain filtering).

Authorized licensed use limited to: Monash University. Downloaded on March 22,2022 at 09:25:19 UTC from IEEE Xplore. Restrictions apply.

discrete samples $\mathbf{s}, \mathbf{r}$ can then be written in terms of the delay-time samples $\tilde{\mathbf{x}}_m$ and $\tilde{\mathbf{y}}_m$ as

$$\mathbf{s}(m+nM) = \tilde{\mathbf{x}}_m(n),$$
$$\mathbf{r}(m+nM) = \tilde{\mathbf{y}}_m(n). \tag{7}$$

In this case, the transmitted and received discrete time domain signal samples can be related to the delay-Doppler domain information symbols as

$$\mathbf{s} = \text{vec}(\mathbf{X} \cdot \mathbf{F}_N^\dagger) \quad \text{and} \quad \mathbf{r} = \text{vec}(\mathbf{Y} \cdot \mathbf{F}_N^\dagger). \tag{8}$$

The operation in (8) in the literature is known as the inverse discrete Zak transform [16].

The simplified transmitter and receiver baseband equivalent model for rectangular pulse shaping waveforms and *two* MRC based detection methods (to be discussed in Section IV) are shown in Fig. 1 (a) and (b). The last $l_{\max}$ symbol vectors (rows) of the transmitted delay-Doppler grid, where $l_{\max}$ is the maximum channel delay spread index, are made zero to avoid inter-block interference in the time-domain. These zero vectors aid in reducing the complexity of detection for OTFS (explained in Section III-B) by allowing parallel processing of the N independent time domain blocks of duration T.

For the rest of the paper, to differentiate with the basic OTFS scheme, as discussed in [1], [9], we refer to the above scheme including zero padding as the ZP-OTFS. Our main motivation behind adding the delay-Doppler domain ZP is the design of a low complexity detector for OTFS, [3]. Adding a ZP along the delay dimension in the OTFS delay-Doppler grid can be seen as analogous to the time-domain CP or ZP added in orthogonal frequency division multiplexing (OFDM), which allows the design of a single tap equalizer in the time-frequency domain, and hence contribute to reduction in detector complexity. Moreover, in OTFS, the ZP can be used as guard band for the pilot in the delay-Doppler domain [10], and hence reduction in detector complexity can be achieved at little cost, which is convenient for the ZP-OTFS system.

C. Continuous Time Baseband Channel Model

Consider a baseband equivalent channel model[3] with P propagation paths, where h_i is the complex *path gain*, ℓ_i and κ_i are the *normalized delay shift* and *normalized Doppler shift*, respectively, associated with the i-th path, where $\ell_i, \kappa_i \in \mathbb{R}$ are not necessarily integers. The actual delay and Doppler shift for the i-th path is given by $\tau_i = \frac{\ell_i}{M\Delta f} < \tau_{\max} = \frac{\ell_{\max}}{M\Delta f}$, $\nu_i = \frac{\kappa_i}{NT}$ with $|\nu_i| < \nu_{\max}$. We assume that the channel is *under-spread*, i.e., $\tau_{\max}\nu_{\max} \ll 1$. Under the under-spread assumption, $\ell_{\max} < M$ and the normalized Doppler shifts $-N/2 < \kappa_i < N/2$. Since the number of channel coefficients P in the delay-Doppler domain is typically limited, the channel response has a sparse representation [1], [9]:

$$h(\tau, \nu) = \sum_{i=1}^{P} h_i \delta(\tau - \tau_i)\delta(\nu - \nu_i). \tag{9}$$

[3]We do not consider the effects of carrier frequency and antenna gains in this paper.

Alternatively, we can write,

$$h(\tau, \nu) = \sum_{\ell \in \mathcal{L}'} \sum_{\kappa \in \mathcal{K}_\ell} \nu_\ell(\kappa)\delta(\tau - \ell T/M)\delta(\nu - \kappa\Delta f/N) \tag{10}$$

where $\mathcal{L}' = \{\ell_i\}$ is the set of $L' = |\mathcal{L}'|$ distinct *normalized delay shifts* among the P paths in the delay-Doppler domain, $\mathcal{K}_\ell = \{\kappa_i \mid \ell = \ell_i\}$ is the set of *normalized Doppler shifts* for each path with *normalized delay shift* ℓ_i, and

$$\nu_\ell(\kappa) = \begin{cases} h_i, & \text{if } \ell = \ell_i \text{ and } \kappa = \kappa_i \\ 0, & \text{otherwise.} \end{cases} \tag{11}$$

is the ℓ-th delay tap *Doppler response*. The magnitude of a *Doppler response* function $\nu_\ell(\kappa)$ evaluated at integer delay and Doppler shifts is shown in Fig. 1.

The corresponding continuous time-varying channel impulse response function can be written, for all $\ell \in \mathcal{L}'$, as

$$g(\tau, t) = \int_\nu h(\tau, \nu) \mathrm{e}^{j2\pi\nu(t-\tau)}\, d\nu. \tag{12}$$

Substituting (11) into (12) and evaluating (12) at $\tau = \ell T/M$, we get,

$$g(\ell T/M, t) = \sum_{\kappa \in \mathcal{K}_\ell} \nu_\ell(\kappa) \mathrm{e}^{j2\pi\kappa\frac{\Delta f}{N}(t-\ell T/M)} \tag{13}$$

which represents the *delay-time channel response*, for all $\ell \in \mathcal{L}'$.

D. Discrete Time Baseband Channel Model

At the transmitter, the OTFS frame of bandwidth $B = M\Delta f$ is up-converted to a carrier frequency f_c to occupy a pass band channel, assuming $f_c \gg B$. At the receiver, the channel impaired signal is down-converted to baseband and sampled at $M\Delta f$ Hz, thereby limiting the received waveform to NM complex samples. Therefore, from a communication system design point of view, it is convenient to have a discrete baseband equivalent representation of the system, [14].

In the previous section, we looked at the continuous time model of the channel. The discrete time model is obtained by sampling the received waveform $r(t)$ at sampling intervals $t = qT/M$, where $0 \le q \le NM - 1$, which discretizes the delay-time channel. The set of *normalized delay shifts*, $\mathcal{L}'$ is therefore replaced as $\mathcal{L}$ with the set of $L = |\mathcal{L}|$ discrete delay taps representing delay shifts at integer multiples of the sampling period T/M. Recall that $\frac{\Delta f}{N}$ and $\frac{T}{M}$ are the Doppler and delay resolution, respectively, of the delay-Doppler grid, given $T\Delta f = 1$. Following from the sampling theorem [14], the discrete baseband delay-time channel model of (13) is given as,

$$g^{\mathrm{s}}(l, q) = \sum_{\ell \in \mathcal{L}'} \left(\sum_{\kappa \in \mathcal{K}_\ell} \nu_\ell(\kappa) z^{\kappa(q-l)} \right) \mathrm{sinc}(l - \ell) \tag{14}$$

where $\mathrm{sinc}(x) = \sin(\pi x)/(\pi x)$ and $z = \mathrm{e}^{\frac{j2\pi}{NM}}$.

Note that, due to fractional delays, the sampling at the receiver introduces interference between Doppler responses at different delay shifts. This is due to sinc reconstruction of the delay-time response at fractional delay points (ℓ), [14]. However, under the assumption that the channel delay shifts can be modelled as

Authorized licensed use limited to: Monash University. Downloaded on March 22,2022 at 09:25:19 UTC from IEEE Xplore. Restrictions apply.

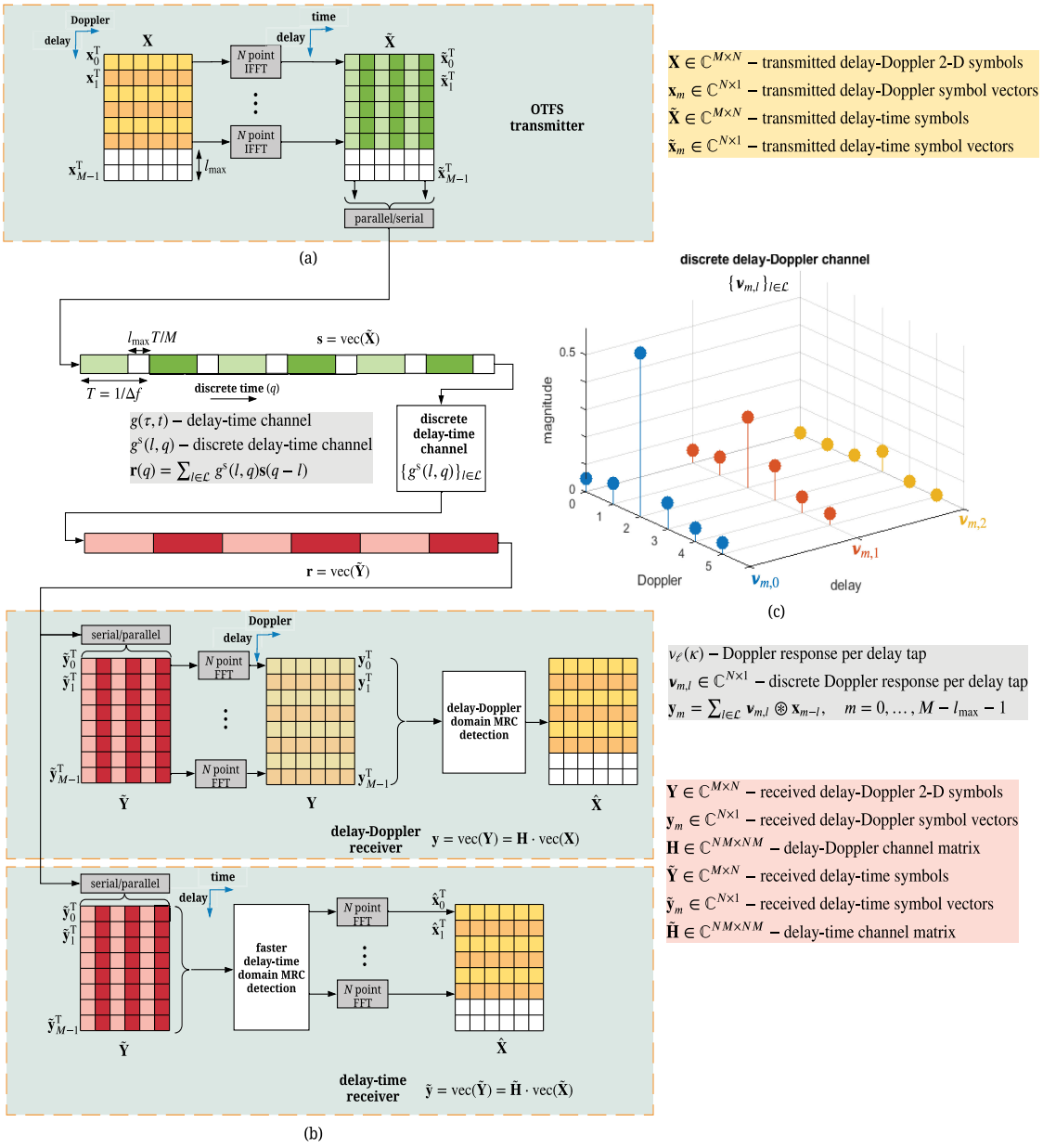

Fig. 1. Discrete baseband model of the ZP-OTFS system for $N = 6$, $M = 8$ for (a) transmitter (b) receiver and (c) the discrete delay-Doppler channel at the set of discrete delay tap indices $\mathcal{L} = \{0, 1, 2\}$. The samples shown using the same colour in (c) represent the Doppler response in the same delay tap. In (b), two versions of the proposed Rake receiver are presented (see Section IV). The receiver chain on the top part of (b) operates directly in the information symbol domain, i.e., the delay-Doppler domain (see Algorithm 1 in Section IV.A) and the bottom part of (b) is the faster version (see Algorithm 2 in Section IV.B) which operates in the delay-time domain.

integer delay shifts without loss of accuracy, i.e., when $\mathcal{L}' = \mathcal{L}$ and hence $\ell = l' \in \mathbb{Z}$, the sinc function in (14) reduces to

$$\mathrm{sinc}(l - l') = \begin{cases} 1, & \text{if } l' = l \\ 0, & \text{otherwise.} \end{cases} \tag{15}$$

Consequently, the relation between the actual Doppler response and the sampled time-domain channel at each integer delay tap $l \in \mathcal{L}$ in (14) reduces to

$$g^s(l, q) = \sum_{\kappa\in\mathcal{K}_l} \nu_l(\kappa) z^{\kappa(q-l)}. \tag{16}$$

Authorized licensed use limited to: Monash University. Downloaded on March 22,2022 at 09:25:19 UTC from IEEE Xplore. Restrictions apply.

Here we want to remind the readers that the effective channel as seen by the receiver depends on the actual channel response as well as the operation parameters (delay and Doppler resolution) of the receiver.

For the rest of the paper, to clearly differentiate between the real continuous channel and the effective discrete channel as seen by the receiver, we use ℓ and κ to denote the normalized delay and Doppler shifts (not necessarily integers) associated with the channel whereas l and k is used only to denote integer delay and Doppler shift indices, respectively, associated with the channel sampled on the OTFS delay-Doppler grid.

E. Input-Output Relations in Delay-Doppler Domain

In this section, we reformulate the input-output relation with rectangular pulse shaping waveforms, for the ZP-OTFS system shown in Fig. 1.

Starting from the received time-domain signal $r(t)$, the continuous time domain input-output relation can be written as

$$r(t) = \int_0^{\tau_{\max}} g(\tau, t) s(t-\tau)\, d\tau. \tag{17}$$

From (14), the corresponding discrete time-domain input-output relation when the transmitted and received time-domain signals are sampled at $t = qT/M$ can be written as

$$\mathbf{r}(q) = \sum_{l\in\mathcal{L}} g^{\mathrm{s}}(l, q)\mathbf{s}(q-l) \tag{18}$$

where $\mathbf{r}(q) = r(q\frac{T}{M})$, $\mathbf{s}(q) = s(q\frac{T}{M})$. Using the relations in (7), we split the time index $q = 0, \ldots, MN-1$ in terms of the delay and Doppler frame indices as $q = (m + nM)$, where the $m = 0, 1, \ldots, M-1$ and $n = 0, 1, \ldots, N-1$. Then replacing $\tilde{\boldsymbol{\nu}}_{m,l}(n) = g^{\mathrm{s}}(l, m+nM)$, we can rewrite (18) in terms of the delay-time symbol vectors as

$$\tilde{\mathbf{y}}_m(n) = \sum_{l\in\mathcal{L}} \tilde{\boldsymbol{\nu}}_{m,l}(n)\tilde{\mathbf{x}}_{m-l}(n) \tag{19}$$

where $\tilde{\boldsymbol{\nu}}_{m,l} \in \mathbb{C}^{N\times 1}$ is given as

$$\tilde{\boldsymbol{\nu}}_{m,l}(n) = \sum_{\ell\in\mathcal{L}'} \left(\sum_{\kappa\in\mathcal{K}_l} \nu_\ell(\kappa) z^{\kappa(m-l)} \mathrm{e}^{\frac{j2\pi\kappa n}{N}} \right) \mathrm{sinc}(l-\ell). \tag{20}$$

For integer delay tap channel assumption, i.e., $l = \ell \in \mathbb{Z}$, (20) becomes,

$$\tilde{\boldsymbol{\nu}}_{m,l}(n) = \sum_{\kappa\in\mathcal{K}_l} \nu_l(\kappa) z^{\kappa(m-l)} \mathrm{e}^{\frac{j2\pi\kappa n}{N}}. \tag{21}$$

We can note from (21) that the discrete delay-time response $\tilde{\boldsymbol{\nu}}_{m,l}(n)$ for each delay tap l at time instants $t = \frac{m}{M}T + nT$ is related to the inverse Fourier transform of the *Doppler response* $\nu_l(\kappa)$ of the l-th delay tap sampled at time $t = \frac{m}{M}T$. We may ignore the case in (19) when $m - l < 0$ i.e., when there is inter-block interference due to channel delay spread, by making $\tilde{\mathbf{x}}_m(n) = 0$ for all n when $m - l < 0$ such that,

$$\tilde{\boldsymbol{\nu}}_{m,l}(n)\tilde{\mathbf{x}}_{m-l}([n-k]_N) = 0, \text{ if } m < l \tag{22}$$

This is equivalent to placing null symbol vectors $\mathbf{0}_N$ in the last $l_{\max}$ rows of $\mathbf{X}$ (zero padding along the delay dimension of the OTFS grid). Hence, we can set, for $n = 0, \ldots, N-1$,

$$\mathbf{x}_m(n) = \tilde{\mathbf{x}}_m(n) = 0, \text{ if } m \geq M - l_{\max} \tag{23}$$

The delay-Doppler domain received symbols can be obtained by taking an N-point FFT of the delay-time received symbol vectors (6)

$$\begin{aligned}\mathbf{y}_m = \mathbf{F}_N \cdot \tilde{\mathbf{y}}_m &= \sum_{l\in\mathcal{L}} \mathbf{F}_N \cdot (\tilde{\boldsymbol{\nu}}_{m,l} \circ \tilde{\mathbf{x}}_{m-l}) \\ &= \sum_{l\in\mathcal{L}} (\mathbf{F}_N \cdot \tilde{\boldsymbol{\nu}}_{m,l}) \circledast (\mathbf{F}_N \cdot \tilde{\mathbf{x}}_{m-l}) \\ &= \sum_{l\in\mathcal{L}} \boldsymbol{\nu}_{m,l} \circledast \mathbf{x}_{m-l}\end{aligned} \tag{24}$$

where,

$$\boldsymbol{\nu}_{m,l}(k) = \frac{1}{\sqrt{N}} \sum_{n=0}^{N-1} \tilde{\boldsymbol{\nu}}_{m,l}(n) \mathrm{e}^{\frac{-j2\pi kn}{N}} \tag{25}$$

for $0 \leq k \leq N-1$, $0 \leq m < M - l_{max}$, is the discrete *Doppler spread vector* in the l-th channel delay tap, experienced by all the symbols in the $(m-l)$-th row of the $M \times N$ OTFS delay-Doppler grid. Fig. 1 (c) shows the discrete Doppler spread vectors $\boldsymbol{\nu}_{l,l}$ for $\mathbf{x}_0$. Substituting (14), (21) and (20) in (25), we can write the discrete Doppler spread vector $\boldsymbol{\nu}_{m,l} \in \mathbb{C}^{N\times 1}$ in terms of the channel *Doppler response* $\nu_\ell(\kappa)$, for a channel model assuming:

1) Fractional Delay and Fractional Doppler Shifts:

$$\boldsymbol{\nu}_{m,l}(k) = \frac{1}{\sqrt{N}} \sum_{\ell\in\mathcal{L}'} \left(\sum_{\kappa\in\mathcal{K}_\ell} \nu_\ell(\kappa) z^{\kappa(m-l)} \zeta_N(\kappa - k) \right) \mathrm{sinc}(l-\ell) \tag{26}$$

where $\ell, \kappa \in \mathbb{R}$ and the *periodic sinc function* $\zeta(\cdot)$ includes the extra phase and magnitude variations in the Doppler spread vectors due to fractional Doppler shifts, given as

$$\zeta_N(x) = \frac{1}{\sqrt{N}} \sum_{n=0}^{N-1} \mathrm{e}^{\frac{j2\pi xn}{N}} = \frac{1}{\sqrt{N}} \frac{\sin(\pi x)}{\sin(\pi x/N)} \mathrm{e}^{\frac{j\pi x(N-1)}{N}} \tag{27}$$

2) Integer Delay and Fractional Doppler Shifts: For integer values of $(l-\ell)$, the function $\mathrm{sinc}(l-\ell)$ evaluates to 1 when $l = \ell$ and *zero* else where. Hence (26) reduces to

$$\boldsymbol{\nu}_{m,l}(k) = \frac{1}{\sqrt{N}} \sum_{\kappa\in\mathcal{K}_l} \nu_\ell(\kappa) z^{\kappa(m-l)} \zeta_N(\kappa - k) \tag{28}$$

for $l = \ell \in \mathbb{Z}$ and $\kappa \in \mathbb{R}$

3) Integer Delay and Integer Doppler Shifts: For integer values of x, the function $\zeta_N(x)$ evaluates to $\sqrt{N}$ when $x = 0$ and *zero* else where. Hence (28) reduces to the simple form

$$\boldsymbol{\nu}_{m,l}(k) = \begin{cases} \nu_\ell(\kappa) z^{\kappa(m-l)}, & \text{if } l = \ell \text{ and } k = [\kappa]_N \\ 0, & \text{otherwise.} \end{cases} \tag{29}$$

for $\ell, \kappa \in \mathbb{Z}$.

Remark – The above three cases result in phase changes $z^{\kappa(m-l)}$ due to the rectangular pulse shaping waveforms. For the ideal pulse shaping waveform assumption, it was shown in [3], [9] that the Doppler spread vectors $\boldsymbol{\nu}_{m,l}$ are invariant on the 2-D

Authorized licensed use limited to: Monash University. Downloaded on March 22,2022 at 09:25:19 UTC from IEEE Xplore. Restrictions apply.

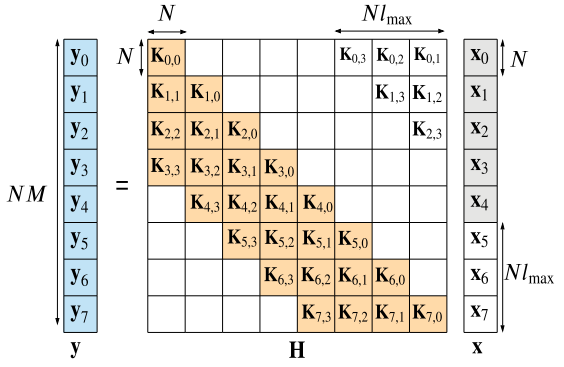

Fig. 2. Delay-Doppler domain input-output relation $\mathbf{y} = \mathbf{H} \cdot \mathbf{x}$ after adding null symbols only contains the shaded blocks for $N = M = 8$ and $l_{max} = 3$.

delay-Doppler grid and hence not dependent on the row index m. The phase variations $z^{\kappa(m-l)}$ can be ignored in (26), (28) and (29). As a result (24) is a simple time-invariant 2-D circular convolution as shown in [3], [9]. It is important to note that ignoring such phase variations in the detection process results in significant performance degradation. □

For the rest of the paper and simulations, we assume integer delays and fractional Doppler shifts for rectangular pulse shaping waveforms, i.e., we consider the discrete input-output relation of the form given in (24) and (28) where $\mathcal{L}' = \mathcal{L} \in \mathbb{Z}$.

The OTFS delay-Doppler domain discrete system for the ZP OTFS system can be expressed in the matrix form as

$$\mathbf{y} = \mathbf{H} \cdot \mathbf{x} + \mathbf{w}; \tag{30}$$

where $\mathbf{x}, \mathbf{y}, \mathbf{w} \in \mathbb{C}^{NM \times 1}$ and $\mathbf{H} \in \mathbb{C}^{NM \times NM}$ is the OTFS channel matrix when transmitted and received symbol-vectors, $\mathbf{x}_m, \mathbf{y}_m \in \mathbb{C}^{N \times 1}$ are grouped and stacked as $\mathbf{y} = [\mathbf{y}_0^{\mathrm{T}}, \mathbf{y}_1^{\mathrm{T}}, \ldots, \mathbf{y}_{M-1}^{\mathrm{T}}]^{\mathrm{T}}$, $\mathbf{x} = [\mathbf{x}_0^{\mathrm{T}}, \mathbf{x}_1^{\mathrm{T}}, \ldots, \mathbf{x}_{M-1}^{\mathrm{T}}]^{\mathrm{T}}$ and $\mathbf{w} = [\mathbf{w}_0^{\mathrm{T}}, \mathbf{w}_1^{\mathrm{T}}, \ldots, \mathbf{w}_{M-1}^{\mathrm{T}}]^{\mathrm{T}}$ is independent and identically distributed (iid) additive white guassian noise (AWGN) with variance σ_w^2. Referring to the vectorized form shown in Fig. 2, we convert the circular convolution between two vectors into the product of a matrix and a vector by defining $\mathbf{K}_{m,l} \in \mathbb{C}^{N \times N}$ to be a banded matrix for $l \in \mathcal{L}$ and an all zero matrix otherwise

$$\mathbf{K}_{m,l} = \mathrm{circ}[\boldsymbol{\nu}_{m,l}(0), \ldots, \boldsymbol{\nu}_{m,l}(N-1)]$$

$$= \begin{bmatrix} \boldsymbol{\nu}_{m,l}(0) & \boldsymbol{\nu}_{m,l}(N-1) & \cdots & \boldsymbol{\nu}_{m,l}(1) \\ \boldsymbol{\nu}_{m,l}(1) & \boldsymbol{\nu}_{m,l}(0) & \cdots & \boldsymbol{\nu}_{m,l}(2) \\ \vdots & \ddots & \ddots & \vdots \\ \boldsymbol{\nu}_{m,l}(N-1) & \boldsymbol{\nu}_{m,l}(N-2) & \cdots & \boldsymbol{\nu}_{m,l}(0) \end{bmatrix}.$$

We note that the band width of each submatrix $\mathbf{K}_{m,l}$ of $\mathbf{H}$ is equal to the maximum Doppler spread $k_{\max} \leq N/2$ and the full channel matrix $\mathbf{H}$ has a band width equal to $N(l_{\max}+1)$. We can then write (24) as

$$\mathbf{y}_m = \sum_{l \in \mathcal{L}} \mathbf{K}_{m,l} \cdot \mathbf{x}_{m-l}. \tag{31}$$

Note that $\mathbf{K}_{m,l}$ (or $\boldsymbol{\nu}_{m,l}$) can be considered as the linear time-variant channel between the receiver grid delay index m and transmitter grid delay index $m-l$ in the OTFS delay-Doppler grid. Now (24) and (31) gives us a very simple equation relating the transmitted and received symbol-vectors that we defined at the start of this section.

III. Input-Output Relation in Other Domains

In this section, we discuss the ZP-OTFS input-output relation between the transmitted and received delay-time symbol vectors and discuss the advantages of carrying out significant part of the OTFS receiver processing in the delay-time domain. We also highlight some properties of the delay-time and time-domain channel matrices to later analyze the convergence of the proposed detector.

When N and M are sufficiently large, considering the channel normalized delay and Doppler shifts (ℓ_i and κ_i) as integers has negligible effect on the accuracy of the channel representation. However, the effect of fractional Doppler is more pronounced for short OTFS frames, [22]. When N is small, a single path with fractional Doppler shift is seen as a cluster of paths with integer Doppler shifts at the receiver. Depending on the resolution, more channel coefficients along the Doppler dimension are required to fully represent the channel state information needed for accurate detection at the receiver, [9]. This increases the total number of paths P for the discrete channel. To mitigate such problem, the value of N may be increased, which, in turn, will increase the frame duration NT. However, the frame duration is limited by the *delay-Doppler coherence time*,[4] i.e., the time over which the delay-Doppler channel coefficients remain constant.

Another way of solving the fractional Doppler issue is by dealing with the delay-Doppler channel coefficients in the delay-time domain. As Doppler shifts cannot be resolved in this domain, the number of delay-time channel coefficients is neither affected by the fractional Doppler shifts nor by the Doppler spread of that delay tap. Therefore, to fully take advantage of the OTFS performance in a rich Doppler spread regime (i.e., large $|\mathcal{K}_l|$'s), it is convenient to design a receiver with low complexity that is independent of the Doppler spread.

A. Delay-Time Domain

For the purpose of delay-time detection analysis in Section IV, we look at the matrix representation of the delay-time input-output relation. The matrices $\mathbf{K}_{m,l}$ in the delay-Doppler domain can be diagonalized to $\tilde{\mathbf{K}}_{m,l}$ in the corresponding Fourier domain (delay-time domain) as

$$\mathbf{K}_{m,l} = \mathbf{F}_N \cdot \tilde{\mathbf{K}}_{m,l} \cdot \mathbf{F}_N^{\dagger},$$
$$\Rightarrow \tilde{\mathbf{K}}_{m,l} = \mathrm{diag}[\tilde{\boldsymbol{\nu}}_{m,l}(0), \ldots, \tilde{\boldsymbol{\nu}}_{m,l}(N-1)]$$
$$\text{where } \tilde{\boldsymbol{\nu}}_{m,l} = \mathbf{F}_N^{\dagger} \boldsymbol{\nu}_{m,l}$$

thereby transforming the delay-Doppler domain channel matrix $\mathbf{H}$ into the delay-time domain channel matrix $\tilde{\mathbf{H}}$ by replacing the sub-matrices $\mathbf{K}_{m,l}$ in $\mathbf{H}$ with $\tilde{\mathbf{K}}_{m,l}$. Given the input-output

[4]This coherence time should not be confused with the traditional notion related to the inverse of the Doppler spread, [3].

Authorized licensed use limited to: Monash University. Downloaded on March 22,2022 at 09:25:19 UTC from IEEE Xplore. Restrictions apply.

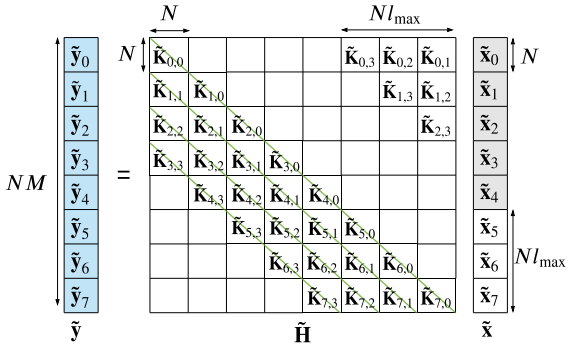

Fig. 3. Delay-time domain input-output relation ($\tilde{\mathbf{y}} = \tilde{\mathbf{H}} \cdot \tilde{\mathbf{x}}$) after adding null symbols for $N = M = 8$ and $l_{\max} = 3$.

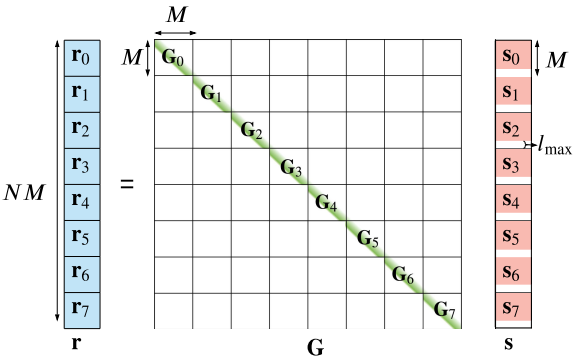

Fig. 4. Time-domain input-output relation $\mathbf{r} = \mathbf{G} \cdot \mathbf{s}$ after shuffling the matrix $\tilde{\mathbf{H}}$ as $\mathbf{G} = \mathbf{P} \cdot \tilde{\mathbf{H}} \cdot \mathbf{P}^{\mathrm{T}}$ for $N = M = 8$ and $l_{\max} = 3$.

relation in (30) was simplified in (31) by placing null symbols in the delay-Doppler grid as given in (23), the strictly upper triangular blocks of $\tilde{\mathbf{H}}$ can also be set to zero. The input-output relation in the delay-time domain, illustrated in Fig. 3, can then be written in the matrix form as

$$\tilde{\mathbf{y}} = \tilde{\mathbf{H}} \cdot \tilde{\mathbf{x}} + \tilde{\mathbf{w}}; \tag{32}$$

where

$$\begin{aligned} &\tilde{\mathbf{y}} = (\mathbf{I}_M \otimes \mathbf{F}_N^{\dagger}) \cdot \mathbf{y}, \quad \tilde{\mathbf{x}} = (\mathbf{I}_M \otimes \mathbf{F}_N^{\dagger}) \cdot \mathbf{x}, \\ &\tilde{\mathbf{H}} = (\mathbf{I}_M \otimes \mathbf{F}_N^{\dagger}) \cdot \mathbf{H} \cdot (\mathbf{I}_M \otimes \mathbf{F}_N), \end{aligned} \tag{33}$$

and $\tilde{\mathbf{w}}$ is the time domain AWGN vector. In this domain, the complexity of matrix multiplication is significantly reduced as the sparsity L/N of $\tilde{\mathbf{H}}$ is less than or equal to the sparsity P/N of $\mathbf{H}$, where L is the number of unique delay taps and P is the total number of propagation paths. The delay-time domain channel matrix $\tilde{\mathbf{H}}$ is a banded block matrix (with a bandwidth of $Nl_{\max} + 1$), where $\tilde{\mathbf{K}}_{m,l} \in \mathcal{C}^{N \times N}$ are non-zero diagonal matrices for $m \geq l$ and $l \in \mathcal{L}$ and zero matrices otherwise. Consequently, the delay-Doppler domain input-output relation in (24) becomes

$$\tilde{\mathbf{y}}_m = \sum_{l \in \mathcal{L}} \tilde{\boldsymbol{\nu}}_{m,l} \circ \tilde{\mathbf{x}}_{m-l}, \quad \tilde{\mathbf{x}}_m = \mathbf{0}_N \text{ for } m \geq M - l_{\max}. \tag{34}$$

in the delay-time domain, where $\tilde{\mathbf{x}} = [\tilde{\mathbf{x}}_0^{\mathrm{T}}, \ldots, \tilde{\mathbf{x}}_{M-1}^{\mathrm{T}}]^{\mathrm{T}}$ and $\tilde{\mathbf{y}} = [\tilde{\mathbf{y}}_0^{\mathrm{T}}, \ldots, \tilde{\mathbf{y}}_{M-1}^{\mathrm{T}}]^{\mathrm{T}}$.

B. Time Domain

Here, we show how the time domain input-output relation is connected to the delay-Doppler and the delay-time domain input-output relations.

From (7), it can be seen that the delay-time vectors $\tilde{\mathbf{x}}$ and $\tilde{\mathbf{y}}$ in (32) are simply shuffled versions of the time domain transmitted and received vectors $\mathbf{s}$ and $\mathbf{r}$, respectively. Let $\mathbf{s}$ and $\mathbf{r}$ be split into N blocks each of size M, such that $\mathbf{s} = [\mathbf{s}_0^{\mathrm{T}}, \ldots, \mathbf{s}_{N-1}^{\mathrm{T}}]^{\mathrm{T}}$ and $\mathbf{r} = [\mathbf{r}_0^{\mathrm{T}}, \ldots, \mathbf{r}_{N-1}^{\mathrm{T}}]^{\mathrm{T}}$. Then $\tilde{\mathbf{x}}_m = [\mathbf{s}_0(m), \ldots, \mathbf{s}_{N-1}(m)]^{\mathrm{T}}$ and $\tilde{\mathbf{y}}_m = [\mathbf{r}_0(m), \ldots, \mathbf{r}_{N-1}(m)]^{\mathrm{T}}$.

Let

$$\mathbf{P} = \begin{bmatrix} \mathbf{E}_{1,1} & \mathbf{E}_{2,1} & \cdots & \mathbf{E}_{M,1} \\ \mathbf{E}_{1,2} & \mathbf{E}_{2,2} & \cdots & \mathbf{E}_{M,2} \\ \vdots & \ddots & \ddots & \vdots \\ \mathbf{E}_{1,N} & \mathbf{E}_{2,N} & \cdots & \mathbf{E}_{M,N} \end{bmatrix} \in \mathbb{C}^{NM \times NM} \tag{35}$$

be the row-column interleaver permutation matrix such that $\mathbf{s} = \mathbf{P} \cdot \tilde{\mathbf{x}}$ and $\mathbf{r} = \mathbf{P} \cdot \tilde{\mathbf{y}}$ where $\mathbf{E}_{i,j} \in \mathbb{C}^{M \times N}$ is defined as

$$\mathbf{E}_{i,j}(i', j') = \begin{cases} 1, & \text{if } i' = i \text{ and } j' = j \\ 0, & \text{otherwise.} \end{cases} \tag{36}$$

Such permutation is known in the literature as a *perfect shuffle,* and has the following property [17]: given square matrices $\mathbf{A}$ and $\mathbf{B}$

$$\mathbf{A} \otimes \mathbf{B} = \mathbf{P} \cdot (\mathbf{B} \otimes \mathbf{A}) \cdot \mathbf{P}^{\mathrm{T}}. \tag{37}$$

The input-output relation in (32) can now be written as

$$(\mathbf{P}^{\mathrm{T}} \cdot \mathbf{r}) = \tilde{\mathbf{H}} \cdot (\mathbf{P}^{\mathrm{T}} \cdot \mathbf{s}) + \tilde{\mathbf{w}}. \tag{38}$$

Multiplying both sides of (38) on the left by $\mathbf{P}$, the input-output relation can be expressed in terms of the time-domain channel matrix $\mathbf{G} = \mathbf{P} \cdot \tilde{\mathbf{H}} \cdot \mathbf{P}^{\mathrm{T}}$ as

$$\mathbf{r} = \mathbf{G} \cdot \mathbf{s} + \tilde{\mathbf{w}}. \tag{39}$$

We note that $\mathbf{G}$ and $\tilde{\mathbf{H}}$ are *similar* matrices and hence share the same eigenvalues [18]. From (33) using the perfect shuffle property in (37), the time domain channel matrix $\mathbf{G}$ can be related to the delay-Doppler domain channel matrix $\mathbf{H}$ as

$$\mathbf{G} = (\mathbf{F}_N^{\dagger} \otimes \mathbf{I}_M) \cdot (\mathbf{P} \cdot \mathbf{H} \cdot \mathbf{P}^{\mathrm{T}}) \cdot (\mathbf{F}_N \otimes \mathbf{I}_M). \tag{40}$$

As shown in Fig. 4 the null symbols added in the delay-Doppler domain act as interleaved guard bands of length $l_{\max}$ in the time-domain vector $\mathbf{s}$ and thus help in avoiding interference between the time domain blocks $\mathbf{r}_n$ for $n = 0, \ldots, N-1$. This forces $\mathbf{G}$ to be a block-diagonal matrix. As a result, the large matrix equation in (39) can be split into N parallel smaller linear matrix equations with the blocks $\mathbf{G}_0, \ldots, \mathbf{G}_{N-1} \in \mathbb{C}^{M \times M}$ as the corresponding channel matrices. $\mathbf{G}_n$ are the diagonal blocks of $\mathbf{G}$ each with a bandwidth of $l_{\max} + 1$. The system equation

Authorized licensed use limited to: Monash University. Downloaded on March 22,2022 at 09:25:19 UTC from IEEE Xplore. Restrictions apply.

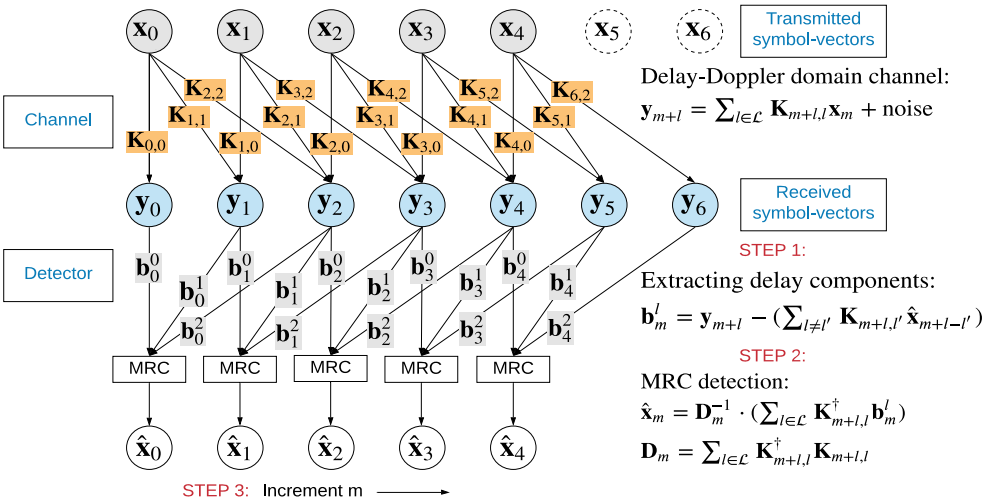

Fig. 5. MRC delay-Doppler domain operation for $M = 7$ and the set of discrete delay indices $\mathcal{L} = 0, 1, 2$.

in (39) can be split and written as

$$\mathbf{r}_n = \mathbf{G}_n \cdot \mathbf{s}_n + \bar{\mathbf{w}}_n \quad \text{where } n = 0, \ldots, N-1. \tag{41}$$

Since $\mathbf{G} = \mathbf{P} \cdot \tilde{\mathbf{H}} \cdot \mathbf{P}^{\mathrm{T}}$, the non-zero entries of the $M \times M$ time domain channel sub-matrices $\mathbf{G}_n$ are related to the entries of the $N \times N$ delay-time channel sub-matrices $\tilde{\mathbf{K}}_{m,l}$ and the time-varying complex channel gain for each delay tap $g^{\mathrm{s}}(l, q)$ as

$$g^{\mathrm{s}}(l, q) = \mathbf{G}_n(m, m-l) = \tilde{\mathbf{K}}_{m,l}(n, n) = \tilde{\boldsymbol{\nu}}_{m,l}(n) \tag{42}$$

where $q = m + nM$, $m \in \{l \leq i < M | l \in \mathcal{L}\}$ and $0 \leq n < N$.

IV. Low Complexity Iterative Rake Detector

We can think of the proposed MRC detector as the maximal ratio combining of the channel impaired signal components received at $L = |\mathcal{L}| \leq P$ different delay branches in the delay-Doppler grid analogous to a CDMA rake receiver as shown in Fig. 5. The noise plus interference (NPI) power in each of these branches is different and depends on the channel response. In each detector iteration, we cancel the estimated inter symbol-vector interference in the branches selected for combining, thereby iteratively improving the post MRC signal to interference plus noise ratio (SINR).

The input output relation between the transmitted and received symbol-vectors $\mathbf{x}_m$ and $\mathbf{y}_m$ in (24) is given by

$$\mathbf{y}_{m+l} = \sum_{l\in\mathcal{L}} \mathbf{K}_{m+l,l} \cdot \mathbf{x}_m + \mathbf{w}_{m+l} \tag{43}$$

where $\mathbf{w}_m$ is iid AWGN noise with variance σ_n^2. From (43), due to the inter-symbol interference caused by delay spread ($l_{\max}T/M$), all symbol-vectors $\mathbf{x}_m$ have a signal component in L received symbol-vectors $\mathbf{y}_{m+l}$, for $l \in \mathcal{L}$. Let $\mathbf{b}_m^l \in \mathbb{C}^{N\times 1}$ be the channel impaired signal component of $\mathbf{x}_m$ in the received $\mathbf{y}_{m+l}$ vector at delay index $m + l$ after removing the interference of the other transmitted symbol-vectors $\mathbf{x}_k$ for $k \neq m$. Assuming we have the estimates of symbol-vectors $\mathbf{x}_m$ from previous iterations, we can then write $\mathbf{b}_m^l$ for $l \in \mathcal{L}$ as

$$\mathbf{b}_m^l = \mathbf{y}_{m+l} - \sum_{l'\in\mathcal{L}, l'\neq l} \mathbf{K}_{m+l,l'} \cdot \hat{\mathbf{x}}_{m+l-l'}. \tag{44}$$

Then from (43) and (44) for $l \in \mathcal{L}$, we have L equations for the symbol-vector estimates $\hat{\mathbf{x}}_m$ given as

$$\mathbf{b}_m^l = \mathbf{K}_{m+l,l} \cdot \hat{\mathbf{x}}_m + \mathbf{w}_{m+l} + \text{interference} \tag{45}$$

in the delay branch with index l due to error in the current estimates of the interfering symbol-vectors $\mathbf{x}_{m+l-p}$ for $l \neq p$. In the proposed scheme, instead of estimating the transmitted symbol-vector $\hat{\mathbf{x}}_m$ separately from each of the L equations in (45), we perform maximal ratio combining (46) of the estimates $\mathbf{b}_m^l$ followed by symbol-by-symbol QAM demapping using (49). The vector output of the maximal ratio combiner, $\mathbf{c}_m \in \mathbb{C}^{N\times 1}$, is given by

$$\mathbf{c}_m = \mathbf{D}_m^{-1} \cdot \mathbf{g}_m \tag{46}$$

where

$$\mathbf{D}_m = \sum_{l\in\mathcal{L}} \mathbf{K}_{m+l,l}^{\dagger} \cdot \mathbf{K}_{m+l,l} \tag{47}$$

$$\mathbf{g}_m = \sum_{l\in\mathcal{L}} \mathbf{K}_{m+l,l}^{\dagger} \cdot \mathbf{b}_m^l \tag{48}$$

and the hard estimates are given by

$$\hat{\mathbf{x}}_m(n) = \arg\min_{a_j\in\mathcal{Q}} |a_j - \mathbf{c}_m(n)|. \tag{49}$$

where a_j is signal from the QAM alphabet $\mathcal{Q}$, with $j = 1, \ldots, |\mathcal{Q}|$ and $n = 0, \ldots, N-1$. Let $\mathcal{D}(.)$ denote the decision on the estimate $\mathbf{c}_m$ in every iteration such that $\hat{\mathbf{x}}_m^{(i)} = \mathcal{D}(\mathbf{c}_m^{(i)})$. Hard-decision function $\mathcal{D}(c)$ is given by the maximum likelihood (ML) criterion in (49).

Once we update the estimate $\hat{\mathbf{x}}_m$, we increment m and repeat the same to estimate all $M' = M - l_{max}$ information

Authorized licensed use limited to: Monash University. Downloaded on March 22,2022 at 09:25:19 UTC from IEEE Xplore. Restrictions apply.

Algorithm 1: MRC in delay-Doppler domain.

Input: $\mathbf{H}$, $\mathbf{D}_m$, $\mathbf{y}_m$, $\mathbf{x}_m = \mathbf{0}_N \quad \forall\ m = 0, \ldots, M-1$
for *i=1:max iterations* **do**
  for $m = 0 : M' - 1$ **do**
    for $l \in \mathcal{L}$ **do**
      $\mathbf{b}_m^l = \mathbf{y}_{m+l} - \sum_{p \neq l} \mathbf{K}_{m+l,p} \cdot \hat{\mathbf{x}}_{m+l-p}$
    end
    $\mathbf{g}_m = \sum_{l \in \mathcal{L}} \mathbf{K}_{m+l,l}^{\dagger} \cdot \mathbf{b}_m^l$
    $\mathbf{c}_m = \mathbf{D}_m^{-1} \cdot \mathbf{g}_m$
    $\hat{\mathbf{x}}_m = \mathcal{D}(\mathbf{c}_m) \quad (\text{or} \quad \hat{\mathbf{x}}_m = \mathbf{c}_m)$[5]
  end
end
Output: $\hat{\mathbf{x}}_m$

symbol-vectors $\hat{\mathbf{x}}_m$ using the updated estimates.[5] of the previously decoded symbol-vectors in the form of a decision feedback equalizer (DFE) as shown in Fig. 5. Note that the DFE action leads to sequential updates whereas alternatively, using only the previous iteration estimates leads to parallel updates. We verified experimentally that parallel updates result in slower convergence. Algorithm 1 shows the delay-Doppler domain MRC operation (also see Fig. 5).

A. Reduced Complexity Delay-Time Domain Implementation

In (44), for each symbol-vector $\mathbf{x}_m$, we need to compute L vectors $\mathbf{b}_m^l$. This operation requires $L(L-1)$ products between matrices $\mathbf{K}_{m,l}$ and estimated symbol-vectors $\hat{\mathbf{x}}_{m-l}$. We can take advantage of the redundant operations to reduce the complexity. Let us define the *residual noise plus interference* (RNPI) term in the i-th iteration

$$\Delta\mathbf{y}_m^{(i)} = \mathbf{y}_m - \sum_{l \in \mathcal{L}} \mathbf{K}_{m,l} \cdot \hat{\mathbf{x}}_{m-l}^{(i)} \tag{50}$$

which can be considered as the residual error in the reconstructed received delay-Doppler domain symbols due to error in estimation of the transmitted symbols. Note that symbol-vectors $\hat{\mathbf{x}}_m$ are estimated in increasing order for $m = 0, \ldots, M'-1$. Therefore, for estimating the symbol-vector $\mathbf{x}_m$, only the symbol-vectors $\hat{\mathbf{x}}_{m+p}$, for $p < 0$, have updated estimates available in the current iteration. For $p \geq 0$, the previous iteration estimates are used. From (44) and (50), $\mathbf{b}_m^l$ computation for estimating the symbol-vector $\mathbf{x}_m$ in the i-th iteration can be written as

$$\mathbf{b}_m^l = \Delta\mathbf{y}_{m+l}^{(i)} + \mathbf{K}_{m+l,l} \cdot \hat{\mathbf{x}}_m^{(i-1)}. \tag{51}$$

Substituting (51) for $\mathbf{b}_m^l$ in (48), the direct computation of $\mathbf{b}_m^l$ can be avoided by writing $\mathbf{g}_m^{(i)}$ for the i-th iteration as

$$\begin{aligned}\mathbf{g}_m^{(i)} &= \sum_{l \in \mathcal{L}} \mathbf{K}_{m+l,l}^{\dagger} \cdot \Delta\mathbf{y}_{m+l}^{(i)} + \left(\sum_{l \in \mathcal{L}} \mathbf{K}_{m+l,l}^{\dagger} \cdot \mathbf{K}_{m+l,l} \right) \cdot \hat{\mathbf{x}}_m^{(i-1)} \\ &= \sum_{l \in \mathcal{L}} \mathbf{K}_{m+l,l} \cdot \Delta\mathbf{y}_{m+l}^{(i)} + \mathbf{D}_m \cdot \hat{\mathbf{x}}_m^{(i-1)}. \end{aligned} \tag{52}$$

[5]Alternatively, a soft estimate can also be used in conjunction with an outer coding scheme as described in Section V-B.

Then from (46) and (52), the MRC output at the i-th iteration can be written as

$$\mathbf{c}_m^{(i)} = \hat{\mathbf{x}}_m^{(i-1)} + \mathbf{D}_m^{-1} \cdot \Delta\mathbf{g}_m^{(i)} \tag{53}$$

where

$$\Delta\mathbf{g}_m^{(i)} = \sum_{l \in \mathcal{L}} \mathbf{K}_{m+l,l}^{\dagger} \cdot \Delta\mathbf{y}_{m+l}^{(i)} \tag{54}$$

The vector $\Delta\mathbf{g}_m^{(i)}$ in (54) is the maximal ratio combining of the RNPI's in all the delay branches ($\mathbf{y}_{m+l}$ for $l \in \mathcal{L}$) having a component of $\mathbf{x}_m$ in them.

In the i-th iteration, for every estimated symbol-vector $\mathbf{x}_m$, L RNPI vectors $\Delta\mathbf{y}_{m+l}^{(i)}$ need to be updated. which costs L^2 matrix-vector products. However, the complexity of (50) can be reduced by storing and updating the initial RNPI vectors $\Delta\mathbf{y}_m^{(0)}$. The L RNPI vectors which have a component of the most recently estimated symbol-vector are updated as follows,

$$\Delta\mathbf{y}_{m+l}^{(i)} \leftarrow \Delta\mathbf{y}_{m+l}^{(i)} - \mathbf{K}_{m+l,l} \cdot (\mathbf{x}_m^{(i)} - \mathbf{x}_m^{(i-1)}). \tag{55}$$

The number of matrix-vector products required to compute $\Delta\mathbf{y}_m^{(i)}$ has now been reduced from L^2 in (50) to L in (55). Moreover, as described in Section II-E, the matrix-vector products in (54) and (55) are products between circulant matrices $\mathbf{K}_{m,l} \in \mathbb{C}^{N \times N}$ and column vectors $\mathbf{x}_m$ or $\Delta\mathbf{y}_m \in \mathbb{C}^{N \times 1}$ which can be converted to element-wise product of vectors $\tilde{\boldsymbol{\nu}}_{m,l} \circ \tilde{\mathbf{x}}_m$ or $\tilde{\boldsymbol{\nu}}_{m,l} \circ \tilde{\boldsymbol{\Delta}}\mathbf{y}_m$, respectively, in the delay-time domain with a complexity of N complex multiplications. Let the superscript $\sim$ denotes the N-IFFT of a vector (i.e., $\tilde{\mathbf{a}} = \mathbf{F}_N^{\mathrm{H}} \cdot \mathbf{a}$). The equations (53), (54) and (55) can now be written in corresponding delay-time domain as

$$\tilde{\mathbf{c}}_m^{(i)} = \tilde{\mathbf{x}}_m^{(i-1)} + \Delta\tilde{\mathbf{g}}_m^{(i)} \oslash \tilde{\mathbf{d}}_m \tag{56}$$

$$\Delta\tilde{\mathbf{g}}_m^{(i)} = \sum_{l \in \mathcal{L}} \tilde{\boldsymbol{\nu}}_{m+l,l}^{*} \circ \Delta\tilde{\mathbf{y}}_{m+l}^{(i)} \tag{57}$$

$$\Delta\tilde{\mathbf{y}}_{m+l}^{(i)} \leftarrow \Delta\tilde{\mathbf{y}}_{m+l}^{(i)} - \tilde{\boldsymbol{\nu}}_{m+l,l} \circ (\tilde{\mathbf{x}}_m^{(i)} - \tilde{\mathbf{x}}_m^{(i-1)}) \tag{58}$$

where

$$\tilde{\mathbf{d}}_m = \sum_{l \in \mathcal{L}} \tilde{\boldsymbol{\nu}}_{m+l,l}^{\dagger} \circ \tilde{\boldsymbol{\nu}}_{m+l,l} \tag{59}$$

which can be computed in only NL complex multiplications.

1) Computational Complexity Per Iteration: Overall complexity per iteration for calculating $\Delta\tilde{\mathbf{g}}_m^{(i)}$, $\tilde{\mathbf{c}}_m^{(i)}$ and $\Delta\tilde{\mathbf{y}}_m^{(i)}$ for all symbol-vectors is $M'(2L+1)N$ complex multiplications. The redundant FFT computations can be avoided by storing the Fourier transform of the $M'L$ Doppler spread vectors $\boldsymbol{\nu}_{m,l}$, the M' initial symbol-vector estimates $\mathbf{x}_m^{(0)}$ and the RNPI vectors $\Delta\tilde{\mathbf{y}}_m^{(0)}$ in (55). The hard decision estimates require the delay-time vectors to be transformed into the delay-Doppler domain and back using *two* N-IFFT operations (which requires $2N\log_2(N)$ complex multiplications) per symbol-vector. Algorithm 2 shows the low complexity delay-time domain MRC implementation. The detector iterations are stopped when the overall RNPI error $\Delta\tilde{\mathbf{y}} = [\Delta\tilde{\mathbf{y}}_0^{\mathrm{T}}, \Delta\tilde{\mathbf{y}}_1^{\mathrm{T}}, \ldots, \Delta\tilde{\mathbf{y}}_{M-1}^{\mathrm{T}}]^{\mathrm{T}}$ due to the estimation error in symbol-vectors stops reducing.

Authorized licensed use limited to: Monash University. Downloaded on March 22,2022 at 09:25:19 UTC from IEEE Xplore. Restrictions apply.

Algorithm 2: Reduced complexity MRC in delay-time domain .

Input: $\tilde{\mathbf{H}}$, $\tilde{\mathbf{d}}_m$, $\tilde{\mathbf{x}}_m^{(0)}$, $\tilde{\mathbf{y}}_m$ $\forall\ m = 0, \ldots, M-1$
for $m = 0 : M' - 1$ **do**
  $\Delta\tilde{\mathbf{y}}_m^{(0)} = \tilde{\mathbf{y}}_m - \sum_{l\in\mathcal{L}} \tilde{\boldsymbol{\nu}}_{m,l} \circ \tilde{\mathbf{x}}_{m-l}^{(0)}$
end
for *i=1:max iterations* **do**
  $\Delta\tilde{\mathbf{y}}^{(i)} = \Delta\tilde{\mathbf{y}}^{(i-1)}$
  for $m = 0 : M' - 1$ **do**
    $\Delta\tilde{\mathbf{g}}_m^{(i)} = \sum_{l\in\mathcal{L}} \tilde{\boldsymbol{\nu}}_{m+l,l}^{*} \circ \Delta\tilde{\mathbf{y}}_{m+l}^{(i)}$
    $\tilde{\mathbf{c}}_m^{(i)} = \tilde{\mathbf{x}}_m^{(i-1)} + \Delta\tilde{\mathbf{g}}_m^{(i)} \oslash \tilde{\mathbf{d}}_m$
    $\tilde{\mathbf{x}}_m^{(i)} = \mathbf{F}_N^{\dagger} \cdot \mathcal{D}(\mathbf{F}_N \cdot \tilde{\mathbf{c}}_m^{(i)})$ (or $\tilde{\mathbf{x}}_m^{(i)} = \tilde{\mathbf{c}}_m^{(i)}$)
    for $l \in \mathcal{L}$ **do**
      $\Delta\tilde{\mathbf{y}}_{m+l}^{(i)} \leftarrow \Delta\tilde{\mathbf{y}}_{m+l}^{(i)} - \tilde{\boldsymbol{\nu}}_{m+l,l} \circ (\tilde{\mathbf{x}}_m^{(i)} - \tilde{\mathbf{x}}_m^{(i-1)})$
    end
  end
  if $(||\Delta\tilde{\mathbf{y}}^{(i)}|| \geq ||\Delta\tilde{\mathbf{y}}^{(i-1)}||)$ **then EXIT**
end
Output: $\hat{\mathbf{x}}_m = \mathcal{D}(\mathbf{F}_N \cdot \tilde{\mathbf{x}}_m)$

2) Initial Computational Complexity: In the proposed detector, the initial computations include generating all the entries of the matrices $\mathbf{H}$ and $\tilde{\mathbf{H}}$, which requires computing the vectors $\boldsymbol{\nu}_{m,l}$ and their Fourier transform $\tilde{\boldsymbol{\nu}}_{m,l}$ for all $m = 0, \ldots, M'-1$ and $l \in \mathcal{L}$. Assuming the integer delay-Doppler channel parameters (h_i, k_i, l_i) are known for $i = 1, 2, \ldots, P$, the channel Doppler spread vectors $\boldsymbol{\nu}_{m,l}$ can be easily computed using the relations given in (11) and (29).

Let K_l be the number of non-zero channel coefficients in each vector $\boldsymbol{\nu}_{m,l}$ (or paths with different Doppler shift in the same delay bin $l \in \mathcal{L}$) such that total number of channel coefficients or propagation paths as seen by the OTFS receiver is $P = \sum_{l\in\mathcal{L}} K_l$. The number of complex multiplications required to compute the $M'L$ vectors $\boldsymbol{\nu}_{m,l}$ using (29) is $M' \sum_{l\in\mathcal{L}} K_l = M'P$. The OTFS channel matrix $\mathbf{H}$ (or equivalently the vectors $\boldsymbol{\nu}_{m,l}$) can then be generated in $M'P$ complex multiplications.

For the delay-time domain MRC operation in Algorithm 2, $\tilde{\boldsymbol{\nu}}_{m,l}$ (N-IFFT of $\boldsymbol{\nu}_{m,l}$) can be computed in $\min\{Nk_l, N\log_2(N)\}$ complex multiplications, since there are only K_l non-zero channel coefficients in each delay tap l. Then, the number of complex multiplications required to compute $\tilde{\mathbf{H}}$ (or equivalently all the $\tilde{\boldsymbol{\nu}}_{m,l}$) is upper bounded by $M'N\sum_l K_l = M'NP$.

Alternatively, for the fractional Doppler case, the complexity of initial computations remains unaffected for the delay-time domain detector as $\tilde{\boldsymbol{\nu}}_{m,l}$ can be generated directly from the channel gains, delays, and Doppler shifts (h_i, κ_i, ℓ_i) of the P paths, using (11) and (21) with $M'NP$ complex multiplications.

B. Low Complexity Initial Estimate

In Algorithm 1 and 2, we initially assume that all the $\mathcal{Q}$-QAM signals a_j are equally likely and the mean of a_j's is zero and so we initialize $\hat{\mathbf{x}}_m^{(0)} = \mathbf{0}_N$, for all m. The MRC detector complexity per iteration is of the order $O(NML)$ and the overall complexity scales linearly with the number of iterations.

However, a better initial estimate of the OTFS symbols instead of $\hat{\mathbf{x}}_m = \mathbf{0}_N$ may reduce the required number of MRC iterations and to reach convergence. Assuming ideal pulse shaping waveform, a single tap equalizer in the time-frequency domain can provide an improved low complexity initial estimate.

Following the remark in Section II-E and [3], we define $\mathbf{H}_{\text{dd}} \in \mathbb{C}^{M\times N}$, the delay-Doppler domain channel impulse response matrix for the ideal pulse shaping waveform case,

$$\mathbf{H}_{\text{dd}}(m,n) = \begin{cases} \nu_l(\kappa), & \text{if } m = l, n = [\kappa]_N \\ 0, & \text{otherwise.} \end{cases} \tag{60}$$

For the fractional Doppler case (when κ is a real number). the ideal channel response can be written in terms of the Doppler spread vectors as $\mathbf{H}_{\text{dd}} = [\boldsymbol{\nu}_{0,0}, \boldsymbol{\nu}_{1,1}, \ldots, \boldsymbol{\nu}_{M-1,M-1}]^{\text{T}}$. The corresponding time-frequency channel response for the ideal pulse shaping waveform is obtained by an inverse symplectic finite fourier transform (ISFFT) operation on the delay-Doppler channel as

$$\begin{aligned} \mathbf{H}_{\text{tf}} &= \mathbf{F}_M \cdot \mathbf{H}_{\text{dd}} \cdot \mathbf{F}_N^{\text{H}} &(61)\\ &= \mathbf{F}_M \cdot [\boldsymbol{\nu}_{0,0}, \boldsymbol{\nu}_{1,1}, \ldots, \boldsymbol{\nu}_{M-1,M-1}]^{\text{T}} \cdot \mathbf{F}_N^{\text{H}} \\ &= \mathbf{F}_M \cdot [\tilde{\boldsymbol{\nu}}_{0,0}, \tilde{\boldsymbol{\nu}}_{1,1}, \ldots, \tilde{\boldsymbol{\nu}}_{M-1,M-1}]^{\text{T}}. &(62)\end{aligned}$$

Similarly, the received time-frequency samples can be obtained by the ISFFT operation on the received delay-Doppler domain samples as

$$\mathbf{Y}_{\text{tf}} = \mathbf{F}_M \cdot \mathbf{Y} \cdot \mathbf{F}_N^{\text{H}} = \mathbf{F}_M \cdot [\tilde{\mathbf{y}}_0, \tilde{\mathbf{y}}_1, \cdots \tilde{\mathbf{y}}_{M-1}]^{\text{T}}. \tag{63}$$

Since in the ideal pulse shaping waveform case, circular convolution of the channel and transmitted symbols in the delay-Doppler domain transforms to element-wise product in the time-frequency domain, we estimate the transmitted samples in the time-frequency domain by a single tap minimum mean square error (MMSE) equalizer

$$\hat{\mathbf{X}}_{\text{tf}}(m,n) = \frac{\mathbf{H}_{\text{tf}}^{*}(m,n) \cdot \mathbf{Y}_{\text{tf}}(m,n)}{|\mathbf{H}_{\text{tf}}(m,n)|^2 + \sigma_w^2} \tag{64}$$

for $m = 0, \ldots, M-1$ and $n = 0, \ldots, N-1$.

The time-delay domain initial estimates of the OTFS symbol-vectors can then be obtained by the Heisenberg transform operation on the time-frequency domain estimates as

$$[\tilde{\mathbf{x}}_0^{(0)}, \tilde{\mathbf{x}}_1^{(0)}, \cdots \tilde{\mathbf{x}}_{M-1}^{(0)}]^{\text{T}} = \mathbf{F}_M^{\dagger} \cdot \hat{\mathbf{X}}_{\text{tf}}. \tag{65}$$

Note that $\bar{\boldsymbol{\nu}}_{m,l} = \mathbf{0}_N$ for $l \notin \mathcal{L}$ and hence the operation in (62) can be computed in $\min\{NML, NM\log_2(M)\}$ complex multiplications. Since we have already computed $\tilde{\boldsymbol{\nu}}_{m,l}$, and $\tilde{\mathbf{y}}$ is just a shuffled version of the received time-domain samples, the overall number of computations (for the steps in (62), (63), (64) and (65)) required for the initial estimate is upper bounded by $NM(L + 2\log_2(M) + 3)$, which is comparable to the complexity of one detector iteration $NM'(2L+1)$.

Authorized licensed use limited to: Monash University. Downloaded on March 22,2022 at 09:25:19 UTC from IEEE Xplore. Restrictions apply.

C. Condition for Detector Convergence

In this section, we cast the delay-time algorithm (Algorithm 2) in the time-domain with the purpose of analysing the detector convergence using the properties of Jacobi and Gauss Seidel iterative methods for solving linear equations [19], [20]. The basic principle of iterative MRC operation in the delay-time domain with sequential updates given in (56)-(58) can be compactly expressed as

$$\tilde{\mathbf{x}}^{(i)} = \tilde{\mathbf{x}}^{(i-1)} + \tilde{\mathbf{D}}^{-1}\tilde{\mathbf{H}}^{\dagger}(\tilde{\mathbf{y}} - \tilde{\mathbf{H}}\tilde{\mathbf{x}}^{(i-1)}) \tag{66}$$

when using parallel updates (i.e. without DFE), where $\tilde{\mathbf{D}}$ is the matrix containing diagonal elements of $\tilde{\mathbf{H}}^{\dagger}\tilde{\mathbf{H}}$. The rows and columns of the delay-time channel matrix $\tilde{\mathbf{H}}$ are perfectly shuffled using the permutation matrix $\mathbf{P}$ to obtain a *similar*, block diagonal time-domain channel matrix $\mathbf{G}$ as explained in Section II-F. This allows the equivalent operation in (66) to be split and executed in parallel for each independent time domain block $\mathbf{G}_n$ as

$$\mathbf{s}_n^{(i)} = \mathbf{s}_n^{(i-1)} + \mathbf{D}_n^{-1}\mathbf{G}_n^{\dagger}(\mathbf{r}_n - \mathbf{G}_n\mathbf{s}_n^{(i-1)}) \tag{67}$$

where $\mathbf{D}_n$ is the matrix containing the diagonal elements of $\mathbf{G}_n^{\dagger}\mathbf{G}_n$. Equation (67) can be written in the form

$$\begin{aligned} &\mathbf{s}_n^{(i)} = -\mathbf{T}_n^{\mathrm{J}} \cdot \mathbf{s}_n^{(i-1)} + \mathbf{Q}_n^{\mathrm{J}} \cdot \mathbf{z}_n \\ &\mathbf{T}_n^{\mathrm{J}} = \mathbf{D}_n^{-1} \cdot (\mathbf{L}_n + \mathbf{L}_n^{\dagger}), \quad \mathbf{Q}_n^{\mathrm{J}} = \mathbf{D}_n^{-1}, \quad \mathbf{z}_n = \mathbf{G}_n^{\dagger}\mathbf{r}_n \end{aligned} \tag{68}$$

where $\mathbf{L}_n$ and $\mathbf{L}_n^{\dagger}$ are the matrices containing the strictly lower and upper triangular parts of the Hermitian matrix $\mathbf{R}_n = \mathbf{G}_n^{\dagger}\mathbf{G}_n$. Finally, we observe that the parallel update formulation in (68) matches the classic Jacobi iterative method (hence the superscript 'J' in $\mathbf{T}_n^{\mathrm{J}}$) for solving linear equations, [19].

We now focus on the sequential update method given in Algorithm 1 and 2 based on the DFE operation. Note that, in Algorithm 2, the linear matrix equation in (66) is solved block-wise with low complexity, where the latest estimates of the symbol-vectors calculated in the current iteration are used in estimating the next symbol-vector as in a DFE

$$\mathbf{s}_n^{(i)} = \mathbf{s}_n^{(i-1)} + \mathbf{D}_n^{-1}(\mathbf{z}_n - \underbrace{\mathbf{L}_n\mathbf{s}_n^{(i)}}_{(a)} - \underbrace{\mathbf{L}_n^{\dagger}\mathbf{s}_n^{(i-1)}}_{(b)}) \tag{69}$$

where (a) and (b) denote the contribution of the current and previous-iteration estimates, respectively. We can modify (68) for the DFE iterative method in (69) as

$$\begin{aligned} &\mathbf{s}_n^{(i)} = -\mathbf{T}_n^{\mathrm{GS}} \cdot \mathbf{s}_n^{(i-1)} + \mathbf{Q}_n^{\mathrm{GS}} \cdot \mathbf{z}_n \\ &\mathbf{T}_n^{\mathrm{GS}} = (\mathbf{D}_n + \mathbf{L}_n)^{-1} \cdot \mathbf{L}_n^{\dagger}, \quad \mathbf{Q}_n^{\mathrm{GS}} = (\mathbf{D}_n + \mathbf{L}_n)^{-1} \end{aligned} \tag{70}$$

and observe that Algorithm 2 coincides with the well studied Gauss Seidel (GS) method available in the literature [19], [20]. Algorithm 3 shows the equivalent time domain GS method implementing Algorithm 2.

Both Jacobi and GS methods are used to iteratively find the least squares solution

$$\hat{\mathbf{s}}_n = \min_{\hat{\mathbf{s}}_n} ||\mathbf{z}_n - \mathbf{R}_n\hat{\mathbf{s}}_n||^2 \tag{71}$$

Algorithm 3: MRC delay-time domain operation principle in the form of time domain Gauss-Seidel method

Input: $\mathbf{r}$, $\mathbf{G}$
for $n = 0 : N-1$ **do**
  $\mathbf{R}_n = \mathbf{G}_n^{\dagger} \cdot \mathbf{G}_n$
  $\mathbf{z}_n = \mathbf{G}_n^{\dagger} \cdot \mathbf{r}_n$
  $\mathbf{L}_n$ = strictly lower triangular part$\{\mathbf{R}_n\}$
  $\mathbf{T}_n^{\mathrm{GS}} = (\mathbf{D}_n + \mathbf{L}_n)^{-1} \cdot \mathbf{L}_n^{\dagger}$
  $\mathbf{Q}_n^{\mathrm{GS}} = (\mathbf{D}_n + \mathbf{L}_n)^{-1}$
end
$\hat{\mathbf{s}}^{(0)} = \mathbf{P} \cdot (\mathbf{I}_M \otimes \mathbf{F}_N^{\dagger}) \cdot \hat{\mathbf{x}}^{(0)}$
for $i = 1$*:max iterations* **do**
  for $n = 0 : N-1$ **do**
    $\hat{\mathbf{s}}_n^{(i)} = -\mathbf{T}_n^{\mathrm{GS}} \cdot \hat{\mathbf{s}}_n^{(i-1)} + \mathbf{Q}_n^{\mathrm{GS}} \cdot \mathbf{z}_n$
  end
  if $(||\mathbf{r} - \mathbf{G} \cdot \hat{\mathbf{s}}^{(i)}|| \geq ||\mathbf{r} - \mathbf{G} \cdot \hat{\mathbf{s}}^{(i-1)}||)$ **then EXIT**
end
Output: $\hat{\mathbf{x}} = (\mathbf{I}_M \otimes \mathbf{F}_N) \cdot (\mathbf{P} \cdot \hat{\mathbf{s}}^{(i)})$

of the M-dimensional linear system of equations

$$\mathbf{z}_n = \mathbf{R}_n \cdot \mathbf{s}_n + \bar{\mathbf{w}}_n \tag{72}$$

where $\mathbf{R}_n \in \mathbb{C}^{M \times M}$ and $\hat{\mathbf{s}}_n, \mathbf{z}_n \in \mathbb{C}^{M \times 1}$. We further assume that the time-domain correlation matrix $\mathbf{R}_n = \mathbf{G}_n^{\dagger}\mathbf{G}_n$ is non-singular and hence positive definite Hermitian.

In [19], [20], it is shown that the iteration method (68) for the linear system in (72) is convergent, if $\rho(\mathbf{T}_n^{\mathrm{GS}}) < 1$, where $\rho(\mathbf{T}_n^{\mathrm{GS}})$ is the spectral radius[6] of the square matrix $\mathbf{T}_n^{\mathrm{GS}}$ [19], [20]. For the Jacobi method, $\rho(\mathbf{T}_n^{\mathrm{J}}) < 1$ if $\mathbf{R}_n$ is diagonally dominant, which depends on the channel and cannot be guaranteed. However, the GS method is known to converge faster and convergence is guaranteed under more general conditions than the Jacobi method [19], [20]. In Appendix we prove the following lemma

Lemma 1: The GS iterative method for the solution of (72) is converging (i.e., $\rho(\mathbf{T}_n^{\mathrm{GS}}) < 1$) if $\mathbf{R}_n$ is a positive definite Hermitian matrix. Furthermore, $\rho(\mathbf{T}_n^{\mathrm{GS}}) = 1$ if $\mathbf{R}_n$ is a positive semi-definite Hermitian matrix.

We note that the algorithm may still converge even for some channels that result in a positive semi-definite Hermitian matrix $\mathbf{R}_n$ (i.e., $\rho(\mathbf{T}_n^{\mathrm{GS}}) = 1$), but this is not guaranteed.

Even though the implementation of the iterative MRC detector in Algorithm 3 looks simpler than the one in Algorithm 2, the complexity of initial computations for directly calculating $\mathbf{R}_n$, $\mathbf{T}_n^{\mathrm{GS}}$ and $\mathbf{Q}_n^{\mathrm{GS}}$ is $O(NML^2)$ complex multiplications since $\mathbf{G}_n$ is a banded matrix with L non-zero elements in each row. However, in Algorithm 2, the circulant property of the blocks of the channel matrix $\mathbf{H}$ (due to the placement of null symbols in the OTFS grid as shown in Fig. 2) is utilized to reduce the overall complexity of the initial computations to $O(NML)$ complex multiplications as explained in Section III-A.

[6]Spectral radius of a matrix is the largest absolute value of its eigenvalues.

Authorized licensed use limited to: Monash University. Downloaded on March 22,2022 at 09:25:19 UTC from IEEE Xplore. Restrictions apply.

V. Further Improvements

A. Successive Over Relaxed (SOR) Iterative Rake Detector

In time domain, the proposed iterative Rake detector is similar to doing N parallel GS iterations on the matched filtered received waveform, as shown in Section III-C. GS and its variants such as successive over-relaxation (SOR) method are well presented in [19]–[21]. The SOR method is obtained by introducing a relaxation parameter ω in the GS method (69) as,

$$\mathbf{s}_n^{(i)} = \mathbf{s}_n^{(i-1)} + \omega \mathbf{D}_n^{-1}(\mathbf{z}_n - \mathbf{L}_n \mathbf{s}_n^{(i)} - \mathbf{L}_n^{\dagger} \mathbf{s}_n^{(i-1)}). \tag{73}$$

The corresponding GS iteration matrix $\mathbf{T}_n^{\mathrm{GS}}$ and $\mathbf{Q}_n^{\mathrm{GS}}$ in Algorithm 3 can be modified as

$$\mathbf{T}_n^{\omega} = (\mathbf{D}_n + \omega \mathbf{L}_n)^{-1} \cdot ((\omega - 1)\mathbf{D}_n + \omega \mathbf{L}_n^{\dagger}) \tag{74}$$

$$\mathbf{Q}_n^{\omega} = (\mathbf{D}_n + \omega \mathbf{L}_n)^{-1}. \tag{75}$$

In Appendix we prove the following lemma.

Lemma 2: The SOR GS iterative method for the solution of (72) is converging (i.e., $\rho(\mathbf{T}_n^{\omega}) < 1$) if $\mathbf{R}_n$ is a positive definite Hermitian matrix and $0 < \omega < 2$.

We can then simply modify the proposed delay-time detector Algorithm 2 by rewriting (56) as

$$\tilde{\mathbf{c}}_m^{(i)} = \tilde{\mathbf{c}}_m^{(i-1)} + \omega(\Delta \tilde{\mathbf{q}}_m^{(i-1)} \oslash \tilde{\mathbf{d}}_m). \tag{76}$$

Note that when $\omega = 1$, (76) coincides with (56). The relaxation parameter when $\omega > 1$ is called the over-relaxation parameter and when $\omega < 1$ is called the under relaxation parameter. The computation of the optimal SOR parameter $\omega = \omega_{\mathrm{opt}}$ which minimizes the spectral radius $\rho(\mathbf{T}_n^{\omega})$ requires computing the eigenvalues of the iteration matrix $\mathbf{T}_n^{\omega}$, [19], [20].

The aim is to find the range of values of ω for which the SOR method converges (see Lemma 2), the set of which denotes the region of convergence, and, if possible, the best value ω_{opt}. The optimum SOR parameter can be analytically calculated given the spectral radius of the Jacobi matrix $\rho(\mathbf{T}_n^{\mathrm{J}}) < 1$ [21]. However, it is known that $\rho(\mathbf{T}_n^{\mathrm{J}}) < 1$ only if $\mathbf{R}_n$ is diagonally dominant, but this is not guaranteed for all channels. In such cases, the numerical calculation of ω_{opt} is not practical for large system matrices, rather a region of good performance, within the region of convergence, is easier to find, as suggested by [21]. Further, when the power delay profile statistical model of the channel is given, the good region for the SOR parameter can be optimized offline by simulation.

In this paper, we try to analyse the effect of ω and the range of values of good performance by simulation. Fig. 6 show the BER plot for 64-QAM for different values of ω. In Fig. 7, we plot the required (abbreviated as reqd. in the plot legend) SNR (labelled as 'Q-QAM reqd. SNR') on the left y-axis alongside the required number of iterations (labelled as 'Q-QAM reqd. iters') on the right y-axis, to achieve a BER of 10^{-3} for different modulation sizes, respectively, for different values of $\omega \in [1, 1.5]$. The y-axis of the plot represents the SNR (dB) or the iterations depending on the corresponding curve. The maximum number of iterations is set to 50. It can be seen that the optimum ω for the standard

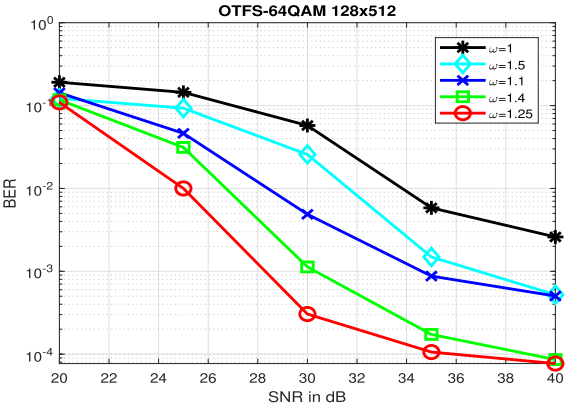

Fig. 6. 64-QAM BER performance for different relaxation parameters ω.

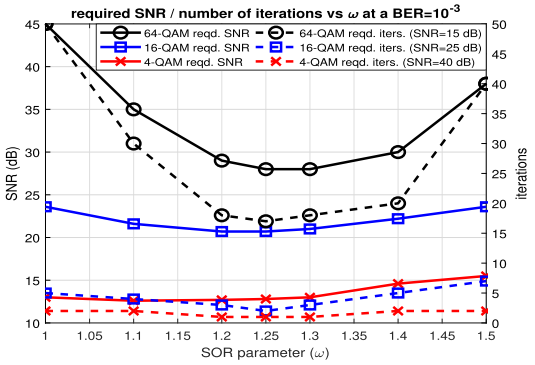

Fig. 7. Error performance and convergence speed of different relaxation parameters ω for different modulation sizes $|\mathbb{Q}|$ at BER 10^{-3}.

extended vehicular A (EVA) [7] channel model [13] consistently lies in the interval [1.2,1.3]. We can observe that there is a 2.5 dB and 17 dB gain at a BER of 10^{-3} for 16-QAM and 64-QAM, respectively, due to just the over-relaxation parameter with almost no extra computational complexity. The effect of the SOR parameter on the convergence speed of the MRC detector can be seen in Fig. 7 (right y-axis). It shows the number of iterations required to achieve a BER of 10^{-3} for different modulation sizes at the corresponding SNR values as given in the plot legend. It can be seen that the biggest reduction in complexity comes at 64-QAM where, the number of iterations required is significantly reduced (by almost 3 times) as compared to the case when SOR parameter $\omega = 1$. For 4-QAM and 16-QAM, the optimum SOR parameter approximately halves the number of required iterations.

Finally, if no prior knowledge of the channel statistical model is available, we observed by simulation that some performance improvement can still be achieved by setting the value of ω to

[7]The EVA channel power-delay profile (with a maximum speed = 120 km/hr) is given by [0, -1.5, -1.4, -3.6, -0.6, -9.1, -7.0, -12.0, -16.9] dB with excess delay taps $\mathcal{L}' = \mathcal{L} = \{0, 1, 2, 3, 4, 5, 8, 13, 19\}$ normalized to the delay resolution $1/(M\Delta f)$ of an OTFS grid with bandwidth $M\Delta f$, where $M = 512$ and $\Delta f = 15$ kHz.

Authorized licensed use limited to: Monash University. Downloaded on March 22,2022 at 09:25:19 UTC from IEEE Xplore. Restrictions apply.

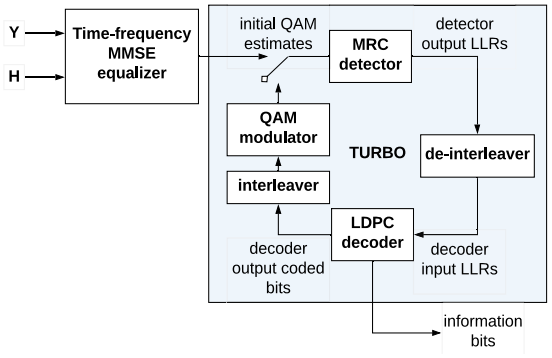

Fig. 8. OTFS iterative rake turbo decoder operation.

slightly above 1. The optimization of ω with low complexity, for different SNR, channel profiles and number of multipaths will be investigated in future work.

B. Iterative Rake Turbo Decoder

In order to improve FER performance, the turbo decoder principle shown in Fig. 8 is proposed. The encoded bits are random interleaved in the frame so as to enhance the delay-Doppler diversity.

The detector output bit log likelihood ratios (LLR) after random de-interleaving is fed to the low-density parity check (LDPC) decoder. The hard decision coded bits from the LDPC decoder after interleaving and QAM modulation is then fed back to the MRC detector as the input symbol-vector estimates and the process repeats. Overall, one turbo iteration involves one iteration of MRC detector, de-interleaver, LDPC decoder, interleaver, and the QAM modulator. As shown in Fig. 8, for the first iteration, the initial estimate of the QAM symbols is provided by the low complexity MMSE equalizer as explained in Section III-B, after which the initial estimate comes form the LDPC decoder.

From (53), the soft estimate of the delay-Doppler domain symbol-vector $\mathbf{c}_m$ after MRC combining can be written as

$$\mathbf{c}_m = \mathbf{x}_m + \mathbf{e}_m \qquad m = 0, \dots M' - 1 \tag{77}$$

where $\mathbf{x}_m$ is the transmitted symbol-vector at delay index m and $\mathbf{e}_m$ denotes the normalized post MRC NPI vector. We assume that $\mathbf{e}_m$ follows a zero mean Gaussian distribution with variance σ_m^2. This assumption becomes more accurate as the number of interfering terms increases. Then, the LLR $L_{m,n,b}^{(i)}$ of bit b of the n-th transmitted symbol in the estimated symbol-vector $\mathbf{c}_m^{(i)}$ in the i-th iteration can be obtained by

$$\begin{aligned} L_{m,n,b}^{(i)} &= \log\left(\frac{Pr(b=0|\mathbf{c}_m^{(i)}(n))}{Pr(b=1|\mathbf{c}_m^{(i)}(n))}\right) \\ &= \log\left(\frac{\sum_{q\in\mathcal{Q}_0}\exp(-|\mathbf{c}_m^{(i)}(n)-q|^2/\sigma_m^2)}{\sum_{q'\in\mathcal{Q}_1}\exp(-|\mathbf{c}_m^{(i)}(n)-q'|^2/\sigma_m^2)}\right) \end{aligned} \tag{78}$$

where $\mathcal{Q}_0$ and $\mathcal{Q}_1$ are the subsets of QAM symbols, where the b-th bit of the symbol is 0 and 1, respectively. The complexity of LLR calculation can be reduced by the max-log approximated LLR obtained as

$$\tilde{\mathbf{L}}_{m,n,b}^{(i)} = \frac{1}{\sigma_m^2}\left(\min_{q\in\mathcal{Q}_0}\left|\mathbf{c}_m^{(i)}(n)-q\right|^2 - \min_{q'\in\mathcal{Q}_1}\left|\mathbf{c}_m^{(i)}(n)-q'\right|^2\right). \tag{79}$$

In order to compute the bit LLRs, an estimate of the post MRC NPI variance σ_m^2 is required. Accurate estimation of σ_m^2 is not straightforward and requires knowledge of the correlation between all the estimated symbol-vectors and RNPI vectors which changes every iteration as well. Since the entries of channel Doppler spread vectors $\boldsymbol{\nu}_{m,l}$ can be assumed to be zero mean, i.i.d. and normal distributed [13], the channel Doppler spread for different delay taps can be assumed to be uncorrelated. i.e., $E[\boldsymbol{\nu}_{m,l}^{\dagger}\cdot\boldsymbol{\nu}_{m,'p}] = 0$ for $l \neq p$. Furthermore, for the purpose of a simple estimate of the post MRC NPI variance, we assume that RNPI $\Delta\mathbf{y}_m^{(i)}$ in the different delay branches are uncorrelated (i.e., $E[\Delta\mathbf{y}_m^{\dagger}\cdot\Delta\mathbf{y}_p] = 0$ for $m \neq p$ in all iterations) and follows Gaussian distribution. The covariance matrix of the delay-time RNPI vector $\Delta\tilde{\mathbf{y}}_m$ in the i-th iteration

$$\boldsymbol{C}_m^{(i)}(j,k) = (\Delta\tilde{\mathbf{y}}_m^{(i)}(j) - E\{\Delta\tilde{\mathbf{y}}_m^{(i)}\})(\Delta\tilde{\mathbf{y}}_m^{(i)}(k) - E\{\Delta\tilde{\mathbf{y}}_m^{(i)}\})^* \tag{80}$$

for $j,k = 0,\dots,N-1$ and $E\{\Delta\tilde{\mathbf{y}}_m^{(i)}\} = \frac{1}{N}\sum_{n=1}^{N}\Delta\tilde{\mathbf{y}}_m^{(i)}(n)$. Since Fourier transformation is a unitary transformation, the NPI variance remains the same in both domains, and we approximate the post MRC NPI variance for the symbol-vector soft estimate $\mathbf{c}_m^{(i)}$ in the i-th iteration as

$$\sigma_m^{2(i)} = \mathrm{Var}(\tilde{\mathbf{e}}_m^{(i)}) \approx \frac{1}{N}\sum_{l\in L}\eta_{m,l}\mathrm{tr}(\boldsymbol{C}_{m+l}^{(i)}) \tag{81}$$

where $\eta_{m,l} = ||\tilde{\boldsymbol{\nu}}_{m+l,l} \oslash \tilde{\mathbf{d}}_m||^2$ is the normalized post MRC channel power in the different delay branches selected for combining. The bit LLR calculation in (79) and NPI variance calculation in (81) has a complexity of $2NM\log_2(|\mathcal{Q}|)$ and NML, respectively. The LDPC decoder complexity is of the order $C_{\mathrm{LDPC}} = O(\log_2(|\mathcal{Q}|)NM)$. The overall complexity of detection increases by $C_{\mathrm{LDPC}} + NM(2\log_2(|\mathcal{Q}|) + L) +$ for every turbo iteration.

VI. Simulation Results and Discussion

For simulations we generate OTFS frames for $N = 128$ and $M = 512$. The sub-carrier spacing Δf is taken as 15 kHz. The maximum delay spread (in terms of integer taps) is taken to be 32 ($l_{\max} = 31$) which is approximately 4 μs. The channel delay model is generated according to the standard EVA model (with a speed of 120 km/h) with the Doppler shift for the i-th path generated from a uniform distribution $U(0, \nu_{max})$, where ν_{max} is the maximum Doppler shift [13]. We consider one Doppler shifted path per delay tap with $L = 9$ and $k_{max} = 16$. For our simulations, we assume perfect knowledge of the channel state information at the receiver (see [10] for practical channel estimation in OTFS). For BER plots, 10^5 frames are send for every point in the BER curve and for FER plots, all simulations

Authorized licensed use limited to: Monash University. Downloaded on March 22,2022 at 09:25:19 UTC from IEEE Xplore. Restrictions apply.

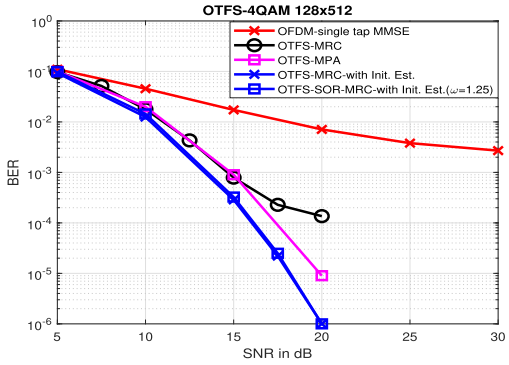

Fig. 9. Uncoded 4-QAM BER Plot : MRC vs MPA vs MMSE-OFDM.

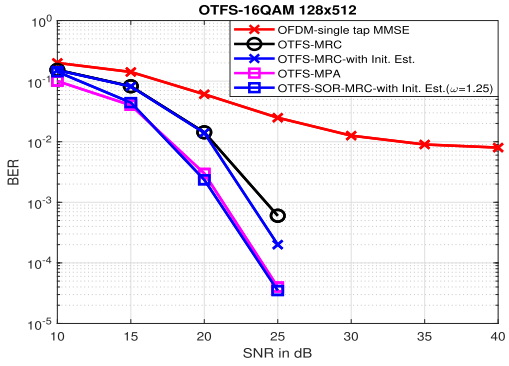

Fig. 10. Uncoded 16-QAM BER Plot : MRC vs MPA vs MMSE-OFDM.

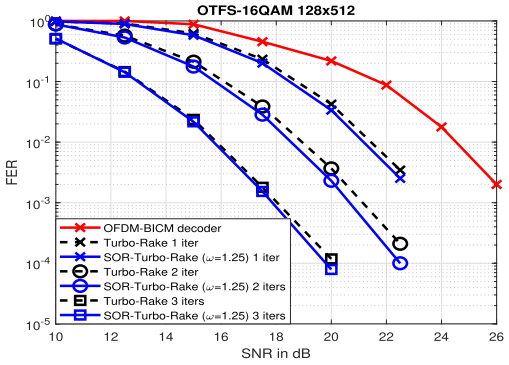

Fig. 11. Turbo 16-QAM FER Plot: MRC vs BIC-MMSE-OFDM.

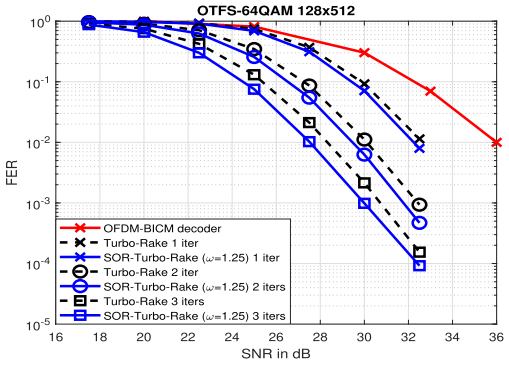

Fig. 12. Turbo 64-QAM FER Plot: MRC vs BIC-MMSE-OFDM.

run for a minimum of 10^5 frames or until 100 OTFS frame errors are encountered. BER is plotted to show uncoded performance, while FER is used when an outer coding scheme is applied.

Fig. 9 shows the BER plot for the MRC detector, with and without the initial estimate in Section III-B, for 4-QAM modulated OTFS waveform with a maximum of 10 iterations.[8]. Performance is compared with the state of the art *message passing algorithm* (MPA) described in [22], [23] (labeled as OTFS-MPA in Fig. 9 and 10) with a maximum of 10 iterations.[9] and the OFDM single tap MMSE equalizer. It can be seen that with the initial estimate (labeled as OTFS-MRC with Init. Est.[10]), there is a $\approx$1 dB gain over the MPA algorithm at a BER of 10^{-3}. This gain is contributed by the improved SNR due to the MRC operation (or matched-filtering) at the receiver and the initial time-frequency MMSE estimate, which is more reliable for lower modulation sizes like BPSK and 4-QAM, thereby increasing the convergence speed (due to the initial estimates begin closer to the solution).

Note that the same initial estimates could also be used to improve the performance of MPA. However, the estimates need to be transformed into the delay-Doppler domain and $\mathcal{Q}$-QAM alphabet probabilities for all the information symbols need to be calculated. This would incur a high complexity just to get the improved initial estimate. Moreover, similar to MRC detection, MPA can also be applied on the matched-filtered system matrix $\mathbf{H}^{\dagger}\mathbf{H}$ instead of $\mathbf{H}$, but this approximately doubles the MPA complexity, which scales linearly with the number of non-zero elements in the matrix. [22], [23].

Fig. 10 shows the BER plot for the MRC detector for 16-QAM modulation with maximum 15 iterations compared to the MPA-based detector with maximum 30 iterations. It can be seen that with the over-relaxed iterative detection (labeled as OTFS-SOR-MRC with Init. Est. ($\omega = 1.25$)), the BER performance is improved by around 2.5 dB at BER $= 10^{-3}$. Moreover, the SOR-iterative algorithm converges on average in less than 8 iterations for SNR $>$ 15 dB. We can see from Fig. 6 and 7 that the SOR parameter has more impact at higher modulation schemes, where the initial low complexity estimate is less accurate and the convergence is generally slow without SOR. Fig. 11 and 12 shows the frame error performance of the plain and SOR-turbo-Rake decoder with initial low complexity estimate for 16 and 64 QAM modulation, respectively, compared with bit interleaved coded OFDM with MMSE detection scheme (labeled as OFDM BICM decoder). A half-rate LDPC code of

[8]Iterations are stopped according to the residual NPI convergence criteria in Algorithm 2.

[9]The MPA stopping criteria is based on the convergence of the estimated symbol probabilities [22].

[10]Init. Est. refers to detection with the Initial Estimate in Section III-B.

Authorized licensed use limited to: Monash University. Downloaded on March 22,2022 at 09:25:19 UTC from IEEE Xplore. Restrictions apply.

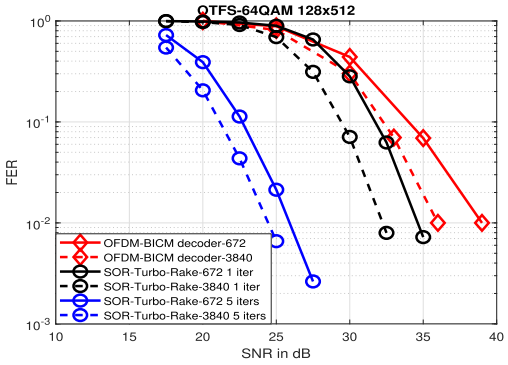

Fig. 13. Turbo 64-QAM FER Plot: MRC vs BIC–MMSE-OFDM for codeword lengths: 672, 3840.

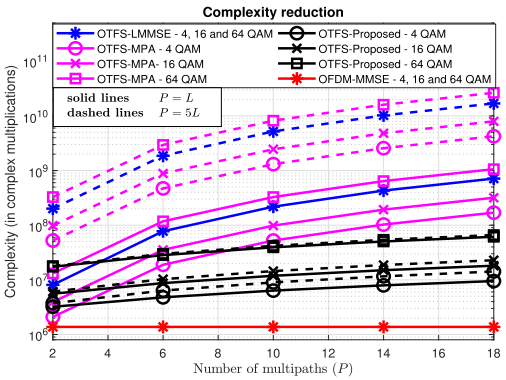

Fig. 14. Complexity comparison with other linear detectors, for different modulation sizes, for an OTFS frame of size $N = 128$, $M = 512$ for $P = L$, i.e., for *one* Doppler path per delay tap (solid lines) and $P = 5L$, i.e., for *five* Doppler paths per delay tap (dashed lines).

TABLE I
SUMMARY AND COMPARISON OF OVERALL COMPLEXITY OF ITERATIVE RAKE RECEIVER

Computations per iteration	(I)	$NM'(2L+1+2\log_2(N))$
Initial computations	(II)	$NM'(P+2L)$
	(III)	$NM[L+2\log_2(M)+3]$

length $N_c = 3840$ bits from [25] is used and every OTFS frame contains $\lfloor NM\log_2(|\mathcal{Q}|)/N_c \rfloor$ codewords.

Turbo iterations are stopped when all the decoded codewords within the frame satisfy the LDPC parity check. It can be observed that just 1 iteration of turbo MRC detector (labeled as Turbo-Rake 1 iter) is required to achieve better error performance than the bit interleaved coded MMSE OFDM. Moreover, with the over-relaxation parameter $\omega = 1.25$ (labeled as SOR-Turbo-Rake), a gain of ≈ 0.2 dB (for 16 QAM with 3 turbo iterations) and ≈ 1 dB (for 64 QAM with 3 turbo iterations) is achieved in the FER performance. The overall detector complexity in terms average number of iterations to converge is significantly reduced by using turbo iterations along with the initial estimates from the time-frequency single tap equalizer.

Fig. 13 shows the FER performance of the proposed detector vs BICM-OFDM for different codeword lengths: long (labeled as SOR-Turbo-Rake-3840) and short (labeled as SOR-Turbo-Rake-672). For a fair comparison with the OFDM scheme, the FER plot for a single turbo iteration is also plotted alongside. It can be observed that, the proposed detector with single turbo iteration has a gain of ≈ 3 dB and ≈ 4 dB for codeword length of 3840 and 672, respectively, as compared to the OFDM scheme at a FER of 10^{-2}. It can be noted that more iterations are required for short codewords to achieve the same performance as long codewords.

VII. Detector Complexity

In Table I, we summarize and compare the overall complexity of the iterative Rake receiver (in terms of complex multiplications), including initial computations and Fourier domain transformations as discussed in Section IV.

Term (I) accounts for the computations inside each detector iteration, which includes calculating $\Delta\tilde{\mathbf{g}}_m^{(i)}$, $\Delta\tilde{\mathbf{y}}_m^{(i)}$, $\tilde{\mathbf{c}}_m^{(i)}$, and the symbol-vector hard decision estimates $\tilde{\mathbf{x}}_m^{(i)}$ in Algorithm 2. Term (II) is for initial computations, which involves calculating $M'L$ delay-time Doppler spread vectors $\tilde{\boldsymbol{\nu}}_{m,l}$, initial M' residual vectors $\Delta\tilde{\mathbf{y}}_m^{(0)}$ in (58), and M' vectors $\tilde{\mathbf{d}}_m$ and term (III) is to compute the low complexity initial time-frequency estimate $\hat{\mathbf{x}}_m^{(0)}$ in (64).

The detectors for OTFS with complexity linear in NM and with non-ideal pulse shaping waveform (rectangular) are discussed in [22], [24]. The complexity of the MPA detector per iteration scales with the number of paths on the discrete delay-Doppler grid and the alphabet size $|\mathcal{Q}|$, and has a complexity of the order $O(P|\mathcal{Q}|NM)$ [22]. The linear minimum mean square error detector proposed in [24] even though is a non-iterative detector has a computational complexity of $O((l_{\max}^2 + k_{\max}P^2)NM)$ whereas the proposed detector has a complexity of $O(SLNM)$ where $L \leq P$ and S is the number of MRC detector iterations as given in Fig. 7.

The complexity of the proposed detector is compared with other linear complexity OTFS detectors, for different modulation sizes, number of multipaths in Fig. 14. The dashed lines represents the case when there are 5 paths with distinct Doppler shifts in each delay tap i.e., $P = 5L$. It can be concluded from Fig. 14 that the proposed detector complexity is significantly lower than the one of other OTFS detectors and closer to that of an OFDM single tap MMSE equalizer.

For the iterative operation, the storage requirement for the MRC detector is $(L+2)NM$ complex numbers as only the LNM delay-time channel coefficients, the M RNPI vectors, and the M' symbol vector estimates need to be stored for each iteration. For MPA, the storage requirement is much higher and of the order $O(P|\mathcal{Q}|NM)$ [22].

VIII. Conclusion

We reformulated the OTFS input-output relation and proposed *two* versions of a *linear complexity* iterative rake detector algorithm for ZP-OTFS modulation based on the maximal ratio

Authorized licensed use limited to: Monash University. Downloaded on March 22,2022 at 09:25:19 UTC from IEEE Xplore. Restrictions apply.

combining principle. We show that the MRC detector along with a low complexity initial estimate of symbol-vectors can achieve similar or better BER performance than the MPA detector with lower complexity and storage requirements. Based on the well studied Gauss-Seidel method, we introduced a successive over relaxation parameter to improve error performance and faster convergence of the proposed detector. The MRC detector performance was further improved with the aid of an outer error control coding scheme using turbo iterations. An additional advantage of the MRC detector is that the complexity is linear in L (number of delay taps) rather than P (total number of paths), thanks to the vector decomposition of the 2-D convolution with the channel.

APPENDIX

A. Proof of Lemma (1)

Consider the M dimensional linear system of equations $\mathbf{z}_n = \mathbf{R}_n \cdot \mathbf{s}_n$ without the noise term in (72). The positive definite Hermitian system matrix $\mathbf{R}_n$ can be split as $\mathbf{D}_n + \mathbf{L}_n + \mathbf{L}_n^{\dagger}$, where $\mathbf{D}_n$ and $\mathbf{L}_n \in \mathbb{C}^{M\times M}$ are the matrices containing the diagonal and strictly lower-triangular elements, respectively. Pre and post-multiplying both sides of (72) by $\mathbf{D}_n^{-1/2}$ and $\mathbf{D}_n^{1/2}$, respectively, we get the re-scaled system of equations

$$\mathbf{z}'_n = \mathbf{R}'_n \cdot \mathbf{s}'_n \tag{82}$$

where

$$\mathbf{R}'_n = \mathbf{D}_n^{-1/2}\cdot\mathbf{R}_n\cdot\mathbf{D}_n^{-1/2}, \quad \mathbf{z}'_n = \mathbf{D}_n^{-1/2}\cdot\mathbf{z}_n, \quad \mathbf{s}'_n = \mathbf{D}_n^{1/2}\cdot\mathbf{s}_n \tag{83}$$

$\mathbf{R}'_n$ is the re-scaled system matrix, which can be split as

$$\mathbf{R}'_n = \mathbf{I}_M + \mathbf{L}'_n + \mathbf{L}'^{\dagger}_n \tag{84}$$

where $\mathbf{L}'_n = \mathbf{D}_n^{-1/2} \cdot \mathbf{L}_n \cdot \mathbf{D}_n^{-1/2}$.

Since $\mathbf{R}'_n$ is a positive definite Hermitian matrix, any non-zero vector $\mathbf{u}$ such that $\mathbf{u}^{\dagger} \cdot \mathbf{u} = \beta > 0$ satisfies,

$$\begin{aligned} &\mathbf{u}^{\dagger} \cdot (\mathbf{I}_M + \mathbf{L}'_n + \mathbf{L}'^{\dagger}_n) \cdot \mathbf{u} > 0 \\ &\Rightarrow \beta + 2\Re[\mathbf{u}^{\dagger} \cdot \mathbf{L}'_n \cdot \mathbf{u}] > 0. \end{aligned} \tag{85}$$

The inequality in (85) can now be written as

$$a = \Re[\mathbf{u}^{\dagger} \cdot \mathbf{L}'_n \cdot \mathbf{u}] = \Re[\mathbf{u}^{\dagger} \cdot \mathbf{L}'^{\dagger}_n \cdot \mathbf{u}] > -\frac{\beta}{2} \tag{86}$$

where $\Re[\cdot]$ denotes the real part. Also note that

$$b = \Im[\mathbf{u}^{\dagger} \cdot \mathbf{L}'_n \cdot \mathbf{u}] = -\Im[\mathbf{u}^{\dagger} \cdot \mathbf{L}'^{\dagger}_n \cdot \mathbf{u}] \tag{87}$$

where $\Im[\cdot]$ denotes the imaginary part.

Solving (72) is equivalent to solving the linear system of equations in (82) and re-scaling its solution vector as given in (83). The equivalent GS iteration matrix $\mathbf{T}_n^{\mathrm{GS}}$ for (83) can be written as

$$\mathbf{T}_n^{\mathrm{GS}} = (\mathbf{I}_M + \mathbf{L}'_n)^{-1} \cdot \mathbf{L}'^{\dagger}_n. \tag{88}$$

Now, the GS method for the system equation given in (70) is guaranteed to converge if $|\lambda(\mathbf{T}_n^{\mathrm{GS}})| < 1$, where $\lambda(\mathbf{T}_n^{\mathrm{GS}})$ denotes any eigenvalue of $\mathbf{T}_n^{\mathrm{GS}}$, which satisfy $\mathbf{T}_n^{\mathrm{GS}} \cdot \mathbf{v} = \lambda(\mathbf{T}_n^{\mathrm{GS}})\mathbf{v}$, for the corresponding eigenvectors $\mathbf{v}$, i.e.,

$$(\mathbf{I}_M + \mathbf{L}'_n)^{-1} \cdot \mathbf{L}'^{\dagger}_n \cdot \mathbf{v} = \lambda(\mathbf{T}_n^{\mathrm{GS}})\mathbf{v}. \tag{89}$$

After multiplying both sides of (89) by $\mathbf{v}^H \cdot (\mathbf{I}_M + \mathbf{L}'_n)$, we can write $\lambda(\mathbf{T}_n^{\mathrm{GS}})$ as

$$\begin{aligned} \lambda(\mathbf{T}_n^{\mathrm{GS}}) &= \frac{\mathbf{v}_n^{\dagger} \cdot \mathbf{L}'^{\dagger}_n \cdot \mathbf{v}_n}{\beta + \mathbf{v}_n^{\dagger} \cdot \mathbf{L}'_n \cdot \mathbf{v}_n} = \frac{|a - jb|}{|\beta + a + jb|} \\ &= \frac{\sqrt{a^2 + b^2}}{\sqrt{(\beta + a)^2 + b^2}}. \end{aligned} \tag{90}$$

From (86), (87) and (90), it can be seen that $|\lambda(\mathbf{T}_n^{\mathrm{GS}})| < 1$. Similarly for the case when $\mathbf{R}_n$ is positive semi-definite, i.e., (86) becomes $a \geq -\beta/2$, the eigenvalue inequality becomes $|\lambda(\mathbf{T}_n^{\mathrm{GS}})| \leq 1$. Since $\rho(\mathbf{T}_n^{\mathrm{GS}})$ is equal to the largest absolute value of the eigenvalues of $\mathbf{T}_n^{\mathrm{GS}}$, the positive definiteness of $\mathbf{R}_n$ ensures that $\rho(\mathbf{T}_n^{\mathrm{GS}}) < 1$.

B. Proof of Lemma (2)

Following the steps above, (90) can be modified for the eigenvalues of the SOR-GS iteration matrix $\mathbf{T}_n^{\omega}$ defined in (74) as

$$\lambda(\mathbf{T}_n^{\omega}) = \frac{(\omega - 1)(\mathbf{v}^{\dagger} \cdot \mathbf{v}) + \omega(\mathbf{v}^{\dagger} \cdot \mathbf{L}'^{\dagger}_n \cdot \mathbf{v}_n)}{\mathbf{v}^{\dagger} \cdot \mathbf{v} + \omega(\mathbf{v}^{\dagger} \cdot \mathbf{L}'_n \cdot \mathbf{v})}. \tag{91}$$

The condition for eigenvalues $\lambda(\mathbf{T}_n^{\mathrm{GS}})$ in (90) can then be modified for the SOR case as

$$|\lambda(\mathbf{T}_n^{\omega})| = \frac{\sqrt{((\omega - 1)\beta + \omega a)^2 + (\omega b)^2}}{\sqrt{(\beta + \omega a)^2 + (\omega b)^2}}. \tag{92}$$

It can be seen from (92) that $|\lambda(\mathbf{T}_n^{\omega})| < 1$, if $|(\omega - 1)\beta + \omega a| < |\beta + \omega a|$, which is guaranteed if $0 < \omega < 2$.

REFERENCES

[1] R. Hadani *et al.*, "Orthogonal time frequency space modulation," in *Proc. IEEE Wireless Commun. Netw. Conf.*, San Francisco, CA, USA, Mar. 2017, pp. 1–6.

[2] P. Raviteja, Y. Hong, E. Viterbo, and E. Biglieri, "Effective diversity of OTFS modulation," *IEEE Wireless Commun. Lett.*, vol. 9, no. 2, pp. 249–253, Feb. 2020.

[3] T. Thaj and E. Viterbo, "Low complexity iterative rake detector for orthogonal time frequency space modulation," in *Proc. IEEE Wireless Commun. Netw. Conf.*, Seoul, Korea (South), May 2020, pp. 1–6.

[4] D. G. Brennan, "Linear diversity combining techniques," in *Proc. IRE*, vol. 47, pp. 1075–1102, Jun. 1959.

[5] S. Kondo and B. Milstein, "Performance of multicarrier DS CDMA systems," *IEEE Trans. Commun.*, vol. 44, no. 2, pp. 238–246, Feb. 1996.

[6] S. Imada and T. Ohtsuki, "Pre-RAKE diversity combining for UWB systems in IEEE 802.15 UWB multipath channel," in *Proc. Int. Workshop UWBST and IWUWBS*, Kyoto, Japan, 2004, pp. 236–240.

[7] Xiaofei Dong and N. C. Beaulieu, "Optimal maximal ratio combining with correlated diversity branches," *IEEE Commun. Lett.*, vol. 6, no. 1, pp. 22–24, Jan. 2002.

[8] R. M. Buehrer, S. P. Nicoloso, and S. Gollamudi, "Linear versus non-linear interference cancellation," *J. Commun. Netw.*, vol. 1, no. 2, pp. 118–133, Jun. 1999.

[9] P. Raviteja, Y. Hong, E. Viterbo, and E. Biglieri, "Practical pulse-shaping waveforms for reduced-cyclic-prefix OTFS," *IEEE Trans. Veh. Technol.*, vol. 68, no. 1, pp. 957–961, Jan. 2019.

[10] P. Raviteja, K. T. Phan, and Y. Hong, "Embedded pilot-aided channel estimation for OTFS in delay-doppler channels," *IEEE Trans. Veh. Technol.*, vol. 68, no. 5, pp. 4906–4917, May 2019.

Authorized licensed use limited to: Monash University. Downloaded on March 22,2022 at 09:25:19 UTC from IEEE Xplore. Restrictions apply.

[11] T. Ebihara and G. Leus, "Doppler-resilient orthogonal signal-division multiplexing for underwater acoustic communication," *IEEE J. Ocean. Eng.*, vol. 41, no. 2, pp. 408–427, Apr. 2016.

[12] M. Stojanovic and J. Preisig, "Underwater acoustic communication channels: Propagation models and statistical characterization," *IEEE Commun. Mag.*, vol. 47, no. 1, pp. 84–89, Jan. 2009.

[13] "LTE evolved universal terrestrial radio access (E-UTRA); Base station (BS) radio transmission and reception," 3GPP TS 36.104 version 8.6.0 Release 8, Jul. 2009, ETSI TS, doi: 10.1109/MCOM.2009.4752682.

[14] D. Tse and P. Viswanath, *Fundamentals of Wireless Commun.*, 3rd ed. Oxford, U.K.: Cambridge Univ. Press, 2005.

[15] A. Farhang, A. RezazadehReyhani, L. E. Doyle, and B. Farhang-Boroujeny, "Low complexity modem structure for OFDM-based orthogonal time frequency space modulation," *IEEE Wireless Commun. Lett.*, vol. 7, no. 3, pp. 344–347, Jun. 2018.

[16] R. Hadani *et al.*, "Orthogonal time frequency space modulation," Aug. 2018, *arXiv:1808.00519v1*, [Online]. Available: https://arxiv.org/abs/1808.00519v1

[17] C. F. V. Loan, "The ubiquitous Kronecker product," *J. Comput. Appl. Math.*, vol. 123, no. 1-2, pp. 85–100, 2000.

[18] R. A. Beezer, *A First Course in Linear Algebra*, 3rd ed. Washington, DC, USA: Congruent Press, pp. 404–406, 1973.

[19] A. Björck, *Numer. Methods for Least Squares Problems*, Philadelphia, PA, USA: SIAM, 1996, doi: 10.1137/1.9781611971484.

[20] Y. Saad, *Iterative Methods for Sparse Linear Syst.*, 2nd ed. Philadelphia, PA, USA: SIAM, 2003, doi: 10.1137/1.9780898718003.

[21] A. Hadjidimos, "Successive overrelaxation (SOR) and related methods," *J. Comput. Appl. Math.*, vol. 123, no. 1-2, pp. 177–199, Nov. 2000.

[22] P. Raviteja, K.T. Phan, Yi Hong, and E. Viterbo, "Low-complexity iterative detection for orthogonal time frequency space modulation," in *Proc. IEEE Wireless Commun. Netw. Conf.*, Barcelona, Spain, Apr. 2018, pp. 1–6.

[23] P. Raviteja, K.T. Phan, Yi Hong, and E. Viterbo, "Interference cancellation and iterative detection for orthogonal time frequency space modulation," *IEEE Trans. Wireless Commun.*, vol. 17, no. 10, pp. 6501–6515, Oct. 2018.

[24] S. Tiwari, S.S. Das, and V. Rangamgari, "Low-complexity LMMSE receiver for OTFS," *IEEE Commun. Lett.*, vol. 23, no. 12, pp. 2205–2209, Dec. 2019.

[25] T. T. B. Nguygen, T. N. Tan, and H. Lee, "Effecient QC-LDPC encoder for 5G new radio," *Electronics*, vol. 8, no. 668, pp. 1–15, Jun. 2019.

Tharaj Thaj received the B.Tech. degree in electronics and communication engineering from the National Institute of Technology, Calicut, India, in 2012, and the M.Tech. degree in telecommunication systems engineering from the Indian Institute of Technology, Kharagpur, India in 2015. He is currently working toward the Ph.D. degree with the Department of Electrical and Computer Systems Engineering, Monash University, Australia. From 2012 to 2013, he was with Verizon Data Services India, Chennai, as a Software Engineer, focussing on network layer routing algorithms and protocols. From 2015 to 2017, he worked as a Senior Engineer with the Communication, Navigation and Survellance (CNS) Department of Honeywell Technology Solutions Lab, Bengaluru. His current research interests include physical layer design and implementation of wireless communication systems for next generation wireless networks.

Emanuele Viterbo (Fellow, IEEE) received the Ph.D. degree in electrical engineering, from the Politecnico di Torino, Torino, Italy, in 1995. He is currently a Professor with the ECSE Department, Monash University, Melbourne, Australia. From 1990 to 1992, he was with the European Patent Office, The Hague, The Netherlands, as a Patent Examiner in the field of dynamic recording and error-control coding. Between 1995 and 1997, he held a Postdoctoral Position with the Dipartimento di Elettronica of the Politecnico di Torino. In 1997–98 he was a Postdoctoral Research Fellow with the Information Sciences Research Center of AT T Research, Florham Park, NJ, USA. From 1998 to 2005, he worked as an Assistant Professor and then an Associate Professor, with the Dipartimento di Elettronica, Politecnico di Torino. From 2006 to 2009, he worked with DEIS, University of Calabria, Italy, as a Full Professor. He Viterbo is an ISI Highly Cited Researcher since 2009. His main research interests are in lattice codes for the Gaussian and fading channels, algebraic coding theory, algebraic space-time coding, digital terrestrial television broadcasting, digital magnetic recording, and irregular sampling. He was an Associate Editor for IEEE TRANSACTIONS ON INFORMATION THEORY, *European Transactions on Telecommunications* and *Journal of Communications and Networks*, and a Guest Editor for IEEE JOURNAL OF SELECTED TOPICS IN SIGNAL PROCESSING: SPECIAL ISSUE MANAGING COMPLEXITY IN MULTIUSER MIMO SYSTEMS. He was the recipient of the NATO Advanced Fellowship in 1997 from the Italian National Research Council.

Authorized licensed use limited to: Monash University. Downloaded on March 22,2022 at 09:25:19 UTC from IEEE Xplore. Restrictions apply.

Chapter 4

Low-Complexity Linear Diversity-Combining Detector for MIMO-OTFS

Citing info:

T. Thaj and E. Viterbo, "Low-Complexity Linear Diversity-Combining Detector for MIMO-OTFS" in *IEEE Wireless Communications Letters*, vol. 11, no. 2, pp. 288-292, Feb. 2022, doi: 10.1109/LWC.2021.3125986.

Publishing Journal Info:

Impact factor: 4.348, CiteScore: 8.2, JCI ranked 16/105 (category TELECOMMUNICATIONS)

Copyright Statement:

©[2019] IEEE. Reprinted, with permission, from [Tharaj Thaj, Emanuele Viterbo, 'Low-Complexity Linear Diversity-Combining Detector for MIMO-OTFS, IEEE Wireless Communications Letters, 2022]

288 IEEE WIRELESS COMMUNICATIONS LETTERS, VOL. 11, NO. 2, FEBRUARY 2022

Low-Complexity Linear Diversity-Combining Detector for MIMO-OTFS

Tharaj Thaj, *Graduate Student Member, IEEE*, and Emanuele Viterbo, *Fellow, IEEE*

***Abstract*—This letter presents a low complexity detector for multiple-input multiple-output (MIMO) systems based on the recently proposed orthogonal time frequency space (OTFS) modulation. In the proposed detector, the copies of the transmitted symbol-vectors received through the different diversity branches (propagation paths and receive antennas) are linearly combined using the maximum ratio combining (MRC) technique to iteratively improve the signal to interference plus noise ratio (SINR) at the output of the combiner. To alleviate the performance degradation due to spatial correlation at the receiver antennas, we present a sample-based method to estimate such correlation and find the optimized combining weights for MRC from the estimated correlation matrix. The detector performance and complexity improve over the linear minimum mean square error (LMMSE) and message passing (MP) detectors proposed in the literature for MIMO-OTFS.**

***Index Terms*—OTFS, detector, rake, maximum ratio combining, delay-doppler, MIMO, spatial correlation.**

I. Introduction

RELIABLE communications in high mobility wireless channel scenarios are essential to satisfy the wireless network requirements of 6G mobile communications. Orthogonal frequency division multiplexing (OFDM), at the core of the physical layer of 4G/5G, multiplex information symbols on closely spaced orthogonal sub-carriers. This results in performance degradation in high-mobility wireless channels due to the loss of orthogonality among the sub-carriers.

The recently proposed orthogonal time frequency space (OTFS) modulation is based on the idea of multiplexing the information symbols in the delay-Doppler (DD) domain, resulting in significant performance gains over OFDM in high-mobility channels, [1]. In OFDM, each information symbol is transmitted over a single time-frequency resource, which is susceptible to frequency and time-selective fading effects, whereas OTFS multiplexes each information symbol over 2D orthogonal basis functions that span the entire time and frequency domain, but are localized in the DD domain. As a result, all information symbols experience a constant flat fading equivalent channel.

Multiple-input multiple-output (MIMO) based on OTFS (MIMO-OTFS) can further increase the spectral efficiency to meet the data rate demands of 6G. The superior performance of MIMO-OTFS over MIMO-OFDM and its system model, detection, and channel estimation methods have been well studied in the literature, [2]–[7]. The biggest challenge with a MIMO system is the high processing complexity at the receiver. The message passing (MP) algorithm proposed for MIMO-OTFS in [2] offers excellent performance but still suffers from high complexity, especially in high Doppler spread channels and high-order modulation. Further, spatial correlation can degrade the error performance of the MIMO system, especially if the correlation of the antennas is not taken into account while designing receiver algorithms, [8].

In this letter, we propose a linear-complexity detector for MIMO-OTFS with rectangular pulse-shaping waveform, based on the maximum ratio combining (MRC) diversity-combining principle proposed for SISO-OTFS in [9], to efficiently combine the distinct antenna and multipath copies of the transmitted symbols. Differently from [9], the combining weights of the MRC algorithm are optimized to combat the adverse effects of spatial correlation at the receiver (Rx). We further propose a sample-based method to estimate the spatial correlation between the channels from the estimated channel coefficients at different Rx antennas. Further, we analyze via simulations the performance of the proposed detection method with spatial correlation and practical channel estimation at the Rx. Finally, we show that the proposed detector is linear in the number of transmitted symbols and antennas, making the detector complexity convenient even for large MIMO systems.

Notations: The following notations will be used: a, $\mathbf{a}$, $\mathbf{A}$ represent a scalar, vector, and matrix, respectively; $\mathbf{a}[n]$ and $\mathbf{A}[m,n]$ represent the n-th and (m,n)-th element of $\mathbf{a}$ and $\mathbf{A}$, respectively; $\mathbf{A}^{\dagger}$, $\mathbf{A}^{*}$ and $\mathbf{A}^{n}$ represent the Hermitian transpose, complex conjugate and n-th power of $\mathbf{A}$. The set of $M \times N$ dimensional matrices with complex entries is denoted by $\mathbb{C}^{M\times N}$. Let $\otimes$ denote the Kronecker product, $|\mathcal{S}|$ the cardinality of the set $\mathcal{S}$, and vec($\mathbf{A}$) the column-wise vectorization of the matrix $\mathbf{A}$. Let $\mathbf{F}_N$ be the normalized N point discrete Fourier transform (DFT) matrix and $\mathbf{I}_M$ the $M \times M$ identity matrix.

II. System Model

Consider a MIMO-OTFS system with n_{T} and n_{R} transmit and receiver antennas, respectively. Let $\mathbf{X}^{(t)}$ and $\mathbf{Y}^{(r)}$ be the $M \times N$ DD domain OTFS information symbols, transmitted from the t-th antenna and received at the r-th antenna, respectively. All transmitted frames of duration NT [s] occupy the same bandwidth of $M\Delta f$ [Hz], with $T\Delta f = 1$. The time-domain samples transmitted from the t-th antenna and the received samples at the r-th antenna are given by

$$\mathbf{s}^{(t)} = \mathrm{vec}(\mathbf{X}^{(t)} \cdot \mathbf{F}_N^{\dagger}), \quad \mathbf{r}^{(r)} = \mathrm{vec}(\mathbf{Y}^{(t)} \cdot \mathbf{F}_N^{\dagger}) \tag{1}$$

At the transmitter, a cyclic prefix (CP) or zero-padding (ZP) of length L_{G} greater than the channel delay spread is inserted before each of the N time-domain blocks of the OTFS frame.

Manuscript received October 7, 2021; accepted November 3, 2021. Date of publication November 8, 2021; date of current version February 17, 2022. This work was supported by the Australian Research Council through the Discovery Project under Grant DP200100096. The associate editor coordinating the review of this article and approving it for publication was G. L. A. A. Baduge. *(Corresponding author: Emanuele Viterbo.)*

The authors are with the ECSE Department, Monash University, Clayton, VIC 3800, Australia (e-mail: tharaj.thaj@monash.edu; emanuele.viterbo@monash.edu).

Digital Object Identifier 10.1109/LWC.2021.3125986

2162-2345 © 2021 IEEE. Personal use is permitted, but republication/redistribution requires IEEE permission.
See https://www.ieee.org/publications/rights/index.html for more information.

Authorized licensed use limited to: Monash University. Downloaded on March 22,2022 at 09:30:39 UTC from IEEE Xplore. Restrictions apply.

A. Channel

Let $h_i^{(r,t)}$, $\tau_i^{(r,t)}$ and $\nu_i^{(r,t)}$ be the complex path gain, delay and Doppler shift, respectively, associated with the *i*-th path in the channel between the *r*-th receive antenna and the *t*-th transmit antenna (the (*r*, *t*) sub-channel). The DD domain representation of the MIMO multipath channel is given by

$$h^{(r,t)}(\tau,\nu) = \sum_{i=1}^{P^{(r,t)}} h_i^{(r,t)}\delta(\tau-\tau_i^{(r,t)})\delta(\nu-\nu_i^{(r,t)}) \quad (2)$$

for $t = 1,\ldots,n_{\mathrm{T}}$ and $r = 1,\ldots,n_{\mathrm{R}}$, where $P^{(r,t)}$ is the number of DD domain paths in the (*r*, *t*) sub-channel. The corresponding delay-time (DT) channel can be written as

$$g^{(r,t)}(\tau,\theta) = \int_{\nu} h^{(r,t)}(\tau,\nu)\mathrm{e}^{j2\pi\nu(\theta-\tau)}\,d\nu \quad (3)$$

where θ is the continuous-time variable.

The receiver samples the incoming signals at integer multiples of the sampling period $1/M\Delta f$. Let $\ell_i = \tau_i M\Delta f$ and $\kappa_i = \nu_i NT$ be the *normalized delay* and *normalized Doppler-shift* associated with the *i*-th path. Following [9], the discrete-time equivalent channel is obtained by sampling (3) at times $\theta = \frac{q}{M\Delta f}$ and delays $\tau = \frac{\ell}{M\Delta f}$ with $q, \ell \in \mathbb{Z}$ as

$$g^{(r,t)}[\ell,q] = \sum_{i=1}^{P^{(r,t)}} h_i^{(r,t)} z^{(q-\ell)\kappa_i^{(r,t)}}\delta[\ell-\ell_i^{(r,t)}] \quad (4)$$

where we assume integer *normalized delays*, i.e., $\ell_i^{(r,t)} \in \mathbb{Z}$ and $z = \mathrm{e}^{\frac{j2\pi}{MN}}$. No assumption is made on $\kappa_i^{(r,t)}$ to be integer.

B. Spatial Correlation

In MIMO systems, there is often correlation among the (*r*, *t*) sub-channels depending on the propagation environment, antenna patterns, and the relative locations of the Tx and Rx antennas. If we assume that the transmitter and receiver are sufficiently separated, then the correlation matrices $\mathbf{R}_{\mathrm{tx}}$ and $\mathbf{R}_{\mathrm{rx}}$ characterize the correlations among the sub-channels at the transmitter and at the receiver, respectively.

In this letter we consider the exponential correlation matrix in [8] with elements given as

$$\mathbf{R}_{\mathrm{rx}}[j,i] = \begin{cases} \rho_{\mathrm{rx}}^{j-i}, & i \le j \\ (\rho_{\mathrm{rx}}^{i-j})^*, & i > j \end{cases}, \quad i,j \in \{1,\ldots,n_{\mathrm{R}}\} \quad (5)$$

where ρ_{rx} denotes the level of correlation at the Rx. The corresponding correlation matrix at the transmitter $\mathbf{R}_{\mathrm{tx}}$ can be obtained by replacing ρ_{rx} with ρ_{tx} in (5).

Let $\mathbf{A}_i$ be the $n_{\mathrm{R}} \times n_{\mathrm{T}}$ MIMO matrix with iid complex Gaussian random entries, i.e., $\mathbf{A}_i[r,t] \sim \mathcal{CN}(0,\sigma_i^2(r,t))$, where $\sigma_i^2(r,t)$ denotes the average power associated with *i*-th path of the (*r*, *t*) sub-channel. The spatially correlated channel coefficients in (2) are then generated as $h_i^{(r,t)} = \bar{\mathbf{A}}_i[r,t]$ where

$$\bar{\mathbf{A}}_i = \mathbf{C}_{\mathrm{rx}} \cdot \mathbf{A}_i \cdot \mathbf{C}_{\mathrm{tx}}^{\dagger} \quad (6)$$

and where the *correlation-shaping* matrices $\mathbf{C}_{\mathrm{tx}}$ and $\mathbf{C}_{\mathrm{rx}}$ are the lower-triangular matrices obtained by the Cholesky decomposition of $\mathbf{R}_{\mathrm{tx}}$ and $\mathbf{R}_{\mathrm{rx}}$, i.e., $\mathbf{R}_{\mathrm{tx}} = \mathbf{C}_{\mathrm{tx}} \cdot \mathbf{C}_{\mathrm{tx}}^{\dagger}$ and $\mathbf{R}_{\mathrm{rx}} = \mathbf{C}_{\mathrm{rx}} \cdot \mathbf{C}_{\mathrm{rx}}^{\dagger}$.

C. Input-Output Relations

1) Time Domain: Let $\mathcal{L}^{(r,t)} = \{\ell_i^{(r,t)}\}$ for $i = 1,\ldots,P^{(r,t)}$ be the set of distinct *normalized delays* in the (*r*, *t*) sub-channel. Using (4), the time domain input-output relation for one frame can be written as

$$\mathbf{r}^{(r)}[q] = \sum_{t=1}^{n_{\mathrm{T}}} \sum_{\ell\in\mathcal{L}^{(r,t)}} g^{(r,t)}[\ell,q]\mathbf{s}^{(t)}[q-\ell] + \mathbf{z}^{(r)}[q] \quad (7)$$

where $q = m + n(M + L_{\mathrm{G}})$ for $m = 0,\ldots,M+L_{\mathrm{G}}-1$, $n = 0,\ldots,N-1$ and $\mathbf{z}^{(r)}[q]$ is the AWGN noise in the *r*-th receive antenna. Let $\mathbf{G}^{(r,t)}$ be the time-domain channel matrix for the (*r*, *t*) sub-channel, with entries

$$\mathbf{G}^{(r,t)}[m+nM,[m-\ell]_M+nM] = g^{(r,t)}[\ell,m+n(M+L_{\mathrm{G}})] \quad (8)$$

for $\ell \in \mathcal{L}^{(r,t)}$ and *zero* otherwise. The modulo-*M* operation $[\,\cdot\,]_M$ is due to the time-domain CP per block. In the case of ZP per block, $\mathbf{G}^{(r,t)}$ becomes a lower triangular matrix, i.e., $\mathbf{G}^{(r,t)}[q,[q-\ell]_{MN}] = 0$ if $q < \ell$, [9].

The time-domain input-output relation in (7) can be written in a simple matrix form as

$$\mathbf{r}^{(r)} = \sum_{t=1}^{n_{\mathrm{T}}} \mathbf{G}^{(r,t)}\mathbf{s}^{(t)} + \mathbf{z}^{(r)}, \quad r = 1,\ldots,n_{\mathrm{R}}. \quad (9)$$

2) Delay-Doppler Domain: From (1), the DD information symbols are related to the time domain samples:

$$\mathbf{s}^{(t)} = \mathbf{P}\cdot(\mathbf{I}_M \otimes \mathbf{F}_N^{\dagger})\cdot\mathbf{x}^{(t)},\ \mathbf{r}^{(r)} = \mathbf{P}\cdot(\mathbf{I}_M \otimes \mathbf{F}_N^{\dagger})\cdot\mathbf{y}^{(r)} \quad (10)$$

where $\mathbf{x}^{(t)} = \mathrm{vec}((\mathbf{X}^{(t)})^{\mathrm{T}})$, $\mathbf{y}^{(r)} = \mathrm{vec}((\mathbf{Y}^{(r)})^{\mathrm{T}})$ and $\mathbf{P}$ is the row-column interleaver permutation matrix given in [9]. Substituting (10) in (9), the corresponding DD domain input-output relation at the *r*-th receive antenna can be written as

$$\mathbf{y}^{(r)} = \sum_{t=1}^{n_{\mathrm{T}}} \mathbf{H}^{(r,t)}\mathbf{x}^{(t)} + \mathbf{w}^{(r)} \quad (11)$$

where

$$\mathbf{H}^{(r,t)} = (\mathbf{I}_M \otimes \mathbf{F}_N)\cdot(\mathbf{P}^{\mathrm{T}}\cdot\mathbf{G}^{(r,t)}\cdot\mathbf{P})\cdot(\mathbf{I}_M \otimes \mathbf{F}_N^{\dagger}) \quad (12)$$

$$\mathbf{w}^{(r)} = (\mathbf{I}_M \otimes \mathbf{F}_N)\cdot(\mathbf{P}^{\mathrm{T}}\cdot\mathbf{z}^{(r)}) \quad (13)$$

To describe the proposed detection method (in Section III) we partition the $NM \times 1$ vectors $\mathbf{x}^{(t)}$ and $\mathbf{y}^{(r)}$ into *M symbol-vectors* of length *N* as

$$\mathbf{x}^{(t)} = [\mathbf{x}_0^{(t)\mathrm{T}},\ldots,\mathbf{x}_{M-1}^{(t)\mathrm{T}}]^{\mathrm{T}},\ \mathbf{y}^{(r)} = [\mathbf{y}_0^{(r)\mathrm{T}},\ldots,\mathbf{y}_{M-1}^{(r)\mathrm{T}}]^{\mathrm{T}} \quad (14)$$

Following the SISO-OTFS notations in [9], the input-output relation for MIMO-OTFS in (11) can be written for each symbol-vector as

$$\mathbf{y}_m^{(r)} = \sum_{t=1}^{n_{\mathrm{T}}} \sum_{\ell\in\mathcal{L}^{(r,t)}} \mathbf{K}_{m,\ell}^{(r,t)}\cdot\mathbf{x}_{[m-\ell]_M}^{(t)} + \mathbf{w}_m^{(r)},\ m = 0,\ldots,M-1 \quad (15)$$

where $\mathbf{K}_{m,\ell}^{(r,t)} \in \mathbb{C}^{N\times N}$ is the (*r*, *t*) sub-channel between the *m*-th received symbol vector of the *r*-th receive antenna and the $[m-\ell]_M$-th transmit symbol vector of the *t*-th transmit

Authorized licensed use limited to: Monash University. Downloaded on March 22,2022 at 09:30:39 UTC from IEEE Xplore. Restrictions apply.

antenna, i.e., $\mathbf{K}_{m,\ell}^{(r,t)}$ is the $(m,[m-\ell]_M)$-th sub-matrix of $\mathbf{H}^{(r,t)}$ in (11). It was shown in [9] that for rectangular pulse shaping waveforms, $\mathbf{K}_{m,\ell}^{(r,t)}$ are circulant matrices.

3) Delay-Time Domain: Here, we discuss the MIMO input-output relation in the DT domain, where detection can be performed with the least complexity (see Section III). Vectors with a tilde denote the corresponding DT domain symbol-vectors and are related by the *N*-point DFTs as

$$\widetilde{\mathbf{x}}_m^{(t)} = \mathbf{F}_N^{\dagger} \cdot \mathbf{x}_m^{(t)}, \quad \widetilde{\mathbf{y}}_m^{(r)} = \mathbf{F}_N^{\dagger} \cdot \mathbf{y}_m^{(r)}, \tag{16}$$

Since the DD domain sub-matrices $\mathbf{K}_{m,\ell}^{(r,t)}$ are circulant with $\mathbf{h}_{m,\ell}^{(r,t)} \in \mathbb{C}^{N\times 1}$ as their first column, (15) can be written in form of element-wise multiplication in the corresponding Fourier transformed domain (i.e., the DT domain) as

$$\widetilde{\mathbf{y}}_m^{(r)}[n] = \sum_{t=1}^{n_{\mathrm{T}}} \sum_{\ell\in\mathcal{L}^{(r,t)}} \widetilde{\mathbf{h}}_{m,\ell}^{(r,t)}[n]\widetilde{\mathbf{x}}_{[m-\ell]_M}^{(t)}[n] + \widetilde{\mathbf{w}}_m^{(r)}[n] \tag{17}$$

for $n = 0,\ldots,N-1$, where $\widetilde{\mathbf{w}}_m^{(r)}$ is the AWGN noise and $\widetilde{\mathbf{h}}_{m,\ell}^{(r,t)} = \mathbf{F}_N^{\dagger} \cdot \mathbf{h}_{m,\ell}^{(r,t)}$ are the DT channel vectors, [9].

III. MIMO-OTFS Detection

This section proposes a low-complexity linear diversity-combining detector for MIMO-OTFS in the DT domain, based on the MRC principle. Consider the DT domain input-output relation in (17). For ease of illustration, we consider the number of distinct delay taps in all the sub-channels to be equal, i.e., $L = |\mathcal{L}^{(r,t)}| \ \forall\ r,t$. Then, due to multipath and spatial diversity, L copies of each transmitted symbol-vector $\mathbf{x}_m^{(t)}$ arrive at each of the n_{R} receiver antennas along with multipath echoes of other symbol-vectors due to inter-delay and inter-antenna interference. The basic idea of the proposed detection method is to extract and combine the received signal components in all the diversity branches to improve the signal to interference plus noise ratio (SINR) of the desired signal in each iteration. To clearly view the desired signal and interference components in each branch for a given ℓ and *r*, the input-output relation in (17) is rewritten for $n = 0,\ldots,N-1$ as

$$\begin{aligned}\widetilde{\mathbf{y}}_{m+\ell}^{(r)}[n] &= \sum_{t=1}^{n_{\mathrm{T}}}\sum_{\ell'} \widetilde{\mathbf{h}}_{m+\ell,\ell'}^{(r,t)}[n]\widetilde{\mathbf{x}}_{m+\ell-\ell'}^{(t)}[n] + \widetilde{\mathbf{w}}_{m+\ell}^{(r)}[n] \\ &= \widetilde{\mathbf{h}}_{m+\ell,\ell}^{(r,t)}[n]\widetilde{\mathbf{x}}_m^{(t)}[n] + \widetilde{\mathbf{v}}_{m,\ell}^{(r,t)}[n] + \widetilde{\mathbf{w}}_{m+\ell}^{(r)}[n] \end{aligned} \tag{18}$$

for $r = 1,\ldots,n_{\mathrm{R}}$ and $\ell \in \mathcal{L}^{(r,t)}$, where $\mathbf{w}_{m+\ell}^{(r)}$ is the AWGN noise vector, and the $N \times 1$ *interference vector*:

$$\begin{aligned}\widetilde{\mathbf{v}}_{m,\ell}^{(r,t)}[n] = &\underbrace{\sum_{\ell'\in\mathcal{L}^{(r,t)},\ell'\neq\ell} \widetilde{\mathbf{h}}_{m+\ell,\ell'}^{(r,t)}[n]\widetilde{\mathbf{x}}_{[m+\ell-\ell']_M}^{(t)}[n]}_{\text{inter-delay interference}} \\ &+ \underbrace{\sum_{t'\neq t}\sum_{\ell'\in\mathcal{L}^{(r,t')}} \widetilde{\mathbf{h}}_{m+\ell,\ell'}^{(r,t')}[n]\mathbf{x}_{[m+\ell-\ell']_M}^{(t')}[n]}_{\text{inter-antenna interference}} \end{aligned} \tag{19}$$

Let $\widetilde{\mathbf{b}}_{m,l}^{(r,t)}[n]$ be the interference-cancelled component of $\widetilde{\mathbf{x}}_m^{(t)}$ received in the ℓ-th delay branch of the (*r*, *t*)-th sub-channel:

$$\widetilde{\mathbf{b}}_{m,l}^{(r,t)}[n] = \widetilde{\mathbf{y}}_{m+\ell}^{(r)}[n] - \widetilde{\mathbf{v}}_{m,\ell}^{(r,t)}[n] \tag{20}$$

If the estimates of the transmitted time domain samples $\widetilde{\mathbf{x}}_m^{(t)}$ are available, then the interference $\widetilde{\mathbf{v}}_{m,\ell}^{(r,t)}$ can be computed from (19) and substituted in (20) to cancel the inter-antenna and inter-delay interference. However, since the information symbols are unknown at the receiver, the interference is only partially cancelled. To improve the SINR, we maximal ratio combine the received copies of $\widetilde{\mathbf{x}}_m^{(t)}$ in each iteration as:

$$\hat{\widetilde{\mathbf{x}}}_m^{(t)\{i\}}[n] = \frac{\sum_{r=1}^{n_{\mathrm{R}}}\sum_{\ell\in\mathcal{L}} \widetilde{\mathbf{h}}_{m+\ell,\ell}^{(r,t)*}[n]\mathbf{b}_{m,l}^{(r,t)\{i\}}[n]}{\sum_{r=1}^{n_{\mathrm{R}}}\sum_{\ell\in\mathcal{L}} |\widetilde{\mathbf{h}}_{m+\ell,\ell}^{(r,t)*}[n]|^2} \tag{21}$$

where $\widetilde{\mathbf{b}}_{m,l}^{(r,t)\{i\}}$ is the interference-cancelled copy of $\widetilde{\mathbf{x}}_m^{(t)}$ in the *i*-th iteration computed using the current estimates $\hat{\widetilde{\mathbf{x}}}_m^{(t)\{i\}}$. Let us define $\hat{\widetilde{\mathbf{y}}}_m^{(r)\{i\}}$ to be the reconstructed received waveform from the current estimates of the symbol-vectors:

$$\hat{\widetilde{\mathbf{y}}}_{m+\ell}^{(r)\{i\}}[n] = \sum_{r=1}^{n_{\mathrm{R}}}\sum_{\ell\in\mathcal{L}^{(r,t)}} \widetilde{\mathbf{h}}_{m+\ell,\ell}^{(r,t)}[n] \cdot \hat{\widetilde{\mathbf{x}}}_m^{(t)\{i\}}[n] \tag{22}$$

From (18) and (19), the interference-cancelled component in (20) of $\mathbf{x}_m^{(t)}$ in the $(i+1)$-th iteration can be written as

$$\mathbf{b}_{m,\ell}^{(r,t)\{i+1\}}[n] = \widetilde{\mathbf{h}}_{m+\ell,\ell}^{(r,t)}[n] \cdot \tilde{\mathbf{x}}_m^{(t)\{i\}}[n] + \Delta\widetilde{\mathbf{y}}_{m+\ell}^{(r)}[n] \tag{23}$$

where $\Delta\widetilde{\mathbf{y}}_{m+\ell}^{(r)} = \widetilde{\mathbf{y}}_{m+\ell}^{(r)}[n] - \hat{\widetilde{\mathbf{y}}}_{m+\ell}^{(r)\{i\}}[n] \in \mathbb{C}^{N\times 1}$ is the error in reconstructing the received DT waveform from current symbol-vector estimates. Substituting (23) in (21), we get the MRC estimate of the DT samples for the next iteration

$$\begin{aligned}\hat{\widetilde{\mathbf{x}}}_m^{(t)\{i+1\}}[n] &= \hat{\widetilde{\mathbf{x}}}_m^{(t)\{i\}}[n] \\ &\quad + \widetilde{\mathbf{d}}_m^{(t)}[n]\left(\sum_{r=1}^{n_{\mathrm{R}}}\sum_{\ell\in\mathcal{L}^{(r,t)}} \widetilde{\mathbf{h}}_{m+\ell,\ell}^{(r,t)*}[n]\cdot\Delta\widetilde{\mathbf{y}}_{m+\ell}^{(r)}[n]\right) \end{aligned} \tag{24}$$

where $\widetilde{\mathbf{d}}_m^{(t)}[n] = (\sum_{r=1}^{n_{\mathrm{R}}}\sum_{\ell\in\mathcal{L}^{(r,t)}} |\widetilde{\mathbf{h}}_{m+\ell,\ell}^{(r,t)}[n]|^2)^{-1}$. For the first iteration, we can assume all $\hat{\widetilde{\mathbf{x}}}_m^{(t)\{0\}}[n] = 0$ for $n = 0,\ldots,N-1$. Then, as each sample $\hat{\widetilde{\mathbf{x}}}_m^{(t)\{i\}}[n]$ is estimated, the $n_{\mathrm{R}}L$ reconstruction error samples $\Delta\widetilde{\mathbf{y}}_{m+\ell}^{(r)}[n]$ for $\ell \in \mathcal{L}^{(r,t)}$ and $r = 1,\ldots,n_{\mathrm{R}}$ need to be updated:

$$\Delta\widetilde{\mathbf{y}}_{m+\ell}^{(r)}[n] \leftarrow \Delta\widetilde{\mathbf{y}}_{m+\ell}^{(r)}[n] - \widetilde{\mathbf{h}}_{m+\ell,\ell}^{(r,t)}[n]\Delta\widetilde{\mathbf{x}}_m^{(t)\{i+1\}}[n] \tag{25}$$

where $\Delta\widetilde{\mathbf{x}}_m^{(t)\{i+1\}}[n] = \hat{\widetilde{\mathbf{x}}}_m^{(t)\{i+1\}}[n] - \hat{\widetilde{\mathbf{x}}}_m^{(t)\{i\}}[n]$.

From (16), the estimated DD information symbol-vectors at the end of *i*-th iteration is given by

$$\hat{\mathbf{x}}_m^{(t)\{i+1\}} = \hat{\mathbf{x}}_m^{(t)\{i\}} + \mathbf{F}_N \cdot \Delta\widetilde{\mathbf{x}}_m^{(t)\{i+1\}} \tag{26}$$

followed by a hard-decision $\mathcal{D}(\hat{\mathbf{x}}_m^{(t)\{i\}})$ on the symbol-vectors to get the QAM estimates. To improve convergence speed, we use a weighted average of the DD information symbol estimate with its hard decision as: $\hat{\mathbf{x}}_m^{(t)\{i\}} \leftarrow (1-\delta)\hat{\mathbf{x}}_m^{(t)\{i\}} +$

Authorized licensed use limited to: Monash University. Downloaded on March 22,2022 at 09:30:39 UTC from IEEE Xplore. Restrictions apply.

$\delta\mathcal{D}(\hat{\mathbf{x}}_m^{(t)\{i\}})$. The iterations are stopped when the residual error does not decrease any more or when the maximum number of iteration is reached.

A. Optimal Combining Weights for Spatial Correlation at Rx

It is well known that MRC is optimal when the noise in the combining diversity branches is uncorrelated, [10], [11]. However in MIMO, due to spatial correlation, the interference in the diversity branches are correlated, resulting in performance degradation with MRC. In such scenarios, a whitening filter can be applied at the Rx to decorrelate the diversity branches. The MRC weights then need to be optimized to match the SINR of the whitened diversity branches. In this work, we consider only the correlation between the Rx antennas and assume that a whitening filter is applied at the Tx to mitigate the effect of the Tx correlation.

Assuming the Rx correlation matrix is known, we first group the combining weights corresponding to the $n_{\mathrm{R}}L$ diversity branches $\widetilde{\mathbf{h}}_{m+\ell,\ell}^{(r,t)}[n]$ for $\ell \in \mathcal{L}$ and $r \in \{1,\ldots,n_{\mathrm{R}}\}$ in (24) into *L antenna weight vectors* of length n_{R}. The purpose of this grouping is to separate the diversity branches into correlated and uncorrelated branches. The combining step in (24) can be written in terms of the $n_{\mathrm{R}}\times 1$ *antenna weight vectors* for the ℓ-th delay branch with entries $\widetilde{\mathbf{h}}_{m,n,\ell}^{(t)}[r] = \widetilde{\mathbf{h}}_{m+\ell,\ell}^{(r,t)}[n]$, as

$$\Delta\widetilde{\mathbf{x}}_m^{(t)\{i+1\}}[n] = \frac{\sum_\ell \widetilde{\mathbf{h}}_{m,n,\ell}^{(t)\dagger}\Delta\widetilde{\mathbf{y}}_{m+\ell,n}}{\sum_\ell \widetilde{\mathbf{h}}_{m,n,\ell}^{(t)\dagger}\widetilde{\mathbf{h}}_{m,n,\ell}^{(t)}} \tag{27}$$

where the $n_{\mathrm{R}}\times 1$ corresponding *antenna residual error vector* with components $\Delta\widetilde{\mathbf{y}}_{m+\ell,n}[r] = \Delta\widetilde{\mathbf{y}}_{m+\ell}^{(r)}[n]$ for $1 \le r \le n_{\mathrm{R}}$.

We assume that the channel coefficients corresponding to different delay branches are uncorrelated, i.e., $\mathrm{E}[\widetilde{\mathbf{h}}_{m,n,\ell}^{(t)\dagger}\widetilde{\mathbf{h}}_{m,n,\ell'}^{(t)}] = 0$ for $\ell \neq \ell'$. However, due to correlation between the receiver antennas, the components of each antenna weight vector are correlated, i.e., $\mathbf{R}_{\mathrm{rx}} = \mathrm{E}[\widetilde{\mathbf{h}}_{m,n,\ell}^{(t)}\widetilde{\mathbf{h}}_{m,n,\ell}^{(t)\dagger}]$ has non-zero off-diagonal elements.

To alleviate performance loss, the antenna residual error vectors and the antenna weight vectors must be decorrelated before employing the MRC, [11]. To this end, consider the Cholesky decomposition of the covariance matrix $\mathbf{R}_{\mathrm{rx}} = \mathbf{C}_{\mathrm{rx}}\cdot\mathbf{C}_{\mathrm{rx}}^{\dagger}$, where $\mathbf{C}_{\mathrm{rx}}$ is the *correlation-shaping matrix*. Let $\mathbf{W}_{\mathrm{rx}} = \mathbf{C}_{\mathrm{rx}}^{-1}$ be the *whitening matrix*. Then, the antenna weight and residual error vectors in (27) can be replaced with the corresponding whitened vectors as

$$\widetilde{\mathbf{h}}_{m,n,\ell}^{(t)} \leftarrow \mathbf{W}_{\mathrm{rx}}\cdot\widetilde{\mathbf{h}}_{m,n,\ell}^{(t)}, \quad \Delta\widetilde{\mathbf{y}}_m^n \leftarrow \mathbf{W}_{\mathrm{rx}}\cdot\Delta\widetilde{\mathbf{y}}_m^n \tag{28}$$

The MRC combining operation in (27) is modified to include the decorrelation operation in (28) as

$$\Delta\widetilde{\mathbf{x}}_m^{(t)\{i+1\}}[n] = \frac{\sum_\ell \widetilde{\mathbf{h}}_{m,n,\ell}^{(t)\dagger}\cdot\mathbf{R}_{\mathrm{rx}}^{-1}\cdot\Delta\widetilde{\mathbf{y}}_{m+\ell,n}}{\sum_\ell \widetilde{\mathbf{h}}_{m,n,\ell}^{(t)\dagger}\cdot\mathbf{R}_{\mathrm{rx}}^{-1}\cdot\widetilde{\mathbf{h}}_{m,n,\ell}^{(t)}} \tag{29}$$

If we assume that the Rx has no prior knowledge of the correlation parameters, the correlation matrix can be estimated at the Rx for each frame. First the channel between all Tx-Rx pairs are estimated based on the single pilot method proposed in [2]. The correlation between the channel observed at the r-th and r'-th Rx antennas is computed from the estimated DT channel coefficients for $r, r' \in \{1,\ldots n_{\mathrm{R}}\}$ as

$$\hat{\mathbf{R}}_{\mathrm{rx}}[r,r'] = \mathrm{E}[\hat{\widetilde{\mathbf{h}}}_{m,l}^{(r',t)\dagger}\hat{\widetilde{\mathbf{h}}}_{m,l}^{(r,t)}] \propto \sum_{t=1}^{n_{\mathrm{T}}}\sum_{\ell\in\mathcal{L}}\sum_{m=0}^{M-1}\frac{\hat{\widetilde{\mathbf{h}}}_{m,\ell}^{(r',t)\dagger}\hat{\widetilde{\mathbf{h}}}_{m,\ell}^{(r,t)}}{|\hat{\widetilde{\mathbf{h}}}_{m,\ell}^{(r',t)}|\,|\hat{\widetilde{\mathbf{h}}}_{m,\ell}^{(r,t)}|}. \tag{30}$$

Detection Complexity: We now discuss the complexity of the proposed detection method. The core steps of the MRC method without the whitening operation are (25) and (27), and with whitening are (25) and (29). To distinguish both the methods, we will refer to the method using (27) as 'MRC' and the one with (29) as 'MRCw'. The operation in (25) requires $n_{\mathrm{R}}L$ complex multiplications (CM) per transmitted information symbol per iteration. The denominator of (27) and (29) needs to calculated only once and requires $n_{\mathrm{R}}L$ CM and $(n_{\mathrm{R}}^2+n_{\mathrm{R}})L$ CM, respectively. The term $\widetilde{\mathbf{h}}_{m,n,\ell}^{(t)\dagger}\cdot\hat{\mathbf{R}}_{\mathrm{rx}}^{-1}$ is computed only once and reused for all iterations. The estimation of $\mathbf{R}_{\mathrm{rx}}$ in (30) and then $\mathbf{R}_{\mathrm{rx}}^{-1}$ requires $3NMn_{\mathrm{T}}n_{\mathrm{R}}L + O(n_{\mathrm{R}}^3)$ CMs. Then. the numerator in both (27) and (29) requires only $n_{\mathrm{R}}L$ CM per transmitted information symbol per iteration. At the end of each iteration the hard decision estimates in (26) requires $n_{\mathrm{T}}MN\log_2(N)$ CMs per iteration.

Assuming S iterations are required, the overall number of CMs required for detecting all information symbols including the correlation matrix estimation operation is $n_{\mathrm{T}}NM[(4n_{\mathrm{R}}+n_{\mathrm{R}}^2)L + S(3n_{\mathrm{R}}L + 2\log_2 N + 1)] + O(n_{\mathrm{R}}^3)$ CMs. This is significantly lower than the complexity of detection in MP ($O(n_{\mathrm{T}}n_{\mathrm{R}}^2NMSP^2Q)$) and linear minimum mean square error (LMMSE) ($O((n_{\mathrm{T}}n_{\mathrm{R}}NM)^3)$) detectors.

IV. Simulation Results and Discussion

In this section, we present the uncoded BER performance of MIMO-OTFS[1] with the proposed detector and compare it with the MP and LMMSE detection methods. We generate OTFS frames of size $N = M = 32$. The sub-carrier spacing Δf is taken as 15 kHz, and the carrier frequency is set to 4 GHz. The number of paths in the channel $P^{(r,t)}$ is taken to be 5 with an uniform power delay profile with the set of delay taps $\mathcal{L}^{(r,t)} = \{0,\ldots,4\}$ and the Doppler shift for each path $\nu_i = \nu_{\max}\cos\theta_i$, with θ_i uniformly distributed over $(-\pi,\pi)$, where $\nu_{\max}$ is the maximum Doppler shift corresponding to a maximum UE speed of 500 km/hr. For BER plots, 10^5 frames are sent for every point in the BER curve. In Figs. 1 and 2, we assume perfect knowledge of the channel at the receiver.

In Fig. 1, we present the 4-QAM BER performance of OTFS-MIMO with the proposed MRC detector and compare it with MP and LMMSE detectors. The maximum number of iterations is set to 20 for both MRC (with $\delta = 0.125$) and MP. The MIMO-OFDM performance with LMMSE detector is plotted alongside to show the superior performance of OTFS in high mobility channels. It can be observed that even though MP offers slightly better performance at very low SNR, MRC performs better at high SNR for the same number of iterations. We observed via simulations that both MP and MRC performance improve allowing for more iterations.

Fig. 2 shows the 2×2 and 4×4 MIMO-OTFS performance of MRC compared with LMMSE and MPA detectors for different values of Rx spatial correlation (ρ_{rx}). The curves labelled as 'MRCw' denote the proposed detector with

[1] We consider *N* ZPs per frame, noting that when practical channel estimation is used, this results in the same overhead as OTFS with a single CP per frame since the ZPs are used anyway as part of the guard symbols around the pilot.

Authorized licensed use limited to: Monash University. Downloaded on March 22,2022 at 09:30:39 UTC from IEEE Xplore. Restrictions apply.

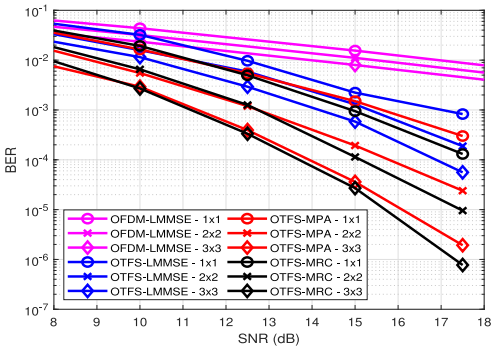

Fig. 1. 4-QAM MIMO-OTFS uncoded BER performance for MRC detector compared with LMMSE and MP detectors for a frame size of $N = M = 32$ for different number of antennas.

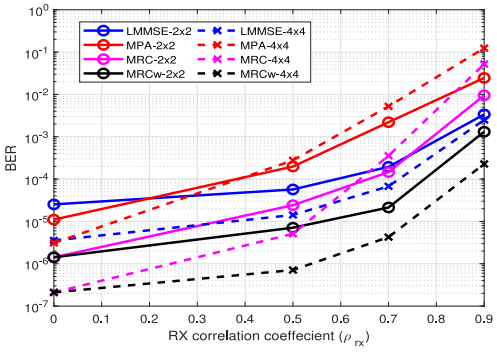

Fig. 2. 4-QAM 2×2 and 4×4 MIMO-OTFS uncoded BER performance at a SNR of 20 dB for a frame size of $N = M = 32$ for different Rx correlation levels ρ_{rx}.

combining weights optimized according to the estimated Rx correlation matrix in (29), while 'MRC' denotes the curves without the use of the whitening matrices for combining using (27). It can be observed that spatial correlation degrades the performance of all the detectors. However the proposed MRCw detector offers the best performance followed by the LMMSE detection. Both the MPA and MRC detection suffer some degradation in spatially correlated channels.

Fig. 3 presents the 4-QAM 2×2 MIMO-OTFS BER performance for low $(\rho_{\mathrm{rx}} = 0)$ and high $(\rho_{\mathrm{rx}} = 0.9)$ correlation at the Rx. We consider practical channel estimation, where the channel coefficients are obtained using the single pilot method proposed in [2], [12]. The pilot symbol energy for each OTFS frame is given as $E_{\mathrm{p}} = \beta E_{\mathrm{s}}$, where E_{s} is the average symbol energy. The LMMSE detection performance is plotted alongside for comparison. The quality of the channel estimation depends on the pilot power as observed in this figure. It can be observed that the MRCw detector offers around 5dB gain compared to LMMSE for the same excess pilot power $\beta = 30dB$ for both low and high correlation at the Rx. For the perfect CSI case (dashed lines), it can be noted for both MRCw and LMMSE, that a spatial correlation of 0.9 causes a performance degradation of around 7 dB due to reduction in available space diversity as compared to the case with no correlation. In both cases MRCw gains 2dB over LMMSE at a much lower complexity.

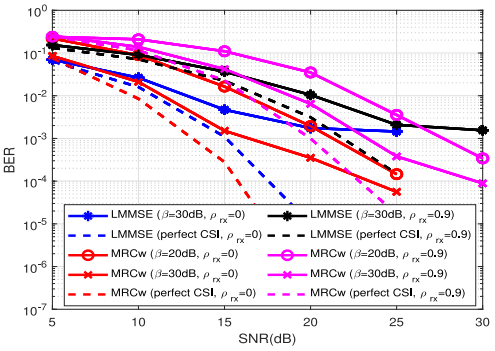

Fig. 3. 4-QAM 2×2 MIMO OTFS uncoded BER performance with MRC and LMMSE detector for a frame size of $N = M = 32$ for excess pilot power (β) and Rx spatial correlation coefficient $\rho_{\mathrm{rx}} = 0$ and $\rho_{\mathrm{rx}} = 0.9$.

V. Conclusion

In this letter, we proposed a low complexity detection method for MIMO-OTFS based on the MRC principle. The detection complexity was shown to be linear in number of information symbols and the number of receive and transmit antennas. We showed that the detector offers better error performance than MP and LMMSE detection methods with significantly lower complexity even with spatially correlated channels and practical channel estimation.

References

[1] R. Hadani *et al.*, "Orthogonal time frequency space modulation," in *Proc. IEEE Wireless Commun. Netw. Conf. (WCNC)*, San Francisco, CA, USA, Mar. 2017, pp. 1–6.

[2] M. K. Ramachandran and A. Chockalingam, "MIMO-OTFS in high-doppler fading channels: Signal detection and channel estimation," in *Proc. IEEE Global Commun. Conf. (GLOBECOM)*, Abu Dhabi, UAE, Dec. 2018, pp. 206–212.

[3] R. M. Augustine, G. D. Surabhi, and A. Chockalingam, "Space-time coded OTFS modulation in high-doppler channels," in *Proc. IEEE 89th Veh. Tech. Conf. (VTC)*, May 2019, pp. 1–6.

[4] G. D. Surabhi and A. Chockalingam, "Low-complexity linear equalization for 2×2 MIMO-OTFS signals," in *Proc. IEEE 21st Int. Workshop Signal Process. Adv. Wireless Commun. (SPAWC)*, 2020, pp. 1–5.

[5] A. Rezazadehreyhani, A. Farhang, M. Ji, R. R. Chen, and B. Farhang-Boroujeny, "Analysis of discrete-time MIMO OFDM-based orthogonal time frequency space modulation," in *Proc. IEEE Int. Conf. Commun. (ICC)*, May 2018, pp. 1–6.

[6] B. C. Pandey, S. K. Mohammed, P. Raviteja, Y. Hong, and E. Viterbo, "Low complexity precoding and detection in multi-user massive MIMO OTFS downlink," *IEEE Trans. Veh. Technol.*, vol. 70, no. 5, pp. 4389–4405, May 2021.

[7] P. Singh, H. B. Mishra, and R. Budhiraja, "Low-complexity linear MIMO-OTFS receivers," in *Proc. IEEE Int. Conf. Commun. Workshops (ICC Workshops)*, Jun. 2021, pp. 1–6.

[8] S. L. Loyka, "Channel capacity of MIMO architecture using the exponential correlation matrix," *IEEE Commun. Lett.*, vol. 5, no. 9, pp. 369–371, Sep. 2001.

[9] T. Thaj and E. Viterbo, "Low complexity iterative rake decision feedback equalizer for zero-padded OTFS systems," *IEEE Trans. Veh. Technol.*, vol. 69, no. 12, pp. 15606–15622, Dec. 2020.

[10] D. G. Brennan, "Linear diversity combining techniques," *Proc. IRE*, vol. 47, pp. 1075–1102, Jun. 1959.

[11] X. Dong and N. C. Beaulieu, "Optimal maximal ratio combining with correlated diversity branches," *IEEE Commun. Lett.*, vol. 6, no. 1, pp. 22–24, Jan. 2002.

[12] P. Raviteja, K. T. Phan, and Y. Hong, "Embedded pilot-aided channel estimation for OTFS in delay–Doppler channels," *IEEE Trans. Veh. Technol.*, vol. 68, no. 5, pp. 4906–4917, May 2019.

Authorized licensed use limited to: Monash University. Downloaded on March 22,2022 at 09:30:39 UTC from IEEE Xplore. Restrictions apply.

Chapter 5

Orthogonal Time Sequency Multiplexing Modulation: Analysis and Low-Complexity Receiver Design

Citing info:

T. Thaj, E. Viterbo and Y. Hong, "Orthogonal Time Sequency Multiplexing Modulation: Analysis and Low-Complexity Receiver Design" in *IEEE Transactions on Wireless Communications*, vol. 20, no. 12, pp. 7842-7855, Dec. 2021, doi: 10.1109/TWC.2021.3088479.

Publishing Journal Info:

Impact factor: 7.016, CiteScore: 15.2, JCI ranked 9/105 (category TELECOMMUNICATIONS)

Copyright Statement:

©[2019] IEEE. Reprinted, with permission, from [Tharaj Thaj, Emanuele Viterbo, Yi Hong, Orthogonal Time Sequency Multiplexing Modulation: Analysis and Low-Complexity Receiver Design, IEEE Transactions on Wireless Communications (TWC),

2021]

7842 IEEE TRANSACTIONS ON WIRELESS COMMUNICATIONS, VOL. 20, NO. 12, DECEMBER 2021

Orthogonal Time Sequency Multiplexing Modulation: Analysis and Low-Complexity Receiver Design

Tharaj Thaj, *Graduate Student Member, IEEE*, Emanuele Viterbo, *Fellow, IEEE*, and Yi Hong, *Senior Member, IEEE*

***Abstract*— This paper proposes *orthogonal time sequency multiplexing (OTSM)*, a novel single carrier modulation scheme that places information symbols in the delay-sequency domain followed by a cascade of time-division multiplexing (TDM) and Walsh-Hadamard sequence multiplexing. Thanks to the Walsh Hadamard transform (WHT), the modulation and demodulation do not require complex domain multiplications. For the proposed OTSM, we first derive the input-output relation in the delay-sequency domain and present a low complexity detection method taking advantage of zero-padding. We demonstrate via simulations that OTSM offers high performance gains over orthogonal frequency division multiplexing (OFDM) and similar performance to orthogonal time frequency space (OTFS), but at lower complexity owing to WHT. Then we propose a low complexity time domain channel estimation method. Finally, we show how to include an outer error control code and a turbo decoder to improve error performance of the coded system.**

***Index Terms*— OTFS, Walsh Hadamard transform, orthogonal time sequency multiplexing, delay–sequency, detector, channel estimation, delay–Doppler channel, turbo decoder.**

I. Introduction

ORTHOGONAL frequency division multiplexing (OFDM) is the physical-layer modulation scheme deployed in 4G and 5G mobile systems, where the wireless channel typically exhibits time-varying multipath fading due to mobility. OFDM is known to achieve a near-capacity performance over such channels when the Doppler effect is limited [1]–[3], but suffers from severe performance degradation in high-mobility environments [4]. Hence, new modulation techniques that are robust in both slow and fast time-varying channels are needed.

Recently, orthogonal time frequency space (OTFS) modulation has been proposed in [4], showing significant advantages over OFDM in high-mobility environments. OTFS places information symbols in the delay-Doppler (DD) domain to capture the channel geometry that models mobile terminals and reflectors in a high mobility scene. Leveraging on this representation, the OTFS modulator multiplexes each information symbol over 2D orthogonal basis functions (IFFT along Doppler and FFT along delay), which span across the entire time–frequency domain required to transmit a frame. The set of basic functions is designed to combat the dynamics of the time-varying multipath channel.[1] Further, it was shown in [5] that any 2-D orthogonal transformation (precoding) with *constant modulus* basis functions operating on the time-frequency domain enables the receiver to exploit maximum time-frequency diversity. Since the Fourier basis are constant modulus, OTFS guarantees that the information symbols experience the same signal-to-noise ratio (SNR). In the recent few years, there has been a number of efforts dedicated to the development of OTFS (e.g. [5]–[21] and references therein).

In this paper, we propose a novel single-carrier modulation scheme: *orthogonal time sequency multiplexing* (OTSM). The key idea is to multiplex information symbols in the *delay-sequency* domain, rather than the DD domain of OTFS, where *sequency* is defined as the number of zero-crossings per unit time interval[2] [22], [23]. Specifically, OTSM transforms the information symbols placed in the *delay-sequency domain* into the *delay-time domain*, followed by time domain signal transmission and reception. Such domain transformation is realized by using the inverse Walsh-Hadamard transform (IWHT) along the sequency domain, instead of IFFT along the Doppler domain in OTFS, as shown in Fig. 1. In such a way, OTSM allows channel delay spread and Doppler spread to cause inter-symbol interference (ISI) along the delay and sequency dimensions, respectively, while remaining *separable* at the receiver, like in OTFS [4], [17]. Note that this separability cannot be achieved by OFDM, since channel delay spread and Doppler spread jointly cause interference in OFDM along the frequency dimension. Hence, single-tap equalization fails due to the loss of orthogonality between the OFDM sub-carriers. Our single carrier OTSM scheme uses only 1-D orthogonal WHT transform and is different from the multi-carrier OTFS schemes in [5], where arbitrary 2-D unitary transform (such as

Manuscript received December 12, 2020; revised April 12, 2021; accepted June 7, 2021. Date of publication June 18, 2021; date of current version December 10, 2021. This work was supported by the Australian Research Council under Discovery Project DP200100096. The associate editor coordinating the review of this article and approving it for publication was M. Xiao. *(Corresponding author: Yi Hong.)*

The authors are with the Department of Electrical and Computer Systems Engineering, Monash University at Clayton, Clayton, VIC 3800, Australia (e-mail: tharaj.thaj@monash.edu; emanuele.viterbo@monash.edu; yi.hong@monash.edu).

Color versions of one or more figures in this article are available at https://doi.org/10.1109/TWC.2021.3088479.

Digital Object Identifier 10.1109/TWC.2021.3088479

[1] A similar scheme to OTFS was independently proposed in [25] for underwater acoustic communications.

[2] In the case of discrete Walsh functions, sequency denotes the number of sign changes per unit time.

1536-1276 © 2021 IEEE. Personal use is permitted, but republication/redistribution requires IEEE permission.
See https://www.ieee.org/publications/rights/index.html for more information.

Authorized licensed use limited to: Monash University. Downloaded on March 22,2022 at 09:29:49 UTC from IEEE Xplore. Restrictions apply.

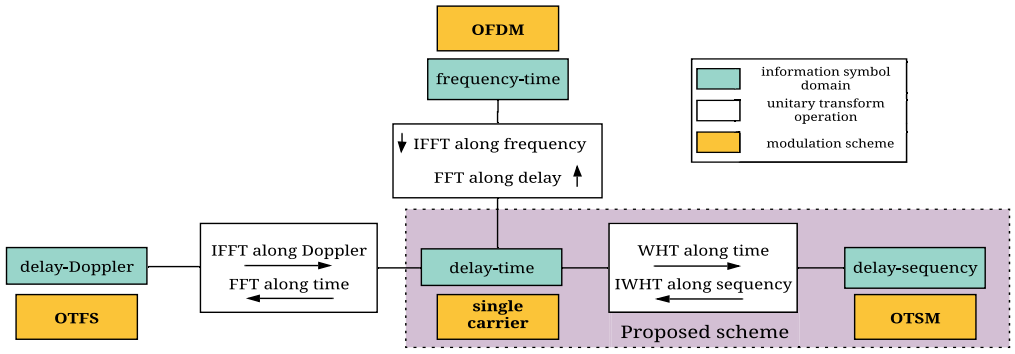

Fig. 1. Relation between the different discrete information symbol domains and the corresponding modulation schemes.

DFT, WHT, discrete prolate spheroidal sequences) is applied to the time-frequency domain.

For the proposed OTSM modulation, we derive its delay-sequency domain input-output relation and present a low complexity detection scheme.[3] Similar to OTFS, we find that OTSM's information symbols experience approximately the same SNR at the receiver, thanks to the constant modulus WHT. As a result, OTSM offers similar performance to OTFS in both static and high mobility channels, but at *lower complexity*, since WHT only requires addition and subtraction operations.

Further, we introduce the use of zero-padding (ZP) between every block in the time domain to avoid inter-block interference to reduce the detection complexity and to simultaneously allow for the insertion of pilots for channel estimation. Then we propose a low complexity *time domain* channel estimation method based on reconstruction of the delay-time channel from the time domain pilots.[4] We compare the performance of OTFS and OTSM using the delay-time channel reconstruction method and observe that they offer similar performance. Finally, we show how an outer error-correcting code can be used to improve the error performance and reduce the pilot power required for accurate detection.

Overall, the proposed OTSM modulation offers the following advantages. The OTSM transceiver has low complexity (appealing for hardware implementation), but achieves the advantages of a multi-carrier system without sacrificing performance. Similar to OTFS, OTSM can be easily overlaid on top of existing OFDM based systems, where time-frequency samples can be generated using the relations given in Fig. 1 (IWHT and FFT) and then transmitted as an OFDM signal. Different from other single carrier and OFDM systems, OTSM has excellent performance in the presence of multiple Doppler paths, making it suitable for high mobility and under-water acoustic wireless communications.

Due to the use of WHTs, the time domain samples take integer values if the information symbols are integer. Hence, a smaller number of bits may be used to represent the transmit signal without incurring any quantization error. Thanks to this feature, OTSM is suitable for integer forcing linear receivers with significantly reduced complexity [27].

Channel estimation benefits from using a sparse representation of the channel. In OTFS, the delay-Doppler domain offers such sparse representation, when the channel Doppler shifts are integer multiples of the receiver Doppler resolution. However, the sparsity reduces significantly with fractional Doppler shifts, which are commonly present in the channel. The sequency domain may offer a sparsity similar to the one of OTFS with fractional Doppler in all cases.

The rest of the paper is organized as follows. In Section II, we discuss the basic OTSM concepts. In Section III, we present the OTSM system model followed by comparison with the OTFS scheme in Section IV. In Section V, we present a low complexity detection scheme. In Section VI, we propose a time domain channel estimation algorithm for OTSM. We further propose a turbo decoder for OTSM in Section VII. Section VIII presents the simulation results and discussions followed by our concluding remarks in Section IX.

Notations: The following notations are used: a, $\mathbf{a}$, $\mathbf{A}$ represent a scalar, vector, and matrix, respectively; $\mathbf{a}(n)$ and $\mathbf{A}(m,n)$ represent the n-th and (m,n)-th element of $\mathbf{a}$ and $\mathbf{A}$, respectively; $\mathbf{A}^{\dagger}$, $\mathbf{A}^{*}$ and $\mathbf{A}^{n}$ represent the Hermitian transpose, complex conjugate and n-th power of $\mathbf{A}$. The set of $M \times N$ dimensional matrices with complex entries are denoted by $\mathbb{C}^{N\times M}$. Let $\circledast$ represent circular convolution, $\otimes$, the Kronecker product, $\circ$, the Hadamard product (i.e., the element wise multiplication) and, $\oslash$, the Hadamard division (i.e., the element wise division). Let $[.]_M$ denote the modulo-M operation, $|\mathcal{S}|$ the cardinality of the set $\mathcal{S}$, $\mathrm{tr}(A)$, the trace of the square matrix $\mathbf{A}$, $\mathrm{vec}(\mathbf{A})$, the column-wise vectorization of the matrix $\mathbf{A}$ and $\mathrm{vec}^{-1}_{N,M}(\mathbf{a})$ is the matrix formed by folding a vector $\mathbf{a}$ into a $N \times M$ matrix by filling it column wise. Let $\mathbf{F}_N$ and $\mathbf{W}_N$ be the normalized N point discrete Fourier transform (DFT) matrix and the normalized N-point WHT matrix, respectively.

II. Background

Traditionally the communication theory has been based on the complete orthogonal set of sine and cosine functions. The

[3] A preliminary version of the detection scheme was presented in [26].

[4] Note that the proposed channel estimation can also be employed for OTFS systems.

Authorized licensed use limited to: Monash University. Downloaded on March 22,2022 at 09:29:49 UTC from IEEE Xplore. Restrictions apply.

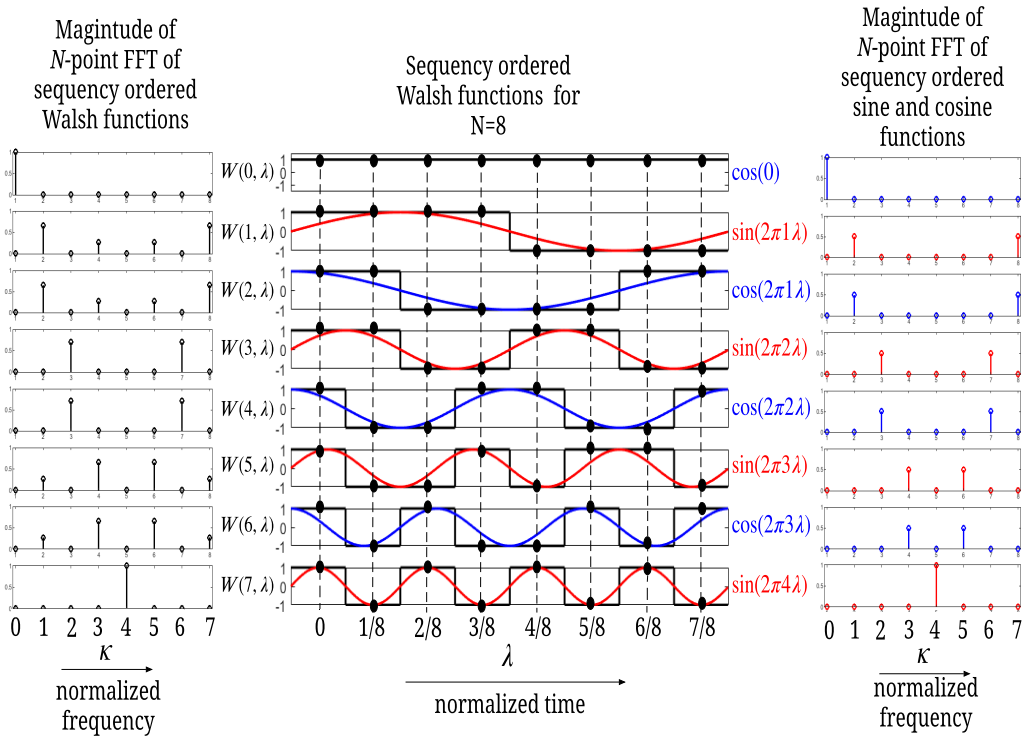

Fig. 2. The N-point discrete spectrum of sequency-ordered Walsh basis functions (black) vs sequency-ordered Fourier basis functions (red and blue), where $N = 8$. Vertical dashed lines represent sampling times.

concept of *frequency* is a consequence of these basis functions being periodic and hence characterized by distinct frequencies. Even though frequency domain representation of signals offers several advantages including close resemblance to the physical channel models, there are other basis functions that can equally be used to represent a signal. The Walsh functions, introduced by Joseph L. Walsh in 1923, constitute another *complete set* of orthogonal functions, which assume only the values '+1' and '−1'. This means that almost any waveform can be uniquely synthesized to any desired degree of accuracy by a linear combination of Walsh functions, [22], [23]. There are a number of formal definitions of Walsh functions in the literature. In this paper, we are primarily concerned with the sequency-ordered Walsh functions.

A. Sequency Vs Frequency

In 1969, Harmuth introduced the concept of sequency as the number of zero crossings per unit time, [22]. Since Walsh functions are aperiodic, they cannot be represented using a single frequency index, but they can be uniquely identified by a *sequency* index, [23]. The continuous Walsh functions over the interval $0 \leq \lambda < 1$ will be denoted by $W(n, \lambda)$, where the sequency index $n = 0, \ldots, N-1$. The corresponding Fourier basis functions in the unit interval are given by $\sin(2\pi\kappa\lambda)$ and $\cos(2\pi\kappa\lambda)$, where κ represents the frequency index.

Fig. 2 shows the first 8 sequency-ordered continuous Walsh functions. For comparison, the Fourier basis functions (blue and red) are plotted alongside the sequency ordered Walsh functions (black). It can be easily observed that the sequency of the sine and cosine Fourier basis functions are related to the odd and even sequency continuous Walsh basis functions, since they have the same sequency (i.e., same number of zero crossings). Since we are dealing with discrete-time, we consider the samples $W(n, m/N + 0.5/N)$, where $m = 0, \ldots, N-1$ denotes the index of sampling points (shown by the vertical dashed lines in Fig. 2) of the n-th sequency Walsh basis function. The elements of the normalized WHT matrix are related to these samples as $\mathbf{W}_N(n, m) = (1/\sqrt{N})W(n, m/N + 0.5/N)$. In Fig. 2, we compare the magnitude of the 8-point discrete frequency spectrum of the Walsh (left) and Fourier (right) basis functions. We notice that Walsh basis functions have $1, 2$, or 4 non-zero spectral lines, while Fourier basis functions only have 1 or 2 non-zero spectral lines. In general, due to the even/odd symmetries, the spectra of Walsh functions can spread across at most $N/2$ frequency indices. This implies that information symbols multiplexed on a single Walsh basis function are spread over multiple Fourier basis functions and vice versa. Further, the two dominant spectral lines of the Walsh functions coincide with the ones of the Fourier harmonics. One advantage of Walsh basis functions over Fourier basis functions is the compactness

Authorized licensed use limited to: Monash University. Downloaded on March 22,2022 at 09:29:49 UTC from IEEE Xplore. Restrictions apply.

of the sequency domain representation of a time-series with sharp discontinuities, when "it makes little sense to correlate the data with smooth sine and cosine waves" [23].

B. Dyadic Vs Cyclic Convolution

We discuss an important property differentiating the DFT and WHT, which will be used in deriving the delay-sequency domain input-output relations, as well as in comparing OTSM with OTFS. One of the most widely used applications of the DFT is its convolution and multiplication property. It is well known that the product of a pair of functions is equal to the cyclic convolution of their Fourier transforms and vice versa. Given two N length vectors $\mathbf{a}$ and $\mathbf{b}$. The circular convolution between these two vectors is defined as

$$(\mathbf{a} \circledast \mathbf{b})(n) = \sum_{k=0}^{N-1} \mathbf{a}(k)\mathbf{b}([n-k]_N) \tag{1}$$

The multiplication property for DFT can be written as

$$\mathbf{F}_N \cdot (\mathbf{a} \circledast \mathbf{b}) = (\mathbf{F}_N \cdot \mathbf{a}) \circ (\mathbf{F}_N \cdot \mathbf{b}) \tag{2}$$

Similarly, WHT converts the product of two functions into the dyadic convolution of its transforms and vice versa [28]. The dyadic convolution between two N length vectors $\mathbf{a}$ and $\mathbf{b}$ is defined as

$$(\mathbf{a} \circledbslash \mathbf{b})(n) = \sum_{k=0}^{N-1} \mathbf{a}(k)\mathbf{b}(n \oplus k) \tag{3}$$

where $(n \oplus k)$ represents the decimal number corresponding to the result of XOR of the binary representation of n and k. The multiplication property for WHT can be written as

$$\mathbf{W}_N \cdot (\mathbf{a} \circledbslash \mathbf{b}) = (\mathbf{W}_N \cdot \mathbf{a}) \circ (\mathbf{W}_N \cdot \mathbf{b}) \tag{4}$$

III. OTSM System Model

A. Transmitter and Receiver Operation

Let $\mathbf{x}, \mathbf{y} \in \mathcal{C}^{NM\times 1}$ be the transmitted and received information symbols. The total frame duration and bandwidth of the transmitted OTSM signal frame are $T_f = NT$ and $B = M\Delta f$, respectively, where $\Delta f = 1/T$, i.e., the signal is critically sampled for any pulse shaping waveform, and N is chosen to be a power of 2. Fig. 3 shows the OTSM step-by-step transceiver operation.

1) Transmitter: As illustrated in Fig. 3, at the transmitter, the information symbols $\mathbf{x} = [\mathbf{x}_0^{\mathrm{T}}, \cdots, \mathbf{x}_{M-1}^{\mathrm{T}}]^{\mathrm{T}}$ are split into vectors $\mathbf{x}_m \in \mathbb{C}^{N\times 1}$, $m = 0, \ldots, M-1$. The symbol vectors are arranged into a *delay-sequency* matrix $\mathbf{X} \in \mathbb{C}^{M\times N}$

$$\mathbf{X} = [\mathbf{x}_0, \mathbf{x}_1, \ldots, \mathbf{x}_{M-1}]^{\mathrm{T}} \tag{5}$$

where the matrix column and row indices represent the delay and sequency indices of the delay-sequency grid, respectively. Then, a N-point WHT is applied on each of these symbol vectors (rows) to transform it to the delay-time domain

$$\tilde{\mathbf{X}} = [\tilde{\mathbf{x}}_0, \tilde{\mathbf{x}}_1, \ldots, \tilde{\mathbf{x}}_{M-1}]^{\mathrm{T}} = \mathbf{X} \cdot \mathbf{W}_N. \tag{6}$$

The matrix $\tilde{\mathbf{X}}$ contains the delay-time samples which are column-wise vectorized to obtain the time domain samples $\mathbf{s} \in \mathbb{C}^{NM\times 1}$ to be transmitted into the physical channel

$$\mathbf{s} = \mathrm{vec}(\tilde{\mathbf{X}}). \tag{7}$$

The transmitter operation above can be expressed in the simple matrix form as

$$\mathbf{s} = \mathbf{P} \cdot (\mathbf{I}_M \otimes \mathbf{W}_N) \cdot \mathbf{x} \tag{8}$$

where $\mathbf{P}$ is the row-column interleaver matrix. Such permutation is known in the literature as a *perfect shuffle,* and has the following property [30]:

$$\mathbf{A} \otimes \mathbf{B} = \mathbf{P} \cdot (\mathbf{B} \otimes \mathbf{A}) \cdot \mathbf{P}^{\mathrm{T}} \tag{9}$$

for given square matrices $\mathbf{A}$ and $\mathbf{B}$. Using the perfect shuffle property in (9), the transmitter operation in (8) can be simplified as

$$\mathbf{s} = (\mathbf{W}_N \otimes \mathbf{I}_M) \cdot (\mathbf{P} \cdot \mathbf{x}) \tag{10}$$

A CP of length $l_{\max}$ is added to the time domain samples, which are pulse shaped, digital-to-analog converted, and transmitted into the wireless channel as $s(t)$.

2) Receiver: At the receiver, the received time domain signal $r(t)$ is processed via analog to digital conversion (ADC) and CP removal, yielding time domain vector $\mathbf{r} \in \mathbb{C}^{NM\times 1}$. The received time domain samples $\mathbf{r}$ are folded into the matrix $\tilde{\mathbf{Y}}$ column-wise as

$$\tilde{\mathbf{Y}} = [\tilde{\mathbf{y}}_0, \tilde{\mathbf{y}}_1, \ldots, \tilde{\mathbf{y}}_{M-1}]^{\mathrm{T}} = \mathrm{vec}_{M,N}^{-1}(\mathbf{r}) \tag{11}$$

The received delay-sequency information symbols are obtained by taking a N-point WHT of the rows of received delay-time matrix $\tilde{\mathbf{Y}}$ as

$$\mathbf{Y} = [\mathbf{y}_0, \mathbf{y}_1, \ldots, \mathbf{y}_{M-1}]^{\mathrm{T}} = \tilde{\mathbf{Y}} \cdot \mathbf{W}_N \tag{12}$$

The receiver operation can be rewritten in matrix form as

$$\mathbf{y} = (\mathbf{I}_M \otimes \mathbf{W}_N) \cdot (\mathbf{P}^{\mathrm{T}} \cdot \mathbf{r}) \tag{13}$$

where $\mathbf{y} = [\mathbf{y}_0^{\mathrm{T}}, \cdots, \mathbf{y}_{M-1}^{\mathrm{T}}]^{\mathrm{T}}$.

3) Transceiver System Block Diagram: Fig. 3 shows the OTSM transmitter and receiver block diagram. The key variables are listed in Table I. The overall block diagram is divided into (a) the OTSM transmitter (b) the delay-time channel and (c) the OTSM receiver. At the transmitter, a N-point WHT is applied on each of the rows $\mathbf{x}_m$ of the $M \times N$ 2-D information symbol matrix $\mathbf{X}$. The alternate rows are coloured with different shades to emphasize the row-wise WHT operation. This operation generates the 2-D delay-time matrix $\tilde{\mathbf{X}}$, with rows $\tilde{\mathbf{x}}_m = \mathbf{W}_N \cdot \mathbf{x}_m$. Next, the delay-time matrix $\tilde{\mathbf{X}}$ is vectorized column-wise to generate the time domain signal $\mathbf{s}$, i.e., each column of $\tilde{\mathbf{X}}$ is transmitted one after the other. The alternate columns of $\tilde{\mathbf{X}}$ are coloured with different shades to emphasize the column-wise vectorization operation. The time domain signal $\mathbf{s}$ is split to N time domain blocks as $\mathbf{s} = [\mathbf{s}_0^{\mathrm{T}}, \ldots, \mathbf{s}_{N-1}^{\mathrm{T}}]^{\mathrm{T}}$. The M samples of the time domain blocks $\mathbf{s}_n$ are related to the delay-time symbol vectors $\tilde{\mathbf{x}}_m$ through the row-column interleaving

$$\mathbf{s}_n[m] = \tilde{\mathbf{x}}_m[n] \tag{14}$$

Authorized licensed use limited to: Monash University. Downloaded on March 22,2022 at 09:29:49 UTC from IEEE Xplore. Restrictions apply.

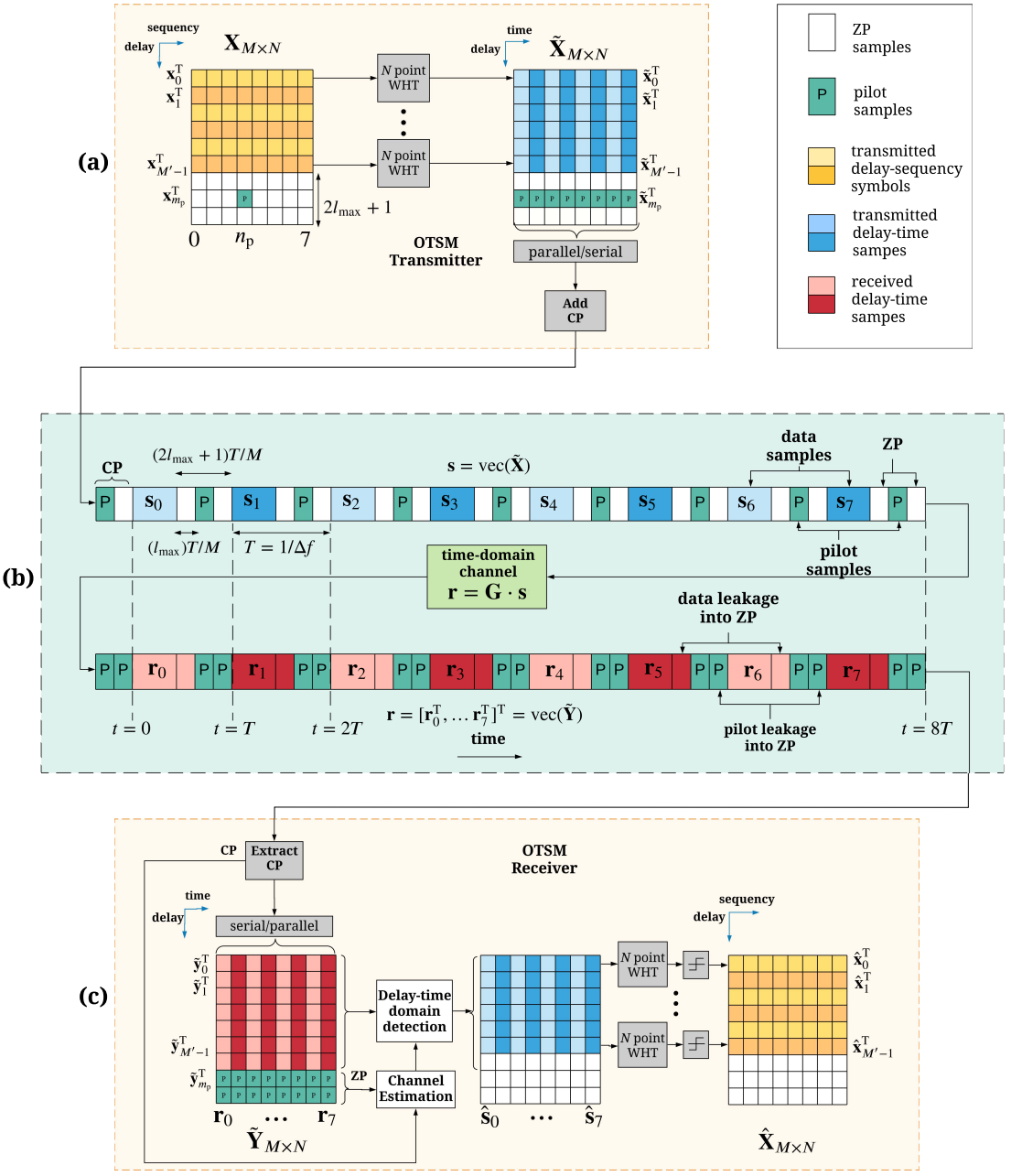

Fig. 3. OTSM transceiver operation for $N = 8, M = 9$ and the maximum discrete delay spread index $l_{\max} = 1$ with the set of delay taps $\mathcal{L} = \{0, 1\}$. The overall OTSM system block diagram is divided into three parts, (a) the OTSM transmitter, (b) the delay-time channel and (c) the OTSM receiver. For channel estimation, the delay-sequency domain pilot symbol is placed at delay and sequency index $m_p = M - l_{\max} - 1$ and n_p, respectively, in the delay-sequency grid. The different color shades are used to highlight if the operations are done row-wise or column-wise.

The last $2l_{\max} + 1$ rows of $\mathbf{X}$ are set to zero to enable insertion pilot and guard samples. The zero samples act as interleaved *zero padding* (ZP) between the blocks in the time domain. These ZP's simplify the detection and channel estimation by removing inter-block interference and interference between data and pilots. Further, a CP is added to the time domain signal to assist in the channel estimation process which will be discussed in Section VI. Fig. 3.b illustrates the baseband discrete-time domain channel. The transmitted signal $\mathbf{s}$ is impaired by the delay-time channel matrix $\mathbf{G}$ resulting in

Authorized licensed use limited to: Monash University. Downloaded on March 22,2022 at 09:29:49 UTC from IEEE Xplore. Restrictions apply.

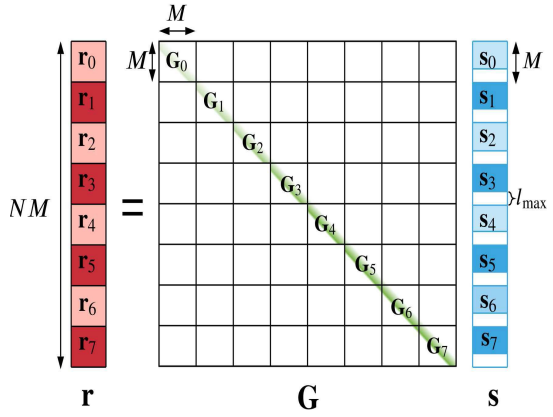

Fig. 4. The delay-time domain input-output relation $\mathbf{r} = \mathbf{G} \cdot \mathbf{s}$ for $N = 8$.

TABLE I
OTSM KEY VARIABLES

Transmitted 2-D delay-sequency information symbols	$\mathbf{X} \in \mathbb{C}^{M \times N}$
Transmitted delay-sequency vectors (rows of $\mathbf{X}$)	$\mathbf{x}_m \in \mathbb{C}^{N \times 1}$
Transmitted 2-D delay-time matrix	$\tilde{\mathbf{X}} = \mathbf{X} \cdot \mathbf{W}_N$
Transmitted delay-time vectors (rows of $\tilde{\mathbf{X}}$)	$\tilde{\mathbf{x}}_m = \mathbf{W}_N \cdot \mathbf{x}_m$
Transmitted time domain signal	$\mathbf{s} = \text{vec}(\tilde{\mathbf{X}})$
Transmitted time domain blocks	$\mathbf{s}_n \in \mathbb{C}^{M \times 1}$
Received 2-D delay-sequency information symbols	$\mathbf{Y} \in \mathbb{C}^{M \times N}$
Received delay-sequency vectors (rows of $\mathbf{Y}$)	$\mathbf{y}_m \in \mathbb{C}^{N \times 1}$
Received 2-D delay-time matrix	$\tilde{\mathbf{Y}} \cdot \mathbf{W}_N$
Received delay-time vectors (rows of $\tilde{\mathbf{Y}}$)	$\tilde{\mathbf{y}}_m = \mathbf{W}_N \cdot \mathbf{y}_m$
Received time domain signal	$\mathbf{r} = \text{vec}(\tilde{\mathbf{Y}})$
Received time domain blocks	$\mathbf{r}_n \in \mathbb{C}^{M \times 1}$

the received time domain signal $\mathbf{r} = \mathbf{G} \cdot \mathbf{s}$. Fig. 3 shows that the data and pilot symbols spread into ZP regions. Thanks to the ZP, the corresponding delay-time input-output relation can then be split block-wise as shown in Fig. 4.

Fig. 3.c shows the receiver operation. The channel impaired signal $\mathbf{r}$, after removing the CP, is folded back into a $M \times N$ delay-time matrix $\tilde{\mathbf{Y}}$ column-wise such that, each received time domain block $\mathbf{r}_n$ becomes a column of $\tilde{\mathbf{Y}}$, i.e,

$$\tilde{\mathbf{y}}_m[n] = \mathbf{r}_n[m] \tag{15}$$

Both channel estimation and detection are performed in the delay-time domain. The estimated delay-time samples are then transformed using the row-wise WHT operation to get back the detected delay-sequency symbols. The details of detection and channel estimation are presented in sections V and VI, respectively.

B. Continuous-Time Baseband Channel Model

Consider a baseband equivalent channel with P paths, where g_i, τ_i and ν_i are the complex path gain, the delay-shift and the Doppler-shift, respectively, associated with the i-th path. Let $\tau_{\max}$ and $\nu_{\max}$ denote the maximum delay and Doppler shift in the channel, respectively, i.e., $0 \leq \tau_i \leq \tau_{\max}$ and $-\nu_{\max} \leq \nu_i \leq \nu_{\max}$. We assume that the channel is *under-spread*, i.e., $\tau_{\max}\nu_{\max} \ll 1$. Since the number of channel coefficients P in the delay-Doppler domain is typically limited, the channel response has a sparse representation typically captured by the ray-tracing channel models [4], [15]:

$$h(\tau, \nu) = \sum_{i=1}^{P} g_i \delta(\tau - \tau_i)\delta(\nu - \nu_i). \tag{16}$$

The corresponding continuous time-varying channel impulse response function can be written as

$$g(\tau, t) = \int h(\tau, \nu) \mathrm{e}^{j2\pi\nu(t-\tau)}\, d\nu = \sum_{i=1}^{P} g_i \mathrm{e}^{j2\pi\nu_i(t-\tau_i)}. \tag{17}$$

C. Discrete-Time Baseband Channel Model

In the previous section, we looked at the continuous-time model of the channel. At the receiver, the channel impaired signal is down-converted to baseband and sampled at $M\Delta f$ Hz, thereby limiting the received waveform to NM complex samples. Therefore, from a communication system design point of view, it is convenient to have a discrete baseband equivalent representation of the system [33].

The discrete-time baseband model is obtained by sampling $r(t)$ at $t = q/M\Delta f$, where $0 \leq q \leq NM - 1$. Let $\mathcal{L} = \{0, \ldots, l_{\max}\}$ be the set of discrete delay taps representing delay shifts at integer multiples of the sampling period $1/M\Delta f$. The receiver sampling discretizes the delay-time channel $g(\tau, t)$ as

$$g^{\mathrm{s}}[l, q] = g(\tau, t)|_{\tau = \frac{l}{M\Delta f}, t = \frac{q}{M\Delta f}} \quad \text{for all} \quad l \in \mathcal{L} \tag{18}$$

Applying the sampling theorem to (17) (see [29], [33]), the discrete baseband delay-time channel at discrete delay taps $l \in \mathcal{L}$ is

$$g^{\mathrm{s}}[l, q] = \sum_{i=1}^{P} g_i z^{\kappa_i(q-l)} \mathrm{sinc}(l - \ell_i) \tag{19}$$

where $\mathrm{sinc}(x) = \sin(\pi x)/(\pi x)$, $z = \mathrm{e}^{\frac{j2\pi}{NM}}$ and, ℓ_i and κ_i are the *normalized delay shift* and *normalized Doppler shift* associated with the i-th path, such that

$$\tau_i = \frac{\ell_i}{M\Delta f}, \quad \nu_i = \frac{\kappa_i}{NT} \tag{20}$$

where $\ell_i, \kappa_i \in \mathbb{R}$. Note that, due to fractional delays, the sampling at the receiver introduces interference between channel responses at different delays. This is due to sinc reconstruction of the delay-time response at fractional delay points (ℓ_i) [33]. However, in practice, the fractional delays are not considered, since the resolution of the sampling time $1/M\Delta f$ is sufficient to approximate the path delays to nearest sampling points in typical wide band systems [33]. If we assume that the channel delays can be approximated as integer multiples of $1/M\Delta f$, i.e., when $\ell_i \in \mathbb{Z}$, then the sinc function in (19) reduces to

$$\mathrm{sinc}(l - \ell_i) = \begin{cases} 1, & \text{if } l = \ell_i \\ 0, & \text{otherwise.} \end{cases} \tag{21}$$

Authorized licensed use limited to: Monash University. Downloaded on March 22,2022 at 09:29:49 UTC from IEEE Xplore. Restrictions apply.

Consequently, the relation between the continuous channel response and the sampled time domain channel at each integer delay tap $l \in \mathcal{L}$ in (19) reduces to

$$g^{\mathrm{s}}[l,q] = \sum_{i=1}^{P} g_i z^{\kappa_i(q-l)} \delta[l-\ell_i] \tag{22}$$

In summary, for a channel model based on ray-tracing with fractional path delays equation (19) should be used to generate the delay-time channel coefficients. However, it is common practice to round the fractional path delays (ℓ_i) of the channel model to the nearest integer multiple of the sampling interval $(1/M\Delta f)$, in which case, (22) can be used.

D. Input-Output Relation in Vector Form

Starting from the received time domain signal $r(t)$, the continuous-time domain input-output relation can be written as

$$r(t) = \int_0^{\tau_{\max}} g(\tau,t)s(t-\tau)\,d\tau + w(t). \tag{23}$$

The discrete-time baseband signal is obtained by sampling the received waveform $r(t)$ at sampling intervals $t = q/M\Delta f$, where $0 \le q \le NM-1$. From (19), the corresponding discrete-time domain input-output relation, when the transmitted and received time domain signals are sampled at $t = q/M\Delta f$, can be written as

$$\mathbf{r}[q] = r\left(\frac{q}{M\Delta f}\right) = \sum_{l\in\mathcal{L}} g^{\mathrm{s}}[l,q]\mathbf{s}[q-l] + \mathbf{w}[q] \tag{24}$$

where $\mathbf{s}[q] = s(\frac{q}{M\Delta f})$ and $\mathbf{w}[q]$ is the AWGN noise with variance σ_w^2. To take advantage of (14) and (15), we then split the discrete-time index $q = 0,\ldots,MN-1$ in terms of the delay and sequency frame indices as $q = (m+nM)$, where the $m = 0,1,\ldots,M-1$ and $n = 0,1,\ldots,N-1$.

The input output relation in (24) can be written in terms of the time domain blocks as (omitting noise for brevity)

$$\mathbf{r}_n[m] = \sum_{l,l\le m} g^{\mathrm{s}}[l,m+nM]\,\mathbf{s}_n[m-l] + \underbrace{\sum_{l,l>m} g^{\mathrm{s}}[l,m+nM]\,\mathbf{s}_{n-1}\left[[m-l]_M\right]}_{\text{inter-block interference}} \tag{25}$$

Due to channel delay spread, there is leakage of the samples from the $(n-1)$-th block to the n-th block, as denoted by the *second* term in (25). We may remove the inter-block interference by using ZP by setting $\mathbf{s}_n[m] = 0$ for all n when $m \ge M - l_{\max}$ so that the *second* term in (25) vanishes. The effective time domain channel matrix using the ZP is shown in Fig. 4.

As illustrated in Fig. 3, this is equivalent to placing null symbol vectors $\mathbf{0}_N$ in the last $l_{\max}$ rows of $\mathbf{X}$ (i.e., ZP along the delay dimension of the OTSM grid). Hence, we can set, for all $n = 0,\ldots,N-1$,

$$\mathbf{x}_m[n] = \tilde{\mathbf{x}}_m[n] = 0, \quad \text{if } m \ge M - l_{\max} \tag{26}$$

Then, defining $\tilde{\mathbf{g}}_{m,l}[n] = g^{\mathrm{s}}[l,m+nM]$, and replacing $\mathbf{r}_n[m]$ with $\tilde{\mathbf{y}}_m[n]$ and $\mathbf{s}_n[m]$ with $\tilde{\mathbf{x}}_m[n]$ from (14) and (15),

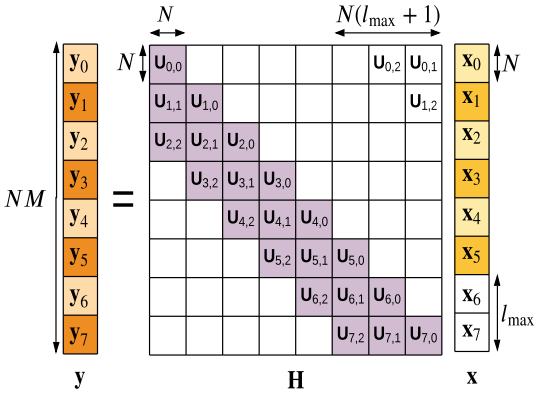

Fig. 5. The delay-sequency domain input-output relation $\mathbf{y} = \mathbf{H}\cdot\mathbf{x}$ after adding null symbols only contains the shaded blocks for $N = M = 8$ and $l_{\max} = 2$.

we can rewrite (25) in terms of the delay-time symbol vectors as

$$\tilde{\mathbf{y}}_m[n] = \sum_{l\in\mathcal{L}} \tilde{\mathbf{g}}_{m,l}[n]\tilde{\mathbf{x}}_{m-l}[n] \tag{27}$$

where $\tilde{\mathbf{g}}_{m,l} \in \mathbb{C}^{N\times 1}$ is the time domain channel for the l-th delay tap at time instants $mT/M + nT$, where $0 \le n \le N-1$.

The delay-sequency domain received symbols can be obtained by taking a N-point WHT of the delay-time received symbol vectors as in (12) and using the WHT multiplicative property in (4) as (omitting the noise vector for brevity, as the noise power remains the same since $\mathbf{W}_N$ is a unitary transformation)

$$\begin{aligned}\mathbf{y}_m = \mathbf{W}_N\cdot\tilde{\mathbf{y}}_m &= \sum_{l\in\mathcal{L}} \mathbf{W}_N\cdot(\tilde{\mathbf{g}}_{m,l}\circ\tilde{\mathbf{x}}_{m-l}) \\ &= \sum_{l\in\mathcal{L}} (\mathbf{W}_N\cdot\tilde{\mathbf{g}}_{m,l}) \circledast (\mathbf{W}_N\cdot\tilde{\mathbf{x}}_{m-l}) \\ &= \sum_{l\in\mathcal{L}} \boldsymbol{u}_{m,l} \circledast \mathbf{x}_{m-l}\end{aligned} \tag{28}$$

for $0 \le k \le N-1$, $0 \le m < M - l_{max}$, where $\boldsymbol{u}_{m,l}$ is the *sequency spread vector* in the l-th channel delay tap, experienced by the symbols in the $(m-l)$-th row of the $M\times N$ OTSM delay-sequency grid. The dyadic convolution in (28) can be expressed in the matrix-vector product form as (see Fig. 5)

$$\mathbf{y}_m = \sum_{l\in\mathcal{L}} \mathbf{U}_{m,l}\cdot\mathbf{x}_{m-l} \tag{29}$$

where the *sequency spread matrix*

$$\mathbf{U}_{m,l} = \mathbf{W}_N\cdot\tilde{\mathbf{G}}_{m,l}\cdot\mathbf{W}_N \tag{30}$$

and the diagonal matrix $\tilde{\mathbf{G}}_{m,l} = \mathrm{diag}[\tilde{\mathbf{g}}_{m,l}(0),\ldots,\tilde{\mathbf{g}}_{m,l}(N-1)]$ and $\boldsymbol{u}_{m,l}$ is the first column or row of $\mathbf{U}_{m,l}$. Note that $\mathbf{U}_{m,l}$ is a symmetric matrix, since it can be diagonalized to $\tilde{\mathbf{G}}_{m,l}$ by pre and post multiplying by $\mathbf{W}_N$, which is orthogonal and symmetric.

Authorized licensed use limited to: Monash University. Downloaded on March 22,2022 at 09:29:49 UTC from IEEE Xplore. Restrictions apply.

E. Input-Output Relation in Matrix Form

It can be seen from Fig. 3 that, the null symbols in the delay-sequency domain act as interleaved guard bands in the time domain, hence preventing inter-block interference. This means that the time domain channel matrix is block diagonal and hence each block can be processed independently. From (24), the time domain input-output relation in the simple matrix form can then be expressed as (see Fig. 4)

$$\mathbf{r} = \mathbf{G} \cdot \mathbf{s} + \mathbf{w}. \tag{31}$$

where $\mathbf{G} \in \mathbb{C}^{NM \times NM}$ is the time domain discrete baseband channel matrix. Note that, the band-width of the matrix $\mathbf{G}$ is $l_{\max} + 1$ and there are L non-zero elements in each row of $\mathbf{G}$, where $L \leq l_{\max} + 1$ is the number of distinct delay taps seen by the discrete receiver.

Substituting (10) and (13) in (31) (and omitting the noise term for brevity) we get

$$(\mathbf{W}_N \otimes \mathbf{I}_M) \cdot (\mathbf{P} \cdot \mathbf{y}) = \mathbf{G} \cdot (\mathbf{W}_N \otimes \mathbf{I}_M) \cdot (\mathbf{P} \cdot \mathbf{x}) \tag{32}$$

Reversing the transmitter operations, the input-output relation in (10) can be expressed in terms of the information symbols as

$$\mathbf{y} = \mathbf{H} \cdot \mathbf{x} + \bar{\mathbf{w}} \tag{33}$$

where the delay-sequency channel and AWGN noise experienced by the information symbols are

$$\begin{aligned} \mathbf{H} &= (\mathbf{I}_M \otimes \mathbf{W}_N) \cdot (\mathbf{P}^{\mathrm{T}} \cdot \mathbf{G} \cdot \mathbf{P}) \cdot (\mathbf{I}_M \otimes \mathbf{W}_N) \quad \text{and} \\ \bar{\mathbf{w}} &= (\mathbf{I}_M \otimes \mathbf{W}_N) \cdot (\mathbf{P}^{\mathrm{T}} \cdot \mathbf{w}). \end{aligned} \tag{34}$$

where $\bar{\mathbf{w}}$ is still i.i.d. due to $\mathbf{W}_N$ being a unitary matrix. The delay-sequency domain channel matrix is shown in Fig. 5. Due to the placement of null symbols (as given in (26)), we can ignore the strictly upper triangular sub-matrices of $\mathbf{H}$ (non shaded in Fig. 5). Note that $\mathbf{H}$ has a bandwidth of $N(l_{\max}+1)$.

IV. Relation With ZP-OTFS

Consider the ZP-OTFS system, with the 2-D information symbols $\mathbf{X}^{\mathrm{OTFS}} \in \mathbb{C}^{M \times N}$ split as symbol vectors $\mathbf{x}_m^{\mathrm{OTFS}} \in \mathbb{C}^{N \times 1}$, similar to the delay-sequency domain symbol vectors $\mathbf{x}_m^{\mathrm{OTSM}}$. Following [29], the vector input-output relation for ZP-OTFS can be written as

$$\mathbf{y}_m^{\mathrm{OTFS}} = \sum_{l \in \mathcal{L}} \mathbf{V}_{m,l} \cdot \mathbf{x}_{m-l}^{\mathrm{OTFS}} = \sum_{l \in \mathcal{L}} \boldsymbol{\nu}_{m,l} \circledast \mathbf{x}_{m-l}^{\mathrm{OTFS}}, \tag{35}$$

where $\mathbf{V}_{m,l}$ and $\boldsymbol{\nu}_{m,l}$ (first column of $\mathbf{V}_{m,l}$) are the circulant *Doppler spread matrix* and *Doppler spread vector*, respectively, at the l-th delay tap experienced by $\mathbf{x}_{m-l}^{\mathrm{OTFS}}$, i.e.,

$$\boldsymbol{\nu}_{m,l} = \mathbf{F}_N \cdot \tilde{\mathbf{g}}_{m,l}. \tag{36}$$

Recall from Fig. 1, the delay-sequency domain information symbols are related to the delay-Doppler domain symbols as

$$\begin{aligned} \mathbf{x}_m^{\mathrm{OTSM}} &= \mathbf{W}_N \cdot \mathbf{F}_N^{\dagger} \cdot \mathbf{x}_m^{\mathrm{OTFS}} \\ \mathbf{y}_m^{\mathrm{OTSM}} &= \mathbf{W}_N \cdot \mathbf{F}_N^{\dagger} \cdot \mathbf{y}_m^{\mathrm{OTFS}} \end{aligned} \tag{37}$$

From (37) and Fig. 1, OTSM can also be interpreted as a 1-D orthogonal precoding, given by a cascade of IFFT and WHT, along the Doppler domain. Combining (35) and (37), we get

$$\mathbf{y}_m^{\mathrm{OTSM}} = \sum_{l \in \mathcal{L}} \mathbf{U}_{m,l} \cdot \mathbf{x}_{m-l}^{\mathrm{OTSM}} = \sum_{l \in \mathcal{L}} \boldsymbol{u}_{m,l} \circledast \mathbf{x}_{m-l}^{\mathrm{OTSM}}, \tag{38}$$

where the *sequency spread matrix*

$$\mathbf{U}_{m,l} = \mathbf{W}_N \cdot \mathbf{F}_N^{\dagger} \cdot \mathbf{V}_{m,l} \cdot \mathbf{F}_N \cdot \mathbf{W}_N \tag{39}$$

and the *sequency spread vector*

$$\boldsymbol{u}_{m,l} = \mathbf{W}_N \cdot \mathbf{F}_N^{\dagger} \cdot \boldsymbol{\nu}_{m,l} \tag{40}$$

The *Doppler spread matrix* $\mathbf{V}_{m,l}$ is a circulant matrix whereas the *sequency spread matrix* $\mathbf{U}_{m,l}$ is a symmetric matrix. Moreover, the circular convolution along the Doppler domain in OTFS is converted to dyadic convolution in the sequency domain. In other words, the ordering of delay-Doppler channel coefficients is independent of the location of the information symbols in the delay-Doppler grid. However, in the case of delay-sequency channel coefficients, the ordering depends on the sequency index of the information symbol in the delay-sequency grid.

OTSM retains the key property of OTFS: all the information symbols experience approximately the same channel gain. The received signal energy $E^{\mathrm{OTFS}}(n,m)$ of each OTFS information symbol $\mathbf{X}^{\mathrm{OTFS}}(m,n)$ (assuming unit symbol energy at the transmitter) can be expressed in terms of the Doppler spread vectors as

$$E^{\mathrm{OTFS}}(n,m) = \sum_{l \in \mathcal{L}} ||\boldsymbol{\nu}_{m,l}||^2 \tag{41}$$

where $||\cdot||$ represent the Euclidean vector norm. Similarly, the received signal power of each OTSM information symbol $\mathbf{X}^{\mathrm{OTSM}}(m,n)$ can be written as

$$E^{\mathrm{OTSM}}(n,m) = \sum_{l \in \mathcal{L}} ||\boldsymbol{u}_{m,l}||^2 \tag{42}$$

From (40), it can be seen that the Doppler spread $\boldsymbol{\nu}_{m,l}$ and sequency spread $\mathbf{u}_{m,l}$ are related using unitary transformations. This means that the Euclidean norm of both these vectors are equal

$$||\boldsymbol{\nu}_{m,l}|| = ||\boldsymbol{u}_{m,l}|| \tag{43}$$

From (41), (42) and (43), it can be concluded that $E^{\mathrm{OTFS}}(n,m) = E^{\mathrm{OTSM}}(n,m)$. Since DFT and WHT are both unitary transformations, the noise power remains the same in both Doppler and sequency domains, which means that the received information symbols in OTFS and OTSM have the same SNR. This shows that OTSM has the potential to offer similar error performance to OTFS but at much lower modulation/demodulation complexity.

Remark – In [31], the OTFS transmitter was interpreted as the inverse *Zak* transform on the delay-Doppler domain, which is based on N-point DFTs across the Doppler domain. Similarly, the OTSM transmitter can be interpreted as an inverse *Walsh Zak* transform on the delay-sequency domain, where the DFT in the traditional Zak is replaced by WHT.

Authorized licensed use limited to: Monash University. Downloaded on March 22,2022 at 09:29:49 UTC from IEEE Xplore. Restrictions apply.

V. Low-Complexity Detection

For completeness, we summarize here the low complexity detection method proposed in [26]. As illustrated in Fig. 3, due to the time domain ZP, the interference between the time domain blocks is prevented. As shown in Fig. 4, this allows the time domain input-output relation in (10) to be split and independently processed as

$$\mathbf{r}_n = \mathbf{G}_n \cdot \mathbf{s}_n + \mathbf{w}_n, \quad n = 0, \ldots, N-1 \tag{44}$$

where $\mathbf{s} = [\mathbf{s}_0^{\mathrm{T}}, \cdots, \mathbf{s}_{N-1}^{\mathrm{T}}]^{\mathrm{T}}$ and $\mathbf{r} = [\mathbf{r}_0^{\mathrm{T}}, \cdots, \mathbf{r}_{N-1}^{\mathrm{T}}]^{\mathrm{T}}$ and $\mathbf{G}_n$ is the time domain channel at the n-th time domain block. Note that all the N time domain blocks have an equal component of each delay-sequency domain information symbol due to the Walsh-Hadamard precoding. In this section, we use the well known Gauss Seidel (GS) method available in the literature [35], [36], for low complexity detection.

In the proposed detector, GS iteration is done on the matched filtered channel matrix blocks $\mathbf{R}_n = \mathbf{G}_n^{\dagger} \cdot \mathbf{G}_n$. The matrix input-output relation in (44) after the matched filtering operation can be written as

$$\mathbf{z}_n = \mathbf{R}_n \cdot \mathbf{s}_n + \bar{\mathbf{w}}_n \tag{45}$$

where $\mathbf{R}_n = \mathbf{G}_n^{\dagger} \cdot \mathbf{G}_n$, $\mathbf{z}_n = \mathbf{G}_n^{\dagger} \cdot \mathbf{r}_n$ and $\bar{\mathbf{w}}_n = \mathbf{G}_n^{\dagger} \cdot \mathbf{w}_n$. The GS method is used to iteratively find the least squares solution

$$\hat{\mathbf{s}}_n = \min_{\mathbf{s}_n} ||\mathbf{z}_n - \mathbf{R}_n \mathbf{s}_n||^2 \tag{46}$$

of the M-dimensional linear system of equations in (45).

Let $\mathbf{D}_n$ and $\mathbf{L}_n$ be the matrix containing the diagonal elements and the strictly lower triangular elements of the matched filter matrix $\mathbf{R}_n$. From [35], [36], the GS iterative method for finding the estimate of $\mathbf{s}_n$ in each iteration is then given as

$$\hat{\mathbf{s}}_n^{(i)} = -\mathbf{T}_n \cdot \hat{\mathbf{s}}_n^{(i-1)} + \mathbf{b}_n \tag{47}$$

$$\mathbf{T}_n = (\mathbf{D}_n + \mathbf{L}_n)^{-1} \cdot \mathbf{L}_n^{\dagger}, \quad \mathbf{b}_n = (\mathbf{D}_n + \mathbf{L}_n)^{-1} \cdot \mathbf{z}_n. \tag{48}$$

where $\mathbf{T}_n \in \mathbb{C}^{M \times M}$ is the GS iteration matrix. The vector $\hat{\mathbf{s}}_n^{(i)} \in \mathbb{C}^{M \times 1}$ represents the estimate of the transmitted time domain samples of the n-th block in the i-th iteration. The delay-sequency domain information symbols in the i-th iteration is then given as

$$\hat{\mathbf{X}}^{(i)} = \mathcal{D}\left(\mathbf{C}^{(i)}\right), \text{ where } \mathbf{C}^{(i)} = [\hat{\mathbf{s}}_0^{(i)}, \hat{\mathbf{s}}_1^{(i)}, \ldots, \hat{\mathbf{s}}_{N-1}^{(i)}] \cdot \mathbf{W}_N \tag{49}$$

where $\mathcal{D}(.)$ denotes the decision making function replacing all the elements of the input with the nearest QAM symbol (in terms of the Euclidean distance). The hard decision estimates are transformed back to the time domain to update the time domain estimate to be used in the next iteration.

$$\hat{\mathbf{s}}^{(i)} \leftarrow (1-\delta)\hat{\mathbf{s}}^{(i)} + \delta \mathrm{vec}\left(\mathbf{X}^{(i)} \cdot \mathbf{W}_N\right) \tag{50}$$

where δ is the relaxation parameter to improve the detector convergence for higher modulation schemes like 64-QAM, [29], [35], [36]. As initial estimates to the iterative detection, we chose $\mathbf{X}^{(0)} = \mathbf{0}_{M \times N}$ or the MMSE solution presented in [26] yielding faster convergence.

VI. Embedded Pilot-Aided Channel Estimation

In this section, we propose a low complexity OTSM channel estimation algorithm. Due to the interleaved time domain pilots, the time domain channel responses in (27) for the l-th delay tap at time instants $mT/M + nT$, are directly estimated in delay-time domain. A linear or spline interpolation is performed to reconstruct the time domain channel coefficients for the entire frame for each delay tap l. We note that a similar scheme was proposed in [32] for OTFS by estimating channel coefficients in delay-time domain using spline interpolation. However, we show that for OTSM, linear interpolation is sufficient. Moreover, the proposed channel estimation differs from the single pilot scheme for OTFS in [14], since our channel estimation is performed in the delay-time domain rather than the DD domain in OTFS. This is because our OTSM delay-time detection algorithm does not use the delay-sequency channel coefficients.

A. Pilot Placement

In the proposed method, a single pilot symbol vector is placed in the delay-sequency domain. To avoid interference between the data and pilot symbol vectors due to delay spread, $l_{\max}$ guard symbol vectors are placed on either side of the pilot symbol vector as shown in Fig. 3. The letter 'P' in Fig. 3 represents the pilot samples. The delay-sequency domain single embedded pilot block placement is described as

$$\mathbf{x}_m(n) = \begin{cases} x_p \delta[n - n_p], & \text{if } m = m_p \\ 0, & \text{if } 0 < |m - m_p| \leq l_{\max} \\ \text{data}, & \text{otherwise} \end{cases} \tag{51}$$

where $0 \leq n < N$ and (m_p, n_p) is the pilot location in the 2-D delay-sequency grid. The delay-time pilot symbol vector is the scaled n_p-th sequency Walsh function given as

$$\tilde{\mathbf{x}}_{m_p} = \mathbf{W}_N \cdot \mathbf{x}_{m_p} = x_p[\mathbf{W}_N(n_p, 0), \cdots, \mathbf{W}_N(n_p, N-1)] \tag{52}$$

After converting to the time domain as shown in Fig. 3, the interleaved pilot locations in the time domain frame allow parallel sub-sampled (by a factor of M) observation of the channel in the entire OTSM frame. Since the first time domain pilot sample location is at the sampling instant m_p, a CP is added to the start of the frame by copying the last $(l_{\max} + 1)$ samples (containing the pilot sample as well) of the time domain frame. The pilot sample in the CP at location $m_p - M$ is necessary to get the delay-time channel coefficients before the m_p-th sample by interpolation.

B. Pilot Power Allocation

We choose the baseline pilot power such that the total transmit power remains fixed with and without pilot (only data). Let $E_{\mathrm{s}} = \mathbb{E}(|\mathbf{x}_m(n)|^2)$ denote the average energy of the delay-sequency domain information symbols and $E_{\mathrm{p}} = |\mathbf{x}_{m_p}(n_p)|^2$ is the energy spent on the pilot symbol. The SNR of data symbols is given as $\mathrm{SNR}_{\mathrm{d}} = E_{\mathrm{s}}/\sigma_w^2$. Let $M' = M - l_{\mathrm{zp}}$, such that NM' is the total number of

Authorized licensed use limited to: Monash University. Downloaded on March 22,2022 at 09:29:49 UTC from IEEE Xplore. Restrictions apply.

information symbols after pilot and guard symbol placement. The ZP length is chosen to be $l_{\rm zp} \geq 2l_{\max}+1$. The total transmit power of the OTSM frame of duration NT can then be written as

$$P_{\rm T} = P_{\rm D} + P_{\rm P} = \frac{1}{NT} NM' E_{\rm s} + \frac{1}{NT} E_{\rm p} \tag{53}$$

where $P_{\rm D}$ and $P_{\rm P}$ represent the total data and pilot power in the frame, respectively. The ratio of pilot power to the total transmit power or *pilot power ratio* (PPR) factor is defined as

$$\eta = \frac{P_{\rm P}}{P_{\rm D}+P_{\rm P}} = \frac{E_{\rm p}}{NM'E_{\rm s}+E_{\rm p}} \tag{54}$$

We set the pilot power such that the total transmit transmit power $P_{\rm T}$ remains the same as in the case without pilot (E_p=0) and no guard symbols ($M'=M$), i.e.,

$$P_{\rm T} = P_{\rm D} + P_{\rm P} = \frac{1}{NT} NME_s + 0. \tag{55}$$

The baseline pilot power can then be calculated from (53) and (55) as

$$E_{\rm p} = N(M-M')E_{\rm s} = Nl_{\rm zp}E_{\rm s} \tag{56}$$

It can be noted from (56), that the pilot power is proportional to $Nl_{\rm zp}$, which is related to the delay spread of the channel. In order to keep the total transmit power (P_T) the same, the pilot power can be increased by increasing the number of guard symbols. The baseline PPR factor in this case is given by

$$\eta_0 = \frac{E_p}{NM'E_{\rm s}+E_{\rm p}} = \frac{l_{\rm zp}}{M} \tag{57}$$

where $l_{\rm zp}$ is generally a small fraction (<10%) of M, under the underspread channel assumption. This is advantageous for frames with large N and M as pilot power increases proportionately and consequently the SNR of pilot samples $E_{\rm p}/\sigma_w^2$.

Now, we consider the case when there is no restriction on the total transmit power $P_{\rm T}$ and the PPR factor η. Let β denote the excess pilot power spend on top of E_p in (56), i.e., $E'_p = \beta E_p$. The β dependent PPR function can be defined as

$$\begin{aligned}\eta(\beta) &= \frac{E'_p}{NM'E_{\rm s}+E'_{\rm p}} = \frac{\beta N l_{\rm zp}E_{\rm s}}{NM'E_{\rm s}+\beta N l_{\rm zp}E_{\rm s}} \\ &= \frac{\beta N l_{\rm zp}E_{\rm s}}{N(M'+\beta l_{\rm zp})E_{\rm s}} = \frac{\beta l_{\rm zp}}{M'+\beta l_{\rm zp}}\end{aligned} \tag{58}$$

From (57) and (58), $\eta(\beta)$ can be related to η_0 as

$$\eta(\beta) = \frac{\beta l_{\rm zp}}{M+(\beta-1)l_{\rm zp}} = \frac{\beta\eta_0}{1+(\beta-1)\eta_0} \tag{59}$$

As a practical example, consider the EVA multipath propagation channel model as per the 3GPP standard, [37]. The maximum delay spread is less than $4\mu s$, which corresponds to $l_{\max}=3$ for $M=64$. The value of $l_{\rm zp}$ is then set to at least 7. For the baseline case (when $\beta=0$dB) the PPR $\eta(\beta)=\eta_0$ is approximately 10%. Increasing the excess pilot power β improves the channel estimation at the cost of increased η, which in turn reduces the energy efficiency, as more energy is spent per information bit. For example, when $\beta=3$dB, the PPR $\eta(\beta)$ increases to approximately 20%.

C. Delay-Time Channel Estimation

Using the input-output relations in (27), the input-output relation for the transmitted delay-time pilot symbol vector can be written as

$$\tilde{\mathbf{y}}_{(m_p+l)}(n) = \sum_{l'\in\mathcal{L}} g^{\rm s}(l', m_p+l+nM)\tilde{\mathbf{x}}_{(m_p+l-l')}(n) + \mathbf{w}(n) \tag{60}$$

where $l \in \mathcal{L}$. From (51), we know that $\tilde{\mathbf{x}}_{(m_p+l-l')}(n)=0$ when $l\neq l'$ and $|l-l'|<l_{\max}$. Then, from (60), the delay-time channel experienced by the pilot delay-time vector $\tilde{\mathbf{x}}_{m_p}$ can be simply estimated from the received delay-time domain pilot symbol vectors as

$$\hat{g}^{\rm s}(l, m_p+l+nM) = \frac{\tilde{\mathbf{y}}_{(m_p+l)}(n)}{\tilde{\mathbf{x}}_{m_p}(n)}, \quad \text{for } l\in\mathcal{L}. \tag{61}$$

The estimated channel coefficients $\hat{\mathbf{g}}^{\rm s}(l, m_p+l+nM)$ can be considered as the sub-sampled delay-time channel at discrete pilot sample locations m_p+nM. The intermediate delay-time channel coefficients of the entire OTSM frame can be reconstructed by interpolating the sub-sampled delay-time channel. As per the Nyquist sampling theorem, to accurately reconstruct a signal, the sampling frequency needs to be greater than twice the maximum frequency component of the signal. Here, to reconstruct channel coefficients, the maximum frequency component is related to the maximum Doppler shift introduced by the channel. The sampling frequency of estimated delay-time channel is M times less than the receiver sampling rate of $M\Delta f$. This implies that the channel can be accurately reconstructed as long as the maximum Doppler shift is less than half the sub-sampled sampling frequency, i.e., $\nu_{\max} < \frac{\Delta f}{2}$, which is a reasonable assumption for an underspread channel. The entire delay-time channel coefficients are then obtained by doing an interpolation of the estimated delay-time channel coefficients $\hat{g}^{\rm s}(l, m_p+l+nM)$.

Fig 6 shows an example of the real part of the time-varying channel at the l-th delay tap for the standard EVA channel model[5] with a speed of 500 km/hr, [37]. The transmitted pilot symbols can be viewed as the periodic delta function at intervals of T, one per each time domain block. The time-variance of the delay-time channel coefficients is due to the different Doppler paths in that delay tap. Since the effect of Doppler shifts can be modeled as a sum of sinusoidal functions, we use spline interpolation to reconstruct the time domain channel.

For low complexity channel estimation, we also consider linear interpolation. As seen in Fig. 6, the linear interpolation method fails to trace the delay-time response accurately, when two successive interpolation points are very close to each other as shown in the zoomed-in section. Spline interpolation, however, captures the channel variations better when the delay-time channel has more oscillations, i.e., when the Doppler spread is high.

[5]The EVA channel power-delay profile is given by [0, −1.5, −1.4, −3.6, −0.6, −9.1, −7.0, −12.0, −16.9] dB with excess tap delays [0, 30, 150, 310, 370, 710, 1090, 1730, 2510] ns.

Authorized licensed use limited to: Monash University. Downloaded on March 22,2022 at 09:29:49 UTC from IEEE Xplore. Restrictions apply.

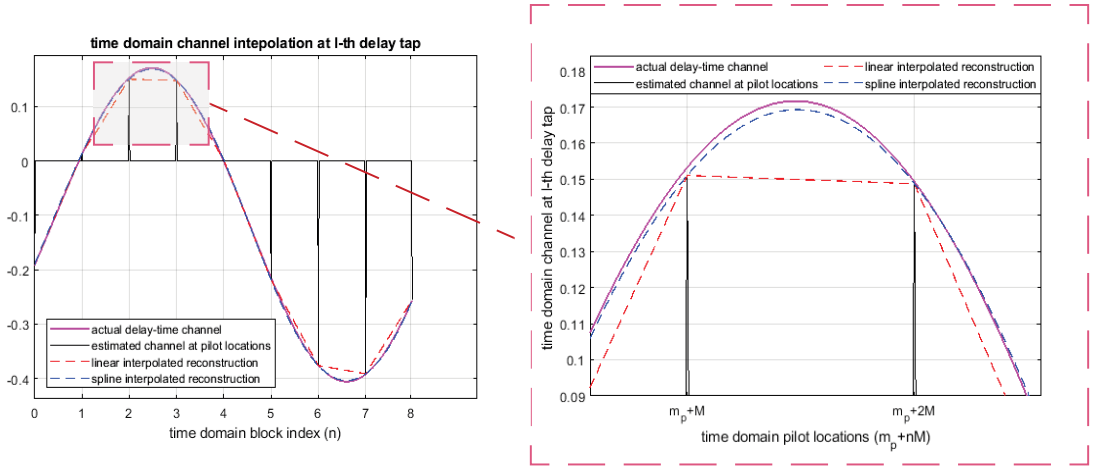

Fig. 6. Reconstruction of the real part of the l-th delay tap channel from the estimated channel $\hat{g}^{\mathrm{s}}(l, m_p + l + nM)$ using linear and spline interpolation for $N = 8$, $M = 64$ and UE speed = 500 km/hr at $\mathrm{SNR_d} = 20\ dB$ and $\beta = 0$ dB.

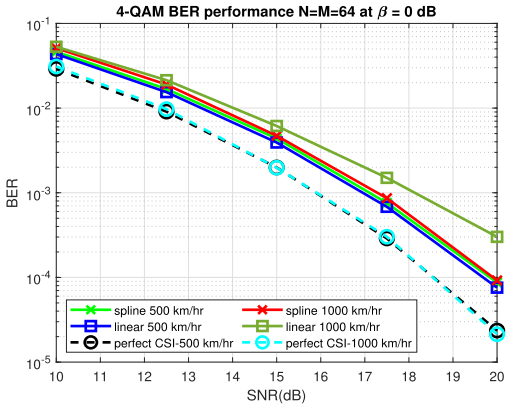

Fig. 7. BER performance using iterative time domain detector with excess pilot power $\beta = 3$ dB for EVA channel with speeds of 500 km/hr and 1000 km/hr.

To highlight the difference between the spline and linear interpolation methods, Fig. 7 shows the BER performance for 4-QAM for some extreme speeds of 500 km/hr and 1000 km/hr. It can be observed that linear interpolation works very similarly to spline interpolation for speeds less than at least 500 km/hr. This means that for the underspread wireless channels under consideration, spline interpolation can be replaced with the linear interpolation method for low complexity channel estimation. Therefore, in the following, we consider only the linear interpolation method.

D. Channel Estimation Complexity

From the initial step of channel estimation, we get the sub-sampled delay-time channel values $\hat{g}^{\mathrm{s}}(l, m_p + l + nM)$. Using linear interpolation, the intermediate delay-time samples $\hat{g}^{\mathrm{s}}(l, m_p + l + u + nM)$ can be reconstructed as

$$\hat{g}^{\mathrm{s}}(l, m_p+l+u+nM) = \hat{g}^{\mathrm{s}}(l, m_p + l + nM) + \alpha^{(n,l)}u \quad (62)$$

where $0 < u < M$, $-1 \leq n < N$ and the n-th piece-wise slope of the estimated channel at l-th delay tap

$$\alpha^{(n,l)} = \frac{\hat{g}^{\mathrm{s}}(l, m_p+l+(n+1)M) - \hat{g}^{\mathrm{s}}(l, m_p+l+nM)}{M} \quad (63)$$

It can be seen that the operation in (62) requires just one scalar multiplication with a complex number per reconstructed sample (ignoring addition operations). Out of the NML delay-time channel coefficients, we already have NL of them available, thanks to channel estimation. The initial operation in (62) then requires $2(N-1)ML$ scalar multiplications. The slope calculation in (63) requires NL scaling operations (by $1/M$), which can be done using bit-shifting operations if M is a power of 2.

VII. Turbo Decoder for Coded OTSM

In this section, we propose a turbo decoder for coded OTSM systems. At the transmitter, the delay-sequency domain information bits are randomly interleaved before converting them to QAM symbols, which is then OTSM modulated to generate the time domain signal. At the receiver, we use the low complexity iterative time domain detector summarized in Section V to obtain the time domain estimates in each iteration followed by a turbo iteration where a LDPC decoder is used to improve the current symbol estimates. One turbo iteration includes at least one detector and decoder iteration each. The number of detector and decoder iterations per turbo iteration can be set according to required BER and complexity requirements.

Fig. 8 shows the operation principle of the proposed turbo decoder. The information symbols estimates at the output of the detector is soft demodulated to obtain the bit LLRs, which are then de-interleaved and passed to a LDPC decoder.

Authorized licensed use limited to: Monash University. Downloaded on March 22,2022 at 09:29:49 UTC from IEEE Xplore. Restrictions apply.

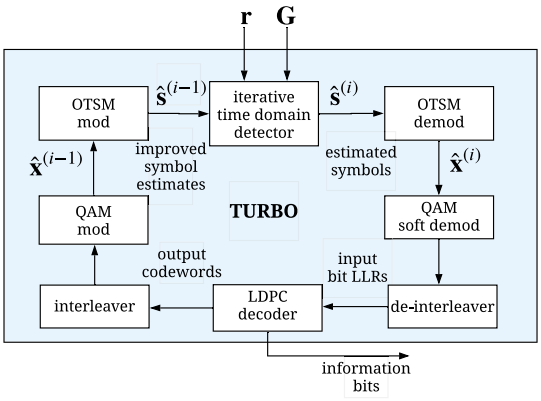

Fig. 8. Turbo operation principle for coded OTSM systems.

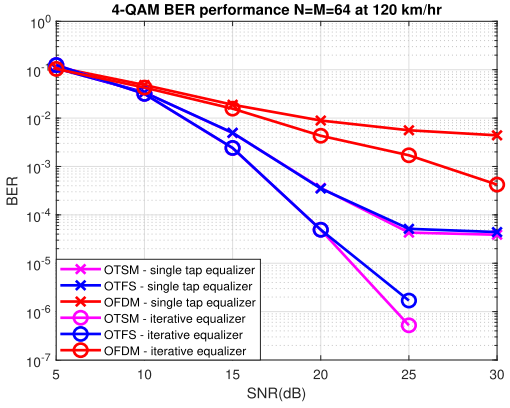

Fig. 9. 4-QAM uncoded BER performance of OTSM using the non-iterative and iterative detector compared with OTFS and OFDM for EVA channel model with speed of 120 km/hr assuming perfect CSI.

The LDPC decoder outputs the coded bits, which are then interleaved, and converted to QAM symbols, and OTSM modulated to get back an improved estimate of the time domain sample. The improved estimate $\mathbf{s}^{(i-1)}$ is used to generate the estimate of the time domain samples to be used for the next iteration $\mathbf{s}^{(i)}$, where the superscript $i \geq 0$ represents the i-th turbo iteration. The initial time domain estimate is initialized as $\mathbf{s}^{(0)} = \mathbf{0}_{NM\times 1}$.

VIII. Simulation Results and Discussion

In the following simulations, we generate OTFS frames for $N = 64$ and $M = 64$. The sub-carrier spacing Δf is 15 kHz and the carrier frequency is 4 GHz. The maximum delay spread (in terms of integer taps) is set to be 4 ($l_{\max} = 3$), which is approximately 4 μs, thereby the maximum number of delay taps as seen by the discrete receiver is $L = 4$. The channel delay model is generated according to the standard EVA model (with a speed of 120 km/h) in [37] with the Doppler shift for the i-th path generated from a uniform distribution $U(0, \nu_{max})$, where ν_{max} is the maximum Doppler

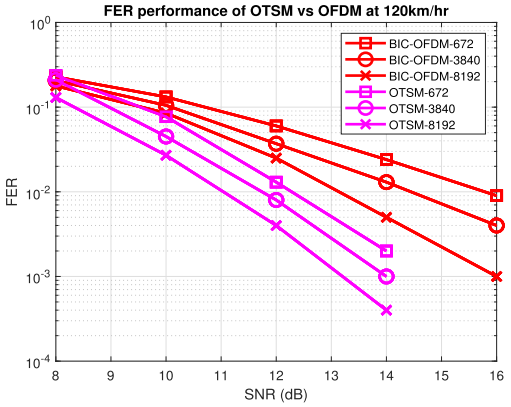

Fig. 10. 4-QAM rate 1/2 coded FER performance of OTSM using turbo decoder for EVA channel model with speed of 120km/hr compared with bit interleaved coded (BIC) OFDM with different LDPC codeword lengths: 672, 3840 and 8192.

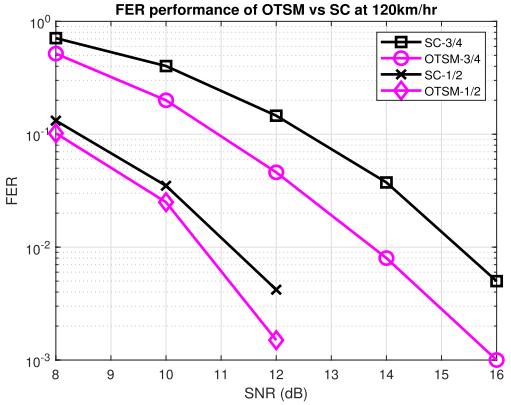

Fig. 11. 4-QAM rate 1/2 and 3/4 coded FER performance of OTSM using the turbo decoder for EVA channel model with speed of 120 km/hr compared with SC, with LDPC codeword length: 3840 bits.

shift. For BER plots, 10^5 frames are sent for every point in the BER curve. For FER plots, all simulations run for a minimum of 10^4 frames or until 100 frame errors are encountered. BER is plotted to show uncoded performance, while FER is used when an outer coding scheme is applied. We use the standard LDPC codes with parity-check matrices from the 3GPP BG1 scheme of 5G NR [38], with code lengths 672, 3840, 8192.

Fig. 9 compares the OTSM uncoded BER performance with perfect CSI with OFDM and OTFS using the two low complexity equalizers (single tap and iterative) presented in Section V. The OTSM offers better performance than OFDM and a similar performance to OTFS, but with lower transmission and detection complexity. The concatenation with a long code reduces the performance gap between uncoded OTSM and uncoded OFDM as illustrated in Fig. 10. We plot the FER performance of OTSM compared with bit interleaved coded (BIC) OFDM for different codeword sizes

Authorized licensed use limited to: Monash University. Downloaded on March 22,2022 at 09:29:49 UTC from IEEE Xplore. Restrictions apply.

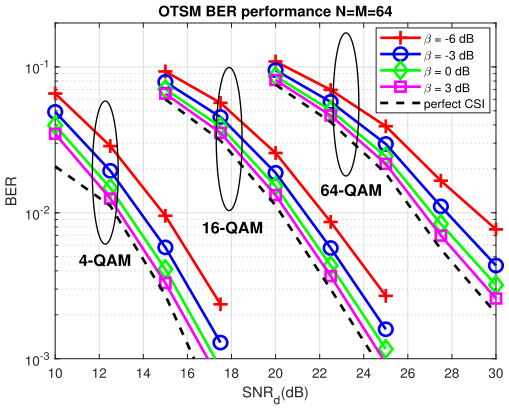

Fig. 12. Uncoded BER performance of OTSM using the iterative time domain detector for EVA channel model with speed of 120 km/hr with different excess pilot power β (dB).

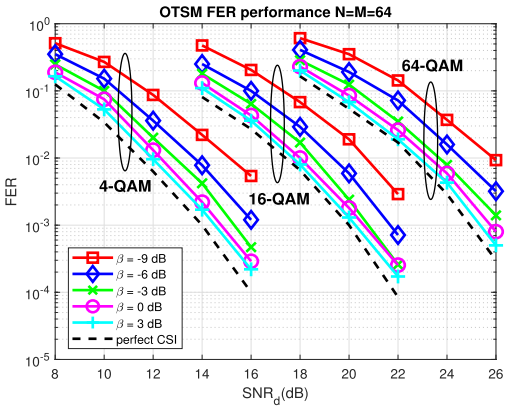

Fig. 13. 1/2 rate coded FER performance of OTSM using turbo decoder with LDPC codeword length of 672 for EVA channel model with speed of 120 km/hr with different excess pilot power β (dB).

of rate $= 1/2$. For fair comparison in terms of detection complexity with OFDM, we use the single tap equalizer for both OTSM and OFDM. As seen in Fig. 10, for a FER of 10^{-2}, coded OTSM has 4 dB gain over OFDM when using the short code ($L_{\mathrm{LDPC}} = 672$ and rate $1/2$), and a 2 dB gain when using the long code ($L_{\mathrm{LDPC}} = 8192$ and rate $1/2$).

In [26] we showed that uncoded OTSM and OTFS significantly outperform the uncoded single carrier (SC) scheme due to the time domain precoding. In Fig. 11, we show the same comparison for the coded case. As expected, the use of a channel code reduces their performance gap, since the code can help SC to recover some diversity from the channel, while uncoded OTSM already achieves a high diversity gain, and coding provides slightly smaller returns, as demonstrated in Fig. 11 for both rates 1/2 and 3/4 with a codeword length $L_{\mathrm{LDPC}} = 3840$ bits and turbo decoding with 4-QAM. Overall, the coded OTSM outperforms the coded SC.

Fig. 12 and Fig. 13 shows the OTSM uncoded BER and coded FER performance for 4, 16 and 64 QAM with the proposed channel estimation (with linear interpolation) for different excess pilot power β (dB). We use an LDPC codeword of length $L_{\mathrm{LDPC}} = 672$ to encode the information bits at the transmitter. The turbo iterations for the coded case are stopped either when all the $\lfloor \frac{NM'Q}{L_{\mathrm{LDPC}}} \rfloor$ LDPC codewords satisfy the parity check condition or when a maximum of 5 turbo iterations is reached.

It can be noted that, for coded OTSM, similar performance to the perfect CSI case is achieved for 16 and 64 QAM with less pilot power as compared to the un-coded case. The required pilot power can be further reduced with longer codewords.

IX. Conclusion

We proposed OTSM as a new modulation scheme that multiplexes the information symbols on the time and sequency shifted versions of a basic rectangular pulse and derived its input-output relation in the delay-sequency domain. By inserting zero padding between every block in the time domain, we proposed a low complexity channel estimation and detection for OTSM. It was shown in simulations that OTSM provides significantly better performance than OFDM and SC transmission and a similar performance to OTFS, but at much lower complexity thanks to the WHT. This makes OTSM a promising solution for future high mobility communication systems requiring low complexity transceivers. Further analysis of channel representation, low complexity channel estimation and detection in the delay-sequency domain will be explored in future work.

References

[1] R. W. Chang, "Synthesis of band-limited orthogonal signals for multichannel data transmission," *Bell Syst. Tech. J.*, vol. 45, no. 10, pp. 1775–1796, Dec. 1966.

[2] Y. G. Li and G. Stuber, *OFDM for Wireless Communications*. Boston, MA, USA: Springer, 2006.

[3] H. Sampath, S. Talwar, J. Tellado, V. Erceg, and A. Paulraj, "A fourth-generation MIMO-OFDM broadband wireless system: Design, performance, and field trial results," *IEEE Commun. Mag.*, vol. 40, no. 9, pp. 143–149, Sep. 2002.

[4] R. Hadani *et al.*, "Orthogonal time frequency space modulation," in *Proc. IEEE Wireless Commun. Netw. Conf. (WCNC)*, San Francisco, CA, USA, Mar. 2017, pp. 1–6.

[5] T. Zemen, M. Hofer, D. Loschenbrand, and C. Pacher, "Iterative detection for orthogonal precoding in doubly selective channels," in *Proc. IEEE 29th Annu. Int. Symp. Pers., Indoor Mobile Radio Commun. (PIMRC)*, Sep. 2018, pp. 1–6.

[6] L. Li *et al.*, "A simple two-stage equalizer with simplified orthogonal time frequency space modulation over rapidly time-varying channels," 2017, *arXiv:1709.02505*. [Online]. Available: http://arxiv.org/abs/1709.02505

[7] T. Zemen, M. Hofer, and D. Loeschenbrand, "Low-complexity equalization for orthogonal time and frequency signaling (OTFS)," 2017, *arXiv:1710.09916*. [Online]. Available: http://arxiv.org/abs/1710.09916

[8] K. R. Murali and A. Chockalingam, "On OTFS modulation for high-Doppler fading channels," in *Proc. Inf. Theory Appl. Workshop (ITA)*, Feb. 2018, pp. 1–10.

[9] P. Raviteja, K. T. Phan, Q. Jin, Y. Hong, and E. Viterbo, "Low-complexity iterative detection for orthogonal time frequency space modulation," in *Proc. IEEE Wireless Commun. Netw. Conf. (WCNC)*, Apr. 2018, pp. 1–6.

[10] A. Rezazadehreyhani, A. Farhang, M. Ji, R. R. Chen, and B. Farhang-Boroujeny, "Analysis of discrete-time MIMO OFDM-based orthogonal time frequency space modulation," in *Proc. IEEE Int. Conf. Commun. (ICC)*, May 2018, pp. 1–6.

Authorized licensed use limited to: Monash University. Downloaded on March 22,2022 at 09:29:49 UTC from IEEE Xplore. Restrictions apply.

[11] P. Raviteja, K. T. Phan, Y. Hong, and E. Viterbo, "Interference cancellation and iterative detection for orthogonal time frequency space modulation," *IEEE Trans. Wireless Commun.*, vol. 17, no. 10, pp. 6501–6515, Oct. 2018.

[12] A. Farhang, A. Rezazadehreyhani, L. E. Doyle, and B. Farhang-Boroujeny, "Low complexity modem structure for OFDM-based orthogonal time frequency space modulation," *IEEE Wireless Commun. Lett.*, vol. 7, no. 3, pp. 344–347, Jun. 2018.

[13] M. Kollengode Ramachandran and A. Chockalingam, "MIMO-OTFS in high-Doppler fading channels: Signal detection and channel estimation," in *Proc. IEEE Global Commun. Conf. (GLOBECOM)*, Dec. 2018, pp. 1–6.

[14] P. Raviteja, K. T. Phan, and Y. Hong, "Embedded pilot-aided channel estimation for OTFS in delay–Doppler channels," *IEEE Trans. Veh. Technol.*, vol. 68, no. 5, pp. 4906–4917, May 2019.

[15] P. Raviteja, Y. Hong, E. Viterbo, and E. Biglieri, "Practical pulse-shaping waveforms for reduced-cyclic-prefix OTFS," *IEEE Trans. Veh. Technol.*, vol. 68, no. 1, pp. 957–961, Jan. 2019.

[16] P. Raviteja, E. Viterbo, and Y. Hong, "OTFS performance on static multipath channels," *IEEE Wireless Commun. Lett.*, vol. 8, no. 3, pp. 745–748, Jun. 2019.

[17] G. D. Surabhi, R. M. Augustine, and A. Chockalingam, "On the diversity of uncoded OTFS modulation in doubly-dispersive channels," *IEEE Trans. Wireless Commun.*, vol. 18, no. 6, pp. 3049–3063, Jun. 2019.

[18] W. Shen, L. Dai, J. An, P. Fan, and R. W. Heath, "Channel estimation for orthogonal time frequency space (OTFS) massive MIMO," *IEEE Trans. Signal Process.*, vol. 67, no. 16, pp. 4204–4217, Aug. 2019.

[19] P. Raviteja, Y. Hong, E. Viterbo, and E. Biglieri, "Effective diversity of OTFS modulation," *IEEE Wireless Commun. Lett.*, vol. 9, no. 2, pp. 249–253, Feb. 2020.

[20] G. D. Surabhi and A. Chockalingam, "Low-complexity linear equalization for OTFS modulation," *IEEE Commun. Lett.*, vol. 24, no. 2, pp. 330–334, Feb. 2020.

[21] T. Thaj and E. Viterbo, "Low complexity iterative rake detector for orthogonal time frequency space modulation," in *Proc. IEEE Wireless Commun. Netw. Conf. (WCNC)*, May 2020, pp. 1–6.

[22] H. F. Harmuth, "Applications of Walsh functions in communications," *IEEE Spectr.*, vol. 6, no. 11, pp. 82–91, Nov. 1969.

[23] D. S. Stoffer, "Walsh-Fourier analysis and its statistical applications," *J. Amer. Stat. Assoc.*, vol. 86, no. 414, pp. 461–479, 1991, doi: 10.2307/2290595.

[24] R. Wang, *Introduction to Orthogonal Transforms: With Applications in Data Processing and Analysis*. Cambridge, U.K.: Cambridge Univ. Press, 2012, ch. 8, pp. 379–411, doi: 10.1017/CBO9781139015158.010.

[25] T. Ebihara and G. Leus, "Doppler-resilient orthogonal signal-division multiplexing for underwater acoustic communication," *IEEE J. Ocean. Eng.*, vol. 41, no. 2, pp. 408–427, Apr. 2016.

[26] T. Thaj and E. Viterbo, "Orthogonal time sequency multiplexing modulation," in *Proc. IEEE Wireless Commun. Netw. Conf. (WCNC)*, Mar. 2021, pp. 1–7, doi: 10.1109/WCNC49053.2021.9417451.

[27] J. Zhan, B. Nazer, U. Erez, and M. Gastpar, "Integer-forcing linear receivers," *IEEE Trans. Inf. Theory*, vol. 60, no. 12, pp. 7661–7685, Dec. 2014.

[28] A. Usakova, J. Kotuliakova, and M. Zajac, "Walsh—Hadamard transformation of a convolution," *Radioengineering*, vol. 11, no. 3, pp. 40–42, 2012.

[29] T. Thaj and E. Viterbo, "Low complexity iterative rake decision feedback equalizer for zero-padded OTFS systems," *IEEE Trans. Veh. Technol.*, vol. 69, no. 12, pp. 15606–15622, Dec. 2020, doi: 10.1109/TVT.2020.3044276.

[30] C. F. V. Loan, "The ubiquitous Kronecker product," *J. Comput. Appl. Math.*, vol. 123, nos. 1–2, pp. 85–100, Nov. 2000.

[31] S. K. Mohammed, "Derivation of OTFS modulation from first principles," 2020, *arXiv:2007.14357*. [Online]. Available: http://arxiv.org/abs/2007.14357

[32] Y. Hebron *et al.*, "Channel acquistion using orthogonal time frequency space modulated pilot signal," U.S. Patent 10 749 651 B2, Aug. 18, 2020.

[33] D. Tse and P. Viswanath, *Fundamentals of Wireless Communication*, 3rd ed. Cambridge, U.K.: Cambridge Univ. Press, 2005.

[34] R. A. Beezer, *A 1st Course Linear Algebra*, 3rd ed. Washington, DC, USA: Congruent Press, 1973, pp. 404–406.

[35] A. Björck, *Numerical Methods for Least Squares Problems*. Philadelphia, PA, USA: SIAM, 1996, doi: 10.1137/1.9781611971484.

[36] Y. Saad, *Iterative Methods for Sparse Linear Systems*, 2nd ed. Philadelphia, PA, USA: SIAM, 2003.

[37] *LTE Evolved Universal Terrestrial Radio Access (E-UTRA); Base Station (BS) Radio Transmission and Reception*, Standard ETSI TS, 3GPP TS 36.104 version 14.3.0 Release 14, Apr. 2017.

[38] T. T. B. Nguyen, T. Nguyen Tan, and H. Lee, "Efficient QC-LDPC encoder for 5G new radio," *Electronics*, vol. 8, no. 6, p. 668, Jun. 2019.

Tharaj Thaj (Graduate Student Member, IEEE) received the B.Tech. degree in electronics and communication engineering from the National Institute of Technology Calicut, India, in 2012, and the M.Tech. degree in telecommunication systems engineering from the Indian Institute of Technology at Kharagpur, Kharagpur, India, in 2015. He is currently pursuing the Ph.D. degree with the Department of Electrical and Computer Systems Engineering, Monash University, Australia. From 2012 to 2013, he was with Verizon Data Services India, Chennai, as a Software Engineer, focusing on network layer routing algorithms and protocols. From 2015 to 2017, he worked as a Senior Engineer with the Department of Communication, Navigation and Surveillance (CNS), Honeywell Technology Solutions Lab, Bengaluru. His current research interest includes physical layer design and implementation of wireless communication systems for next generation wireless networks.

Emanuele Viterbo (Fellow, IEEE) received the Ph.D. degree in electrical engineering from the Politecnico di Torino, Torino, Italy, in 1995. From 1990 to 1992, he was with the European Patent Office, The Hague, The Netherlands, as a Patent Examiner in the field of dynamic recording and error-control coding. From 1995 to 1997, he held a post-doctoral position with the Dipartimento di Elettronica, Politecnico di Torino. From 1997 to 1998, he was a Post-Doctoral Research Fellow with the Information Sciences Research Center of ATT Research, Florham Park, NJ, USA. From 1998 to 2005, he worked as an Assistant Professor and then an Associate Professor with the Dipartimento di Elettronica, Politecnico di Torino. From 2006 to 2009, he worked with the DEIS, University of Calabria, Italy, as a Full Professor. Since 2009, he has been an ISI Highly Cited Researcher. He is currently a Professor with the Department of Electrical and Computer Systems Engineering (ECSE) and an Associate Dean in graduate research with Monash University, Melbourne, Australia. His main research interests include lattice codes for the Gaussian and fading channels, algebraic coding theory, algebraic space-time coding, digital terrestrial television broadcasting, digital magnetic recording, and irregular sampling. He was awarded the NATO Advanced Fellowship from the Italian National Research Council in 1997. He is an Associate Editor of IEEE TRANSACTIONS ON INFORMATION THEORY, *European Transactions on Telecommunications*, and *Journal of Communications and Networks*, and a Guest Editor of IEEE JOURNAL OF SELECTED TOPICS IN SIGNAL PROCESSING: Special Issue Managing Complexity in Multiuser MIMO Systems.

Yi Hong (Senior Member, IEEE) received the Ph.D. degree in electrical engineering and telecommunications from the University of New South Wales (UNSW), Sydney.

From 2018 to 2020, she served on the Australian Research Council College of Experts. She is currently an Associate Professor with the Department of Electrical and Computer Systems Engineering, Monash University, Melbourne, Australia. Her research interests include communication theory, coding, and information theory with applications to telecommunication engineering. She was a technical program committee member for many IEEE leading conferences. She received the NICTA-ACoRN Earlier Career Researcher Award at the Australian Communication Theory Workshop, Adelaide, Australia, in 2007. She was the General Co-Chair of IEEE Information Theory Workshop 2014, Hobart, the Technical Program Committee Chair of Australian Communications Theory Workshop 2011, Melbourne, and the Publicity Chair at the IEEE Information Theory Workshop 2009, Sicily. She was an Associate Editor for IEEE WIRELESS COMMUNICATION LETTERS and *Transactions on Emerging Telecommunications Technologies* (ETT).

Authorized licensed use limited to: Monash University. Downloaded on March 22,2022 at 09:29:49 UTC from IEEE Xplore. Restrictions apply.

Chapter 6

Unitary-Precoded Single-Carrier Waveforms for High Mobility: Detection and Channel Estimation

Citing info:

T. Thaj and E. Viterbo, "Unitary-Precoded Single-Carrier Waveforms for High Mobility: Detection and Channel Estimation" Accepted in *IEEE Wireless Communications and Networking Conference (WCNC)*, 2022, doi: 10.48550/ARXIV.2201.10218.

Copyright Statement:

©[2019] IEEE. Reprinted, with permission, from [Tharaj Thaj, Emanuele Viterbo, Unitary-Precoded Single-Carrier Waveforms for High Mobility: Detection and Channel Estimation, IEEE Wireless Communications and Networking Conference (WCNC), 2022]

Unitary-Precoded Single-Carrier Waveforms for High Mobility: Detection and Channel Estimation

Tharaj Thaj and Emanuele Viterbo

ECSE Department, Monash University, Clayton, VIC 3800, Australia
Email: {tharaj.thaj, emanuele.viterbo}@monash.edu

***Abstract*—This paper presents unitary-precoded single-carrier (USC) modulation as a family of waveforms based on multiplexing the information symbols on time domain unitary basis functions. The common property of these basis functions is that they span the entire time and frequency plane. The recently proposed orthogonal time frequency space (OTFS) and orthogonal time sequency multiplexing (OTSM) based on discrete Fourier transform (DFT) and Walsh Hadamard transform (WHT), respectively, fall in the general framework of USC waveforms. In this work, we present channel estimation and detection methods that work for any USC waveform and numerically show that any choice of unitary precoding results in the same error performance. Lastly, we implement some USC systems and compare their performance with OFDM in a real-time indoor setting using an SDR platform.**

***Index Terms*—OTSM, OTFS, WHT, DFT, DCT, Delay–Sequency, Software-Defined Radio, USRP, Delay–Doppler.**

I. Introduction

Reliable communications in high mobility channels are a key promise of 6G wireless communications. With the advent of high-speed trains, unmanned aerial vehicles (UAVs), and drones, there is an urgent need to address the issue of reliable communication in high-mobility wireless channels. Widely used modulation schemes such as orthogonal frequency division multiplexing (OFDM) multiplex information symbols in the time-frequency domain. The advantage of such data transmission is that the orthogonality property enables the use of a single tap equalizer to detect the transmitted data at the receiver, thereby providing a low complexity solution to reliable communication in frequency selective (static) channels. However, OFDM suffers from performance degradation in time-frequency selective channels due to the loss of orthogonality and unequal SNR of its sub-carriers.

Recently, orthogonal time frequency space (OTFS) modulation was proposed, which multiplexes information symbols in the delay-Doppler domain, [1], [2]. The key advantage compared to OFDM is that all the information symbols experience a roughly flat fading channel. OTFS achieves this by spreading all the information symbols on unitary basis functions that span the entire available time and bandwidth resource using the inverse symplectic fast Fourier transform (ISFFT) operation, thereby exploiting maximum time-frequency diversity. It was proved in [3] that any *constant modulus* 2-D unitary transformation in the time-frequency domain could offer the same performance as OTFS.

This work was supported by the Australian Research Council through the Discovery Project under Grant DP200100096.

However, 2-D precoding in the time-frequency domain may increase the transceiver complexity since an OFDM modulator on top of 2-D precoding is still required for transmission, [4]. One solution to mitigating the 2-D time-frequency precoding complexity in [3] is to restrict the unitary transformation precoding along the frequency dimension to the Fourier transform, specifically FFT as in the case of OTFS. Such precoding along the frequency dimension transforms the time-frequency information samples directly into the delay-time domain, thereby bypassing the need for an OFDM modulator. Using FFT as above, the 2-D precoding along the frequency-time domain is reduced to just a 1-D precoding along the time dimension of the delay-time domain.

Since any arbitrary unitary matrix can be used for precoding, every choice leads to a new waveform with the same error performance. Therefore, it seems reasonable to group such waveforms under a general framework, which we refer to as unitary-precoded single-carrier (USC) waveforms in this work. With such motivation, in this work, we first generalize OTFS and OTSM (proposed in [4], [5]) as a USC waveform with DFT and WHT precoding, respectively, along the time dimension of the delay-time domain. We then present time-domain channel estimation and detection methods that work for any USC waveform and numerically show that any choice of unitary precoding results in the same error performance. Even though OTFS has gained popularity recently, other USC waveforms like OTSM exist that can outperform OTFS for key performance requirements such as transceiver complexity and ease of implementation. Lastly, USC with DFT and WHT unitary matrices are implemented and tested in real-time on an SDR platform to validate its' superior performance over OFDM even in low-mobility channels.

Notations: The following notations will be followed in this paper: a, $\mathbf{a}$, $\mathbf{A}$ represent a scalar, vector, and matrix, respectively; $\mathbf{a}[n]$ and $\mathbf{A}[m,n]$ represent the n-th and (m,n)-th element of $\mathbf{a}$ and $\mathbf{A}$, respectively; $\mathbf{A}^{\mathrm{T}}$, $\mathbf{A}^{\dagger}$, $\mathbf{A}^{*}$ and $\mathbf{A}^{n}$ represent the transpose, Hermitian transpose, complex conjugate and n-th power, respectively, of $\mathbf{A}$. The set of $M \times N$ dimensional matrices with complex entries are denoted by $\mathbb{C}^{M\times N}$. Let $\otimes$ denote the Kronecker product, $|\mathcal{S}|$ denote the cardinality of the set $\mathcal{S}$, $\mathrm{vec}(\mathbf{A})$, the column-wise vectorization of the matrix $\mathbf{A}$ and $\mathrm{vec}^{-1}_{N,M}(\mathbf{a})$ is the matrix formed by

folding a vector $\mathbf{a}$ into a $N \times M$ matrix by filling it column wise. Let $\mathbf{F}_N$ be the normalized N point DFT matrix with elements $\mathbf{F}_N(i,k) = (1/\sqrt{N})\mathrm{e}^{-j2\pi ik/N}$ and $\mathbf{W}_N$ be the normalized N-point WHT matrix, [6],

II. System Model

We will be using the following matrix/vector representation throughout the paper. Let $\mathbf{x}, \mathbf{y} \in \mathbb{C}^{NM\times 1}$ be the transmitted and received information symbols. The total frame duration and bandwidth of the transmitted signal frame are $T_f = NT$ and $B = M\Delta f$, respectively. We consider the case where $T\Delta f = 1$, i.e., the signal is critically sampled for any pulse shaping waveform.

A. Conventional multi-carrier transmission

Let $\mathbf{X} \in \mathbb{C}^{M\times N}$ be the 2-D information symbol matrix. Let $\mathbf{X}_{\mathrm{FT}} \in \mathbb{C}^{M\times N}$ be the frequency-time samples generated by precoding the information symbols in $\mathbf{X}$. $\mathbf{X}_{\mathrm{FT}}(m,n)$ represents the precoded data sample transmitted in the m-th sub-carrier of the n-th time slot, where $m = 0,\ldots,M-1$ and $n = 0,\ldots,N-1$. Let $\widetilde{\mathbf{X}} \in \mathbb{C}^{M\times N}$ be the delay-time samples generated from the time-frequency samples using the Heisenberg transform as

$$\widetilde{\mathbf{X}} = \mathbf{G}_{\mathrm{TX}} \cdot \mathbf{F}_M^{\dagger} \cdot \mathbf{X}_{\mathrm{FT}} \tag{1}$$

where $\mathbf{G}_{\mathrm{TX}}$ is the pulse shaping waveform at the transmitter. We assume the rectangular pulse shaping waveform in this paper, i.e., $\mathbf{G}_{\mathrm{TX}} = \mathbf{I}_M$. The operation is (1) is the conventional OFDM modulator. The $NM \times 1$ time domain samples are generated by vectorizing the delay-time domain samples as

$$\mathbf{s} = \mathrm{vec}(\widetilde{\mathbf{X}}) \tag{2}$$

The time-domain signal are divided into N blocks $\mathbf{s}_n$ of size M as $\mathbf{s} = [\mathbf{s}_0^{\mathrm{T}},\ldots,\mathbf{s}_{N-1}^{\mathrm{T}}]^{\mathrm{T}}$ and finally a guard interval of length L_{G} is added to each time domain block in $\mathbf{s}$ to avoid inter-block interference. The guard intervals can either be filled with a cyclic prefix (CP) or zero-padding (ZP).

B. Generalized 2-D unitary frequency-time precoding

The generalized 2-D unitary precoding can be written in matrix form as

$$\mathbf{X}_{\mathrm{FT}} = \mathbf{U}_{\mathrm{F}} \cdot \mathbf{X} \cdot \mathbf{U}_{\mathrm{T}} \tag{3}$$

where $\mathbf{U}_{\mathrm{F}} \in \mathbb{C}^{M\times M}$ and $\mathbf{U}_{\mathrm{T}} \in \mathbb{C}^{N\times N}$ are the precoding matrices along the frequency and time domain, respectively.

In [3], it was proved that any orthogonal 2-D transformation with *constant modulus* basis functions operating on the entire frequency-time domain allows the receiver to exploit maximum frequency-time diversity in doubly-selective channels. This implies that, in terms of error performance, the best choice for $\mathbf{U}_{\mathrm{F}}$ and $\mathbf{U}_{\mathrm{T}}$ are unitary transforms, such as DFT and WHT. The precoding matrices $\mathbf{U}_{\mathrm{F}}$ and $\mathbf{U}_{\mathrm{T}}$ for different modulation schemes are listed in Table I.

TABLE I
$\mathbf{U}_{\mathrm{F}}$ AND $\mathbf{U}_{\mathrm{T}}$ REPRESENTING DIFFERENT MODULATION SCHEMES

Modulation scheme	$\mathbf{U}_{\mathrm{F}}$	$\mathbf{U}_{\mathrm{T}}$
OFDM	$\mathbf{I}_M$	$\mathbf{I}_N$
SC	$\mathbf{F}_M$	$\mathbf{I}_N$
OTFS	$\mathbf{F}_M$	$\mathbf{F}_N^{\dagger}$
OTSM	$\mathbf{F}_M$	$\mathbf{W}_N$

C. Generalized 1-D unitary time precoding

A 2-D unitary precoding in the frequency-time domain may increase the complexity of transceiver modulation and demodulation. One way to mitigate this complexity is by restricting the unitary transformation along the frequency domain to the FFT, i.e., $\mathbf{U}_{\mathrm{F}} = \mathbf{F}_M$,

$$\mathbf{X}_{\mathrm{FT}} = \mathbf{F}_M \cdot \mathbf{X} \cdot \mathbf{U}_{\mathrm{T}} \tag{4}$$

This simplifies the Heisenberg transform in (1) as (assuming practical rectangular pulse shaping waveforms):

$$\widetilde{\mathbf{X}} = \mathbf{F}_M^{\dagger} \cdot (\mathbf{F}_M \cdot \mathbf{X} \cdot \mathbf{U}_{\mathrm{T}}) = \mathbf{X} \cdot \mathbf{U}_{\mathrm{T}} \tag{5}$$

Now, (5) can be considered as a precoding along the time dimension of the delay-time domain, i.e., the rows of $\widetilde{\mathbf{X}}$. The time-domain signal is then generated as

$$\mathbf{s} = \mathrm{vec}(\widetilde{\mathbf{X}}) \tag{6}$$

The operations in (5) and (6) can be combined as

$$\mathbf{s}[m+kM] = \widetilde{\mathbf{X}}[m,k] = \sum_{n=0}^{N-1} \mathbf{X}[m,n]\mathbf{U}_{\mathrm{T}}[n,k] \tag{7}$$

for $m = 0,\ldots M-1$ and $k = 0,\ldots,N-1$. This 1-D unitary precoding can still achieve maximum time-frequency diversity similar to a 2-D unitary precoding in the frequency-time domain, but with much lower modulation/demodulation complexity. For $\mathbf{U}_{\mathrm{T}} = \mathbf{F}_N^{\dagger}$, the operation in (7) is known in the literature as the inverse discrete Zak transform (IDZT) and is equivalent to the OTFS transmitter for rectangular pulse shaping waveforms, [8], [9].

D. USC Transmitter

Let $\mathbf{X} \in \mathbb{C}^{M\times N}$ be the 2-D information symbols. The transmitted information symbol matrix $\mathbf{X}$ and the delay-time samples are vectorized as

$$\mathbf{x} = \mathrm{vec}(\mathbf{X}^{\mathrm{T}}), \quad \widetilde{\mathbf{x}} = \mathrm{vec}(\widetilde{\mathbf{X}}^{\mathrm{T}}) \tag{8}$$

Let $\mathbf{P}$ be the row-column interleaver matrix which writes the NM samples column-wise into a $N\times M$ matrix and reads the elements out row-wise. The time-domain samples can then be generated using (7) as

$$\mathbf{s} = \mathbf{P} \cdot (\mathbf{I}_M \otimes \mathbf{U}_{\mathrm{T}}) \cdot \mathbf{x} = \mathbf{P} \cdot \widetilde{\mathbf{x}} \tag{9}$$

where $\mathbf{U}_{\mathrm{T}}$ is the precoding matrix along the time-domain given for different waveforms in the literature as given in Table I. The time domain samples are then pulse shaped, digital to analog converted and transmitted into the wireless medium as $s(t)$ at a carrier frequency f_c.

E. Channel

Consider a channel with P paths, where h_i, τ_i and ν_i are the propagation gain, delay and Doppler-shift associated with i-th path. We assume that the delay-Doppler channel response is given by

$$h(\tau,\nu) = \sum_{i=1}^{P} h_i \delta(\tau-\tau_i)\delta(\nu-\nu_i) \tag{10}$$

The delay-time channel in terms of the delay-Doppler response is given as

$$g(\tau,t) = \int_{\nu} h(\tau,\nu) e^{j2\pi\nu(t-\tau)} d\nu \tag{11}$$

The received time-domain signal can then be written as

$$r(t) = \int_{\tau} g(\tau,t)s(t-\tau)d\tau + w(t) \tag{12}$$

where $w(t)$ is the AWGN noise signal. The equivalent discrete-time channel is obtained by sampling the received time-domain waveform at $M\Delta f$ Hz, is given as

$$\mathbf{r}[q] = \sum_{l\in\mathcal{L}} \overline{g}[l,q]\mathbf{s}[q-l] + \mathbf{w}[q] \tag{13}$$

where $\tau = l/M\Delta f$, $t = q/M\Delta f$ and $\mathcal{L}$ denotes the set of discrete integer delay taps. The entries of $\overline{g}[l,q]$ is given as

$$\overline{g}[l,q] = \sum_{i=1}^{P} h_i z^{\kappa_i(q-l_i)} \delta[l-l_i] \tag{14}$$

where $z = e^{\frac{j2\pi}{NM}}$, $l_i = \frac{\tau_i}{M\Delta f}$ and $\kappa_i = \frac{\nu_i}{NT}$ are the *normalized delay* and *normalized Doppler-shift* associated with the i-th path. We assume that the *normalized delays* l_i are integers.

F. USC Receiver

The transmitter operations are then reversed at the receiver. The delay-time received samples are obtained by folding the received signal $\mathbf{r}$ into a $M \times N$ matrix by filling it column-wise.

$$\widetilde{\mathbf{Y}} = \mathrm{vec}^{-1}_{M,N}(\mathbf{r}) \tag{15}$$

The received information symbols can then be obtained as

$$\mathbf{Y} = \widetilde{\mathbf{Y}} \cdot \mathbf{U}_T^{\dagger} \tag{16}$$

The operations in (15) and (16) can be combined as

$$\mathbf{Y}[m,n] = \sum_{k=0}^{N-1} \mathbf{r}[m+kM]\mathbf{U}_{\mathrm{T}}^{\dagger}[k,n] \tag{17}$$

Note that for $\mathbf{U}_{\mathrm{T}} = \mathbf{F}_N^{\dagger}$, the operation in (17) is known in the literature as the discrete Zak transform (DZT) and is equivalent to the OTFS receiver for rectangular pulse shaping waveform, [8], [9]. Let the received 2-D symbol matrices $\mathbf{Y}$ and $\widetilde{\mathbf{Y}}$ be vectorized as

$$\mathbf{y} = \mathrm{vec}(\mathbf{Y}^{\mathrm{T}}), \quad \widetilde{\mathbf{y}} = \mathrm{vec}(\widetilde{\mathbf{Y}}^{\mathrm{T}}) \tag{18}$$

The received vector can then be written in terms of the transmitted vector as

$$\mathbf{y} = (\mathbf{I}_M \otimes \mathbf{U}_{\mathrm{T}}^{\dagger}) \cdot (\mathbf{P}^{\mathrm{T}} \cdot \mathbf{r}) = (\mathbf{I}_M \otimes \mathbf{U}_{\mathrm{T}}^{\dagger}) \cdot \widetilde{\mathbf{y}} \tag{19}$$

G. USC input-output relations

The input-output relation in (14) can be written in the matrix form as

$$\mathbf{r} = \mathbf{G} \cdot \mathbf{s} + \mathbf{w} \tag{20}$$

where $\mathbf{G}$ is the time-domain channel matrix with a band width of $l_{\max}+1$ with entries: $\mathbf{G}[q, q-l] = \bar{g}[l,q]$ for $q \geq l$. Substituting (9) and (19) in (20), we get the input-output relation between the transmitted and received information symbols:

$$\mathbf{y} = \mathbf{H} \cdot \mathbf{x} + \mathbf{z} \tag{21}$$

where $\mathbf{z} = (\mathbf{I}_M \otimes \mathbf{U}_T^{\dagger}) \cdot (\mathbf{P}^{\mathrm{T}} \cdot \mathbf{w})$ is the AWGN noise and the channel matrix

$$\mathbf{H} = (\mathbf{I}_M \otimes \mathbf{U}_T^{\dagger}) \cdot (\mathbf{P}^{\mathrm{T}} \cdot \mathbf{G} \cdot \mathbf{P}) \cdot (\mathbf{I}_M \otimes \mathbf{U}_T) \tag{22}$$

III. Embedded pilot-aided channel estimation

In this section we present a time-domain channel estimation method for USC waveforms with ZP between blocks. Following the pilot placement in [5], [7], a single pilot is embedded in the 2-D information symbol matrix $\mathbf{X}$ at location $(m_{\mathrm{p}}, n_{\mathrm{p}})$. Guard symbols are placed around the single pilot to avoid interference between data and pilot.

$$\mathbf{X}(m,n) = \begin{cases} x_{\mathrm{p}} & \text{if } m = m_{\mathrm{p}}, n = n_{\mathrm{p}} \\ 0 & \text{if } |m-m_{\mathrm{p}}| \leq l_{\max} \\ \text{data symbols} & \text{otherwise.} \end{cases}$$

After transforming the information symbols to the delay-time domain, the matrix $\widetilde{\mathbf{X}}$ containing pilot and data samples can be written as

$$\widetilde{\mathbf{X}}[m,n] = \begin{cases} x_{\mathrm{p}}\mathbf{U}_{\mathrm{T}}[n_{\mathrm{p}},n] & \text{if } m = m_p \\ 0 & \text{if } |m-m_{\mathrm{p}}| \leq l_{\max}, \\ \text{data samples} & \text{otherwise.} \end{cases}$$

The transmitted time domain vector can be written as the superposition of $\mathbf{s}_{\mathrm{d}} \in \mathbb{C}^{NM\times 1}$ containing the data samples and $\mathbf{s}_{\mathrm{p}} \in \mathbb{C}^{NM\times 1}$ contains only the pilot samples:

$$\mathbf{s} = \mathbf{s}_{\mathrm{d}} + \mathbf{s}_{\mathrm{p}} \tag{23}$$

where

$$\mathbf{s}_{\mathrm{p}}[m+nM] = \begin{cases} x_{\mathrm{p}}\mathbf{U}_{\mathrm{T}}[n_{\mathrm{p}},n] & \text{if } m = m_{\mathrm{p}} \\ 0 & \text{otherwise} \end{cases} \tag{24}$$

The interference between the data and pilot samples are avoided due to the guard samples between the data and pilot. This allows the receiver to process the pilot samples for channel estimation separately from data for detection.

From (13), the received pilot samples are related to the transmitted pilot samples as

$$\mathbf{r}_{\mathrm{p}}[q+l] = \bar{g}[l,q+l]\mathbf{s}_{\mathrm{p}}[q] + \mathbf{w}[q+l] \tag{25}$$

where $\mathbf{s}_{\mathrm{p}}[q] = 0$ for $q \neq m_{\mathrm{p}} + nM$. The time domain channel coefficients can then be estimated using the pilot samples at locations $q = (m_{\mathrm{p}} + nM)$ for $n = 0, \ldots, N-1$ and $l = 0, \ldots, l_{\max}$ as

$$\begin{aligned} \hat{\bar{g}}[l, m_{\mathrm{p}}+nM+l] &= \mathbf{r}_{\mathrm{p}}[m_{\mathrm{p}}+nM+l]/\mathbf{s}_{\mathrm{p}}[m_{\mathrm{p}}+nM] \\ &= \mathbf{r}_{\mathrm{p}}[m_{\mathrm{p}}+nM+l]/(x_{\mathrm{p}}\mathbf{U}_{\mathrm{T}}[n_p,n]) \end{aligned} \tag{26}$$

The time-domain channel for the entire frame can then be obtained by interpolating the estimated time domain channel coefficients at locations $(m_{\rm p}+nM+l)$ in (26). The estimated channel coefficients $\hat{\bar{g}}[l,q]$ can be imagined as the delay-time channel sub-sampled by a factor M. Since the time-domain channel for each delay tap can be modelled as the sum of sinusoids (see (14)) corresponding to Doppler-shift of the paths in the delay bin, spline or linear interpolation can be used to reconstruct the delay-time channel coefficients for the entire frame. Successful reconstruction is possible as long as the sampling rate of the delay-time channel (Δf) is at least twice the maximum frequency component (Doppler-shift) of the delay-time channel, i,e., $\nu_{\max} < \Delta f/2$, which is a reasonable assumption for the typical mobile wireless channels.

IV. Low complexity detection

We consider the case when ZPs are inserted between the time-domain blocks since the ZP can be used to embed pilots as shown in the previous section. In this case, the input output relation in (20) can be split into N independent blocks as

$$\mathbf{r}_n = \mathbf{G}_n \cdot \mathbf{s}_n + \mathbf{w}_n, \quad n = 0, \ldots, N-1 \tag{27}$$

where $\mathbf{G}_n \in \mathbb{C}^{M\times M}$ and $\mathbf{w}_n \in \mathbb{C}^{M\times 1}$ are the time-domain channel matrix and the zero-mean noise vector with covariance vector $\sigma_{\rm w}^2\mathbf{I}_M$, respectively, in the n-th time slot.

A. Frequency-domain single tap equalizer

For fair comparison with the traditional OFDM modulation scheme, we use the single tap frequency domain equalizer for USC waveforms. The received time-frequency samples can be obtained by the M-point FFT operation on the received time domain blocks

$$\bar{\mathbf{r}}_n = \mathbf{F}_M \cdot \mathbf{r}_n. \tag{28}$$

as in a standard OFDM receiver. We can then equalize each block in parallel as

$$\bar{\mathbf{s}}_n(m) = \frac{\bar{\mathbf{h}}_n^*[m]\cdot\bar{\mathbf{r}}_n[m]}{|\bar{\mathbf{h}}_n[m]|^2+\sigma_w^2}, \quad m = 0, \ldots, M-1 \tag{29}$$

for $n = 0, \ldots, N-1$ and the frequency domain channel coefficients for each time-domain block are given by

$$\bar{\mathbf{h}}_n = \mathrm{diag}[\mathbf{F}_M \cdot \mathbf{G}_n \cdot \mathbf{F}_M^\dagger] \tag{30}$$

where $\mathrm{diag}[\mathbf{A}]$ denotes the column vector containing the diagonal elements of the square matrix $\mathbf{A}$. The information symbol estimates in the delay-sequency domain can then be obtained by the M-point IFFT operation on the time-frequency domain estimates $\bar{\mathbf{s}}_n$ followed by the N-point WHT as

$$\hat{\mathbf{X}} = \mathbf{F}_M^\dagger \cdot [\bar{\mathbf{s}}_0, \bar{\mathbf{s}}_1, \ldots, \bar{\mathbf{s}}_{N-1}] \cdot \mathbf{U}_{\rm T}^\dagger \tag{31}$$

Fig. 1 shows the QPSK BER performance of USC schemes compared with SC and OFDM modulation at a SNR of 20 dB for different speeds. We consider three different USC waveforms with DFT (OTFS). WHT (OTSM) and DCT. It can be observed that all the USC waveforms offer better performance as compared to OFDM and SC. However, as expected, the time-frequency single tap equalizer performance degrades in the presence of significant Doppler due to significant inter-carrier interference.

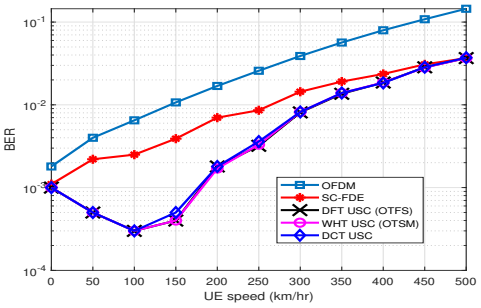

Fig. 1. BER performance of single tap equalizer with QPSK for WHT (OTSM), DFT (OTFS) and DCT compared with OFDM for different speeds at SNR = 20dB

B. Time-domain linear minimum mean-squared error equalizer

The frequency-domain equalizer performance, similar to OFDM, degrades in the presence of high Doppler spread channels (see Fig. 1). In this section we present a block-wise time-domain MMSE equalizer that can provide better performance in the case of time-varying channels. The MMSE equalizer will act as a baseline to compare the performance of the iterative detection methods we present later.

For the input-output relation in (27), the MMSE estimate of the time-domain samples,

$$\hat{\mathbf{s}}_n = (\mathbf{G}_n^\dagger \cdot \mathbf{G}_n + \sigma_w^2\mathbf{I}_M)^{-1} \cdot \mathbf{G}^\dagger \cdot \mathbf{r}_n \tag{32}$$

The information symbols can then be estimated from the delay-time samples as

$$\hat{\mathbf{X}} = [\hat{\mathbf{s}}_0, \hat{\mathbf{s}}_1, \ldots, \hat{\mathbf{s}}_{N-1}] \cdot \mathbf{U}_{\rm T}^\dagger \tag{33}$$

C. Time-domain matched-filtered Gauss Seidel equalizer

The time-domain MMSE equalizer offers good performance, but at the cost of high complexity. To reduce the complexity, we present an iterative detector based on the well known Gauss Seidel (GS) method, [10]. However, different from the traditional method, the GS iteration in this case is done on the matched filtered channel matrix blocks $\mathbf{R}_n = \mathbf{G}_n^\dagger \cdot \mathbf{G}_n$. The matrix input-output relation in (27) after the matched filtering operation can be written as

$$\mathbf{z}_n = \mathbf{R}_n \cdot \mathbf{s}_n + \bar{\mathbf{w}}_n \tag{34}$$

where $\mathbf{R}_n = \mathbf{G}_n^\dagger \cdot \mathbf{G}_n$, $\mathbf{z}_n = \mathbf{G}_n^\dagger \cdot \mathbf{r}_n$ and $\bar{\mathbf{w}}_n = \mathbf{G}_n^\dagger \cdot \mathbf{w}_n$. The GS method is used to iteratively find the least squares solution

$$\hat{\mathbf{s}}_n = \min_{\mathbf{s}_n} ||\mathbf{z}_n - \mathbf{R}_n\mathbf{s}_n||^2 \tag{35}$$

of the M-dimensional linear system of equations in (34).

Let $\mathbf{D}_n$ and $\mathbf{L}_n$ be the matrix containing the diagonal elements and the strictly lower triangular elements of the

matched filter matrix $\mathbf{R}_n$. From [10], the GS iterative method for finding the estimate of $\mathbf{s}_n$ in each iteration is given as

$$\hat{\mathbf{s}}_n^{(i)} = -\mathbf{T}_n \cdot \hat{\mathbf{s}}_n^{(i-1)} + \mathbf{b}_n \tag{36}$$

$$\mathbf{T}_n = (\mathbf{D}_n + \mathbf{L}_n)^{-1} \cdot \mathbf{L}_n^{\dagger}, \quad \mathbf{b}_n = (\mathbf{D}_n + \mathbf{L}_n)^{-1} \cdot \mathbf{z}_n \tag{37}$$

where $\mathbf{T}_n \in \mathbb{C}^{M \times M}$ is the GS iteration matrix. The vector $\hat{\mathbf{s}}_n^{(i)} \in \mathbb{C}^{M \times 1}$ represents the estimate of the transmitted time-domain samples of the n-th block in the i-th iteration. The information symbols in the i-th iteration is then given as

$$\hat{\mathbf{X}}^{(i)} = \mathcal{D}\left(\mathbf{C}^{(i)}\right), \text{ where } \mathbf{C}^{(i)} = [\hat{\mathbf{s}}_0^{(i)}, \hat{\mathbf{s}}_1^{(i)}, \ldots, \hat{\mathbf{s}}_{N-1}^{(i)}] \cdot \mathbf{U}_{\mathrm{T}}^{\dagger} \tag{38}$$

where $\mathcal{D}(.)$ denotes the decision function replacing all the elements of the input with the nearest QAM symbol. The hard decision estimates are transformed back to the time domain to update the time domain estimate to be used in the next iteration.

$$\hat{\mathbf{s}}^{(i)} \leftarrow (1-\delta)\hat{\mathbf{s}}^{(i)} + \delta \mathrm{vec}\left(\mathbf{X}^{(i)} \cdot \mathbf{U}_{\mathrm{T}}\right) \tag{39}$$

where δ is the relaxation parameter to improve the detector convergence for higher modulation schemes like 64-QAM, [8], [10]. As initial estimate to the iterative detection, we can chose either $\mathbf{X}^{(0)} = \mathbf{0}$ or the single-tap solution in (31) yielding faster convergence. Note that the complexity of this algorithm can be significantly reduced by taking advantage of the sparsity of the matrices $\mathbf{G}_n$ and $\mathbf{T}_n$. It is shown in [8], that a delay-time version of this algorithm for OTFS has complexity $O(NML)$, where L is the number of distinct channel delays. The same implementation can be straightforward extended to other USC waveforms.

V. Results and Discussion

For all simulations, we consider QPSK and a frame size of $N = M = 64$. The sub-carrier spacing of 15 kHz is used and the carrier frequency is set to 4 GHz. The maximum delay spread (in terms of integer taps) is taken to be 4 ($l_{\max} = 3$) which is approximately 4 μs, i.e., $L = 4$. The channel delay model is generated according to the standard EVA model with the Doppler shift for the i-th path $\nu_i = \nu_{\max}\cos(\theta_i)$ with θ_i generated from the uniform distribution $U(-\pi, \pi)$, where $\nu_{\max}$ is the maximum Doppler shift [13]. The channel is estimated as described in Section III. For every SNR point in the BER plots, 10^5 frames are simulated.

Fig. 2 shows the BER performance for USC waveforms with DFT (OTFS), WHT (OTSM) and DCT unitary matrix compared with the SC scheme for different UE speeds at 20 dB SNR. It can be observed that as the UE speed increases, the BER performance of the USC schemes improves with increasing Doppler spread where as the SC waveform does not gain from the available Doppler diversity. Further the low-complexity iterative equalizer offers better performance than the high-complexity MMSE equalizer. Fig. 3 shows the BER performance of the USC schemes compared with SC using MMSE and iterative equalizers. It can be observed that the USC scheme for any choice of the unitary matrix $\mathbf{U}_{\mathrm{T}}$ offers around ≈ 6 dB gain at 10^{-3} BER over SC at a UE speed of 500 km/hr.

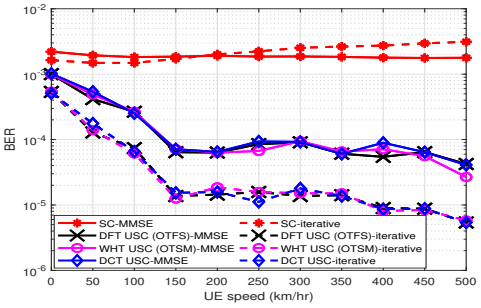

Fig. 2. BER performance of MMSE and iterative equalizer for different speeds at SNR=20 dB

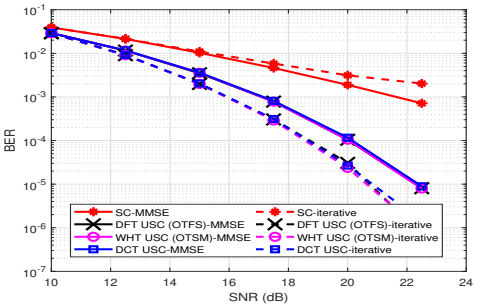

Fig. 3. BER performance with iterative equalizer for OTSM, OTFS, DCT-OTFS compared with SC scheme at 500 km/hr

A. Real-time indoor experiment using SDR

The hardware platform is based on National Instruments universal radio software peripheral (USRP) software defined radio reconfigurable device (NI-USRP-2954R) designed by Ettus Research [12]. A Tx or Rx terminal is implemented with an USRP-2954R connected to a host PC running the National Instruments LabView using PCIe Express x4. The software is based on LabView 2020. We follow the OTFS SDR modem experimental setup described in [11] with the USC experiment parameters listed in Table II.

Fig. 6 presents the BER and FER performance of USC with DFT (OTFS) and WHT (OTSM) unitary matrices compared with OFDM in a real-time indoor channel using the NI USRP-2954 SDR platform. The OFDM frame of bandwidth $B = 2$ MHz is generated according to the IEEE 802.11ac standard for WiFi using 48 out of 64 sub-carriers for data transmission and the rest for pilot and null symbols. The pilot overhead in

TABLE II
Experiment Parameters

Symbol	Parameter	Value
f_c	Carrier frequency	4 GHz
$M \times N$	Number of subcarriers $\times$ time-slots	64×64
T	Symbol Time	32 μs
Δf	Subcarrier spacing	31.25 KHz
d	Tx-Rx Distance	5 meters

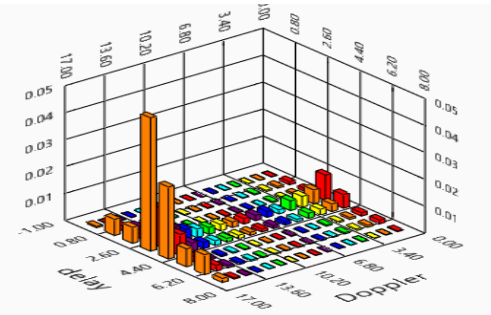

Fig. 4. Received 2-D pilot magnitude for OTFS (delay-Doppler domain) in the indoor wireless channel

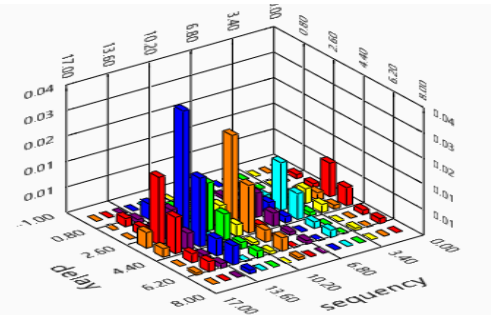

Fig. 5. Received 2-D pilot magnitude for OTSM (delay-sequency domain) in the indoor wireless channel

USC waveforms is generated with a ZP of $L_{\mathrm{G}} = 16$ samples to match the spectral efficiency of above OFDM. The information bits are encoded using a convolutional code of rate $R = 1/2$. At the Rx the single-tap equalizer in Section IV-A is used for low-complexity detection and, the channel estimation method is given in Section III.

An instance of the received 2-D pilot magnitude in the indoor channel measured using the SDR is shown in Figs. 4 and 5 for OTFS and OTSM for a pilot transmitted at $(m_{\mathrm{p}}, n_{\mathrm{p}}) = (3, 0)$. It can be observed that the delay-Doppler domain channel is more localized than the delay-sequency channel. However, the pilot energy is still leaked to all the Doppler bins due to fractional Doppler. Therefore, the entire Doppler axis needs to be reserved for the guard symbols to avoid interference with data. From Fig. 6, both both OTFS and OTSM offer better performance than OFDM in the indoor channel.

One reason for a high error floor in OFDM is due to the lack of CFO compensation at the receiver. OTSM, similar to OTFS, is more robust to CFO as compared to OFDM. Due to the significantly lower complexity of the WHT compared to the DFT and other unitary matrices, the modulation/demodulation complexity of OTSM is the lowest among USC waveforms. Moreover, if the information symbols are integers, the time domain samples after applying the WHT resulting in the least quantization error at the transmitter for the same DAC resolution. Due to above reasons, OTSM can be considered

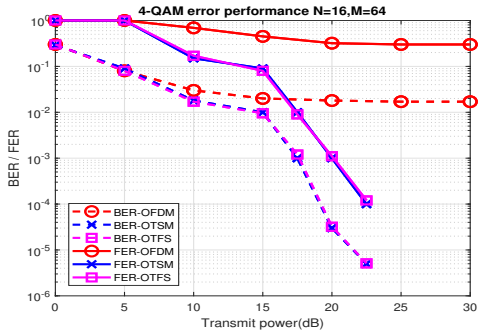

Fig. 6. 4-QAM BER and FER performance of OTSM, OTFS and OFDM using single tap equalizer in real indoor channel

a more energy-efficient waveform than OFDM and OTFS for next-generation wireless channels.

VI. Conclusion

In this paper, we defined a family of waveforms based on precoding the time dimension of the delay-time domain using unitary matrices. We presented channel estimation and detection methods for USC waveforms. Any choice of unitary matrix was shown to offer the same performance as the recently proposed OTFS modulation, but differs in cost of implementation depending on the unitary transform complexity. Finally we verify the performance of USC waveform in a real-time indoor channel using an SDR platform.

References

[1] R. Hadani, S. Rakib, M. Tsatsanis, A. Monk, A. J. Goldsmith, A. F. Molisch, and R. Calderbank, "Orthogonal time frequency space modulation," in *Proc. IEEE Wireless Commun. Netw. Conf. (WCNC)*, San Francisco, CA, USA, Mar. 2017.

[2] Y. Hong, T. Thaj and E. Viterbo, *Delay-Doppler Communications: Principles and Applications*, Academic Press, 2022, ISBN:9780323850285

[3] T. Zemen, M. Hofer, D. Löschenbrand and C. Pacher, "Iterative Detection for Orthogonal Precoding in Doubly Selective Channels," in *Proc. 2018 IEEE 29th Annu. Int. Symp. Personal Indoor and Mobile Radio Commun. (PIMRC)*, Bologna, 2018.

[4] T. Thaj and E. Viterbo, "Orthogonal Time Sequency Multiplexing Modulation" in *Proc. IEEE Wireless Commun. Netw. Conf.*, pp. 1-7, 2021

[5] T. Thaj, E. Viterbo and Y. Hong, "Orthogonal Time Sequency Multiplexing Modulation: Analysis and Low-Complexity Receiver Design" in *IEEE Trans. on Wireless Commun.*, 2021, doi: 10.1109/TWC.2021.3088479.

[6] D. S. Stoffer, "Walsh-Fourier Analysis and Its Statistical Applications," *J. American Statistical Association,* vol. 86, no. 414, pp. 461–479.

[7] P. Raviteja, K. T. Phan, and Y. Hong, "Embedded Pilot-Aided Channel Estimation for OTFS in Delay–Doppler Channels," *IEEE Trans. Veh. Technol.,* vol. 68, no. 5, pp. 4906-4917, May 2019.

[8] T. Thaj and E. Viterbo, "Low Complexity Iterative Rake Decision Feedback Equalizer for Zero Padded OTFS Systems," *IEEE Trans. on Veh. Tech.*, Dec 2020. doi: 10.1109/TVT.2020.3044276

[9] S. K. Mohammed,"Derivation of OTFS Modulation From First Principles." in *IEEE Trans. on Veh. Tech.*, vol. 70, no. 8, pp. 7619-7636, Aug. 2021, doi: 10.1109/TVT.2021.3069913.

[10] A. Björck, *Numerical Methods for Least Squares Problems,* SIAM, 1996. doi: 10.1137/1.9781611971484

[11] T. Thaj and E. Viterbo, "OTFS Modem SDR Implementation and Experimental Study of Receiver Impairment Effects," in *2019 IEEE Int. Conf. on Commun. Workshops,* pp. 1-6, 2019, doi: 10.1109/ICCW.2019.8757167.

[12] USRP-2954 Specifications - National Instruments, Available online: https://www.ni.com/pdf/manuals/375725c.pdf

Chapter 7

Conclusion and Future Directions

In this thesis, we studied waveform design for high mobility wireless channels, focusing on the recently proposed OTFS modulation scheme, which offers significantly better performance than the standard OFDM waveform in high mobility wireless channels. Several aspects of OTFS, including real-time implementation, detection, channel estimation, MIMO, and precoding, were investigated. We summarize our key contributions and discuss some future research directions in the following.

7.1 Contributions

In Chapter 2, we implemented an OTFS transceiver using National Instruments USRP devices, covering aspects of timing synchronization, channel estimation, and detection. We investigated the effects of hardware impairments such as CFO and DC offset on the performance of OTFS. The superior performance of OTFS was verified by comparing it with the standard CP-OFDM waveform in both a real indoor frequency-selective channel and a partially emulated doubly-selective channel. This implementation is among the first academic test-bed for OTFS and gave significant insights into the practical workings of this new modulation scheme.

In Chapter 3, we first derive the OTFS input-output relation in the vector form in the delay-Doppler, delay-time, and time domains. A low-complexity detection method based on the MRC scheme was proposed. The complexity of the proposed method is linear in the number of information symbols and delay taps and is independent of the QAM

size or the channel Doppler spread. The proposed MRC detection was shown to be of significantly lower complexity than that of the state-of-the-art detectors based on MP and LMMSE methods. The proof of convergence and methods to speed up convergence was also provided. We also propose a turbo decoder using LDPC codes to improve the error performance further and speed up convergence. Finally, the performance is compared with the standard OFDM waveform.

In Chapter 4, we first extend the vector input-output relation to a point-to-point MIMO case. Then a linear diversity combining detector is proposed with complexity linear in the number of transmitter and receiver antennas, the number of information symbols, and the number of unique delay taps. The effect of spatial correlation is studied, and a sample-based method is proposed to estimate the spatial correlation at the receiver. The proposed detection method is modified to compensate for the degrading effects of spatial correlation. The performance and complexity of the proposed method are compared with the MP and LMMSE-based detectors as the number of antennas, the level of spatial correlation, and the number of propagation paths are increased.

Chapter 5 proposes a new modulation scheme called OTSM based on multiplexing the information symbols in the delay-sequency domain. We first introduce the concept of sequency and how it is related to the more familiar notion of frequency. We present the OTSM system model and methods for detection and channel estimation. OTSM offers better performance than OFDM and similar performance to OTFS but at a much lower complexity of modulation/demodulation. Finally, the performance of OTSM is compared with SC, OFDM, and OTFS for different UE speeds, propagation paths, and QAM sizes for both uncoded and coded cases and taking into consideration the effects of practical channel estimation.

Finally, in Chapter 6, we present USC modulation, a family of waveforms based on unitary precoding along the time dimension of the delay-time domain. OTFS and OTSM can then be viewed as a USC waveform with DFT and WHT, respectively, as the precoding transforms along the time dimension. All the USC waveforms have the common property that the information symbols are spread in the available time-frequency resource using orthogonal basis functions. The system model for the USC waveform is presented, and the input-output relation is derived. Some detection and channel estimation methods are presented, and the performance of USC waveforms is analyzed

for different choices of the unitary transform matrix, such as DFT, WHT, and DCT. Finally, USC based on DFT and WHT are implemented and compared with the traditional CP-OFDM waveform in a real-time channel using the USRP SDR device similar to which was used in Chapter 1. Finally, we discuss how to choose the appropriate unitary transform for precoding, and based on our experiments, it can be concluded that any USC waveform could be considered a potential candidate waveform for 6G, and the choice of unitary transform depends on the user requirements.

7.1.1 Brief answers to research questions

In this section, we provide brief answers to the research questions posed in Section 1.4.

- **What are the drawbacks of current systems based on OFDM and what is the potential candidate waveform to replace OFDM? Why is the new waveform expected to offer better performance than OFDM?**

  The drawbacks of OFDM were discussed in Section 1.2.2.1 which includes high sensitivity to CFO and phase noise, high PAPR, performance degradation in high mobility wireless channels, and high pilot overhead. OTFS can be considered a potential candidate waveform to replace CP-OFDM in next-generation communications systems. OTFS achieves better error performance than OFDM due to multiplexing information symbols in the delay-Doppler domain. Each information symbol is thus spread in the entire time-frequency plane using 2-D orthogonal basis functions (ISFFT), resulting in roughly the same SNR for all symbols even after passing through a rapidly time-varying channel. This leads to better BER performance than OFDM in double-selective channels. The superior performance of OTFS over OFDM in different settings, including small and large frame sizes and SISO and MIMO channels, were shown in Chapters 2-6. Moreover, only a single pilot is required to estimate the channel in the delay-Doppler domain, whereas, in OFDM, the number of required pilots increases as the delay and Doppler spread increases since more pilots are required to capture and interpolate the rapidly fluctuating time-frequency channel.

- **Has the performance of OTFS been verified in practical scenarios, and what are the issues faced by OTFS when implemented in real hardware? How to compensate for hardware impairments?**

  The practical implementation of OTFS was presented, and the effect of receiver impairments was investigated in Chapter 2. The primary hardware impairments faced by OTFS include CFO, DC offset, IQ imbalance, phase noise, and PA non-linearity. Chapter 2, in particular, investigates the effects of CFO and DC offset and discusses methods to compensate for it. Further, the BER and FER of OTFS were compared and shown to be better than OFDM in both a real-time static and a partially emulated mobile channel.

- **What are available OTFS detection methods in the literature? Can we design an OTFS detector with a complexity comparable to OFDM? Can OFDM get close to OTFS in terms of error performance with the help of a robust error-correcting code?**

  The main OTFS detection methods are based broadly on single tap and SIC frequency domain detection, MMSE-, MP- and MRC- based detection. Several variations of MP and MMSE detection methods are also available in the literature. Chapter 3 proposes an MRC-based detection method. It was shown that the complexity of detection methods could be significantly reduced by performing most of the operations in the delay-time domain instead of the delay-Doppler domain. The MRC detection method, when implemented in the delay-time domain in Chapter 3, was shown to incur a complexity of just $O(NML)$, which is comparable to the OFDM single tap equalizer complexity: $O(NM\log_2(M))$. The performance of the MRC-based OTFS detection method was compared with OFDM for both the coded and uncoded cases. Even though the gap between the OFDM performance and OTFS can be reduced with the help of a robust error-correcting code such as a long LDPC code (for example, codeword length of 8K bits), OTFS still offers better performance than OFDM.

- **How can detection and channel estimation in SISO OTFS be extended to MIMO OTFS, what are the practical issues and challenges faced in a MIMO setting and how to compensate for them? How do the performance and complexity compare against MIMO OFDM?**

The MRC-based detection in Chapter 3 and single pilot channel estimation for SISO-OTFS was extended to the MIMO case in Chapter 4. The major challenges in the case of MIMO-OTFS are the high receiver complexity, channel estimation overhead, and performance degradation due to spatial correlation. The MIMO detection method proposed in Chapter 4 is linear in the number of terminals, frame size, and the number of delay taps and has significantly lower complexity as compared to the MMSE and MP-based methods. Methods to estimate the spatial correlation values for the received pilots and compensate for them in the detection method were also presented in Chapter 3. Further, the performance of OTFS was compared to OFDM for different number of antennas in a high mobility channel to validate the performance gains offered by OTFS.

- **Are there other waveforms that can offer better performance than OTFS in high mobility channels? What is the common property for such waveforms and in what scenarios do they outperform OTFS?**

  In Chapters 5 and 6, we investigate novel waveforms that can offer similar or better performance than OTFS in high mobility channels. OTSM is a novel waveform proposed in Chapter 5 based on multiplexing the information symbols in the delay-sequency domain and is shown to offer similar error performance to OTFS but at much lower modulation/demodulation complexity. This is because OTFS is based on DFT, whereas OTSM is based on the WHT, which requires just additions and subtractions. Chapter 6 presents a family of waveforms that can offer similar error performance to OTFS, called USC waveforms. The common property of all these waveforms is that each information symbol is spread in the entire time-frequency space using 2-D orthogonal transformations: ISFFT in the case of OTFS and IFFT-WHT in the case of OTSM. The major advantage of OTFS is that the delay-Doppler domain offers the sparsest representation of the channel out of all the USC waveforms, leading to low pilot overhead. This leads to the lowest detection complexity of all USC waveforms if detection is performed in the information symbol domain (delay-Doppler for OTFS and delay-sequency for OTSM). However, all these waveforms incur the same cost by performing detection in the time domain. Further, in the case of transmission, OTSM offers the lowest complexity and is suitable for low-power applications due to the WHT.

Further advantages and disadvantages of different unitary precoding transforms are discussed in Chapters 5 and 6.

7.2 Future Directions

We now list some future research directions and extensions to the work presented in this thesis.

- Methods to estimate the actual delay-Doppler channel coefficients in the case of fractional delay and Doppler shifts.
- Methods to reduce the PAPR due to the single pilot-based embedded pilot channel estimation method by designing 2-D pilot sequences and low-complexity estimation algorithms.
- Modelling of very high mobility wireless channels with time-varying channel gains as well delay and Doppler-shifts that vary within a frame, for example: rotating or accelerating scatterers or terminals
- Extension of the MRC detection method to all OTFS variants (i.e., with single/multiple CP/ZPs) and multiuser uplink systems as well as massive MIMO systems. The detection method will also be extended to cases where the channel delay spreads are greater than the block length leading to inter-block interference even in the presence of a CP or ZP.
- OTFS for joint radar and communication systems or integrated sensing and communications along with the use of machine learning for blind/ semi-blind channel estimation and detection.